

## ABSTRACT

Title of Document:                   INFRARED SPECTROSCOPY OF PARENT  
  VOLATILES IN COMETS: CHEMICAL  
  DIVERSITY AND A NEW FLUORESCENCE  
  MODEL FOR THE ETHANE  $\nu_5$  BAND.

Yana Lyubomirova Radeva, Doctor of  
Philosophy, 2010

Directed By:                           Professor Michael F. A'Hearn, Department of  
  Astronomy  
  Doctor Michael J. Mumma, NASA Goddard  
  Space Flight Center

This work investigates the chemical and dynamical diversities of comets, and explores the clues they hold to understanding the formation and evolution of the Solar System. This research is based on analysis of high-resolution infrared spectroscopic data obtained with the Near Infrared Echelle Spectrograph on the Keck II telescope. Gas production rates of parent volatile species released from cometary nuclei are measured, and the relative enrichment of organics in comets, with respect to the dominant volatile - H<sub>2</sub>O - is determined. These measurements require fluorescence models for each species, as well as derivation of an accurate rotational temperature.

A major contribution of this work is the development of a theoretical model of the fluorescence of the infrared  $\text{C}_2\text{H}_6$   $\nu_5$  band in comets (at  $2896\text{ cm}^{-1}$ ), which can be used to derive an accurate rotational temperature for this parent volatile (unlike the  $\text{C}_2\text{H}_6$   $\nu_7$  band at  $2985\text{ cm}^{-1}$ ). As a symmetric hydrocarbon  $\text{C}_2\text{H}_6$  is uniquely observed in the infrared, and now brings the number of molecules for which we can derive a rotational temperature to four (along with  $\text{H}_2\text{O}$ ,  $\text{HCN}$  and  $\text{CO}$ ). Also,  $\text{C}_2\text{H}_6$   $\nu_5$  is observed simultaneously with  $\text{H}_2\text{CO}$ ,  $\text{OH}$ ,  $\text{CH}_4$ ,  $\text{HCN}$ ,  $\text{C}_2\text{H}_2$  and  $\text{H}_2\text{O}$ , which eliminates many systematic effects.

The  $\text{C}_2\text{H}_6$   $\nu_5$  model is applied to cometary spectra, and it used to extract ethane rotational temperatures, production rates and mixing ratios. The rotational temperatures derived from  $\text{C}_2\text{H}_6$   $\nu_5$  agree with those measured for  $\text{H}_2\text{O}$  (and other species). Mixing ratios from the  $\text{C}_2\text{H}_6$   $\nu_7$  band are also confirmed by the  $\nu_5$  band – agreement is within  $1\text{-}\sigma$  ( $2\text{-}\sigma$  in one case).

Analysis of the depleted organic composition of the Oort cloud comet C/2000 WM<sub>1</sub> (LINEAR) is presented, along with the ecliptic comet 2P/Encke, and their compositions are compared with those of other comets. The results from this dissertation contribute to understanding physics in the inner cometary coma, and on a grander scale – to the exploration of cometary origins in terms of Solar System formation and evolution.

INFRARED SPECTROSCOPY OF PARENT VOLATILES IN COMETS:  
CHEMICAL DIVERSITY AND A NEW FLUORESCENCE MODEL FOR THE  
ETHANE  $\nu_5$  BAND.

By

Yana Lyubomirova Radeva.

Dissertation submitted to the Faculty of the Graduate School of the  
University of Maryland, College Park, in partial fulfillment  
of the requirements for the degree of  
Doctor of Philosophy  
2010

Advisory Committee:

Professor Michael F. A'Hearn, Co-Chair

Doctor Michael J. Mumma, Co-Chair

Professor Douglas P. Hamilton

Doctor Jessica M. Sunshine

Doctor Lori M. Feaga

Doctor Neil Dello Russo

Professor Richard J. Walker

© Copyright by  
Yana Lyubomirova Radeva  
2010

## Preface

This work includes the full analysis of the organic composition of comet C/2000 WM<sub>1</sub> (LINEAR), which was published in *Icarus, International Journal of Solar System Studies* (Radeva et al., *Icarus* 2010), and has also been presented at several conferences: Division for Planetary Sciences annual meetings; Astrobiology Science Conference; Asteroids, Comets, Meteors conference. Neither the work on the fluorescence model of the C<sub>2</sub>H<sub>6</sub>  $\nu_5$  band, nor that on the organic composition of comet 2P/Encke was published previously.

To my family, and especially my mother  
who first showed me the magic of the night sky

## Acknowledgements

I am grateful to my advisors Dr. Michael Mumma and Dr. Michael A'Hearn for teaching me and for their guidance throughout the entire research that comprises this dissertation. Their advice and support have been essential in the completion of each stage of this work, from the initial data analysis, through the publication of my first paper, to understanding the physics underlying this research. I feel very fortunate to have had Dr. Mumma and Dr. A'Hearn as my advisors.

I am grateful to the amazing team led by Dr. Mumma at the NASA Goddard Space Flight Center, especially Dr. Geronimo Villanueva, Dr. Boncho Bonev and Dr. Michael DiSanti. I have worked with every one of them on different parts of this research, and thus, they have been my teachers as well. I would like to acknowledge Dr. Villanueva, with whom I worked closely on the creation of the  $C_2H_6$   $v_5$  model, and whose guidance and support have been essential. I would also like to acknowledge Dr. Boncho Bonev for instructing me on all aspects of our data reduction, and for mentoring me during the analysis of comet C/2000 WM<sub>1</sub> (LINEAR), which was my second-year project.

I would like to acknowledge Dr. Neil Dello Russo, who was my advisor at NASA GSFC during my internship in the summer of 2004; and my entire dissertation committee for their feedback and helpful revisions: Dr. Doug Hamilton, Dr. Jessica Sunshine, Dr. Lori Feaga, Dr. Richard Walker and Dr. Neil Dello Russo. I would

also like to acknowledge my Connecticut College professors: Dr. Leslie Brown, who was my undergraduate advisor, and Dr. Michael Monce, who taught most of my physics classes.

My family has supported me throughout all years of higher education. I will never forget the first time my mother took me to the Bulgarian National Astronomical Observatory - Rozhen when I was five years old; and then for many years to come. It was during the warm summers in the beautiful mountain where the Observatory is located, that I first discovered the magical attraction of the night sky. I would also like to thank Paul-Alexandre Rischard for his support throughout the past five years of graduate school, and for introducing me to the beauty of his home country: France.

Finally, I would like to acknowledge everyone at the University of Maryland and NASA GSFC who has supported me and thus, contributed to my experience as a graduate student at one time or another.



## Table of Contents

Preface.....	ii
Acknowledgements.....	iv
Table of Contents.....	vi
List of Tables.....	viii
List of Figures.....	x
Chapter 1: Introduction.....	1
Physical Characteristics of Comets.....	1
Present Day Reservoirs.....	3
Cometary Origins and the Chemical Diversity of Cometary Nuclei.....	6
Chapter 2: Infrared Spectroscopy of Comets.....	10
Ro-vibrational Spectroscopy and Application to Comets.....	10
Summary of Excitation Processes in Cometary Comae.....	16
<i>Radiative Electronic Excitation</i> .....	16
<i>Radiative Vibrational Excitation</i> .....	17
<i>Radiative Rotational Excitation</i> .....	19
<i>Collisional Excitation</i> .....	19
Overview of the Chemical Composition of Comets Analyzed by our Team.....	21
The Astrobiological Importance of Comets.....	24
The $\nu_5$ band of $C_2H_6$ and its Importance.....	26
Chapter 3: Observations with NIRSPEC and Data Analysis.....	28
Overview of NIRSPEC in Cometary Observations.....	28
From Raw Frames to Cometary Emission Spectra.....	30
Rotational Temperature Derivation.....	43
Production Rates of Parent Volatiles.....	46
Chapter 4: The Depleted Organic Composition of Comet C/2000 WM <sub>1</sub> (LINEAR). 49	
Observations of C/2000 WM <sub>1</sub> (LINEAR).....	49
Spectral Gallery.....	50
Rotational Temperatures and Production Rates.....	59

Discussion .....	64
Summary of Composition .....	72
Chapter 5: The Organic Composition of Comet 2P/Encke.....	74
Spectral Gallery .....	75
Rotational Temperatures and Production Rates.....	84
The Organic Composition of Encke in Perspective.....	87
Summary of Composition.....	96
Chapter 6: Development and Application of a Fluorescence Model of the C <sub>2</sub> H <sub>6</sub> v <sub>5</sub>	
Band .....	98
Motivation.....	98
Development of the C <sub>2</sub> H <sub>6</sub> v <sub>5</sub> model .....	99
<i>Building the ground vibrational state</i> .....	99
<i>Building the excited v<sub>5</sub> state</i> .....	106
<i>Determining pumping rates</i> .....	109
<i>Calculating fluorescence efficiency factors</i> .....	110
Application of the C <sub>2</sub> H <sub>6</sub> v <sub>5</sub> model.....	111
<i>Observing Log</i> .....	111
<i>Overview of Comets</i> .....	113
<i>Spectral Gallery</i> .....	116
<i>Rotational Temperatures, Mixing Ratios and Production Rates</i> .....	125
<i>Blends in the C<sub>2</sub>H<sub>6</sub> v<sub>5</sub> region</i> .....	147
<i>Overall Organic Composition</i> .....	148
<i>Summary</i> .....	157
Chapter 7: Summary of Results .....	160
Appendices.....	164
Appendix I. ....	164
Appendix II. ....	169
Bibliography .....	171

## List of Tables

<b>Table 1.1</b>	Dynamical classification of comets (Levison 1996).....	6
<b>Table 2.1</b>	The organic composition of comets based on infrared spectroscopy..	22
<b>Table 4.1</b>	Observing log for C/2000 WM <sub>1</sub> .....	50
<b>Table 4.2</b>	Rotational temperatures for C/2000 WM <sub>1</sub> .....	59
<b>Table 4.3</b>	Production rates for C/2000 WM <sub>1</sub> on 23 Nov. 2001.....	61
<b>Table 4.4</b>	Production rates for C/2000 WM <sub>1</sub> on 24 Nov. 2001.....	62
<b>Table 4.5</b>	Production rates for C/2000 WM <sub>1</sub> on 25 Nov. 2001.....	63
<b>Table 4.6</b>	H <sub>2</sub> O production rates in C/2000 WM <sub>1</sub> .....	68
<b>Table 4.7</b>	Mixing ratios in C/2000 WM <sub>1</sub> : comparison with other groups.....	71
<b>Table 5.1</b>	Observing log for 2P/Encke.....	74
<b>Table 5.2</b>	Production rates and mixing ratios of volatiles in 2P/Encke.....	86
<b>Table 5.3</b>	Rotational temperatures of H <sub>2</sub> O and HCN in a sample of comets, as a function of mean r <sub>h</sub> and overall production rate.....	90
<b>Table 5.4</b>	Sublimation temperatures of molecules.....	95
<b>Table 6.1</b>	Normal vibrations of C <sub>2</sub> H <sub>6</sub> .....	99
<b>Table 6.2</b>	Rotational and vibrational partition functions.....	105
<b>Table 6.3</b>	Observing log.....	112
<b>Table 6.4</b>	G-factors of C <sub>2</sub> H <sub>6</sub> v <sub>5</sub> .....	138
<b>Table 6.5</b>	Comparison of rotational temperatures derived from C <sub>2</sub> H <sub>6</sub> v <sub>5</sub> , H <sub>2</sub> O, HCN and CO.....	140
<b>Table 6.6</b>	Comparison of mixing ratios (%) from C <sub>2</sub> H <sub>6</sub> v <sub>5</sub> and C <sub>2</sub> H <sub>6</sub> v <sub>7</sub> .....	144

<b>Table 6.7</b>	Comparison of production rates derived from $C_2H_6$ $\nu_5$ and $C_2H_6$ $\nu_7$ .	146
<b>Table 6.8</b>	Weighted-mean mixing ratios of $C_2H_6$ .....	148
<b>Table 6.9</b>	The organic composition of comets analyzed by the team at NASA GSFC.....	149
<b>Table 6.10</b>	Overview of comets and their Tisserand parameters.....	152
<b>Table A.1</b>	Quantitative parameters for spectral lines of $C_2H_6$ $\nu_5$ .....	164

## List of Figures

<b>Figure 1.1</b>	Image of comet C/1995 O1 (Hale-Bopp).....	2
<b>Figure 1.2</b>	The orbit of a comet around the Sun.....	3
<b>Figure 2.1</b>	Vibrational modes of H <sub>2</sub> O ( $\nu_1$ , $\nu_2$ and $\nu_3$ ).....	11
<b>Figure 2.2</b>	Illustration of allowed ro-vibrational transitions.....	13
<b>Figure 3.1</b>	Illustration of an echelle grating and a cross disperser grating.....	29
<b>Figure 3.2</b>	Raw frame of six echelle orders.....	31
<b>Figure 3.3</b>	Nodding of the telescope along the slit.....	32
<b>Figure 3.4</b>	Residual raw frame after an A1-B1-B2+A2 sequence.....	33
<b>Figure 3.5</b>	Masks of an echelle order used to remove hot pixels and cosmic ray hits.....	34
<b>Figure 3.6</b>	Illustration of the angles in the echelle grating equation.....	36
<b>Figure 3.7</b>	Spatial straightening of standard star frames.....	37
<b>Figure 3.8</b>	Wavenumber calibration.....	38
<b>Figure 3.9</b>	Terrestrial transmittance model generated with LBLRTM.....	40
<b>Figure 3.10</b>	Echelle order containing C <sub>2</sub> H <sub>6</sub> $\nu_7$ from C/2000 WM <sub>1</sub> .....	41
<b>Figure 3.11</b>	Calibrated stellar frame.....	43
<b>Figure 3.12</b>	The production rate of H <sub>2</sub> O on 25 Nov. in comet C/2000 WM <sub>1</sub> .....	48
<b>Figure 4.1</b>	WM <sub>1</sub> cometary spectrum and superimposed terrestrial transmittance model (CH <sub>3</sub> OH).....	51

<b>Figure 4.2</b>	WM <sub>1</sub> cometary spectrum and superimposed terrestrial transmittance model (C <sub>2</sub> H <sub>6</sub> ).....	52
<b>Figure 4.3</b>	WM <sub>1</sub> cometary spectrum and superimposed terrestrial transmittance model (H <sub>2</sub> O).....	53
<b>Figure 4.4</b>	WM <sub>1</sub> cometary spectrum and superimposed terrestrial transmittance model (H <sub>2</sub> CO).....	54
<b>Figure 4.5</b>	WM <sub>1</sub> cometary spectrum and superimposed terrestrial transmittance model (CH <sub>4</sub> ).....	55
<b>Figure 4.6</b>	WM <sub>1</sub> cometary spectrum and superimposed terrestrial transmittance model (HCN, C <sub>2</sub> H <sub>2</sub> ).....	56
<b>Figure 4.7</b>	WM <sub>1</sub> cometary spectrum and superimposed terrestrial transmittance model (H <sub>2</sub> O).....	57
<b>Figure 4.8</b>	WM <sub>1</sub> cometary spectrum and superimposed terrestrial transmittance model (CO and H <sub>2</sub> O).....	58
<b>Figure 4.9</b>	Excitation analysis for HCN and for H <sub>2</sub> O, on 25 Nov. 2001.....	60
<b>Figure 4.10</b>	Excitation diagram for CO on 25 Nov. 2001.....	64
<b>Figure 4.11</b>	Mixing ratios of parent volatiles in C/2000 WM <sub>1</sub> (LINEAR) measured on 23, 24 and 25 Nov. 2001.....	66
<b>Figure 4.12</b>	Measurements of the production rate of H <sub>2</sub> O in C/2000 WM <sub>1</sub> (LINEAR).....	70
<b>Figure 5.1</b>	Encke cometary spectrum and superimposed terrestrial transmittance model (CH <sub>3</sub> OH).....	76

<b>Figure 5.2</b>	Encke cometary spectrum and superimposed terrestrial transmittance model ( $C_2H_6$ $\nu_7$ ).....	77
<b>Figure 5.3</b>	Encke cometary spectrum and superimposed terrestrial transmittance model ( $H_2O$ ).....	78
<b>Figure 5.4</b>	Encke cometary spectrum and superimposed terrestrial transmittance model ( $H_2CO$ ).....	79
<b>Figure 5.5</b>	Encke cometary spectrum and superimposed terrestrial transmittance model ( $CH_4$ ).....	80
<b>Figure 5.6</b>	Encke cometary spectrum and superimposed terrestrial transmittance model ( $HCN$ and $C_2H_2$ ).....	81
<b>Figure 5.7</b>	Encke cometary spectrum and superimposed terrestrial transmittance model ( $H_2O$ ).....	82
<b>Figure 5.8</b>	Encke cometary spectrum and superimposed terrestrial transmittance model ( $CO$ and $H_2O$ ).....	83
<b>Figure 5.9</b>	Excitation and correlation analysis for $H_2O$ in Panel A and $HCN$ on 4 Nov. 2003.....	85
<b>Figure 5.10</b>	Variation of rotational temperatures of $H_2O$ and $HCN$ in a sample of comets, as a function of mean $r_h$ .....	92
<b>Figure 5.11</b>	Variation of rotational temperatures of $H_2O$ and $HCN$ in a sample of comets, as a function of overall production rate ( $Q$ ).....	93
<b>Figure 6.1</b>	Illustration of the $C_2H_6$ molecule.....	101
<b>Figure 6.2</b>	Vibrational modes of $C_2H_6$ .....	102
<b>Figure 6.3</b>	Symmetric top molecule.....	104

<b>Figure 6.4</b>	Illustration of transitions.....	110
<b>Figure 6.5</b>	17P/Holmes ( $v_5$ ).....	117
<b>Figure 6.6</b>	C/2000 WM <sub>1</sub> (LINEAR) ( $v_5$ ).....	118
<b>Figure 6.7</b>	C/2004 Q2 (Machholz) ( $v_5$ ).....	119
<b>Figure 6.8</b>	C/2001 A2 (LINEAR) ( $v_5$ ).....	120
<b>Figure 6.9</b>	C/2007 N3 (Lulin) ( $v_5$ ).....	121
<b>Figure 6.10</b>	C/2007 W1 (Boattini) ( $v_5$ ).....	122
<b>Figure 6.11</b>	8P/Tuttle ( $v_5$ ).....	123
<b>Figure 6.12</b>	2P/Encke ( $v_5$ ).....	124
<b>Figure 6.13.</b>	17P/Holmes (C <sub>2</sub> H <sub>6</sub> $v_5$ synthetic model superimposed).....	126
<b>Figure 6.14</b>	C/2000 WM <sub>1</sub> (LINEAR) (C <sub>2</sub> H <sub>6</sub> $v_5$ synthetic model superimposed)..	126
<b>Figure 6.15</b>	C/2004 Q2 (Machholz) (C <sub>2</sub> H <sub>6</sub> $v_5$ synthetic model superimposed)....	127
<b>Figure 6.16</b>	C/2001 A2 (LINEAR) (C <sub>2</sub> H <sub>6</sub> $v_5$ synthetic model superimposed).....	127
<b>Figure 6.17</b>	C/2007 N3 (Lulin) (C <sub>2</sub> H <sub>6</sub> $v_5$ synthetic model superimposed).....	128
<b>Figure 6.18</b>	C/2007 W1 (Boattini) (C <sub>2</sub> H <sub>6</sub> $v_5$ synthetic model superimposed).....	128
<b>Figure 6.19</b>	8P/Tuttle (C <sub>2</sub> H <sub>6</sub> $v_5$ synthetic model superimposed).....	129
<b>Figure 6.20</b>	2P/Encke (C <sub>2</sub> H <sub>6</sub> $v_5$ synthetic model superimposed).....	129
<b>Figure 6.21</b>	Spread in production rates from individual lines at the optimal $T_{\text{rot}} = 70^{-10}/_{+11}$ K for 17P/Holmes.....	130
<b>Figure 6.22</b>	Spread in production rates from individual lines at the optimal $T_{\text{rot}} = 69^{-13}/_{+14}$ K for C/2000 WM <sub>1</sub> (LINEAR).....	131



<b>Figure 6.23</b>	Spread in production rates from individual lines at the optimal $T_{\text{rot}} = 86^{-17}/_{+18}$ K for C/2004 Q2 (Machholz).....	132
<b>Figure 6.24</b>	Spread in production rates from individual lines at the optimal $T_{\text{rot}} = 85^{-14}/_{+13}$ K for C/2001 A2 (LINEAR).....	133
<b>Figure 6.25</b>	Spread in production rates from individual lines at the optimal $T_{\text{rot}} = 72^{-11}/_{+12}$ K for C/2007 N3 (Lulin).....	134
<b>Figure 6.26</b>	Spread in production rates from individual lines at the assumed $T_{\text{rot}} = 85$ K for C/2007 W1 (Boattini).....	135
<b>Figure 6.27</b>	Spread in production rates from individual lines at the assumed $T_{\text{rot}} = 50$ K for 8P/Tuttle.....	136
<b>Figure 6.28</b>	Spread in production rates from individual lines at the assumed $T_{\text{rot}} = 24$ K for 2P/Encke.....	137
<b>Figure 6.29</b>	Comparison of rotational temperatures of $\text{C}_2\text{H}_6$ $\nu_5$ , $\text{H}_2\text{O}$ and $\text{HCN}$ ..	142
<b>Figure 6.30</b>	Comparison of mixing ratios of $\text{C}_2\text{H}_6$ $\nu_5$ and $\text{C}_2\text{H}_6$ $\nu_7$ .....	145
<b>Figure 6.31</b>	Model of $\text{H}_2\text{CO}$ (in red) in the $\text{C}_2\text{H}_6$ $\nu_5$ region.....	147
<b>Figure 6.32</b>	Mixing ratios in $\text{WM}_1$ and Encke compared to comets A2 and S4...151	
<b>Figure 6.33</b>	Mixing ratios of $\text{CH}_4$ and $\text{C}_2\text{H}_6$ in comets as a function of $T_J$ .....	154
<b>Figure 6.34</b>	Mixing ratios of $\text{C}_2\text{H}_2$ , $\text{HCN}$ and $\text{H}_2\text{CO}$ as a function of $T_J$ .....	155
<b>Figure 6.35</b>	Mixing ratios of $\text{CH}_3\text{OH}$ and $\text{CO}$ in comets as a function of $T_J$ .....	156

## Chapter 1: Introduction

### *Physical Characteristics of Comets*

The chemical diversity of comets holds key clues to understanding the origin and evolution of our Solar System, and the delivery of water and pre-biotic organics to the young Earth. Comets are remnant debris of the Solar System's formation about 4.6 billion years ago, and are relatively unaltered. A cometary nucleus consists of ice (mostly water) and dust particles. When a comet approaches the sun, the influence of solar radiation causes ices in its nucleus to sublimate, and the escaping gas drags dust particles along with it. Thus, the comet forms a gaseous coma, and tails (dust and gas tails of extremely low density) (see Figure 1.1 & Figure 1.2). Cometary nuclei are irregularly shaped and their sizes range between less than 1 km and tens of kilometers, while the coma can have a diameter of  $10^4$ - $10^5$  km, and the length of the tails can exceed  $10^7$  km. Cometary nuclei have low albedo of approximately 0.04 (geometric albedo - Kelley & Wooden 2009, Li et al. 2007, Lamy et al. 2004).

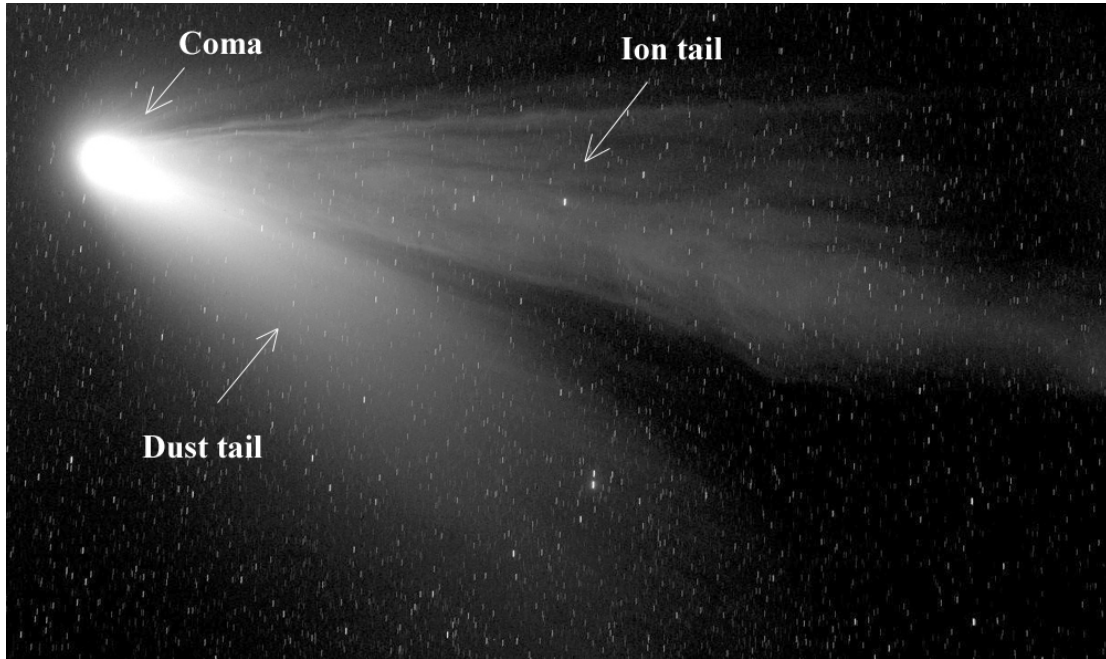


**Figure 1.1.** Image of comet C/1995 O1 (Hale-Bopp) (acquired by V. Radeva & Y. Radeva, 1997, with the 50/70cm Schmidt telescope at the Bulgarian National Astronomical Observatory). The coma, ion and dust tails are marked.

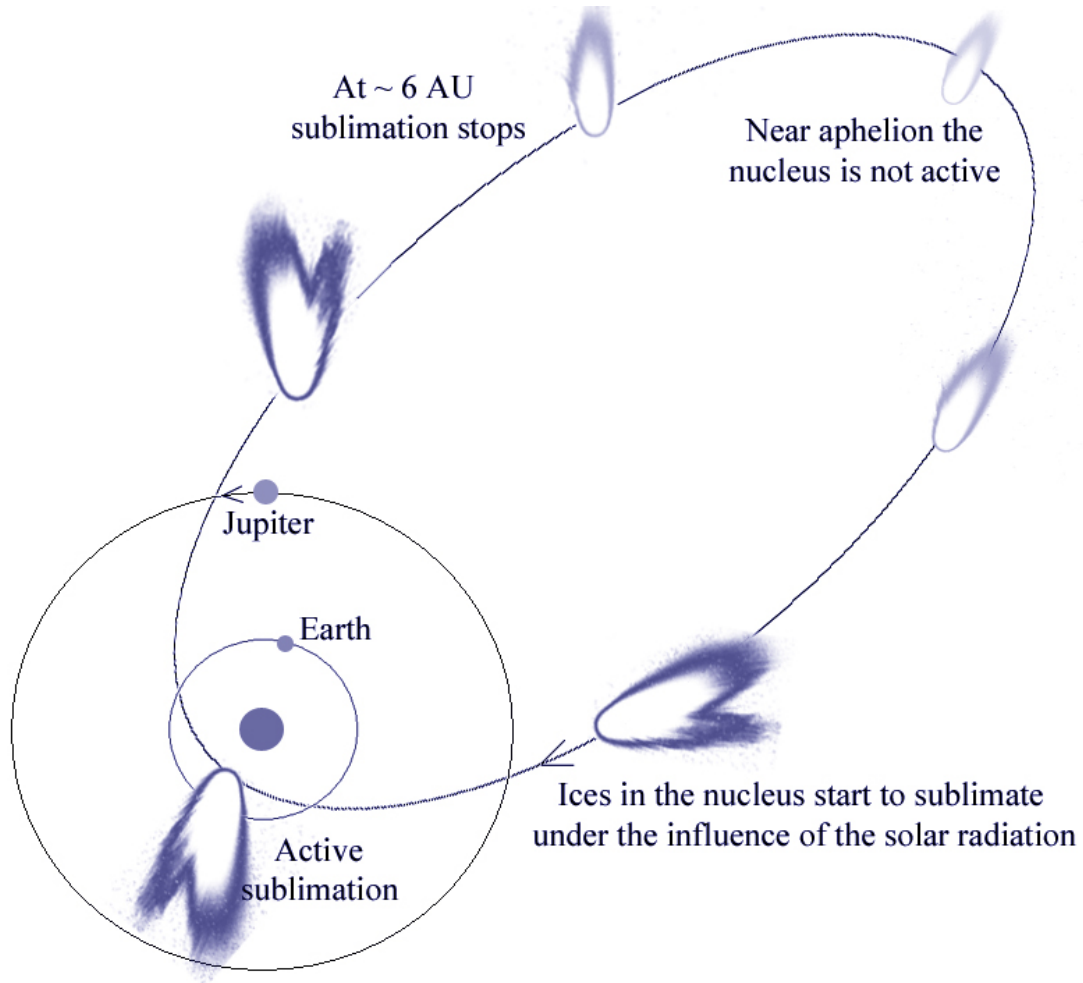


**Figure 1.2.** The orbit of a comet around the Sun: far from the Sun the nucleus is inactive, but close to the Sun ices begin to sublimate and a coma and tails (gas and dust) form.

Present Day Reservoirs

The two major reservoirs for comets in the Solar System are the Kuiper belt (with perihelia spanning the range of 30 to 100 AU from the Sun) and the Oort cloud (an approximately spherical formation covering  $10^4 - 10^5$  AU) (Gladman 2005). The

Kuiper belt includes three structures: the main belt, the scattered disk, and the extended scattered disk. Objects in the main belt have nearly circular orbits, with semi-major axis between 35 and 56 AU. Objects in the scattered disk have highly eccentric orbits, with perihelia ranging between 30 and 38 AU, and aphelia up to 100 - 3000 AU. The scattered disk is believed to be the source of most active short-period comets. Objects in the extended scattered disk have highly eccentric orbits and their perihelia exceed 38 AU.

The existence of the Oort cloud was first proposed by Jan Oort, on the basis of observations of long period comets, and a peak in the number of comets with inverse semi-major axis ( $1/a_0$ ) between 0 and  $10^{-4}$  AU<sup>-1</sup>. The Oort cloud surrounds the entire Solar System and contains approximately  $5 \times 10^{11}$  dormant cometary nuclei (Francis 2008), which can be injected into the inner Solar System as a result of gravitational perturbations (due to passing stars, galactic tides, giant molecular clouds etc.). The orbits of comets newly injected from the Oort cloud are inclined nearly randomly to the ecliptic (since the Oort cloud is a spherical formation).

A comet's orbit is inevitably modified once it enters the inner Solar System due to the gravitational influence of the planets, especially Jupiter. However, its origin from a specific reservoir can be identified on the basis of its orbital Tisserand

parameter ( $T_j$ ). The Tisserand parameter is defined as:  $T_j = \frac{a_j}{a} + 2\sqrt{(1-e^2)\frac{a}{a_j}} \cos(i)$  ,

where  $a_j$  is Jupiter's semi-major axis,  $e$  is the orbital eccentricity,  $i$  is the orbital inclination, and  $a$  is the semi-major axis of the comet (e.g. Levison 1996). The Tisserand parameter is an approximation to the Jacobi constant - an integral of the

motion in the circular restricted three-body problem (the Sun, Jupiter and the comet, whose gravitational potential has a negligible effect on the other two bodies due to its small mass). This parameter should be approximately the same before and after the encounter between the comet and Jupiter (Carusi et al. 1995).

Historically, comets were classified as short period (periods  $< 200$  years), long period (periods  $> 200$  years), and dynamically new (if they are entering the Solar System for the first time) – however, this classification is less descriptive than the dynamical classification proposed by Levison (1996).

In Levison's classification "ecliptic" comets come from the Kuiper belt, and are further classified as Jupiter-family ( $2 < T_j < 3$ ), Chiron-type ( $T_j > 3$  &  $a > a_j$ ), or Encke-type ( $T_j > 3$  &  $a < a_j$ ) comets. Nearly isotropic comets ( $T_j < 2$ ) originate from the Oort cloud, and are further classified as "new" ( $a > 10000$  AU), "external" ( $40$  AU  $< a < 10000$  AU) or "Halley-type" ( $a < 40$  AU) comets. The semi-major axis of "Halley-type" comets is small enough for them to be trapped in a mean-motion resonance with a giant planet, distinguishing them from "external" comets. The boundary is set at Pluto's semi-major axis of 40 AU (Pluto is in a 3:2 mean motion resonance with Neptune) (Levison 1996).

**Table 1.1.** Dynamical classification of comets (Levison 1996).

<p><b><math>a &gt; 10000</math> AU</b></p> <p><b><math>40 \text{ AU} &lt; a &lt; 10000</math> AU</b></p> <p><b><math>a &lt; 40</math> AU</b></p>	<b><math>T_j &lt; 2</math></b>	
	Nearly Isotropic (new)	
	Nearly Isotropic (external)	
	<b><math>2 &lt; T_j &lt; 3</math></b>	
<b><math>a &gt; a_j</math></b>	Ecliptic (Jupiter-family)	Ecliptic (Chiron-type)
<b><math>a &lt; a_j</math></b>	Ecliptic (Jupiter-family)	Ecliptic (Encke-type)

A newly discovered group of comets (five members at this writing) resides in the main asteroid belt (thus are called main belt comets, and Hsieh & Jewitt 2006 report the first discovery). Main belt comets have  $T_j > 3$ , and are dynamically similar to asteroids. It is suggested that main belt comets may have formed from the fragmentation of larger asteroids at their present location, and collisions with smaller bodies could be instigating their cometary activity (Haghighipour 2009).

*Cometary Origins and the Chemical Diversity of Cometary Nuclei*

Although the cosmic reservoir of a given comet can be identified in this way, bodies within a given reservoir may have experienced quite different dynamical histories before entering the reservoir. A comet's current orbital properties do not

preserve that pre-reservoir information, so dynamical information alone cannot identify the formative region of an individual comet. We turn instead to other information preserved from that formative time – the chemical composition of a cometary nucleus, and certain other cosmogonic invariants of its constituent materials.

The diversity among comets from a given reservoir can provide important information on the relationship of their formative regions, subsequent dynamical dispersion, and reservoir formation. There is evidence for strong radial gradients in chemistry and temperature in the proto-planetary disk, and for migration of the cometary formation material (e.g. Brownlee et al. 2006). The "*Nice*" model predicts significant dynamical dispersion in the outer proto-planetary disk (Tsiganis et al. 2005). During the formation of the Solar System some comets that originated in the giant planets' "feeding" zones (5 – 15 AU) were ejected to the Oort cloud and possibly the outer disk (Dones et al. 2004). The outer disk included these scattered comets and also comets that formed between 16 and 30 AU. The outer disk was later disrupted, and comets were scattered from there to both main reservoirs (Duncan 2008). Thus, comets are expected to have diverse composition, reflecting their individual formation regions. The volatile fraction of a cometary nucleus (the "native" or "parent" volatiles) is of special interest, and its characterization forms the central part of this thesis.

The interpretation of cometary diversity is problematic if based on free radical species. Daughter species (such as OH, CN, C<sub>2</sub>, C<sub>3</sub>, NH) can originate from the photo-dissociation of parent volatiles, or from refractory grains, and they often have



multiple parents. Studies of daughter species found that a greater fraction of Kuiper belt comets (about one third) are depleted in C<sub>2</sub> and C<sub>3</sub> radicals than is seen for comets derived from the Oort cloud (A’Hearn et al. 1995, Fink 2009). For isotopologues of CN, remarkable similarity is seen in the <sup>14</sup>N/<sup>15</sup>N ratio among a sample of 18 comets – all are enriched by a factor of two relative to the Solar System value (Jehin et al. 2009). While providing evidence of diversity and similarity among comets, these findings also emphasize a compelling need for complementary studies of the parent volatile composition in a given comet and the diversity of such composition among comets.

Measurements in the infrared provide gas production rates of parent species, using water as a “baseline”, since it is the most abundant volatile (and within 3 AU from the Sun, it controls the sublimation of other volatiles). Absolute production rates of organic species [ $Q$  molecules s<sup>-1</sup>] are expressed as percentages with respect to water (termed “mixing ratios”,  $\frac{Q(\text{organic species})}{Q(\text{H}_2\text{O})} \cdot 100$  [%]), which allows for comparison of the relative organic composition of different comets.

Our group has identified “organics-enriched”, “organics-normal”, and “organics-depleted” comets on the basis of mixing ratios of parent volatiles (Mumma et al. 2003; Crovisier et al. 2007; DiSanti and Mumma 2008). In the current sample, two Oort cloud comets have been identified as organics-enriched (C/2001 A2 (LINEAR), Magee-Sauer et al. 2008; C/2007 W1 (Boattini), Villanueva et al., personal communication), and the comet C/1999 S4 (LINEAR) has been identified as severely depleted (Mumma et al. 2003). Among ecliptic comets, 17P/Holmes is enriched (Salyk et al. 2007, Dello Russo et al. 2008) and 73P/Schwassman-

Wachmann-3 is depleted (Villanueva et al. 2006, Dello Russo et al. 2007). (It should be noted that 17P/Holmes was observed at a greater distance from the Sun (~2.4 AU), and if a certain portion of the water in the inner coma was in the form of ice (Yang et al. 2009), its enrichment in organic volatiles might be overestimated). Thus, depleted and enriched comets are found in each reservoir. The difficulty lies in relating the chemical composition of a comet to its formation region and subsequent dispersion to its long-term reservoir.

## Chapter 2: Infrared Spectroscopy of Comets

### Ro-vibrational Spectroscopy and Application to Comets

The total energy (excepting kinetic) of a molecule can be approximated as the sum of its electronic, vibrational and rotational energy. The simplest classical model represents a diatomic molecule as point masses  $m_1$  and  $m_2$  connected by a massless spring of length  $r$  and rotating with angular velocity  $\omega$ . The moment of inertia  $I$  is

$\frac{m_1 m_2}{m_1 + m_2} r^2$ , and the rotational energy is then  $\frac{I\omega^2}{2}$ . In the harmonic oscillator

approximation, the potential energy of the molecule is  $\frac{kx^2}{2}$ , where  $k$  is Hooke's

constant for the spring, and  $x$  is the displacement from the equilibrium position as a result of the molecular vibrations. In the simplest quantum mechanical model the angular momentum ( $I\omega$ ) is quantized ( $\hbar J$ ), where  $J$  is the total angular momentum quantum number, and  $J = 0, 1, 2, 3 \dots$ . The rotational energy levels are then given by

$E_r = \frac{\hbar^2}{8\pi^2 I} J(J+1)$  (Hollas 1996). The vibrational energy levels are also quantized,

and are given by:  $E_v = \hbar\omega(V + \frac{1}{2})$ , where  $\omega$  is the vibrational frequency

$\nu = \frac{1}{2\pi} \left( \frac{k}{\frac{m_1 m_2}{m_1 + m_2}} \right)^{1/2}$ , and  $V$  is the vibrational quantum number ( $V = 0, 1, 2 \dots$ )

(Hollas 1996) (see Figure 2.1 for an illustration of vibrational motion, i.e. the normal

modes of  $\text{H}_2\text{O}$ ). More complex models account for rotation-vibration interactions, and various other effects.

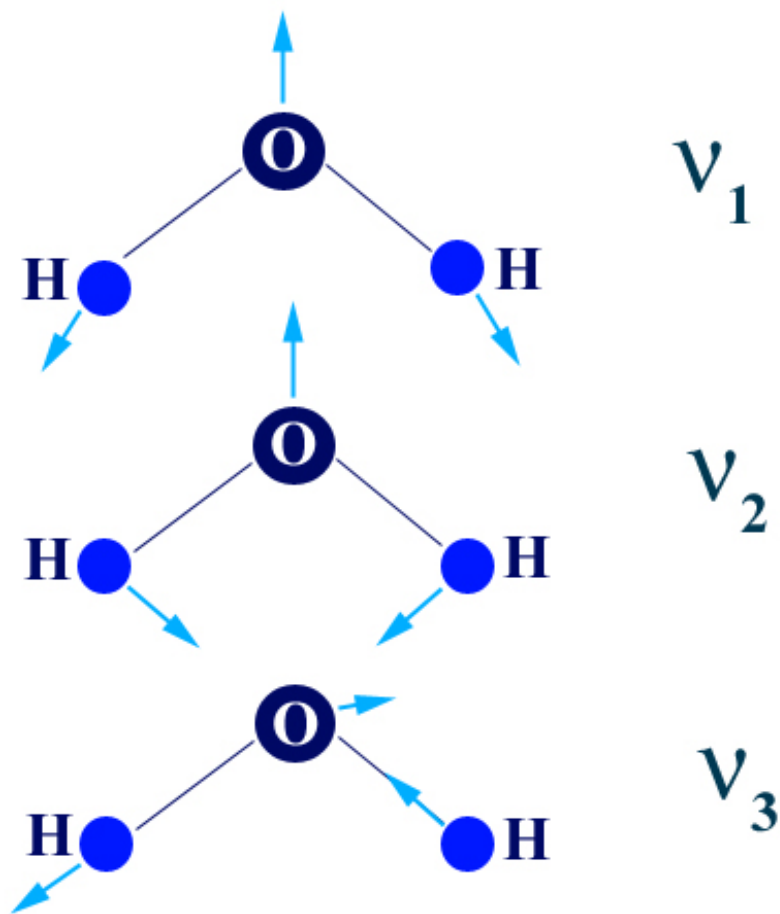
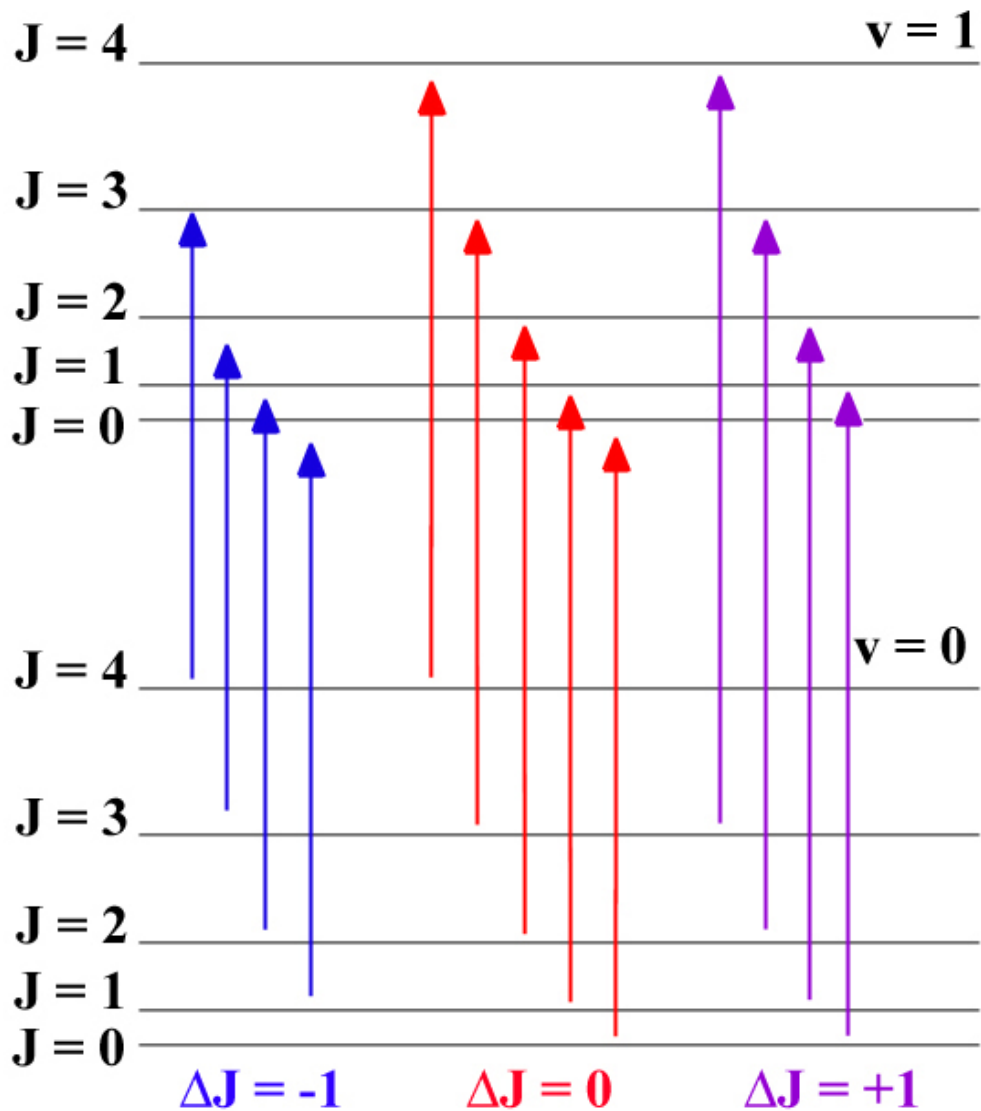


**Figure 2.1.** Vibrational modes of  $\text{H}_2\text{O}$  ( $\nu_1$ ,  $\nu_2$  and  $\nu_3$ ). These are normal modes of vibration, in which all nuclei undergo harmonic motion, with the same frequency, and in phase (although their motion may have different amplitudes). A linear  $N$ -atomic molecule has  $3N-5$  normal modes of vibration, and a non-linear  $N$ -atomic molecule has  $3N-6$  normal modes of vibration (Hollas 1996).

Vibrational modes can be stretching modes ( $\nu$ ) (highest energies), bending modes ( $\delta$ ) or torsional modes ( $\tau$ ) (lower energies). A change in electric dipole moment is necessary for a vibrational transition to occur by electric-dipole radiation (Hollas 1996). Selection rules for ro-vibrational transitions depend on the symmetry of each molecule. For example, for homonuclear diatomic molecules, the electric dipole moment is zero in all vibrational levels, therefore vibrational transitions (within a given electronic state) are forbidden. For linear molecules transitions with  $\Delta J = 0$  give rise to the Q-branch,  $\Delta J = +1$  to the R-branch, and  $\Delta J = -1$  to the P-branch. Figure 2.2 illustrates transitions between the rotational levels ( $J$ ) of two vibrational levels ( $\nu''=0$  and  $\nu'=1$ ) of a simple linear molecule obeying these selection rules. Among molecules studied in this dissertation, HCN and CO do not have a Q-branch, since they have no electronic angular momentum in the ground electronic state ( $\Sigma$ ), and in that case  $\Delta J = \pm 1$  only. Other molecules are bent rotors (e.g.  $\text{H}_2\text{O}$ ), and additional quantum numbers and selection rules apply to them.



## Ro-vibrational transitions

**Figure 2.2.** Illustration of allowed ro-vibrational transitions (pumping from lower to upper states). Cascade transitions are shown in Chapter 5.

For pure rotational transitions (between the rotational levels of the same vibrational level), which are observed at radio wavelengths, a molecule must have a

permanent dipole moment, and the selection rules are  $\Delta J = \pm 1$  (Hollas 1996). That is why symmetric hydrocarbons such as  $C_2H_6$ ,  $C_2H_2$  and  $CH_4$ , which lack a permanent dipole moment, have no allowed pure rotational transitions. They do have strong vibrational bands, and thus can only be observed in the infrared.

Through infrared spectroscopy we study ro-vibrational spectra of parent volatiles in comets, resulting from transitions between the rotational levels of different vibrational levels within the same electronic level. Most polyatomic (and many diatomic) molecules of cometary interest have strong vibrational fundamental bands in the 2.5-5  $\mu m$  region. At infrared wavelengths we observe the innermost region of the cometary coma (several hundred kilometers centered on the nucleus, depending on the geocentric distance of the comet). Approximately  $2/\pi$  (about 64%) of the total fraction of molecules sampled within the beam fall within the "inscribed sphere" (the sphere centered on the nucleus whose radius equals that of the pencil beam – the radius of the sampled region) (Yamamoto 1982). To further illustrate the significantly higher number of molecules found close to the nucleus, their number

density at distance  $r$  from the nucleus can be estimated: 
$$n_{total} = \frac{Q_{H_2O}}{4\pi r^2 V_{outflow}} e^{-r/V_{outflow} \tau}$$

(the exponential factor refers to photodissociation and can be ignored within a few thousand km from the nucleus, given lifetime against photodissociation for a species  $\tau \sim 10^5$  s) (Weaver & Mumma 1984). At a distance  $r = 5$  km from the nucleus:

$$n_{total} \sim \frac{10^{28}}{4\pi(5 \times 10^5)^2 10^5} \sim 3 \times 10^{10} \text{ cm}^{-3} \text{ assuming } Q \sim 10^{28} \text{ s}^{-1} \text{ and } V_{outflow} \sim 1 \text{ km s}^{-1}.$$

The number density of molecules 100 km from the nucleus would then be

$n_{\text{total}} \sim \frac{10^{28}}{4\pi(100 \times 10^5)^2 10^5} \sim 8 \times 10^7 \text{ cm}^{-3}$ , which demonstrates the rapid decrease of number density near the nucleus (within the region sampled in our observations).

In the innermost region of the coma, collisions thermalize the rotational population of the ground vibrational level (this statement is further discussed in the following section and in Chapter 5), and a rotational temperature is determined in order to model this rotational population. Thus, a production rate is derived at a given rotational temperature for each molecule. If the observed lines sample an insufficient spread in excitation energies, a rotational temperature has to be assumed based on measurements for other molecules. This assumes that these molecules are measured in locations in the cometary coma characterized by the same temperature, and as shown previously, they are indeed found within a very small inner region of the coma, close to the nucleus. This also assumes that the rotational level populations are controlled by collisional excitation, rather than radiative processes.

This dissertation provides a valuable comparison among temperatures derived for polar molecules ( $\text{H}_2\text{O}$ ,  $\text{HCN}$ ,  $\text{CO}$  – as previously measured), and a non-polar molecule ( $\text{C}_2\text{H}_6$ ) through the newly developed  $\text{C}_2\text{H}_6$   $v_5$  model. Agreement among measured temperatures for polar and non-polar species would support collisional thermalization of the rotational levels, and would argue against control by radiative pumping and decay (DiSanti et al. 2001).



## Summary of Excitation Processes in Cometary Comae

### *Radiative Electronic Excitation*

For most simple molecules, electronic transitions occur mostly with energies greater than  $\sim 2$  eV, i.e. at UV and optical wavelengths. However, absorption of solar UV radiation often results in photodissociation of polyatomic molecules in comets and formation of daughter species. For example, photodissociation of  $\text{H}_2\text{O}$  produces OH in vibrationally excited and highly rotationally excited states (Bonev et al. 2004). Also, electronic excitation rates are often lower than vibrational excitation rates: for example, the excitation rate of one of the electronic states of CO (near 150 nm) is  $\sim 1-2 \times 10^{-6} \text{ s}^{-1}$  (taken as a typical value) (Tozzi et al. 1998), while the excitation rate of the vibrational CO  $\nu(0-1)$  band at  $4.7 \mu\text{m}$  is  $2.6 \times 10^{-4} \text{ s}^{-1}$  (Chin and Weaver 1984).

Calculations of electronic excitation rates are complicated by the solar Fraunhofer absorption lines in the UV, formed as radiation from hotter layers of the Sun passes through the cooler photosphere. As a comet orbits the Sun and its heliocentric velocity changes, the Doppler effect shifts the positions of the Fraunhofer lines relative to the excitation frequencies (the Swings effect), so that strong cometary lines are seen at frequencies that do not coincide with Fraunhofer lines (and vice versa for weak cometary lines). Thus, the intensities of cometary lines depend on the heliocentric velocity of the comet (Swings 1941).

The Swings effect makes it impossible to use a blackbody approximation for solar radiation in the UV. However, Fraunhofer lines are sparse and weak in the 3-5  $\mu\text{m}$  region, and thus overlap the lines of cometary gases only occasionally and not

systematically. The blackbody approximation for the solar spectrum is adequate for most cometary parent volatiles, excepting CO. CO is prominent in the solar atmosphere, resulting in strong CO absorption features in the 4.7  $\mu\text{m}$  spectral region that must be considered for heliocentric velocities less than  $\sim 10 \text{ km s}^{-1}$  (Kim et al. 1996).

### *Radiative Vibrational Excitation*

Radiative vibrational excitation is the focus of this research. Vibrational bands can be excited by the Solar radiation, or by (thermal or scattered) radiation from the nucleus and dust. The most important process is the excitation of fundamental vibrational bands by the Solar radiation, because they have the highest excitation rates. The pumping rate from the lower (l) to the excited state (u) in a ro-

vibrational transition is  $g_{lu} = \frac{c^3}{8\pi h \nu_{\text{line}}^3} \frac{g_u}{g_l} n \times A_{ul} \rho_v$ , where  $g_l$  and  $g_u$  are the statistical weights of the two levels,  $\nu_{\text{line}}$  is the transition frequency,  $n$  is the fractional population of the lower level,  $A_{ul}$  is the Einstein A coefficient for spontaneous emission, and  $\rho_v$  is the solar radiation density (Bockelee-Morvan et al. 2004). This

can also be expressed as  $g_{lu} = \frac{\Omega_{\text{bb}}}{4\pi} \frac{g_u}{g_l} n \times A_{ul} [e^{h\nu_{\text{line}}/kT_{\text{bb}}} - 1]^{-1}$ , where  $\Omega_{\text{bb}}$  is the solid angle and  $T_{\text{bb}}$  is the black-body temperature of the Sun. The Einstein A coefficient for a given transition can be calculated as:

$$A_{ul} = \frac{8\pi c \nu_{\text{line}}^2 Z_{\text{tot}}(T_{\text{rot}}) S_{\text{line}}}{g_u (1 - e^{-hc\nu_{\text{line}}/(kT_{\text{rot}})}) e^{-hcE_{\text{low}}/(kT_{\text{rot}})}}, \text{ where } S_{\text{line}} \text{ is the strength}$$

of a spectral line,  $T_{\text{rot}}$  is the rotational temperature, and  $E_{\text{low}}$  is the lower state energy (Simeckova et al. 2006).

Typical Einstein A coefficients for the strongest fundamental bands ( $A_{v'v''}$ ) can range between  $10 - 100 \text{ s}^{-1}$ , and band excitation rates ( $g_{v'v''}$ ) are  $\sim 10^{-4} \text{ s}^{-1}$  (Bockelee-Morvan et al. 2004). Pumping from excited vibrational states has lower rates than pumping from the ground vibrational state due to the smaller number of molecules found in such excited states. This can be shown by relating the populations  $n_{v'}$  and  $n_{v''}$  of the excited and the ground state as:  $\frac{n_{v'}}{n_{v''}} = \frac{g_{v'v''}}{A_{v'v''}}$  when there

is equilibrium between pumping and spontaneous decay. Using the approximation

$$\text{for the band rate } g_{v'v''} = \frac{\Omega_{\text{bb}}}{4\pi} A_{v'v''} [e^{h\nu_{\text{band}}/kT_{\text{bb}}} - 1]^{-1} \text{ (Crovisier and Encrenaz 1983),}$$

it follows that  $\frac{n_{v'}}{n_{v''}} = \frac{\Omega_{\text{bb}}}{4\pi} [e^{h\nu_{\text{band}}/kT_{\text{bb}}} - 1]^{-1}$ , which is only dependent on the

frequency of the band and the heliocentric distance (since  $\frac{\Omega_{\text{bb}}}{4\pi} = 5.42 \times 10^{-6} r_{\text{h}}^{-2}$ ,

where  $r$  is the heliocentric distance in AU) (Bockelee-Morvan et al. 2004). At  $r_{\text{h}} \sim 1$

AU, and  $\nu_{\text{band}} \sim 3000 \text{ cm}^{-1}$ ,  $\frac{n_{v'}}{n_{v''}} \sim 5 \times 10^{-6}$ , which illustrates how much smaller the

population of the excited state is, compared to the ground vibrational state. The

excited vibrational state also has a very small radiative lifetime (a fraction of a second) (Bockelee-Morvan et al. 2004).

### *Radiative Rotational Excitation*

The solar flux is very weak at millimeter wavelengths, which makes rotational excitation by solar radiation negligible. The 2.7 K cosmic microwave background, however, can produce rotational excitation for comets beyond 3 AU (Biver et al. 1999a), and would need to be considered in such cases.

### *Collisional Excitation*

Our measurements in the infrared are weighted heavily towards molecules within the innermost coma. Densities in the coma are low, and collisions between neutrals are only important very close to the nucleus, unlike collisions with electrons, which are important throughout a greater extent of the coma (Xie & Mumma 1992).

Cross-sections for collisions between neutrals for vibrational excitation are  $\sigma_{\text{up}} \sim 10^{-18} \text{ cm}^2$ , and the collisional excitation rate can be calculated:  $C_{\text{up}} = n_{\text{total}} \sigma_{\text{up}} V_{\text{thermal}}$ , (where  $n$  is the number density, and  $V_{\text{thermal}}$  is the thermal velocity of molecules).

For  $\text{H}_2\text{O}$ ,  $n_{\text{total}} \sim 10^{13} \text{ cm}^{-3}$  at 1 km from the nucleus, using  $n_{\text{total}} = \frac{Q_{\text{H}_2\text{O}}}{4\pi r^2 V_{\text{outflow}}}$

(Weaver & Mumma 1984), and assuming  $Q_{\text{H}_2\text{O}} \sim 10^{29} \text{ s}^{-1}$ ;  $V_{\text{outflow}} \sim 1 \text{ km s}^{-1}$ ; and  $\text{H}_2\text{O}$

lifetime  $\tau = 7.7 \times 10^4 \text{ s}$ . Given  $V_{\text{thermal}} = \sqrt{\frac{8kT}{\pi\mu}} \sim 10^4 \text{ cm s}^{-1}$  (where  $\mu$  is the reduced

mass of the colliding H<sub>2</sub>O molecules, Weaver & Mumma 1984), the collisional excitation rate for vibrational transitions is  $C_{\text{up}} = 10^{13} \times 10^{-18} \times 10^4 = 0.1$  [collisions s<sup>-1</sup>] at 1 km from the nucleus. At ~ 30 km from the nucleus  $C_{\text{up}}$  would be ~ 10<sup>-4</sup> s<sup>-1</sup>. Given that vibrational excitation rates (by solar radiation) for H<sub>2</sub>O are ~ 10<sup>-4</sup> s<sup>-1</sup>, collisional excitation of vibrations by neutrals is only significant within a few tens of kilometers from the nucleus.

Cross-sections for neutral-neutral collisions for vibrational de-excitation are  $\sigma_{\text{down}} \sim 10^{-14} - 10^{-15}$  cm<sup>2</sup> (Xie & Mumma 1992), and the collisional de-excitation rate at 1 km from the nucleus can be calculated:

$C_{\text{down}} = n_{\text{total}} \sigma_{\text{down}} V_{\text{thermal}} = 10^{13} \times 10^{-15} \times 10^4 = 100$  [collisions s<sup>-1</sup>]. At more than 10 km from the nucleus  $C_{\text{down}}$  would be less than 1 s<sup>-1</sup>. Given Einstein A coefficients for spontaneous emission of order 10 – 100 s<sup>-1</sup>, collisional de-excitation of vibrational levels dominates radiative vibrational de-excitation only within 10 km from the nucleus.

In order to evaluate electron-water scattering, the electron thermal velocity

can be estimated  $V_{\text{thermal}} = \sqrt{\frac{8kT}{\pi m_e}} \sim 10^7$  cms<sup>-1</sup>; the electron number density

$n_e = \frac{1.3 \times 10^7}{r} \sim 10^4$  cm<sup>-3</sup> at  $r \sim 10^3$  km, and  $\sigma \sim 10^{-12}$  cm<sup>2</sup> (formulae from Xie &

Mumma (1992) for comet Halley, based on theoretical and experimental studies of electron-H<sub>2</sub>O collisions, and parameters obtained by the Giotto and Vega missions).

Thus, the time-scale for collisions  $t_{\text{collisions}} \sim \frac{1}{10^4 10^{-12} 10^7} \sim 10$  s at 10<sup>3</sup> km from the

nucleus, and the collision rate would be 0.1 s<sup>-1</sup>. Collisional excitation by electrons

dominates neutral-neutral collisional excitation throughout a greater extent of the coma and can thermalize rotational levels. For example, in the case of the  $0_{00} \rightarrow 1_{11}$  transition of  $\text{H}_2\text{O}$ , collisions between electrons and  $\text{H}_2\text{O}$  dominate over neutral-neutral collisions as far as 3000 km from the nucleus (Xie & Mumma 1992).

Since the energy available in collisions is the (thermal) kinetic energy of each molecule ( $\sim 0.001$  eV for typical thermal velocities), collisions cannot excite vibrational or electronic transitions, however, they excite rotational transitions (de Pater & Lissauer 2005). Also, in the innermost region of the coma observed in the infrared, pure rotational lines are optically thick due to the high density and small escape probability for emitted photons (Bockelee-Morvan 1996). The effect of optical trapping of rotational emission lines would be to increase the distance at which collisions can thermalize rotational level populations.

#### *Overview of the Chemical Composition of Comets Analyzed by our Team*

Mixing ratios of organic parent volatiles with respect to  $\text{H}_2\text{O}$  are presented for a sample of comets analyzed by the team at NASA's GSFC (Table 2.1). Analysis of the organic composition of comet C/2000 WM<sub>1</sub> (LINEAR) (see Radeva et al. 2010) is discussed in Chapter 4 and results are tabulated here.

**Table 2.1.** The organic composition of comets based on infrared spectroscopy(mixing ratios as percentages relative to H<sub>2</sub>O; upper limits are 3- $\sigma$ ).

Mixing Ratio %	C <sub>2</sub> H <sub>6</sub>	C <sub>2</sub> H <sub>2</sub>	HCN	CH <sub>4</sub>	H <sub>2</sub> CO	CH <sub>3</sub> OH	CO
73P/S-W 3-C <sup>I</sup>	0.107 ± 0.011	0.049 ± 0.020	0.242 ± 0.014	<0.25	0.147 ± 0.033	0.149 ± 0.029	0.53 ± 0.13
C/1999 S4 (LINEAR) <sup>II</sup>	0.11 ± 0.02	< 0.12	0.10 ± 0.03	0.18 ± 0.06	-	< 0.15	0.9 ± 0.3
<b>C/2000 WM<sub>1</sub></b> <b>(LINEAR)<sup>III</sup></b>	<b>0.47</b> <b>± 0.03</b>	<b>&lt; 0.05</b>	<b>0.15</b> <b>± 0.01</b>	<b>0.34</b> <b>± 0.03</b>	<b>0.20</b> <b>± 0.03</b>	<b>1.30</b> <b>± 0.08</b>	<b>0.52</b> <b>± 0.12</b>
Five "organics- normal" Oort cloud comets <sup>II</sup>	0.6	0.2-0.3	0.2-0.3	0.5-1.5	-	2	1.8-17
153P/Ikeya- Zhang <sup>II</sup>	0.62 ± 0.13	0.18 ± 0.05	0.18 ± 0.05	0.51 ± 0.06	0.62 ± 0.18	2.5 ± 0.5	4.7 ± 0.8
17P/Holmes <sup>IV</sup>	1.78 ± 0.26	0.344 ± 0.053	0.538 ± 0.075	-	-	2.25 ± 0.43	-
C/2002 T7	-	-	-	-	0.79	-	-

(LINEAR) <sup>V</sup>					± 0.09		
C/2001 A2	1.7	0.5	0.6	1.2	0.24	3.9	3.9
(LINEAR) <sup>VI</sup>	± 0.2	± 0.1	± 0.1	± 0.2	± 0.05	± 0.4	± 1.1

<sup>I</sup>Data from 14.5 May 2006 (Dello Russo et al. 2007), with the exception of CH<sub>4</sub> (7 Apr. 2006, Villanueva et al. 2006), and CO (27, 30 May 2006, DiSanti et al. 2007).

<sup>II</sup>The organics "normal" group consists of: C/1996 B2 Hyakutake, C/1995 O1 Hale-Bopp, C/1999 HI Lee, C/1999 TI McNaught-Hartley and 153P/Ikeya-Zhang; and the organics-depleted comet is C/1999 S4 (LINEAR) (Mumma et al. 2003). Mixing ratio for H<sub>2</sub>CO in 153P is obtained from DiSanti et al. 2002.

<sup>III</sup>The results are weighted means of mixing ratios from 23, 24 and 25 Nov. 2001. C<sub>2</sub>H<sub>2</sub> is the 3- $\sigma$  upper limit of the most sensitive measurement (23 & 25 Nov.) (Radeva et al. 2010). The mixing ratio for CO is from 25 Nov. (23 and 24 Nov. only yield 3- $\sigma$  upper limits, which are consistent with the mixing ratio from 25 Nov.).

<sup>IV</sup>Data from 27.6 Oct. 2007 (Dello Russo et al. 2008).

<sup>V</sup>Weighted mean from 5, 7 and 9 May 2004 (DiSanti et al. 2006).

<sup>VI</sup>Data from 9.5 July 2001, except for CO (10.5 July 2001) (Magee Sauer et al. 2008).

The results are arranged from the most organics-depleted comets through organics-normal comets, to the most enriched members of this group. The volatile composition of comets that formed farther from the Sun would reflect ices remaining from the natal cloud core, rather than significant thermo-chemical processing in the proto-planetary disk (Mumma et al. 2003). Thus, the composition of the severely depleted comet C/1999 S4 is consistent with its formation closer to the young Sun (possibly within 5-10 AU) than other comets in this sample (Mumma et al. 2003). If depletion is indeed dependent on heliocentric distance, the most enriched end-member A2 (LINEAR) may have formed farther from the Sun than did organics-



normal comets. It is extremely difficult to distinguish the effects of conditions in the region where a comet formed (such as temperature of the region, and also whether a comet formed from fragments originating in different regions, such as organics-depleted and organics-enriched), from the effects of other processes. Such processes include radial transport of cometary material, turbulent mixing, the ejection of a comet from its formation region to other dynamical reservoirs, and potential changes in the natal signatures along the way.

### *The Astrobiological Importance of Comets*

Comets that bombarded the young Earth likely delivered some pre-biotic organics and/or water to our home planet – the questions are how much and when? Cosmogonic parameters are measured in an attempt to understand the origin of our biosphere. For example, the formation temperature of water in a cometary nucleus can be inferred from the abundance ratio between ortho and para nuclear spin species of H<sub>2</sub>O. Ortho species have parallel nuclear spin vectors of the hydrogen atoms, and para species have anti-parallel nuclear spin vectors. The lowest energy para level is approximately 34 K below the lowest energy ortho level, and ortho to para ratio of 3 is the equilibrium value at  $T_{\text{spin}} \geq 50$  K (Bonev et al. 2005). Thus, the ortho to para ratio can be used to determine  $T_{\text{spin}}$  of water in comets, and given that transitions between ortho and para species are forbidden, the current spin temperature may reflect the formation temperature of the water molecules.

Isotopic ratios in parent volatiles are also useful. For example, D/H ratios in different groups of comets hold further clues to cometary formation regions (Villanueva et al. 2009). The D/H ratio of Earth's oceans is  $1.56 \times 10^{-4}$  (Vienna Standard Mean Ocean Water - VSMOW), which is twice smaller than the average D/H ratio (from HDO/H<sub>2</sub>O) measured in four comets from the Oort cloud: 1P/Halley (mass spectroscopy), C/1996 B2 Hyakutake (radio observations), C/1995 O1 Hale-Bopp (radio observations), and 8P/Tuttle (infrared spectroscopy by the GSFC team,  $D/H = (4.09 \pm 1.45) \times 10^{-4}$ , Villanueva et al. 2009). These measurements would not support a principal cometary origin for Earth's water. At this point, carbonaceous chondrites would seem more likely to have delivered water to the young Earth, given their D/H enrichment of  $(1.4 \pm 0.1) \times 10^{-4}$  (Lecuyer et al. 1998). However, four comets are not a representative sample, and we do not know the ratio of D/H in comets from the Kuiper disk. If they typically include rocky material formed in the near solar region (like 81P/Wild-2, Brownlee et al. 2006), they likely also incorporate water convected outward from the inner solar system. A mixture of such material with comets more enriched in deuterium could easily match the terrestrial value. Infrared spectroscopic methods provide the most sensitive (and most robust) cometary D/H search measurements, but a statistically significant sample of comets needs to be studied for a reliable comparison between D/H in comets and D/H in Earth's water.

### The $\nu_5$ band of $C_2H_6$ and its Importance

A principal focus of this dissertation is the development of a fluorescence model for the  $\nu_5$  band of  $C_2H_6$  at 3.45  $\mu m$ . A fluorescence model provides the frequency of each observed line, its corresponding excitation energy, and its g-factor, which is a fluorescence efficiency factor, describing how many photons are released per molecule per unit time.

We observe the innermost region of the cometary coma, where collisional excitation of molecules thermalizes the rotational population (described by a rotational temperature) of their ground vibrational state. The new model permits us to make reliable measurements of the rotational temperature of  $C_2H_6$ . A major benefit of having a model for  $C_2H_6 \nu_5$  is that this volatile can now be quantified simultaneously with  $CH_4$ ,  $C_2H_2$ , HCN,  $H_2CO$ ,  $CH_3OH$  and  $H_2O$ , along with  $NH_2$  and OH. All are sampled by a single NIRSPEC instrument setting during observations, and this greatly minimizes systematic effects (due to changes in seeing, flux calibration, etc.). Also, if one instrument setting is sufficient to sample all targeted species, more time could be dedicated to observations with that specific setting, thus, increasing the signal-to-noise ratio of the acquired data. Furthermore, up to this point the rotational temperature indicators have been  $H_2O$ , HCN and CO, and we now have a fourth molecule, which contributes to better constraining rotational temperatures and to understanding the physics of cometary comae (such as the temperature at the location of a measured species in the coma, and its distribution).

Previous measurements of C<sub>2</sub>H<sub>6</sub> production rates have been done using a model of its  $\nu_7$  band at 3.3  $\mu\text{m}$  (Dello Russo et al. 2001). This band includes bright Q-branches, and provides a reliable production rate, however, their unresolved structure prevents the derivation of an accurate rotational temperature (if one can be derived at all). The  $\nu_5$  band, however, includes Q, P and R branch lines, and by measuring the relative line intensities of its resolved P and R branches a rotational temperature can be extracted.

## Chapter 3: Observations with NIRSPEC and Data Analysis

### Overview of NIRSPEC in Cometary Observations

Data presented in this work were obtained with the Near Infrared Echelle Spectrograph (NIRSPEC) at the 10-meter Keck-II telescope on Mauna Kea, HI. NIRSPEC has a 1024 x 1024 InSb detector array; and it provides resolving power  $\lambda/\Delta\lambda \sim 25000$  when the 3 pixel (0.432"x24") entrance slit is used (typical for comet data). In an echelle spectrograph light passes through the entrance slit and then through a collimator, and the echelle grating disperses the collimated light into multiple orders. The grating equation  $m\lambda/d = \sin\alpha \pm \sin\beta$  (where  $m$  is the order number,  $d$  is the groove spacing,  $\alpha$  is the angle of incidence of the collimated beam on the grating and  $\beta$  is the angle of reflection), shows that working in high resolution means working in high orders. Overlapping echelle orders are separated by a lower resolution grating (cross-disperser) (see Figure 3.1). Eventually the cross-dispersed spectra are re-imaged onto the InSb detector array.

The main strengths of NIRSPEC are its high resolving power, and the simultaneous detection of numerous organic species and water, enabled by sampling multiple echelle orders simultaneously. This feature eliminates many systematic uncertainties that could occur if each species was measured separately. NIRSPEC is used to observe organic species and water in the L-band (2.7-4.2  $\mu\text{m}$ ) and the M-band (4.4-5.5  $\mu\text{m}$ ). The three instrument settings used during observations are KL1 (3397 – 2704  $\text{cm}^{-1}$ ), KL2 (3455 – 2753  $\text{cm}^{-1}$ ) and MW\_A (2165 – 1866  $\text{cm}^{-1}$ ). The limits

encompass extreme wavenumbers sampled, but the sampling is only piecewise continuous.

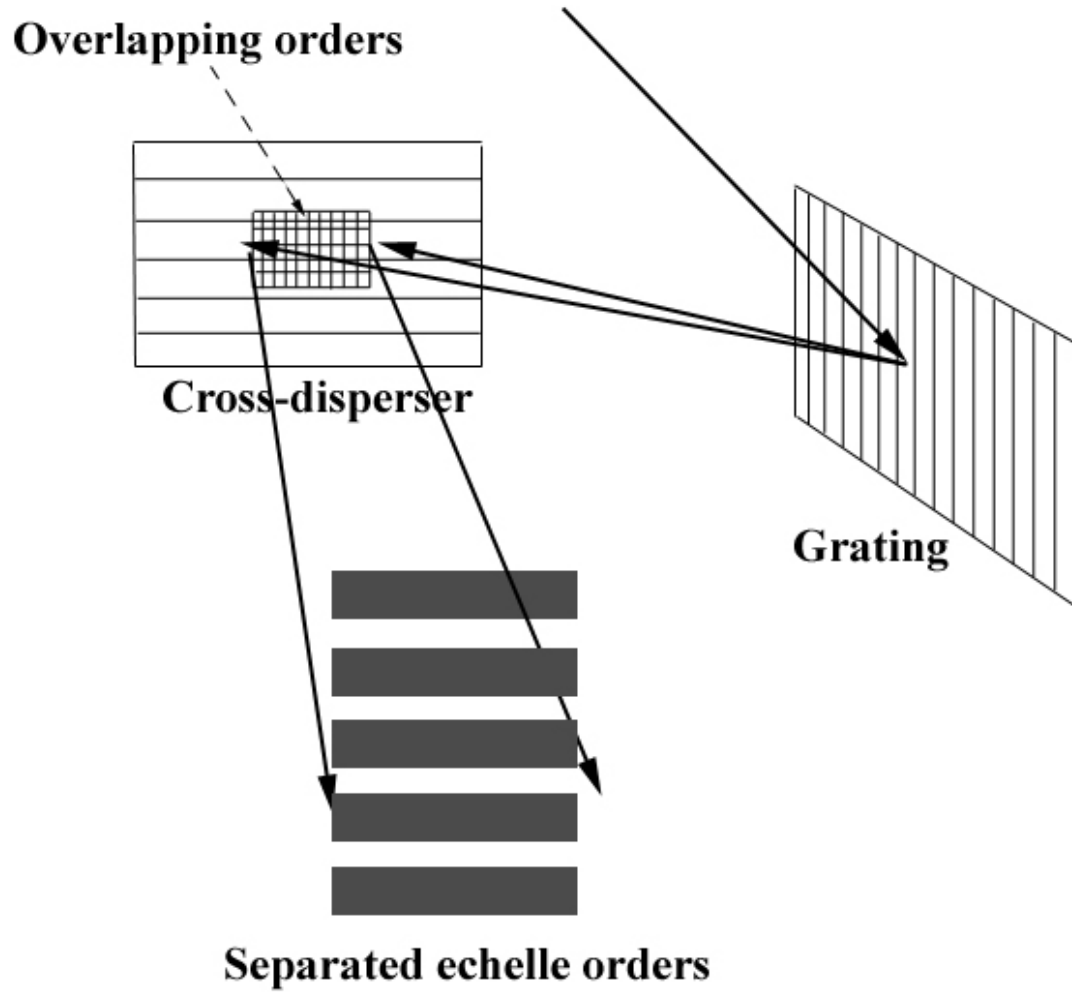


**Figure 3.1.** Illustration of an echelle grating and a cross disperser grating. The cross-disperser separates overlapping echelle orders.

### *From Raw Frames to Cometary Emission Spectra*

A raw cometary frame covers  $1024 \times 1024$  pixels (where each pixel corresponds to  $0.198''$  in the spatial dimension and  $0.144''$  in the spectral dimension – the image scale is different because the camera in the spectrograph has different focal lengths in the spectral and spatial dimensions along the array). A raw frame samples several echelle orders (see Figure 3.2). The thermal background emission is stronger than the comet signal, and the telescope is nodded by  $12''$  ( $\pm 6''$  along slit) in a sequence A1, B1, B2 and A2 (see Figure 3.3), such that the difference in data frames ( $A1-B1-B2+A2$ ) cancels dark current, emission from the sky and telescope (see Figure 3.4).

Each echelle order is cropped and analyzed separately. The frames are divided by their respective flat fields to correct for uneven field illumination and pixel-to-pixel variability in quantum efficiency. Each flat field is corrected by dark frame subtraction. Dark frames measure counts generated in the matrix in the absence of light (thermal noise). Data are “masked” to remove hot pixels and cosmic ray hits using a sigma “mask” (eliminating counts higher than a certain threshold) and afterwards, pixel averaging. A and B frames, as well as the differences of A frames ( $A1-A2$ ) and of B frames ( $B1-B2$ ), are “masked” separately. A typical mask is shown in Figure 3.5 (the green and red lines represent the positions of the A and B beams, and the mask is shown in white).

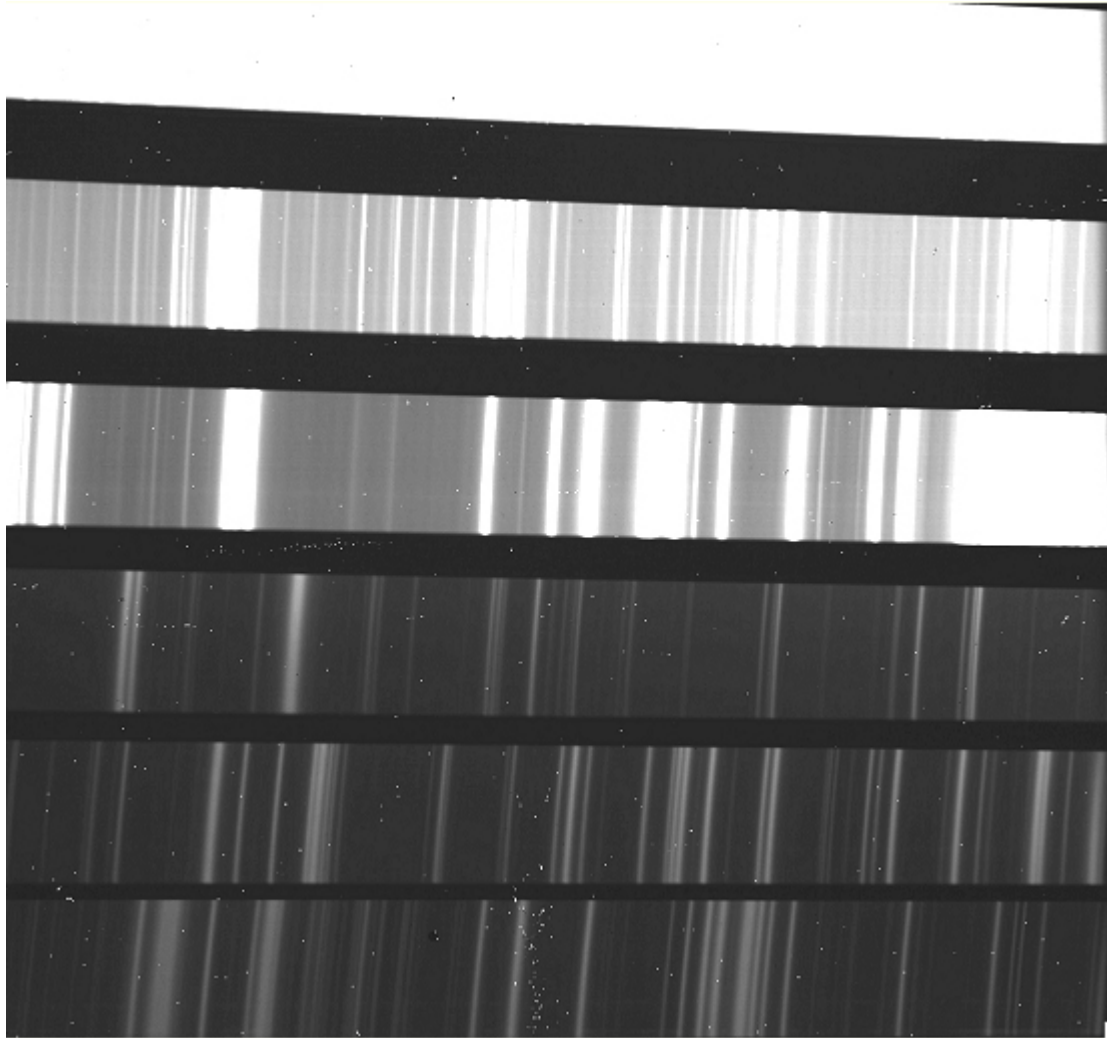


**Figure 3.2.** Raw frame of six echelle orders, dominated by thermal background and sky emission.



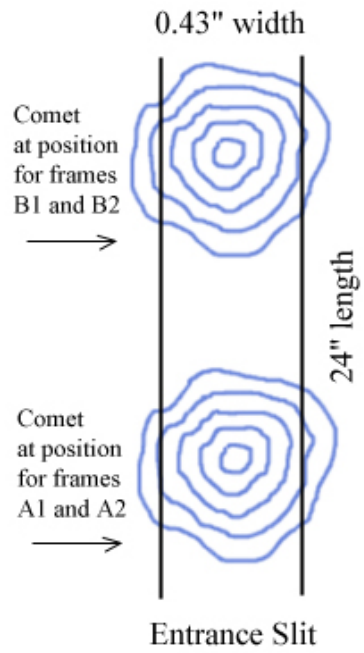
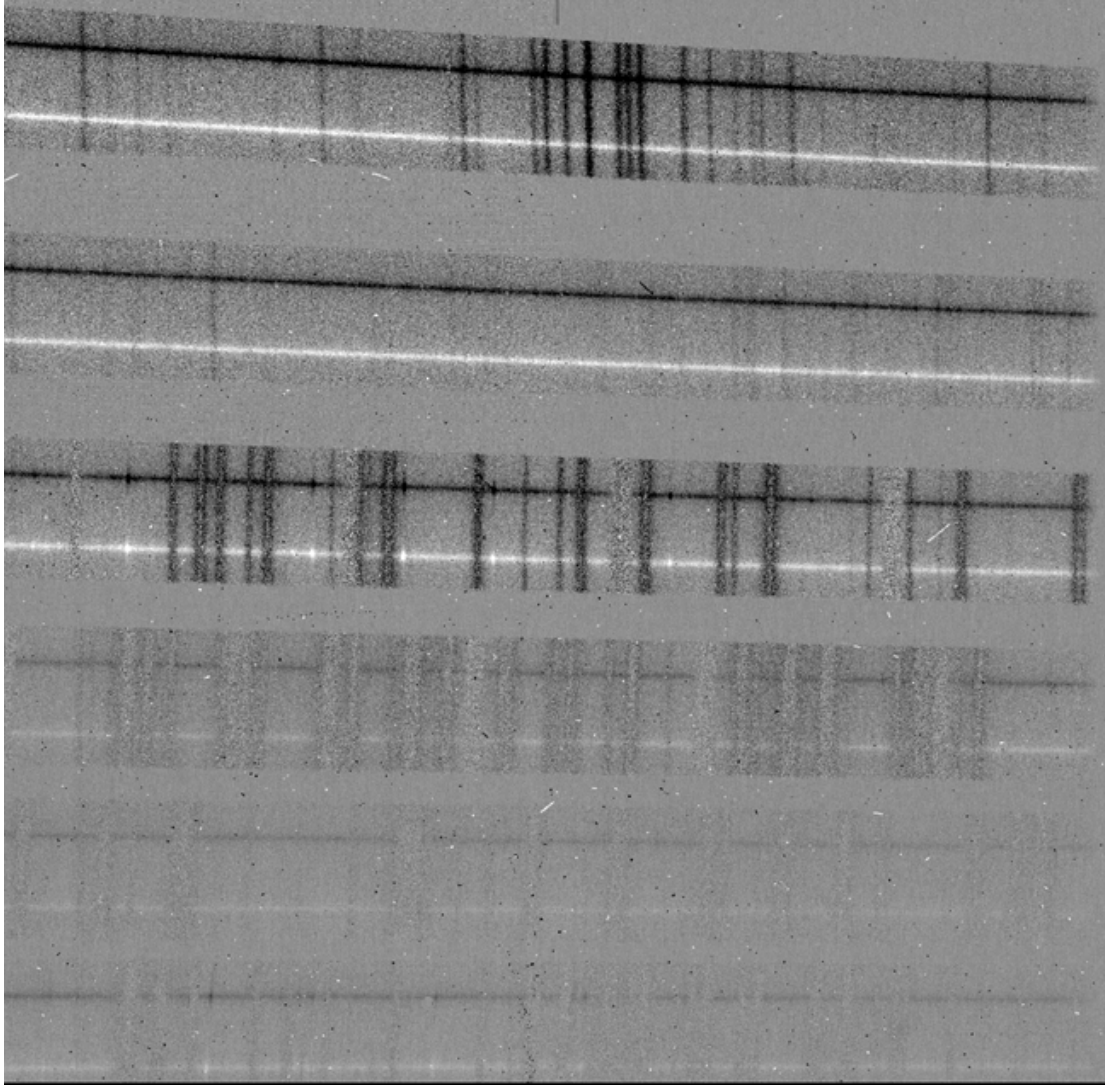
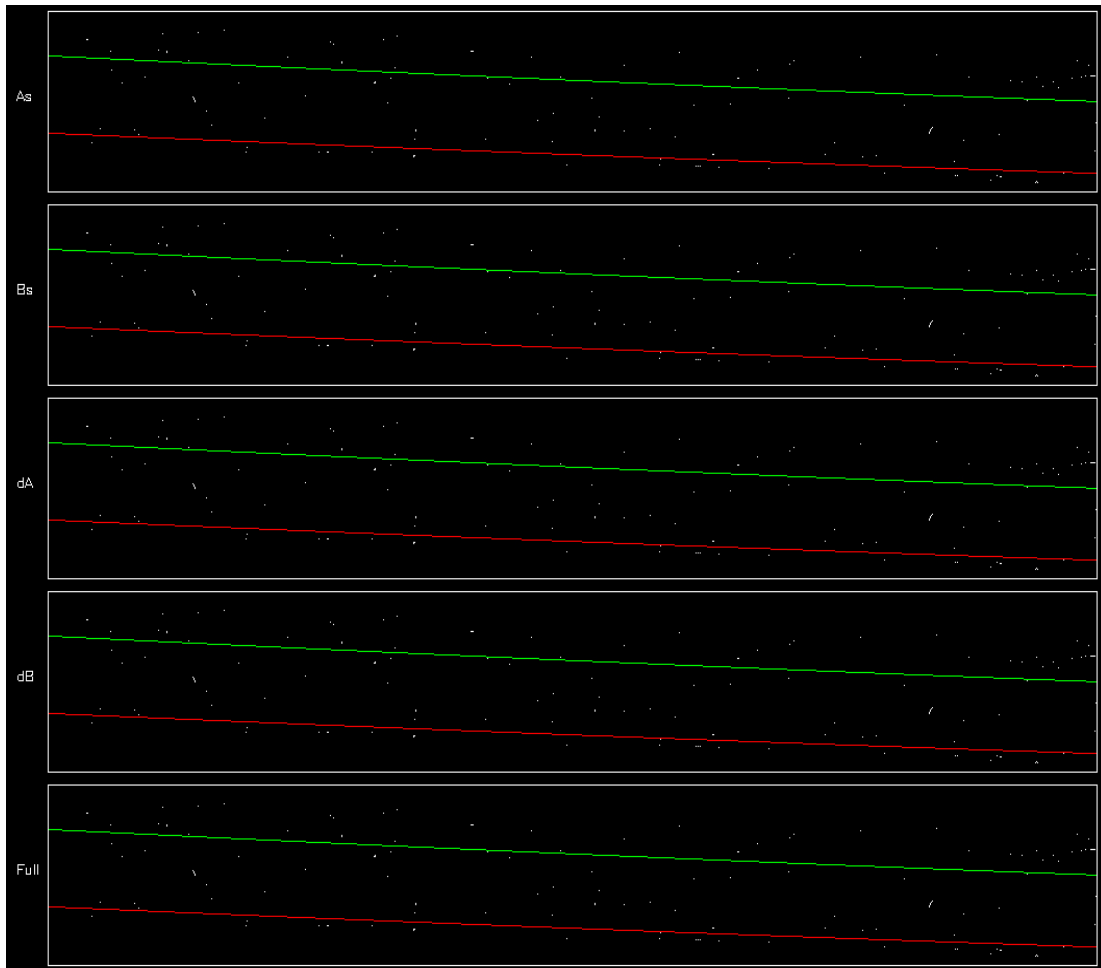


Illustration for on-chip nodding

**Figure 3.3.** Nodding of the telescope along the slit.



**Figure 3.4.** Residual raw frame after an A1-B1-B2+A2 sequence (dark current and sky emission are subtracted). The horizontal white beam (positive signal) marks the A position, and the black beam (negative signal) marks the B position of the comet. The horizontal axis corresponds to the spectral dimension, and the vertical axis – to the spatial dimension.



**Figure 3.5.** Masks of an echelle order used to remove hot pixels and cosmic ray hits. The green and red lines represent the positions of the A and B beams, and the mask outline is shown in white (including the boundaries of the crop region for individual orders in white).

The data are resampled spatially to correct for the initial tilt (from left to right), due to the fact that NIRSPEC has echelle illumination with a non-zero  $\gamma$  angle (Quasi-Littrow Mode) (McLean et al. 1998). This refers to the angle  $\gamma$  in the equation for an echelle grating:  $m\lambda = d[\sin(\theta_b + \theta_i) + \sin(\theta_b - \theta_r)]\cos\gamma$  (Porter 2000) (parameters are illustrated on Figure 3.6). In quasi-Littrow mode  $\gamma > 0$  (thus, the input and output beams are separated), and subsequent projection on the array leads to the tilt of the observed orders. The spatial resampling ensures that each position along the slit corresponds to a single row in the re-sampled data. It is convenient to use stellar frames for this purpose, since the stellar continuum is stronger and the standard star has higher signal-to-noise ratio. The spatial re-sampling (separate for the A and B beams) is done by a Gaussian fit to the data to determine the beam peak rows for each column (see Figure 3.7); and then a second order polynomial fit to relate the peak rows and the column pixel numbers, and thus, to "model" the tilt of the frames, and subsequently, remove the tilt.

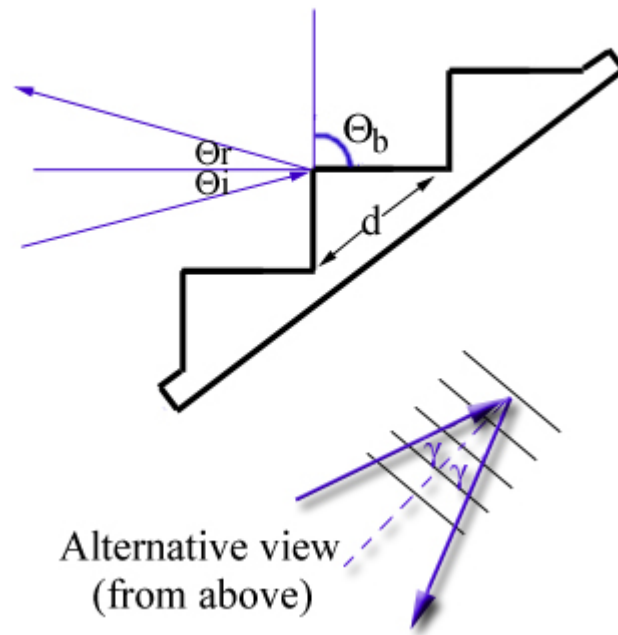


**Figure 3.6.** Illustration of the angles in the echelle grating equation:

$$m\lambda = d[\sin(\theta_b + \theta_i) + \sin(\theta_b - \theta_r)]\cos\gamma.$$

In the case of NIRSPEC

$\gamma > 0$ , and subsequent projection on the array leads to the tilt of the observed orders.

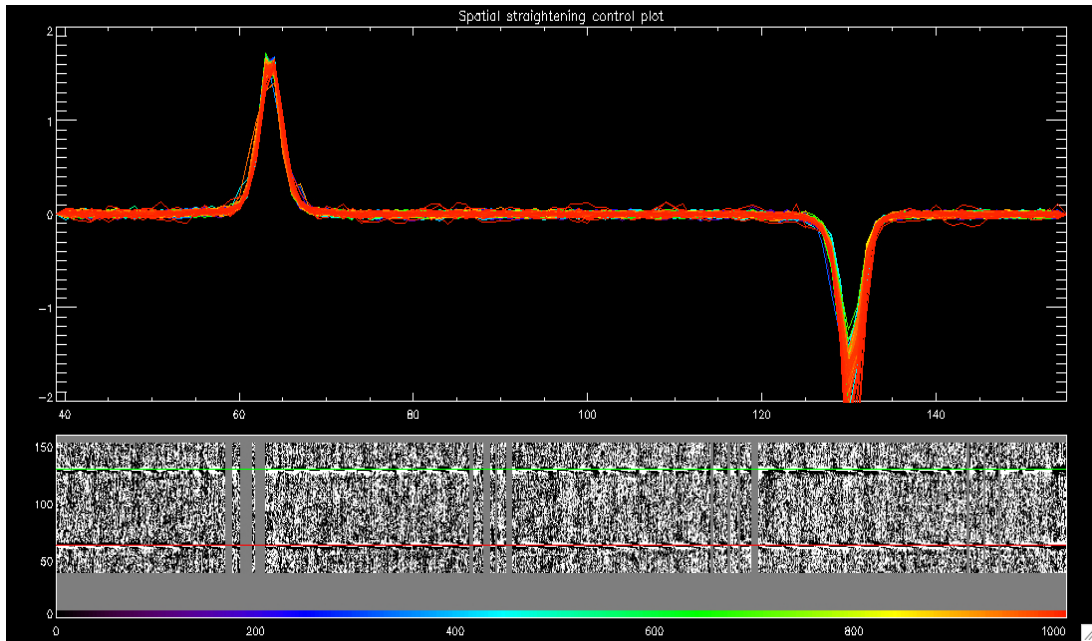


**Figure 3.7.** Spatial straightening of standard star frames. The red and green lines represent the positions of the A and B beams. The rows at which the signal peaks can be seen in the above plot (rows 63 and 130).

We also resample the data in the spectral direction to correct for the projection effects, so that pixels along a given column represent a common central wavenumber. The spectral resampling is done by comparing the measured atmospheric emission spectrum (e.g. in an A or B frame) with a synthetic spectrum modeled for the atmospheric conditions of that observation. This is done for the left and right parts of each order, by matching sky emission lines in the model to those observed in the data. The central wavenumber  $\nu_c$  and first ( $d_1$ ) and second ( $d_2$ ) order dispersion coefficients are adjusted for the best calibration:  $\nu(n) = \nu_c + d_1(n-n_c) + d_2(n-n_c)^2$ , where  $n$  is the column number, and  $n_c$  is the central pixel for each order. This is an iterative process,

and is done for every row in the data. After spectral straightening, all rows are combined to obtain a frequency (wavenumber) calibration by comparison with sky emission lines. Thus, a wavenumber scale is assigned to the data – a sample wavenumber calibration plot is shown in Figure 3.8.

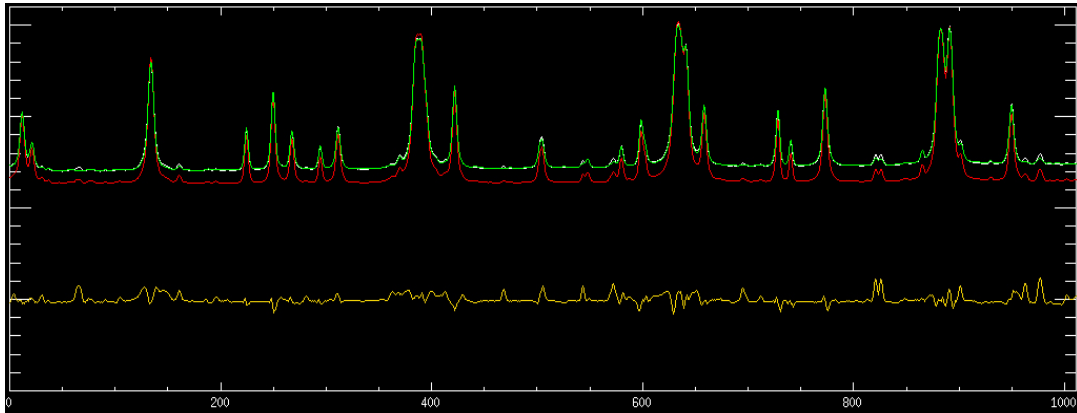


**Figure 3.8.** Wavenumber calibration. The red line is the observed emission, the green line is the modeled sky emission, and the yellow line represents the difference (multiplied by 5 for easier viewing). Dispersion line shapes are minimized, which illustrates accurate calibration.

Synthetic atmospheric models are essential to the data analysis. First, the modeled sky emission features are at the core of spectral calibration. Second, terrestrial transmittance needs to be modeled in order to properly account for the atmospheric absorption features seen in the cometary spectrum and to determine the flux above the terrestrial atmosphere (rather than as measured from the ground) for each cometary emission line. The transmittance model is normalized to the

continuum level in the data, and the residual emission features of the comet are obtained by subtracting the synthetic model from the data frames. I generated terrestrial transmittance spectra using the GENLN2 spectral synthesis program (Edwards 1992) for C/2000 WM<sub>1</sub>. This was changed to using LBLRTM (Layer-by-layer Radiative Transfer Model, Clough et al. 2005) for the analysis of 2P/Encke and all comets, to which I applied the newly developed C<sub>2</sub>H<sub>6</sub> v<sub>5</sub> model. LBLRTM is a newer, improved program, which generates synthetic spectra of the atmosphere with greater precision, higher resolution, and higher speed. It incorporates more atmospheric layers, and includes all parameters in the HITRAN database, including pressure shifts of the observed lines (which GENLN2 did not include by default). LBLRTM is actively supported, while GENLN2 is not. The terrestrial transmittance model generated with LBLRTM for the spectral range of the HCN order is presented in Figure 3.9. The abundances of different species in the terrestrial atmosphere (usually dominated by H<sub>2</sub>O, O<sub>3</sub>, N<sub>2</sub>O, CH<sub>4</sub>, and other molecules (CO<sub>2</sub>, CO) when appropriate) were determined to best fit the absorption features for each observation. The fully-resolved synthetic model (resolving power of 10<sup>7</sup>) was convolved to the resolution of the data (~25000), and the abundances of each molecule were iterated until the best match between the synthetic and measured transmittance spectra. The model was then calculated at full resolution and the transmittance was determined at each position with high precision. This is important because the true emission line flux above the terrestrial atmosphere is obtained by dividing the observed line flux by the (fully resolved) terrestrial transmittance at its exact Doppler-shifted central frequency. The stochastic noise envelope for the residual spectrum is determined



from the statistics of the electron count rates. Given an instrumental gain  $G = 5 \text{ e}^- / \text{ADU}$  (counts), and electron noise  $N_e = \sqrt{G \times \text{ADU}}$ , the photon noise is taken from

$$N[\text{ADU}] = N_e / G = \sqrt{\text{ADU} / G}.$$

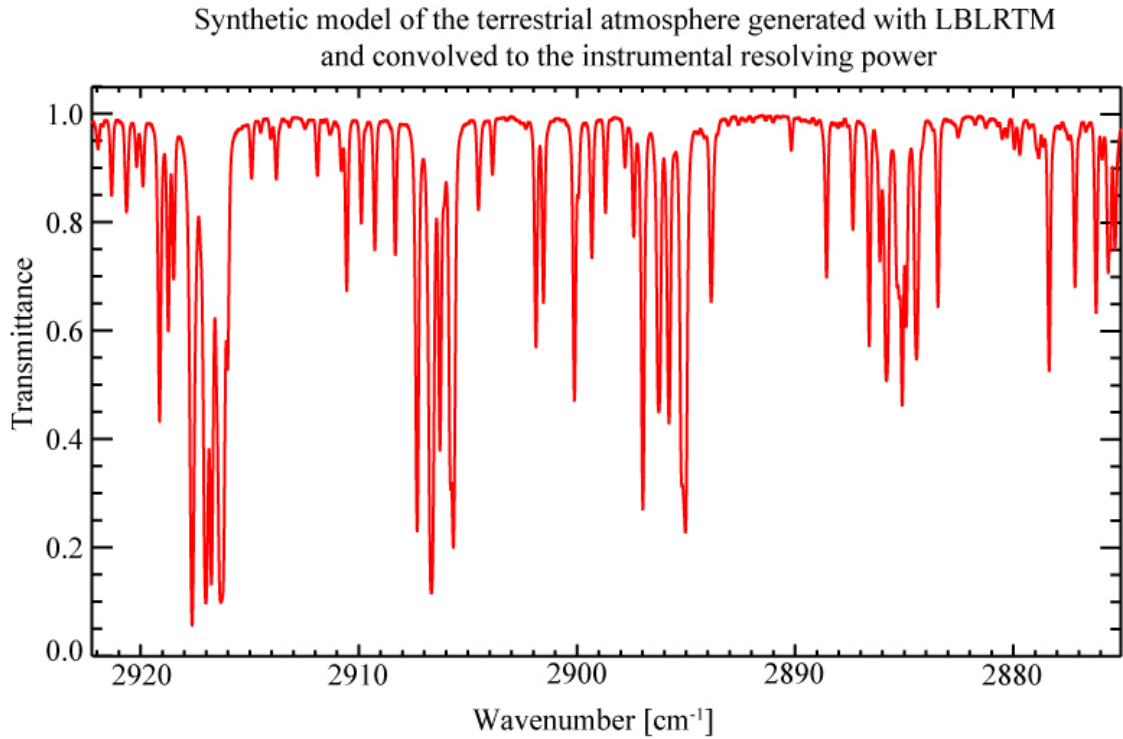


**Figure 3.9.** Terrestrial transmittance model generated with LBLRTM, and convolved to the instrumental resolving power of 25000. This model includes  $\text{CH}_4$  and  $\text{H}_2\text{O}$  (abundances determined from fit to cometary spectrum), which are the dominant species in the terrestrial atmosphere in the presented frequency region.

The comet can appear to shift in position along the slit owing to atmospheric "seeing", slight ephemeris errors, or imperfect guiding. We compensate by shifting

the frames to ensure that all A beam peaks fall along the same row (same for the B beam peaks), and the data are then said to be spatially "registered". A calibrated frame, before residual extraction, is shown on Figure 3.10. A and B beams are eventually combined. The Doppler shift of each comet is calculated, where the frequency shift is  $\Delta\nu = \frac{-V}{c}\nu_0$  ( $V$  is the line-of-sight velocity of the comet relative to the Earth, and  $\nu_0$  is the rest frequency). Spectra in this work are shown at rest frequencies to facilitate identification of cometary emission features.

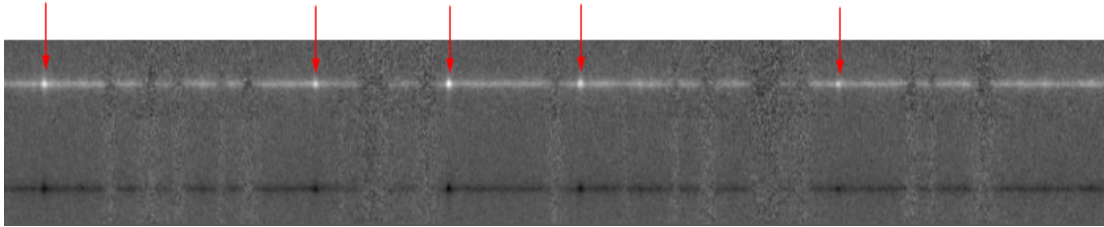


**Figure 3.10.** Echelle order containing  $C_2H_6 v_7$  from C/2000 WM<sub>1</sub> (25 Nov. 2001) after calibration. The x-axis represents the spectral dimension, and the y-axis represents the spatial dimension. The white beam is the positive signal, and the black beam is the negative signal (due to subsequent frame subtraction). Bright  $C_2H_6 v_7$  emission features can be seen on this spectrum, and are marked with red arrows.

Spectra of a standard flux star (observed during the same night as the comet) are used for the purpose of flux calibration. After calibrating the stellar frames (see Figure 3.11), flux conversion factors  $\Gamma [W m^{-2} (cm^{-1})^{-1} (ADU s^{-1})^{-1}]$  are calculated,

where  $\Gamma = \frac{F_v \cdot \tau_v}{C/t \cdot L}$  ( $F_v$  is the stellar flux density [ $\text{W m}^{-2} (\text{cm}^{-1})^{-1}$ ],  $\tau_v$  is the terrestrial transmittance,  $C$  is the stellar continuum intensity level,  $t$  is the integration time, and  $L$  is the slit loss correction factor (stellar spectra are acquired with a 5 pixel slit, rather than an infinitely wide slit, thus, the entire stellar flux is not acquired). The slit loss factor, FWHM and fraction of total flux sampled are obtained through a Gaussian fit to the stellar intensity profile along the slit. Because guiding and seeing may vary from frame to frame, flux calibration factors are obtained from each stellar frame, and the lowest (or mean) flux calibration factor is chosen (corresponding to the sharpest stellar profile, and ideally to the smallest slit loss correction factor). Thus, the counts per second in the comet data are converted to flux density in  $\text{W m}^{-2} [\text{cm}^{-1}]^{-1}$ .

Finally, after the cometary spectrum has been flux-calibrated, the intensities of cometary emission lines are measured and used to extract rotational temperatures and gas production rates for each species. The next section describes excitation analysis as applied to the rotational temperature derivation.

---

<sup>i</sup>In addition to the discussion of preliminary data reduction in this Section, very detailed descriptions of all algorithms and procedures implemented by our team are presented in Dr. Bonev's doctoral dissertation (2005), and in DiSanti et al. 2006 (and references therein). The IDL routines for the entire analysis described here were developed by Dr. Geronimo Villanueva, based on earlier routines by Dr. Michael DiSanti, further modified by Dr. Boncho Bonev (from the team at NASA's GSFC). Routines are constantly being updated and improved.

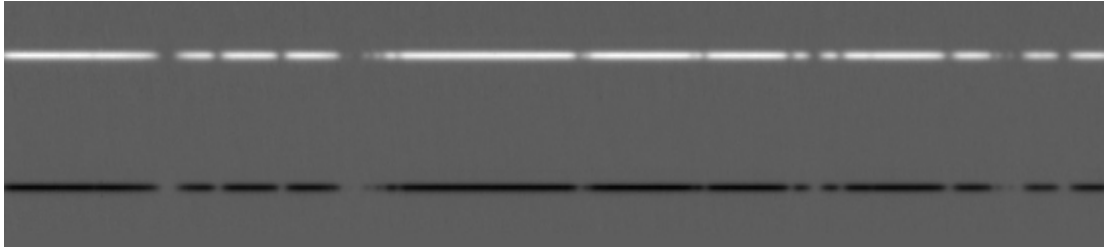


**Figure 3.11.** Calibrated stellar frame (spectrum of standard star): the white beam is the positive stellar signal, and the black beam is the negative signal (due to subsequent frame subtraction). The x-axis represents the spectral dimension, and the y-axis represents the spatial dimension. Note that this frame shows part of the order, rather than the entire order, for better visualization (since the horizontal axis would typically cover 1024 pixels, and the vertical axis would cover 128 pixels).

### Rotational Temperature Derivation

Accurate rotational temperatures are needed in order to extract production rates for parent species, given that in most cases only a sub-set of ro-vibrational levels is sampled. The population of a molecule in rotational levels of the ground vibrational state is characterized by a rotational temperature ( $T_{\text{rot}}$ ), and the individual level populations  $P_m$  are given by:  $P_m = \frac{g_m \exp(-E_m/kT)}{Z(T)}$  where  $g_m$  is the statistical weight of level 'm',  $E_m$  is the energy of the level, and  $Z$  is the partition function. This assumes collisional excitation in the sampled inner coma, such that collisions

thermalize the rotational levels in the ground vibrational state (as discussed in Chapter 2).

The rotational temperature of a given species is obtained by forming the ratios of observed line-flux and predicted g-factor, for each sampled line. The g-factors are temperature dependent, and are modeled for a specific  $T_{\text{rot}}$ . At the correct rotational temperature, the line-flux/g-factor ratios should agree for the sampled lines within error, if assumptions are valid. This approach uses a graphical representation of ratios versus rotational energy. We determine the slope of the graphed data at each rotational temperature (using the method of least squares linear regression). At the correct rotational temperature this slope is zero. If the assumed rotational temperature is lower than the actual temperature, the slope would be negative (since the g-factors for lines with low excitation would be overestimated), and if the assumed temperature is higher than the actual value, the slope would be positive (since the g-factors for the high-excitation lines would be overestimated). We vary the rotational temperature until the best agreement is achieved.

The stochastic and standard errors of the rotational temperature are calculated, and the larger value is assumed as the  $T_{\text{rot}}$  error. The stochastic error is calculated on the basis of errors associated with line flux (based on photon noise), while the standard error is based on the spread of the line-flux/g-factor values around the zero-slope fit. The stochastic error for a linear fit ( $y = ax + b$ , where  $y$  represents the

production rate  $Q$ , and  $x$  represents the excitation energy  $E$  of each line) is defined as:

$$\sigma_{\text{stochastic}} = \sqrt{\frac{1}{\sum_i \frac{1}{\sigma_i^2} \sum_i \frac{y_i^2}{\sigma_i^2} - (\sum_i \frac{y_i}{\sigma_i})^2} \sum_i \frac{1}{\sigma_i^2}}. \text{ The standard error is:}$$

$$\sigma_{\text{standard}} = \sqrt{\frac{\frac{\sum_i (y_i - y_{\text{fit}}[x_i])^2}{\sigma_i^2}}{\frac{1}{N-2} \frac{1}{N} \sum_i \frac{1}{\sigma_i^2}} \frac{\sum_i (x_i - x_{\text{mean}})^2}{N-1} \sqrt{N-1}} \quad (\text{from Bonev 2005, original sources:}$$

Bevington & Robinson 1992, Hoel 1984, and Arkin & Colton 1970). Standard errors usually dominate stochastic errors (which may be underestimated due to modelling offsets, such as errors in g-factors). The above expression illustrates that a larger spread of excitation energies among the sampled lines would provide a data fit that is better constrained. Further details on rotational temperature derivation are presented in Dello Russo et al. 2004, Bonev 2005, DiSanti et al. 2006.

Another important assumption is that of an optically thin medium. Optical depth effects have been explored in detail by the team at NASA GSFC. They need to be considered only very close to the nucleus (within a few kilometers) for a very active comet, such as Ikeya-Zhang (and for some, not all, transitions) (see Dello Russo et al. 2004 for discussion of H<sub>2</sub>O); Hale Bopp (see DiSanti et al. 2001 for discussion of CO), etc. The comet C/2000 WM<sub>1</sub> (analyzed in this research, Chapter 4) is 10 times less active than Ikeya-Zhang and 100 times less active than Hale-Bopp, which allows us to neglect optical depth effects. Similarly, the comet 2P/Encke

(analysis presented in Chapter 5) is 10 times less active than C/2000 WM<sub>1</sub>, which makes optical depth effects negligible.

### Production Rates of Parent Volatiles

The production rate ( $Q_i$ ) of a volatile species is derived from each measured line (i):

$$Q_i = \frac{4\pi\Delta^2 \frac{F_i}{t_i}}{g_i\tau(h\nu)f(x)}$$

, where  $\Delta$  is geocentric distance [m],  $F_i$  is the flux of the  $i^{\text{th}}$  line

measured in a 3x9 pixel box centered on the nucleus,  $t_i$  is the terrestrial transmittance at the frequency of the  $i^{\text{th}}$  line,  $f(x)$  is the fraction of the total coma content of the targeted species sampled by the pencil-beam,  $h\nu$  is the energy of a photon with wavenumber  $\nu$  [ $\text{cm}^{-1}$ ],  $g_i$  is the line "g-factor" at temperature ( $T_{\text{rot}}$ ) at 1 AU, and  $\tau$  is the molecular lifetime at 1 AU (Mumma et al. 2003). This assumes a spherical outflow model with uniform velocity (given by  $0.8 \times R_h^{-0.5} \text{ km s}^{-1}$ ). Given the small inner region of the coma that is sampled,  $f(x) \propto (\tau \times V_{\text{gas}})^{-1}$ , where  $V_{\text{gas}}$  is the outflow velocity. Therefore, derivations are not sensitive to the assumed molecular lifetime. Also, g-factors and lifetimes can be calculated at any heliocentric distance  $R$  [AU] from:  $g(R) = g(1\text{AU}) \times R^{-2}$  and  $\tau(R) = \tau(1\text{AU}) \times R^2$ .

The nucleus-centered production rate ( $Q_{\text{nc}}$ ) is the weighted-mean of individual line production rates ( $Q_i$ ). The weight for each  $Q_i$  is the inverse of the associated

stochastic error (squared). Thus,  $Q_{\text{weighted-mean}} = \frac{\sum_i Q_i / \sigma_i^2}{\sum_i 1 / \sigma_i^2}$ , where  $\sigma_i$  is determined

from the uncertainty in flux measurement for each line. Reported errors are given as the larger of the stochastic uncertainty (signal-to-noise ratio dependent, based on the photon noise level) or the standard uncertainty (dependent on the relative agreement of  $Q_i$  for all measured lines). The stochastic uncertainty of the weighed mean

production rate is:  $\sigma_{\text{stochastic}} = \sqrt{\frac{1}{\sum_i 1 / \sigma_i^2}}$ , and its standard uncertainty is:

$$\sigma_{\text{standard}} = \frac{\sqrt{\frac{1}{N-1} \cdot \frac{\sum_i (Q_i - Q_{\text{weighted\_mean}})^2 / \sigma_i^2}{\frac{1}{N} \cdot \sum_i 1 / \sigma_i^2}}}{\sqrt{N}}.$$

The nucleus-centered productions rates are obtained from extracts with the highest signal-to-noise ratio, however,  $Q_{\text{nc}}$  underestimates the global production rate (as a result of slit losses, for example due to seeing effects). The mean value of production rates extracted at equidistant positions along the spatial profile, on either side of the nucleus (Xie and Mumma 1996), is determined (also correcting for 1-D asymmetries in the gas outflow). Typically at about 1" from the nucleus the production rate reaches a terminal value (illustrated for comet C/2000 WM<sub>1</sub> on Figure 3.12), and these symmetrized production rates are reported as the global (true) production rates (Mumma et al. 2003, Bonev 2005, DiSanti et al. 2006).



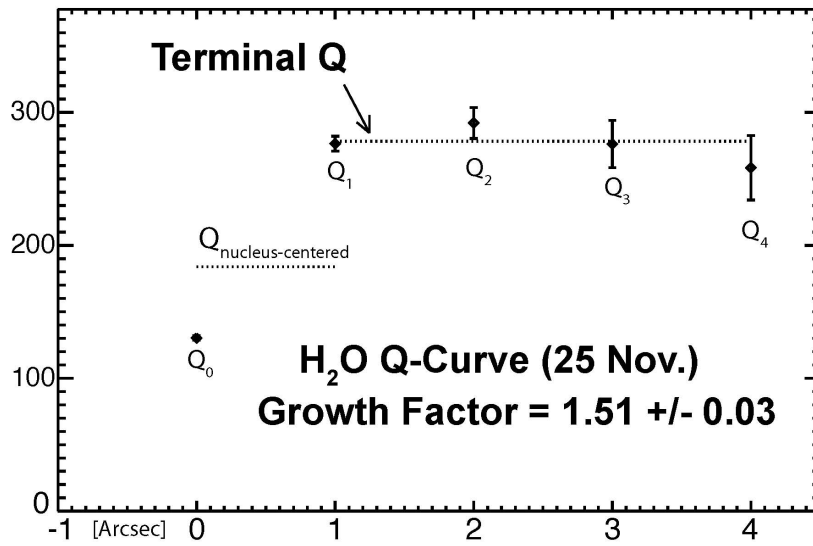


**Figure 3.12.** The production rate of  $\text{H}_2\text{O}$  on 25 Nov. 2001 in comet C/2000 WM<sub>1</sub>, measured at increasing distances from the nucleus. The growth factor is the ratio between the terminal Q and the nucleus-centered Q. ( $Q_{\text{nucleus-centered}}$  is measured over 9 central pixels, and needs to be distinguished from  $Q_0$ , which represents measurement over 3 central pixels only).

## Chapter 4: The Depleted Organic Composition of Comet C/2000

### WM<sub>1</sub> (LINEAR)

This chapter presents the organic composition of comet C/2000 WM<sub>1</sub> (LINEAR). This investigation has been published in *Icarus* (Radeva et al. 2010). The principal results of the analysis are presented here (the figures and tables are adapted or reproduced from Radeva et al. 2010).

#### Observations of C/2000 WM<sub>1</sub> (LINEAR)

C/2000 WM<sub>1</sub> (LINEAR) is an Oort cloud comet with inverse semimajor axis  $1/a = 0.0005222 \text{ AU}^{-1}$  (Nakano Note NK955), which is considered not to be dynamically new. The comet reached perigee at 0.316 AU on 2 Dec. 2001, and reached perihelion at 0.555 AU on 22 Jan. 2002. The Goddard team acquired infrared spectra of WM<sub>1</sub> on 23-25 Nov. 2001, using NIRSPEC on the Keck II telescope. The observing log is given in Table 4.1.

**Table 4.1.** Observing log for C/2000 WM<sub>1</sub>.

UT Time (2001)	Setting <sup>I</sup>	Frequency range of setting [cm <sup>-1</sup> ]	R <sub>h</sub> <sup>II</sup> [AU]	Δ <sup>II</sup> [AU]	Δ <sub>dot</sub> <sup>II</sup> [km s <sup>-1</sup> ]
23 Nov., 05:15 - 06:37	KL1	3397 - 2704	1.355	0.384	-23.87
07:13 - 08:16	KL2	3455 - 2753	1.354	0.383	-23.56
10:08 - 10:17	MW_A	2165 - 1866	1.352	0.381	-23.14
24 Nov., 05:18 - 06:07	KL1	3397 - 2704	1.339	0.371	-21.94
07:30 - 07:51	MW_A	2165 - 1866	1.338	0.370	-21.58
08:23 - 09:25	KL2	3455 - 2753	1.337	0.369	-21.36
25 Nov., 05:12 - 05:29	KL1	3397 - 2704	1.323	0.359	-19.84
06:49 - 07:44	MW_A	2165 - 1866	1.322	0.358	-19.51
08:50 - 09:59	KL2	3455 - 2753	1.321	0.357	-19.10

<sup>I</sup>We measure CH<sub>3</sub>OH, C<sub>2</sub>H<sub>6</sub> & H<sub>2</sub>O simultaneously in KL1; HCN, CH<sub>4</sub>, C<sub>2</sub>H<sub>2</sub>, H<sub>2</sub>CO & H<sub>2</sub>O simultaneously in KL2; and CO & H<sub>2</sub>O simultaneously in MW\_A.

<sup>II</sup>R<sub>h</sub> is the heliocentric distance, Δ - the geocentric distance, and Δ<sub>dot</sub> – the line-of-sight velocity.

### Spectral Gallery

I analyzed the raw data following procedures described in detail in Chapter 3, and extracted flux-calibrated cometary spectra by summing signal from nine rows centered on the nucleus (spanning 1.78'' or ~ 480 km). I present the spectral extracts in Figs. 4.1 - 4.8, showing the modeled terrestrial atmosphere superimposed on the cometary spectrum, the residual features for each date; and the (±1-σ) stochastic (photon) noise envelope. The following parent species were measured: CH<sub>3</sub>OH, C<sub>2</sub>H<sub>6</sub>, H<sub>2</sub>CO, CH<sub>4</sub>, HCN, C<sub>2</sub>H<sub>2</sub>, CO and H<sub>2</sub>O.

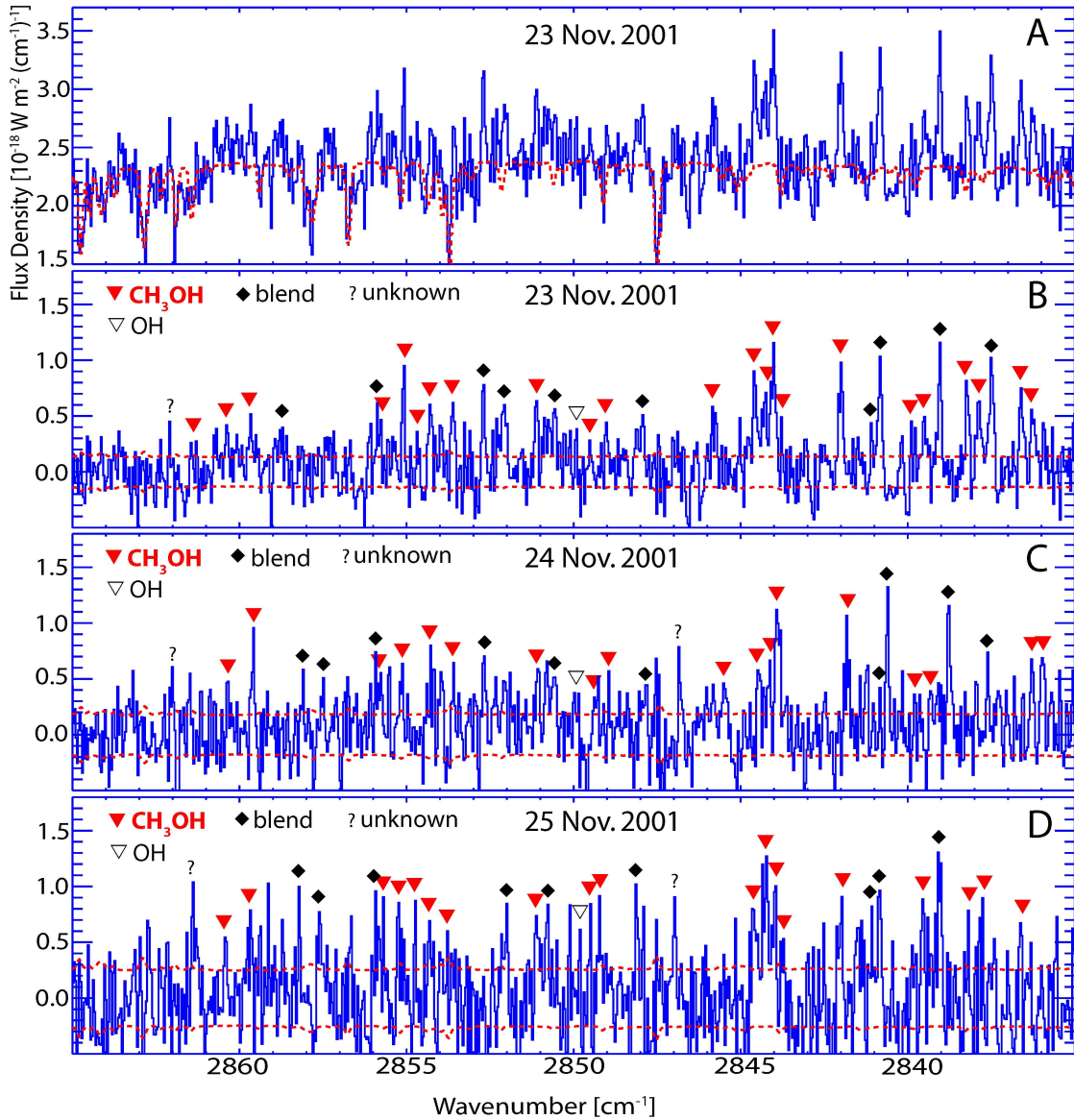


**Figure 4.1:** WM<sub>1</sub> cometary spectrum and superimposed terrestrial transmittance model (dashed line) for 23 Nov. 2001 (panel A), and residual spectra for 23, 24 and 25 Nov. 2001 in panels B-D. Spectral lines of CH<sub>3</sub>OH, OH, blends and unknown species are seen. The flux density scale is shown at left, and the ( $\pm 1\text{-}\sigma$ ) noise envelope is shown as dashed lines centered on zero flux density, in each panel.

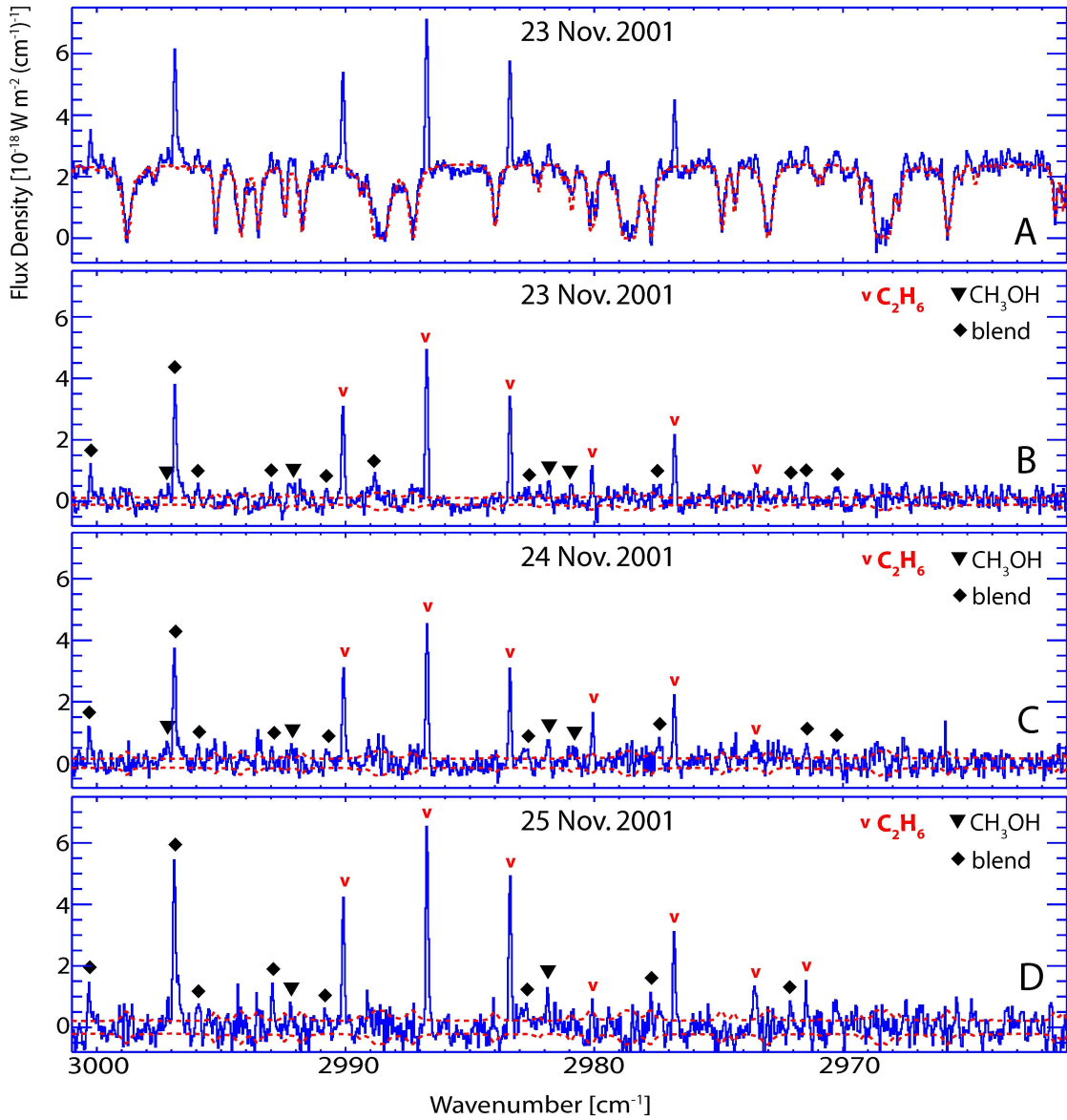


**Figure 4.2:** WM<sub>1</sub> cometary spectrum and superimposed terrestrial transmittance model (dashed line) for 23 Nov. 2001 (panel A), and residual spectra for 23, 24 and 25 Nov. 2001 in panels B-D. Spectral lines of C<sub>2</sub>H<sub>6</sub>, CH<sub>3</sub>OH, and blends are seen. The flux density scale is shown at left, and the ( $\pm 1\text{-}\sigma$ ) noise envelope is shown as dashed lines centered on zero flux density, in each panel.

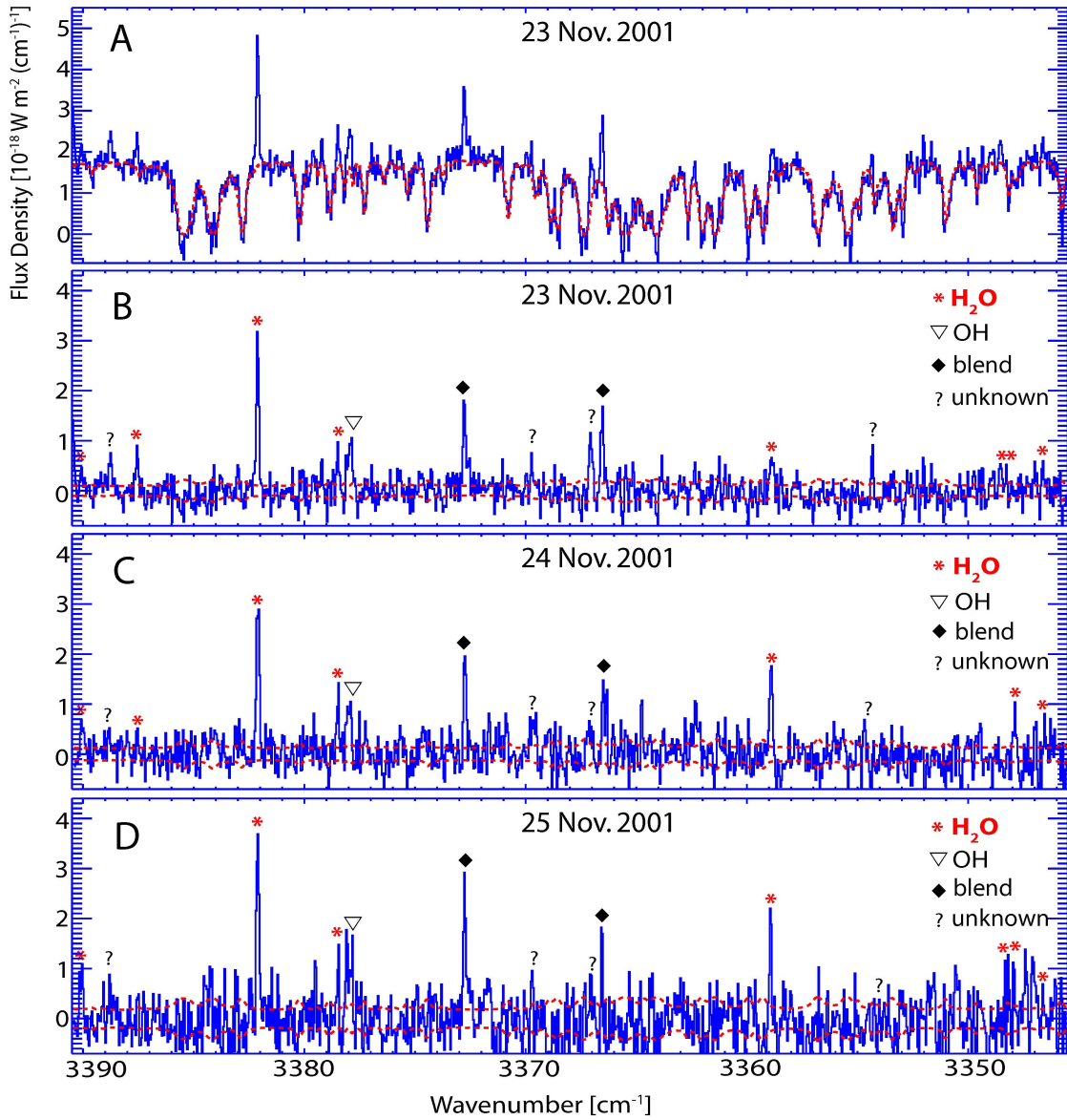


**Figure 4.3:**  $\text{WM}_1$  cometary spectrum and superimposed terrestrial transmittance model (dashed line) for 23 Nov. 2001 (panel A), and residual spectra for 23, 24 and 25 Nov. 2001 in panels B-D. Spectral lines of  $\text{H}_2\text{O}$ , OH, blends and unknown species are seen. The flux density scale is shown at left, and the  $(\pm 1\text{-}\sigma)$  noise envelope is shown as dashed lines centered on zero flux density, in each panel.

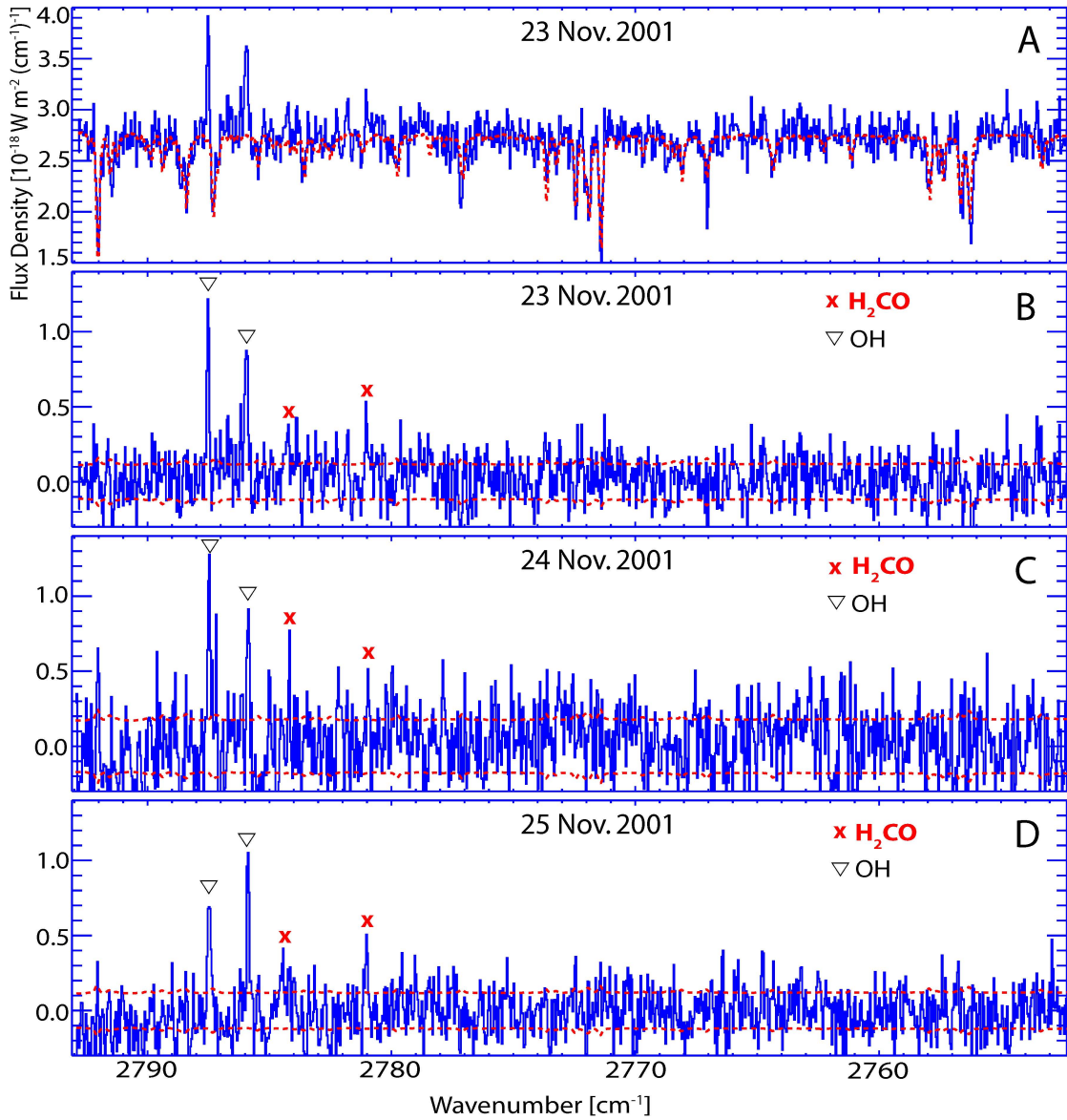


**Figure 4.4:** WM<sub>1</sub> cometary spectrum and superimposed terrestrial transmittance model (dashed line) for 23 Nov. 2001 (panel A), and residual spectra for 23, 24 and 25 Nov. 2001 in panels B-D. Spectral lines of H<sub>2</sub>CO and OH are seen. The flux density scale is shown at left, and the ( $\pm 1\text{-}\sigma$ ) noise envelope is shown as dashed lines centered on zero flux density, in each panel.

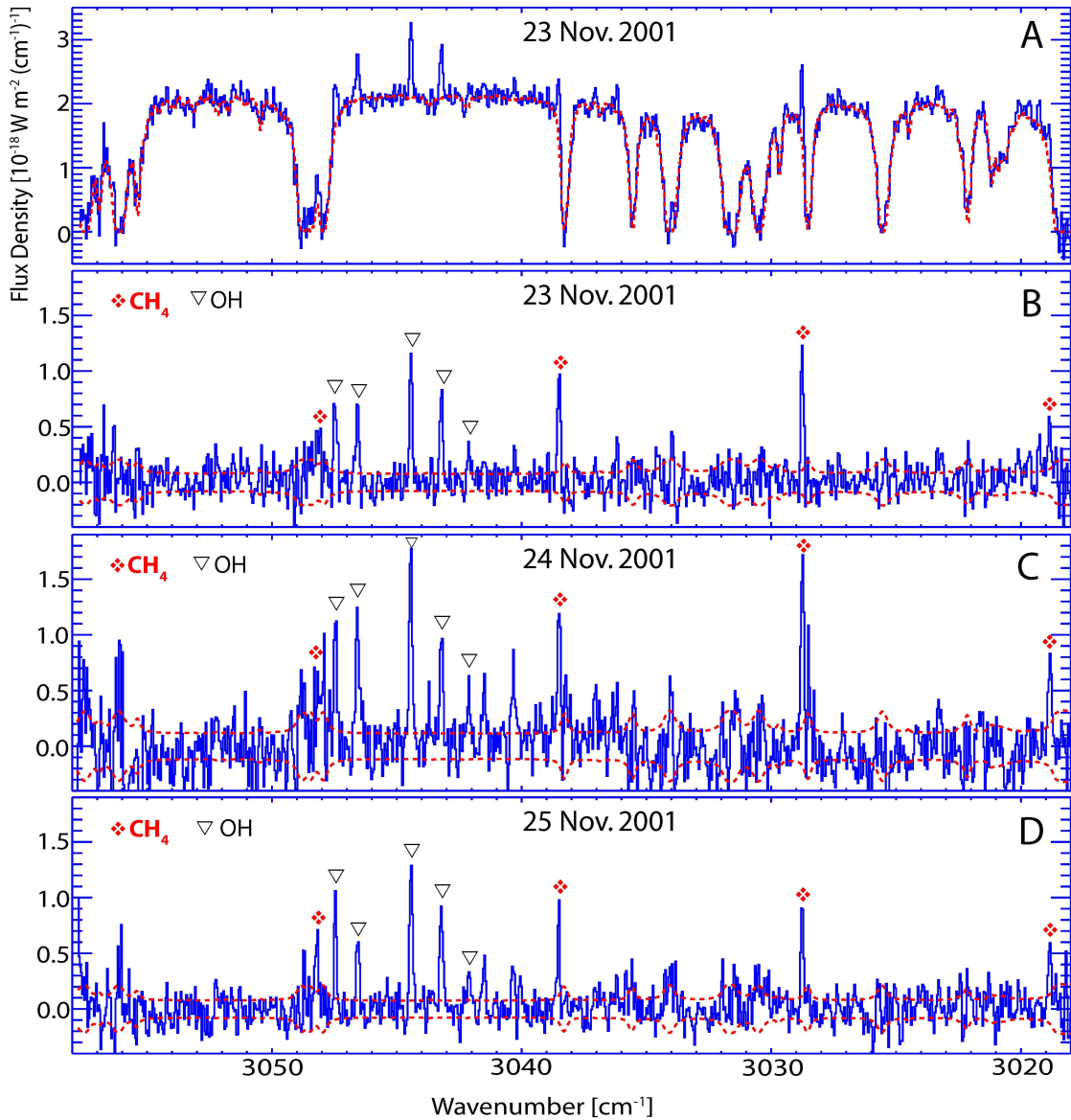


**Figure 4.5:** WM<sub>1</sub> cometary spectrum and superimposed terrestrial transmittance model (dashed line) for 23 Nov. 2001 (panel A), and residual spectra for 23, 24 and 25 Nov. 2001 in panels B-D. Spectral lines of CH<sub>4</sub> and OH are seen. The flux density scale is shown at left, and the ( $\pm 1\text{-}\sigma$ ) noise envelope is shown as dashed lines centered on zero flux density, in each panel.



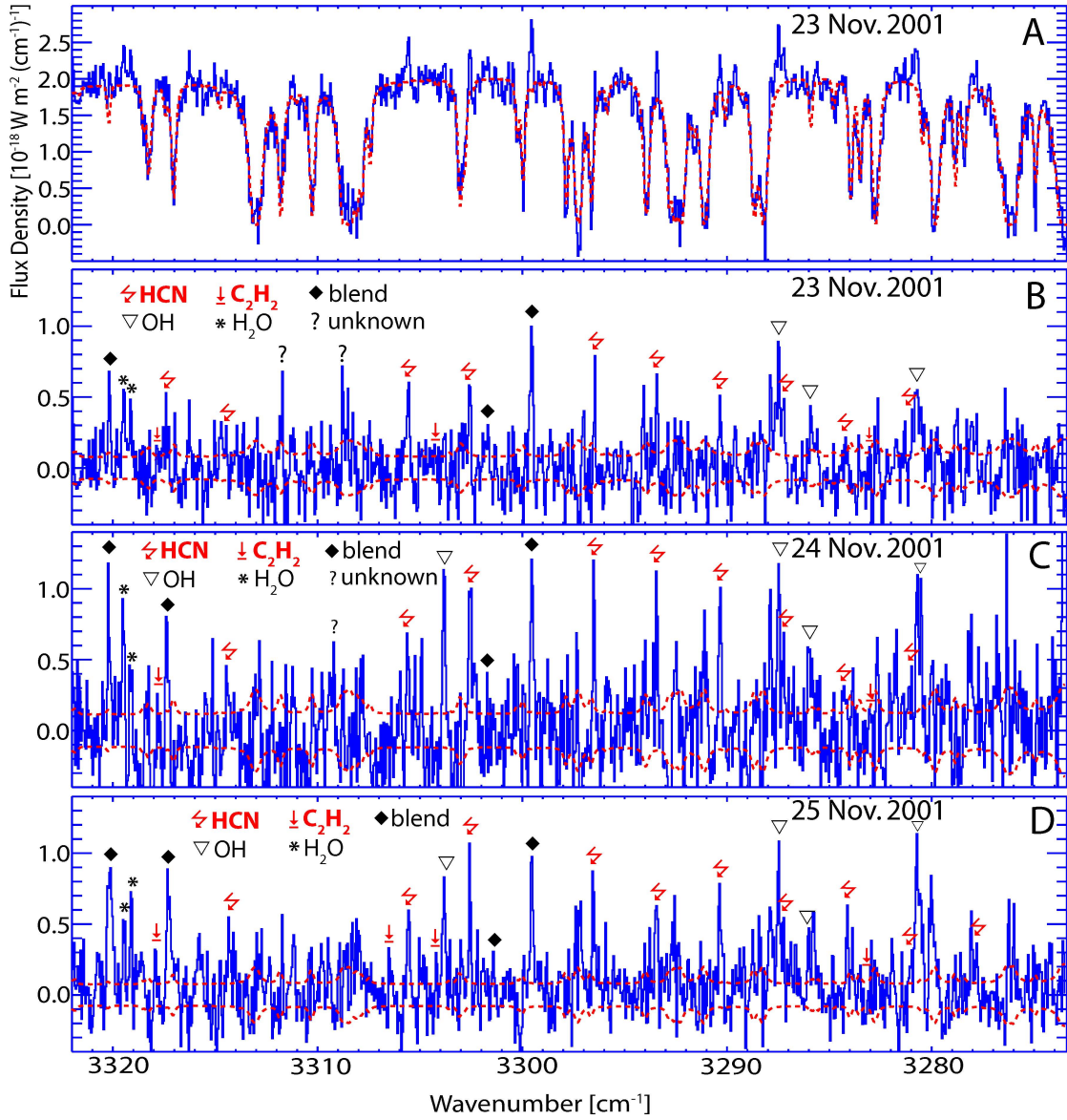


**Figure 4.6:** WM<sub>1</sub> cometary spectrum and superimposed terrestrial transmittance model (dashed line) for 23 Nov. 2001 (panel A), and residual spectra for 23, 24 and 25 Nov. 2001 in panels B-D. Spectral lines of HCN, C<sub>2</sub>H<sub>2</sub>, H<sub>2</sub>O, OH and blends are seen. The flux density scale is shown at left, and the ( $\pm 1\text{-}\sigma$ ) noise envelope is shown as dashed lines centered on zero flux density, in each panel.

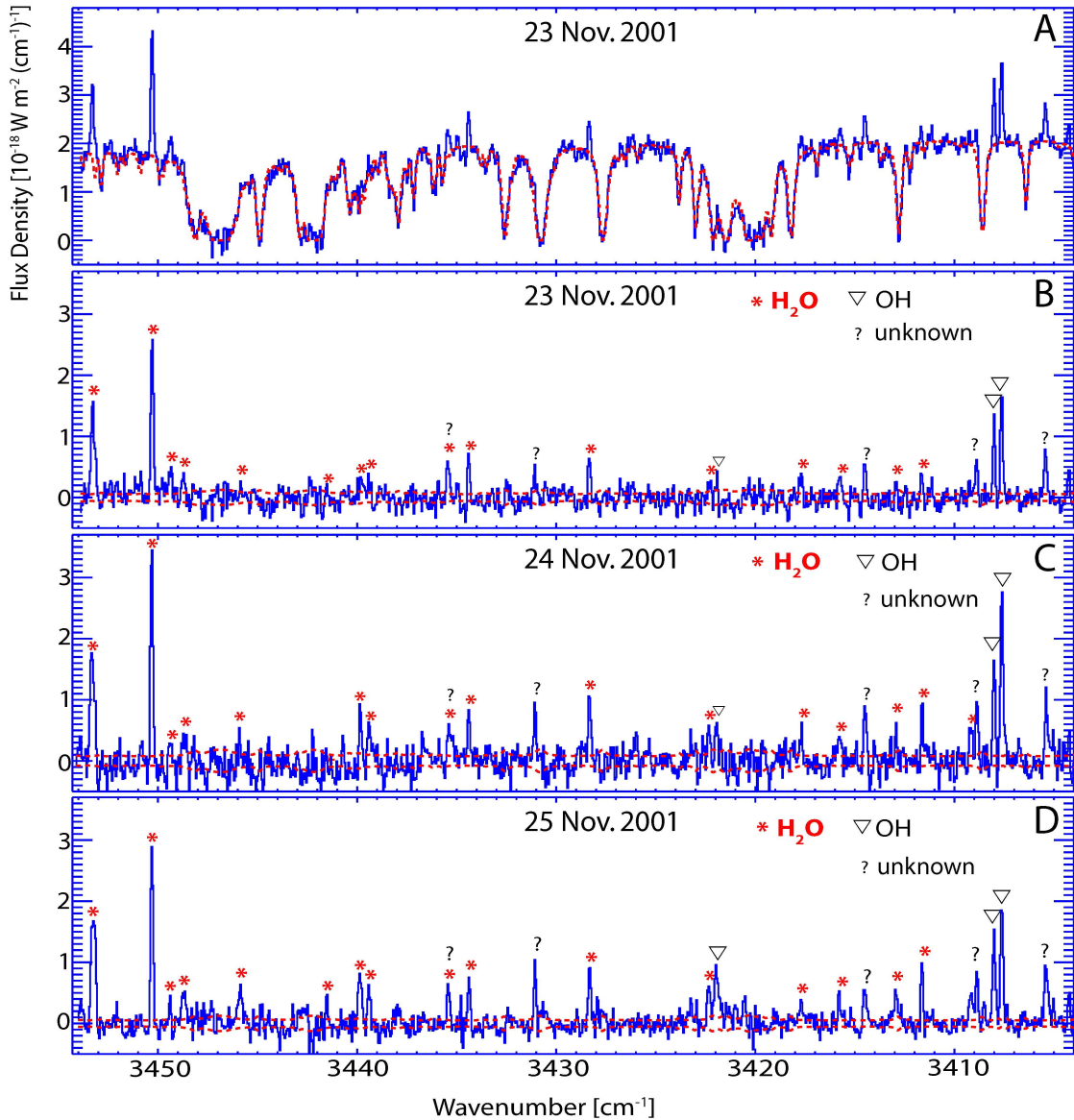


**Figure 4.7:** WM<sub>1</sub> cometary spectrum and superimposed terrestrial transmittance model (dashed line) for 23 Nov. 2001 (panel A), and residual spectra for 23, 24 and 25 Nov. 2001 in panels B-D. Spectral lines of H<sub>2</sub>O, OH, and unknown species are seen. The flux density scale is shown at left, and the ( $\pm 1\text{-}\sigma$ ) noise envelope is shown as dashed lines centered on zero flux density, in each panel.

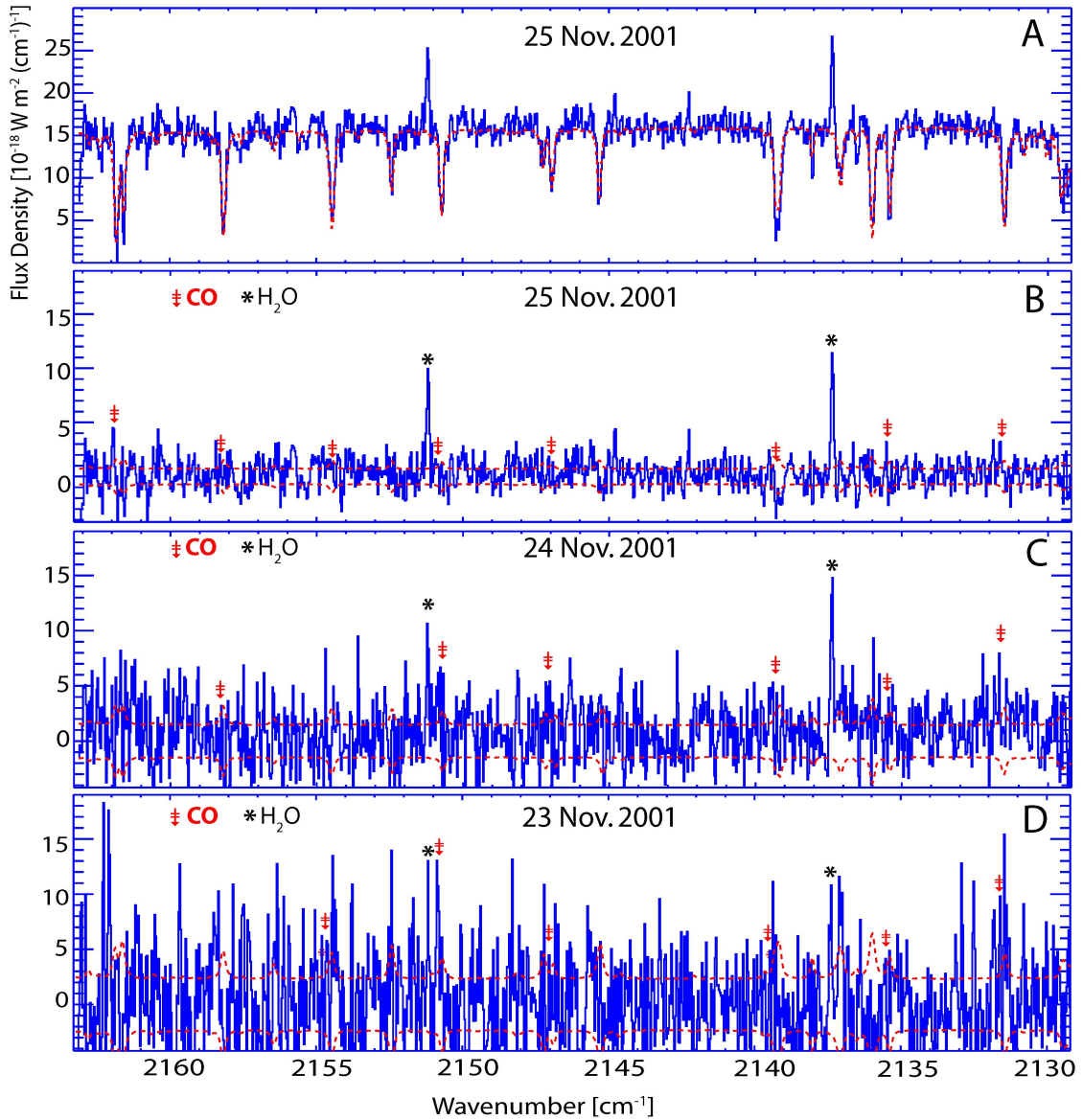


**Figure 4.8:** WM<sub>1</sub> cometary spectrum and superimposed terrestrial transmittance model (dashed line) for 25 Nov. 2001 (panel A), and residual spectra for 25, 24 and 23 Nov. 2001 in panels B-D. The positions expected for lines of CO and H<sub>2</sub>O are marked. The flux density scale is shown at left, and the ( $\pm 1\text{-}\sigma$ ) noise envelope is shown as dashed lines centered on zero flux density, in each panel.

### Rotational Temperatures and Production Rates

I derived rotational temperatures for C/2000 WM<sub>1</sub> from HCN and H<sub>2</sub>O, excluding lines that were blended with those of other species (e.g. C<sub>2</sub>H<sub>2</sub> with HCN v<sub>3</sub>). The detected lines of HCN v<sub>3</sub> sample a wide spread in excitation energies, facilitating their use as a temperature indicator. Rotational temperatures derived for 23, 24 and 25 Nov. for both species are presented in Table 4.5. The weighted mean T<sub>rot</sub> for HCN from 23-25 Nov. (78<sup>-4</sup>/<sub>+5</sub> K) is consistent with that for H<sub>2</sub>O (70<sup>-2</sup>/<sub>+2</sub> K) within 2-σ. I assumed T<sub>rot</sub> (H<sub>2</sub>O) = 70<sup>-2</sup>/<sub>+2</sub> K for all other species, for which reliable rotational temperatures could not be derived: H<sub>2</sub>CO, CH<sub>4</sub>, C<sub>2</sub>H<sub>2</sub>, CH<sub>3</sub>OH, CO.

**Table 4.2.** Rotational temperatures for C/2000 WM<sub>1</sub>.

Date	Molecule	Trot [K]
23 Nov. 2001	H <sub>2</sub> O	70 <sup>-25</sup> / <sub>+6</sub>
	HCN	76 <sup>-13</sup> / <sub>+17</sub>
24 Nov. 2001	H <sub>2</sub> O	69 <sup>-3</sup> / <sub>+3</sub>
	HCN	70 <sup>-7</sup> / <sub>+9</sub>
25 Nov. 2001	H <sub>2</sub> O	70 <sup>-2</sup> / <sub>+2</sub>
	HCN	82 <sup>-5</sup> / <sub>+6</sub>

The excitation analyses for HCN and H<sub>2</sub>O for 25 Nov. 2001 are presented on Figure 4.9. All lines of HCN fall within 1 or 2-σ of the line of zero slope (T<sub>rot</sub> (HCN) = 82<sup>-5</sup>/<sub>+6</sub> K). However, several lines of H<sub>2</sub>O deviate from a straight line fit (Panel B).

The deviating lines have high excitation-energy, and are very weak at  $T_{\text{rot}} = 70^{-2}/_{+2}$  K. They have very large stochastic errors and therefore, small weights in this analysis.

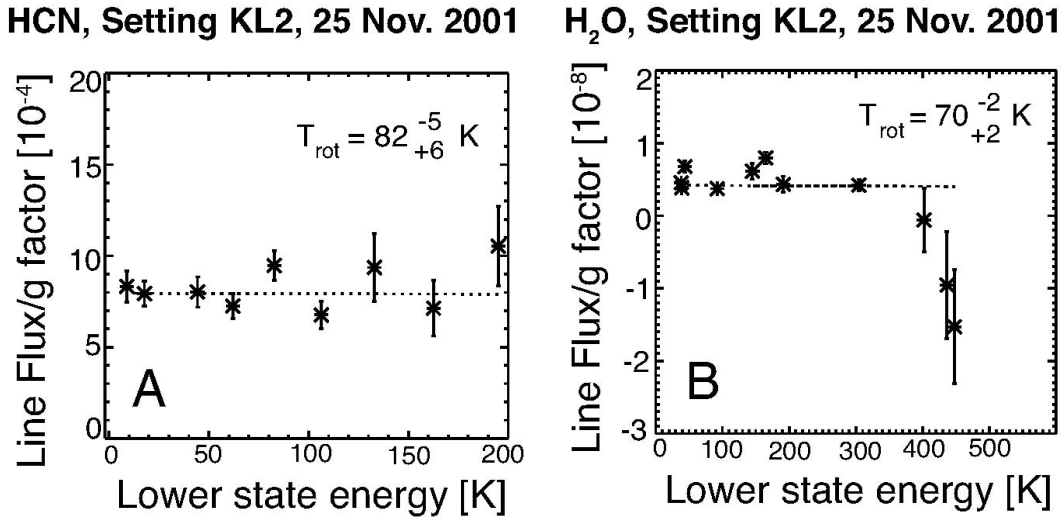


**Figure 4.9.** Excitation analysis for HCN (P2, P3, P5-P11 lines in the  $\nu_3$  band) in panel A, and for H<sub>2</sub>O in panel B, on 25 Nov. 2001. These are fluxes measured above the terrestrial atmosphere, and from nucleus-centered extracts.  $T_{\text{rot}}$  (HCN) =  $82^{-5}/_{+6}$  K and  $T_{\text{rot}}$  (H<sub>2</sub>O) =  $70^{-2}/_{+2}$  K.

I present production rates, rotational temperatures, and mixing ratios for the detected parent species in C/2000 WM<sub>1</sub> in Tables 4.3 - 4.5. (The electronic supplemental material to Radeva et al. (2010) contains a detailed list of line fluxes and g-factors). The confidence limits account for uncertainties in the assumed or derived rotational temperature. In the case of H<sub>2</sub>O, CH<sub>4</sub>, C<sub>2</sub>H<sub>2</sub>, C<sub>2</sub>H<sub>6</sub>, HCN and CO, production rates are derived as weighted means of individual line measurements.

However, for CH<sub>3</sub>OH and H<sub>2</sub>CO, production rates are derived from the integrated Q-branch of each species. Also, spectral lines that are blends of different species are normally excluded. Secure detection of C<sub>2</sub>H<sub>2</sub> cannot be reported, thus, 3- $\sigma$  upper limits for its production rates and mixing ratios are presented. For CO, the best data were obtained on 25 Nov. (22 min. on source, in contrast to 4 min. on 23 Nov., and 10 min. on 24 Nov.). CO is observed in the same echelle order as H<sub>2</sub>O (at 4.7  $\mu$ m), therefore I subtracted a scaled model of H<sub>2</sub>O from the residual spectrum, and afterwards derived a CO production rate (see Figure 4.10 for excitation diagram). 3- $\sigma$  upper limits for CO are presented for 23 and 24 Nov., and detection is reported for 25 Nov.

**Table 4.3.** Production rates for C/2000 WM<sub>1</sub> on 23 Nov. 2001.

<b>Setting / Time on Source</b>	<b>Molecule (measured or adopted T<sub>rot</sub>)</b>	<b>Global Q [10<sup>25</sup> s<sup>-1</sup>]</b>	<b>Mixing Ratio %</b>
KL1 / 56 min	H <sub>2</sub> O (70 K)	2090.61 $\pm$ 164.59	100.00
	C <sub>2</sub> H <sub>6</sub> (70 K)	10.77 $\pm$ 1.02	0.52 $\pm$ 0.05
	CH <sub>3</sub> OH, Q branch (70 K)	31.06 $\pm$ 2.58	1.49 $\pm$ 0.12
KL2 / 52 min	H <sub>2</sub> O (70 <sup>-1</sup> / <sub>+1</sub> K)	2049.03 $\pm$ 155.29	100.00
	H <sub>2</sub> CO, Q branch (70 K)	4.93 $\pm$ 1.15	0.24 $\pm$ 0.06
	CH <sub>4</sub> (70 K)	7.04 $\pm$ 0.44	0.34 $\pm$ 0.06
	HCN (70 K)	2.58 $\pm$ 0.31	0.13 $\pm$ 0.02

	HCN ( $76^{-13}/_{+17}$ K)	$2.63 \pm 0.31$	$0.12 \pm 0.02$
	C <sub>2</sub> H <sub>2</sub> (70 K)	$< 0.95$ at $3\sigma$	$< 0.05$ at $3\sigma$
MW_A / 4 min	H <sub>2</sub> O (80 K)	$1599.29 \pm 266.85$	100.00
	CO (80 K)	$< 22.32$ at $3\sigma$	$< 1.40$ at $3\sigma$

---

**Table 4.4.** Production rates for C/2000 WM<sub>1</sub> on 24 Nov. 2001.

<b>Setting / Time on Source</b>	<b>Molecule (measured or adopted T<sub>rot</sub>)</b>	<b>Global Q [<math>10^{25}</math> s<sup>-1</sup>]</b>	<b>Mixing Ratio %</b>
KL1 / 36 min	H <sub>2</sub> O (70 K)	$2382.76 \pm 307.07$	100.00
	C <sub>2</sub> H <sub>6</sub> (70 K)	$9.47 \pm 1.18$	$0.40 \pm 0.04$
	CH <sub>3</sub> OH, Q branch (70 K)	$25.74 \pm 3.57$	$1.08 \pm 0.13$
KL2 / 52 min	H <sub>2</sub> O ( $70^{-1}/_{+1}$ K)	$2321.49 \pm 130.83$	100.00
	H <sub>2</sub> CO, Q branch (70 K)	$3.95 \pm 1.67$	$0.17 \pm 0.07$
	CH <sub>4</sub> (70 K)	$9.78 \pm 0.63$	$0.42 \pm 0.07$
	HCN ( $70^{-7}/_{+9}$ K)	$3.47 \pm 0.29$	$0.15 \pm 0.01$
	C <sub>2</sub> H <sub>2</sub> (70 K)	$< 1.90$ at $3\sigma$	$< 0.08$ at $3\sigma$
MW_A / 10 min	H <sub>2</sub> O (80 K)	$2097.74 \pm 294.06$	100.00
	CO (80 K)	$< 11.26$ at $3\sigma$	$< 0.54$ at $3\sigma$

---

**Table 4.5.** Production rates for C/2000 WM<sub>1</sub> on 25 Nov. 2001.

<b>Setting / Time on Source</b>	<b>Molecule (measured or adopted T<sub>rot</sub>)</b>	<b>Global Q [10<sup>25</sup> s<sup>-1</sup>]</b>	<b>Mixing Ratio %</b>
KL1 / 16 min	H <sub>2</sub> O (70 K)	2212.44 ± 280.97	100.00
	C <sub>2</sub> H <sub>6</sub> (70 K)	12.30 ± 1.04	0.56 ± 0.06
	CH <sub>3</sub> OH, Q branch (70 K)	28.38 ± 3.54	1.28 ± 0.19
KL2 / 48 min	H <sub>2</sub> O (70 <sup>-1</sup> / <sub>+1</sub> K)	1954.10 ± 75.52	100.00
	H <sub>2</sub> CO, Q branch (70 K)	3.68 ± 1.06	0.19 ± 0.05
	CH <sub>4</sub> (70 K)	5.85 ± 0.97	0.30 ± 0.05
	HCN (70 K)	2.85 ± 0.16	0.15 ± 0.01
	HCN (82 <sup>-5</sup> / <sub>+6</sub> K)	2.96 ± 0.13	0.14 ± 0.01
	C <sub>2</sub> H <sub>2</sub> (70 K)	< 1.03 at 3σ	< 0.05 at 3σ
MW_A / 22 min	H <sub>2</sub> O (80 K)	1770.70 ± 140.93	100.00
	CO (80 K)	9.19 ± 1.94	0.52 ± 0.12



## CO, Setting MW\_A, 25 Nov. 2001

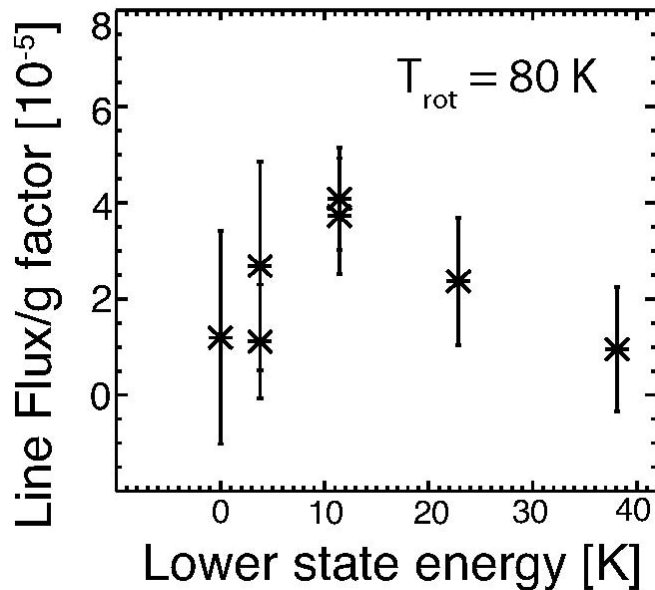


**Figure 4.10.** Excitation diagram for CO on 25 Nov. 2001, demonstrating sufficient lines to claim secure detection (this date had the longest time on source).

### Discussion

The organic composition of comet C/2000 WM<sub>1</sub> was studied on three consecutive dates, which served as a test for chemical heterogeneity of its nucleus. If the nucleus is comprised of fractions of diverse origin and composition, as it rotates and exposes different vents to the incoming solar radiation, varying mixing ratios of the volatile species would be observed (it should be noted that this probes layers closer to the surface rather than the deep interior of the nucleus). Complicating factors would be the number of active vents, the size of the fractions, the rotation

period of the nucleus, etc. As seen on Figure 4.11 (presenting mixing ratios of each species for 23-25 Nov.), CH<sub>4</sub>, HCN, and H<sub>2</sub>CO agree within 1- $\sigma$  on the three dates. C<sub>2</sub>H<sub>6</sub> and CH<sub>3</sub>OH (measured simultaneously within the same setting) decrease by more than 2- $\sigma$  from 23 Nov. to 24 Nov; and C<sub>2</sub>H<sub>6</sub> increases by more than 3- $\sigma$  from 24 Nov. to 25 Nov. However, we only have three data points for each species; the sampling interval was biased by observing on three consecutive dates at similar times; and the rotation period of C/2000 WM<sub>1</sub> is unknown. The behavior of parent volatiles on the three dates does not suggest heterogeneity of this cometary nucleus, however, the data points are not sufficient to draw a firm conclusion on the potential heterogeneity.

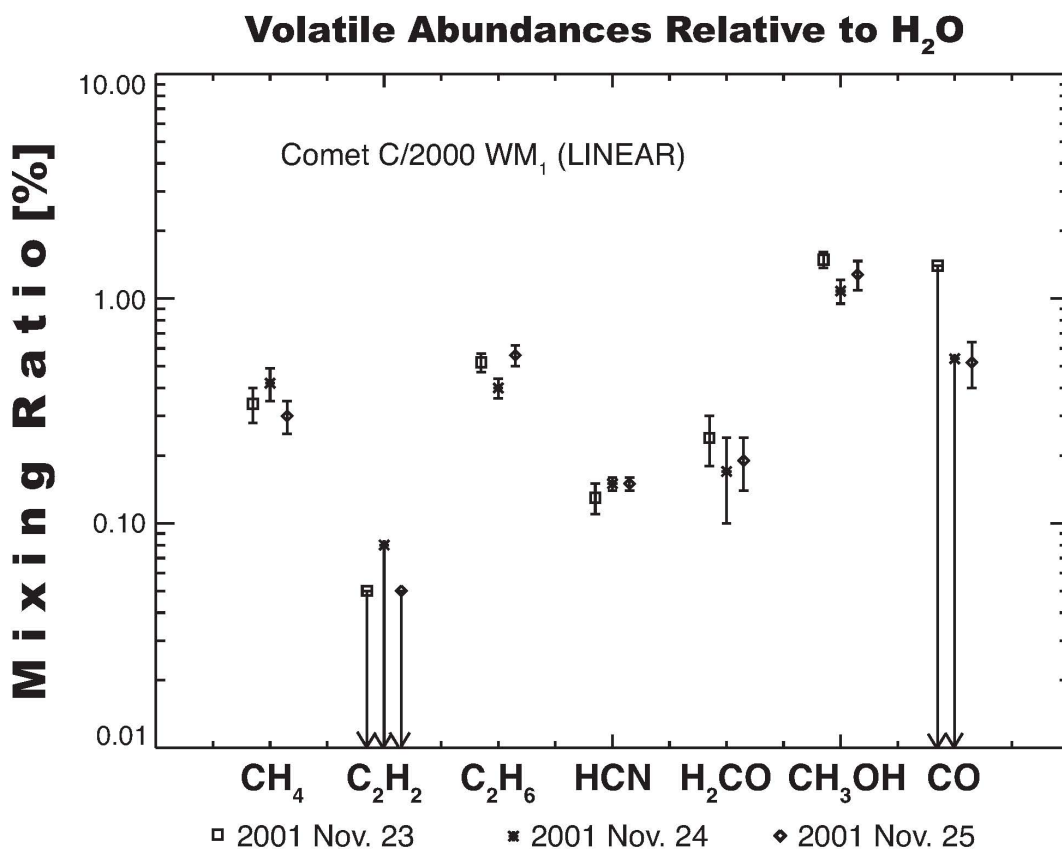


**Figure 4.11.** Mixing ratios of parent volatiles in C/2000 WM<sub>1</sub> (LINEAR) measured on 23, 24 and 25 Nov. 2001. The confidence limits for CH<sub>4</sub>, C<sub>2</sub>H<sub>6</sub>, HCN, H<sub>2</sub>CO and CH<sub>3</sub>OH represent  $\pm 1\text{-}\sigma$  uncertainties. The mixing ratios for C<sub>2</sub>H<sub>2</sub> on all dates, and for CO on 23 & 24 Nov., are 3- $\sigma$  upper limits.

Mixing ratios in C/2000 WM<sub>1</sub>, in comparison to mixing ratios in other comets analyzed by the team at NASA's GSFC, were given in Table 2.1 in Chapter 2. As discussed previously, Mumma et al. 2003 presented a sample of five "organics-normal" Oort cloud comets, and suggested that the organics depletion in the sixth comet – C/1999 S4, may be due to this comet's formation closer to the young Sun

than “organics-normal” comets. C/2000 WM<sub>1</sub> is not as severely depleted: C<sub>2</sub>H<sub>6</sub> is normal; HCN, CH<sub>4</sub>, and CH<sub>3</sub>OH are moderately depleted; and CO and C<sub>2</sub>H<sub>2</sub> are significantly depleted. This overall intermediate depletion may suggest that C/2000 WM<sub>1</sub> also formed closer to the young Sun than “organics-normal” comets but further than the severely depleted C/1999 S4. It is possible that the most depleted end-members in this sample: the Oort cloud comet C/1999 S4, and the ecliptic comet 73P/Schwassmann-Wachmann, formed in a common (or similarly depleted) region. In contrast to these two comets stands the most enriched end-member in the overall sample: the Oort cloud comet C/2001 A2 (LINEAR). It is difficult to separate the influence of the formation region of a comet on its composition, from (previous or subsequent) processes such as turbulent mixing; radial migration; dynamical dispersion as predicted by the “*Nice*” model (Tsiganis et al. 2005); etc.

Despite its significant depletion in C<sub>2</sub>H<sub>2</sub>, WM<sub>1</sub> is not depleted in C<sub>2</sub>H<sub>6</sub>, which could be explained by hydrogenation reactions on the surfaces of icy grains, converting C<sub>2</sub>H<sub>2</sub> into C<sub>2</sub>H<sub>6</sub>, and thus increasing the abundance of the latter. The conversion efficiency for C<sub>2</sub>H<sub>2</sub> is quantified as  $C_2H_6/(C_2H_2 + C_2H_6) > 0.9$ . This may be indicative of greater H-atom densities, and/or lower temperatures in the comet’s formative region, than those typical for comets having a lower C<sub>2</sub>H<sub>2</sub> conversion efficiency. The hydrogenation efficiency for CO is calculated as  $(H_2CO + CH_3OH)/(CO + H_2CO + CH_3OH) = 0.74$ . Assuming that H<sub>2</sub>CO and CH<sub>3</sub>OH are formed solely by hydrogenation of CO, there may have been a smaller abundance of CO in the ice from which C/2000 WM<sub>1</sub> formed (as compared to “organics-normal” comets). Also, CO is the most volatile among the sampled species, and C/2000

WM<sub>1</sub>'s formation in a higher-temperature region could explain CO's depletion (and potentially the depletion of the highly volatile CH<sub>4</sub>).

In addition to investigating mixing ratios in C/2000 WM<sub>1</sub>, H<sub>2</sub>O production rates (weighted means from 23-25 Nov. for the KL2 and KL1 settings – see Table 4.1) were compared with those measured by other groups for the time period 12 Nov. – 21 Dec. (see Table 4.6 & Figure 4.12). The best agreement is between H<sub>2</sub>O production rates in this work and measurements by SWAS (Bensch and Melnick 2006, presented in Combi et al. 2008) of the 577 GHz line of ortho water (in agreement with the production rate derived by Odin (Lecacheux et al. 2003)). Disagreement is found between all of the above results and the production rates obtained from H Ly- $\alpha$  (which represent water production rate averaged over long time intervals, and can be indirectly derived from daughter (OH, H<sub>2</sub>) or granddaughter (H, O) products) (Combi et al. 2008).

**Table 4.6.** H<sub>2</sub>O production rates in C/2000 WM<sub>1</sub>.

UT Date	R <sub>h</sub> [AU]	$\Delta$ [AU]	Q <sub>H2O</sub> [ $10^{25}$ molecules s <sup>-1</sup> ]
23-25 Nov. 2001	1.34	0.37	2046.39 $\pm$ 60.27 <sup>I</sup>
			2167.73 $\pm$ 128.90 <sup>II</sup>
23 Nov. 2001	1.352	0.38	1984 $\pm$ 123 <sup>III</sup>
25 Nov. 2001	1.33-1.34	0.36	4666 $\pm$ 184.9 <sup>IV</sup>

2 Dec. 2001	1.2	0.32	$3154 \pm 3.401^{\text{V}}$
7 Dec. 2001	1.13	0.34	$4200 \pm 900^{\text{VI}}$

---

<sup>I</sup>Our results: weighted mean from 23-25 Nov. 2001, KL2 setting.

<sup>II</sup>Our results: weighted mean from 23-25 Nov. 2001, KL1 setting.

<sup>III</sup>Combi et al. 2008.  $Q_{\text{H}_2\text{O}}$  based on values provided by F. Bensch (Bensch and Melnick 2006) to M. Combi (private communication), from SWAS observations.

<sup>IV</sup>Combi et al. 2008 (SWAN-SOHO), 25 Nov. 2001, during a possible outburst. Combi et al. argue for likely outbursts of  $Q_{\text{H}_2\text{O}}$  30 days before perihelion.

<sup>V</sup>Combi et al. 2008 (SWAN-SOHO), 2 Dec. 2001, during a possible quiescent phase.

<sup>VI</sup>Lecacheux et al. 2003. Odin observations of the 557 GHz rotational line of ortho  $\text{H}_2\text{O}$  on 7 Dec. 2001.

---

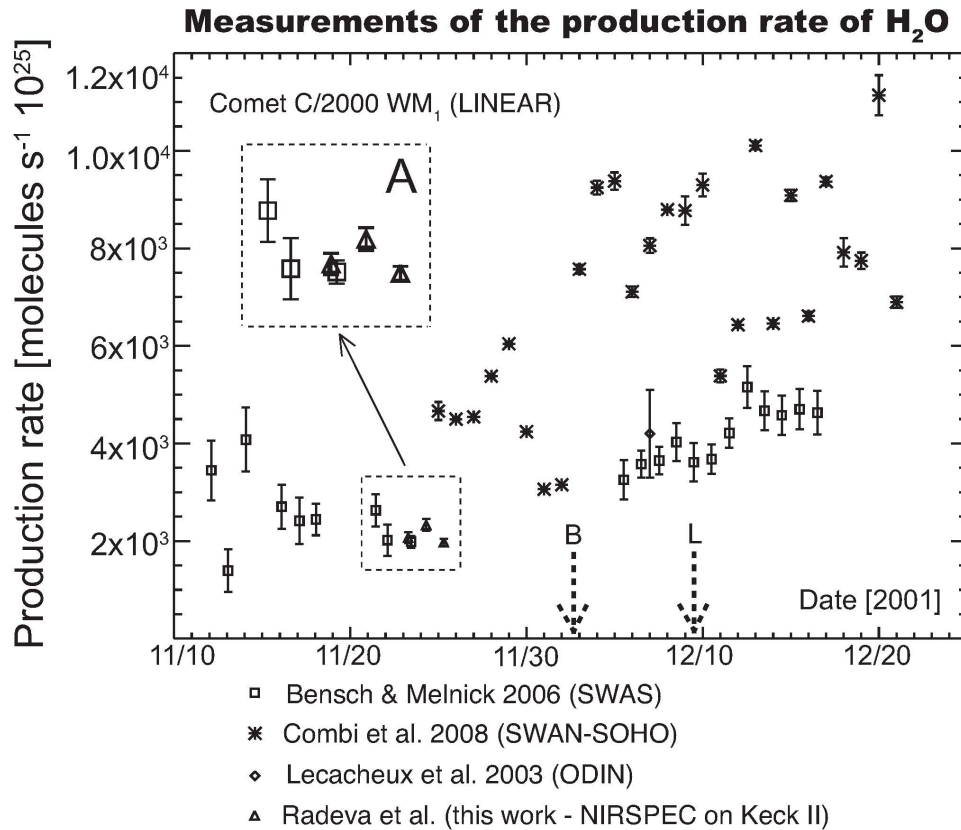


**Figure 4.12.** Measurements of the production rate of H<sub>2</sub>O in C/2000 WM<sub>1</sub> (LINEAR) (our results are presented as weighted means of KL1 and KL2 settings of NIRSPEC for 23, 24 and 25 Nov. 2001). The measurements by Bensch and Melnick 2006 (SWAS) agree with our results on 23 Nov. 2001 (see expanded panel A). The production rates measured by Combi et al. 2008 (SWAN-SOHO) are higher, and are suggestive of possible outbursts in the water production rate or systematic modeling offsets. They represent the mean water production rate derived from H, and averaged over much longer time intervals than do direct measurements of the parent volatile itself, such as provided by the 557 GHz line of H<sub>2</sub>O measured by SWAS and Odin. The dashed arrows indicate the mean dates of measurements reported by Biver et al. (2006) (labeled B), and Lupu et al. (2007) (labeled L), to which mixing ratios from this work were compared.

Mixing ratios for organic species measured in this work were compared with those measured by other groups in Table 4.7. The mixing ratio for CH<sub>4</sub> reported by Gibb et al. (2003) was confirmed, as well as the level of depletion in CH<sub>3</sub>OH and CO (reported by Biver et al. 2006 and Lupu et al. 2007). The mixing ratio for H<sub>2</sub>CO agrees with the range given by Biver et al. (2006). As seen for other comets, the HCN mixing ratio is larger by a factor of two than the measurement of Biver et al. (2006).

**Table 4.7.** Mixing ratios in C/2000 WM<sub>1</sub>: comparison with other groups.

Molecule	Mixing Ratio % (this work)	Mixing Ratio % (previous work & other groups)
CH <sub>4</sub>	0.34 ± 0.06 (23 Nov. 2001)	0.34 ± 0.08 (23 Nov. 2001) <sup>I</sup>
CH <sub>3</sub> OH	1.30 ± 0.08 (weighted mean) <sup>II</sup>	1.3 ± 0.2 <sup>III</sup>
H <sub>2</sub> CO	0.20 ± 0.03 (weighted mean) <sup>II</sup>	0.09 – 0.18 <sup>III</sup>
HCN	0.15 ± 0.01 (weighted mean) <sup>II</sup>	0.08 ± 0.01 <sup>III</sup> < 1.4 <sup>III</sup>
CO	0.52 ± 0.12 (25 Nov. 2001)	0.44 ± 0.03 <sup>IV</sup> 0.4 <sup>V</sup>

<sup>I</sup>Gibb et al. 2003, previous work.

<sup>II</sup>The mean heliocentric distance for the weighted mean mixing ratios is 1.34 AU. All production rates of organic volatiles in this work are extracted simultaneously with H<sub>2</sub>O production rates, greatly reducing any systematic



---

uncertainties (see Figure 13).

- <sup>III</sup>Biver et al. 2006, radio observations with IRAM and CSO (mixing ratios at mean  $R_h = 1.2$  AU). The mixing ratio for  $H_2CO$  is from the parent distribution only.
- <sup>IV</sup>Lupu et al. 2007. Based on UV observations with HST STIS. The CO data from three HST STIS observations on 9 – 10 Dec. 2001 were averaged (mean  $R_h = 1.084$  AU). The water production rate ( $Q_{H_2O} = 8 \pm 1 [10^{28} \text{ molecules s}^{-1}]$ ) was adopted from FUSE observations of  $H_2$ , H I and O I lines (Weaver et al. 2002). UV studies measure CO directly, but  $H_2O$  production was inferred from dissociation fragments, introducing additional systematic uncertainty. In this regard, note that the  $H_2O$  production rate adopted by Lupu et al. is higher than those based on the direct measurements of  $H_2O$  by SWAS and Odin.
- <sup>V</sup>Weaver et al. 2002. Based on FUSE observations on 7 – 10 Dec. 2001 with  $R_h = 1.12$  AU. The authors state that the uncertainty in  $Q_{CO}$  presented in this paper could be about a factor of 2. The water production rate ( $Q_{H_2O} = 8 \pm 1 [10^{28} \text{ molecules s}^{-1}]$ ), adopted from FUSE observations of  $H_2$ , H I and O I lines is consistent with recent reanalysis by Feldman (Feldman et al., private communication), and is higher than production rates derived from direct measurements of  $H_2O$  by SWAS and Odin.

### Summary of Composition

I derived production rates and mixing ratios for parent volatiles ( $H_2O$ ,  $CH_4$ ,  $C_2H_2$ ,  $C_2H_6$ ,  $CH_3OH$ ,  $H_2CO$ , CO, and HCN) in the Oort cloud comet C/2000 WM<sub>1</sub>. I extracted rotational temperatures for  $H_2O$  and HCN, and their weighted averages from 23-25 Nov. agree within 1- $\sigma$ . The moderate depletion of  $CH_3OH$  reported by Biver et al. 2006 was confirmed; as well as the depletion of CO reported by Biver et al. 2006 and Lupu et al. 2007; the range of mixing ratios reported for  $H_2CO$  by Biver et al. 2006; and the  $H_2O$  production rates measured by SWAS (Bensch and Melnick 2006) on 23 Nov. 2001, and presented by Combi et al. (2008). CO and  $C_2H_2$  are severely depleted in C/2000 WM<sub>1</sub>; HCN,  $CH_4$  and  $CH_3OH$  are moderately depleted; and  $C_2H_6$  and  $H_2CO$  fall within the “normal” range. I determined this in comparison

with five “organics-normal” Oort cloud comets (presented by Mumma et al. 2003), and the most enriched and most depleted comets our team has analyzed (A2 (LINEAR) and C/1999 S4, respectively). The results suggest that C/2000 WM<sub>1</sub> may have formed closer to the Sun than average comets, but further than the severely depleted C/1999 S4 or 73P/Schwassmann-Wachmann. This would be expected if depletion in organics is directly related to heliocentric distance of formation, although it is difficult to distinguish between the effects of the formation region, and the subsequent chemical and dynamical evolution, on the composition of a cometary nucleus. Finally, I compared mixing ratios extracted for each species for 23, 24 and 25 Nov. 2001, and found agreement within 1 or 2- $\sigma$ , which suggests homogeneity of the nucleus (however, the rotational period of C/2000 WM<sub>1</sub> is unknown, which precluded determination whether sufficient temporal sampling is available to study potential heterogeneity).

## Chapter 5: The Organic Composition of Comet 2P/Encke

2P/Encke is an Encke-type comet, with  $T_J = 3.025$ , and period of 3.3 years. Its orbital eccentricity is 0.85, and semi-major axis: 2.22 AU. The comet was observed with NIRSPEC on the Keck II telescope on 4 - 6 Nov. 2003. Data acquired on 4 Nov. (Settings KL1 and KL2), and 5 Nov. (Setting MW\_A) are presented (see Table 5.1 for observing log). Encke's perigee was at 0.261 AU on 17 Nov. 2003, and its perihelion was at 0.338 AU on 30 Dec. 2003.

**Table 5.1.** Observing log for 2P/Encke.

UT Time (2003)	Setting <sup>I</sup>	Frequency range of setting [cm <sup>-1</sup> ]	$R_h^{\text{II}}$ [AU]	$\Delta^{\text{II}}$ [AU]	$\Delta_{\text{dot}}^{\text{II}}$ [km s <sup>-1</sup> ]
4 Nov., 05:02 - 07:17	KL2	3521 – 2833	1.210	0.313	-13.59
09:39 - 09:52	KL1	3466 – 2757	1.208	0.312	-13.18
5 Nov., 09:32 – 10:06	MW_A	2163 - 1998	1.193	0.304	-12.25

<sup>I</sup>We measure CH<sub>3</sub>OH, C<sub>2</sub>H<sub>6</sub> & H<sub>2</sub>O simultaneously in KL1 (12 min on source); HCN, CH<sub>4</sub>, C<sub>2</sub>H<sub>2</sub>, H<sub>2</sub>CO & H<sub>2</sub>O simultaneously in KL2 (40 min on source); and CO & H<sub>2</sub>O simultaneously in MW\_A (12 min on source).

<sup>II</sup> $R_h$  is the heliocentric distance,  $\Delta$  - geocentric distance, and  $\Delta_{\text{dot}}$  - radial velocity.

## Spectral Gallery

I analyzed raw data following the procedures described in Chapter 3. I present flux-calibrated spectral extracts, containing signal summed from nine rows centered on the nucleus (spanning 1.78" or ~ 400 km) in Fig. 5.1 - 5.8 (terrestrial atmospheric model superimposed on the cometary spectrum; and residual features). The  $\pm 1\text{-}\sigma$  noise envelope is shown with a dashed line. I extracted the following parent species: CH<sub>3</sub>OH, C<sub>2</sub>H<sub>6</sub>, H<sub>2</sub>CO, CH<sub>4</sub>, HCN, C<sub>2</sub>H<sub>2</sub>, CO and H<sub>2</sub>O; along with unknown volatiles.

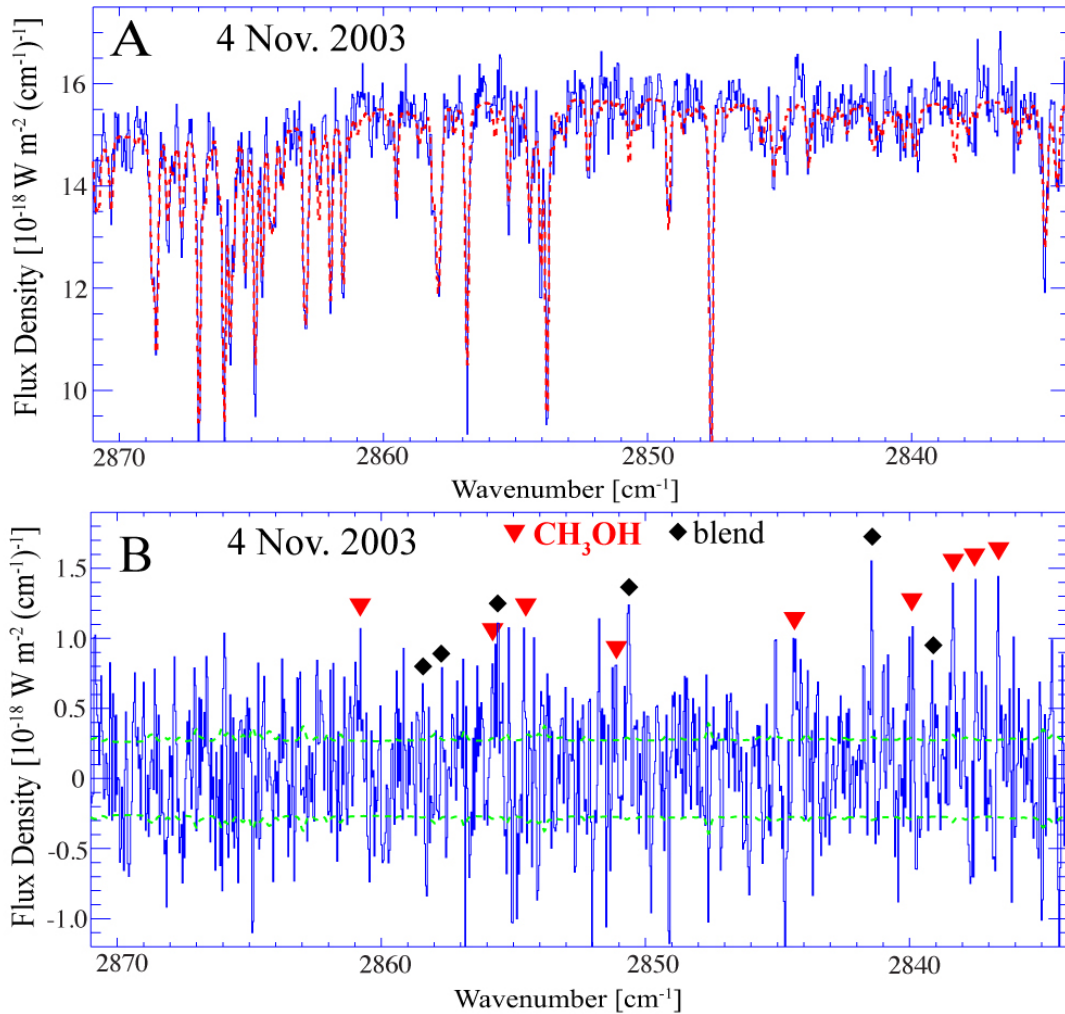


**Figure 5.1:** Encke cometary spectrum and superimposed terrestrial transmittance model (dashed red line) for 4 Nov. 2003 (panel A), and residual spectrum in panel B. Spectral lines of  $\text{CH}_3\text{OH}$ ,  $\text{C}_2\text{H}_6$  and blends are seen. The flux density scale is shown at left, and the  $\pm 1-\sigma$  noise envelope is shown as dashed green lines centered on zero flux density, in panel B.

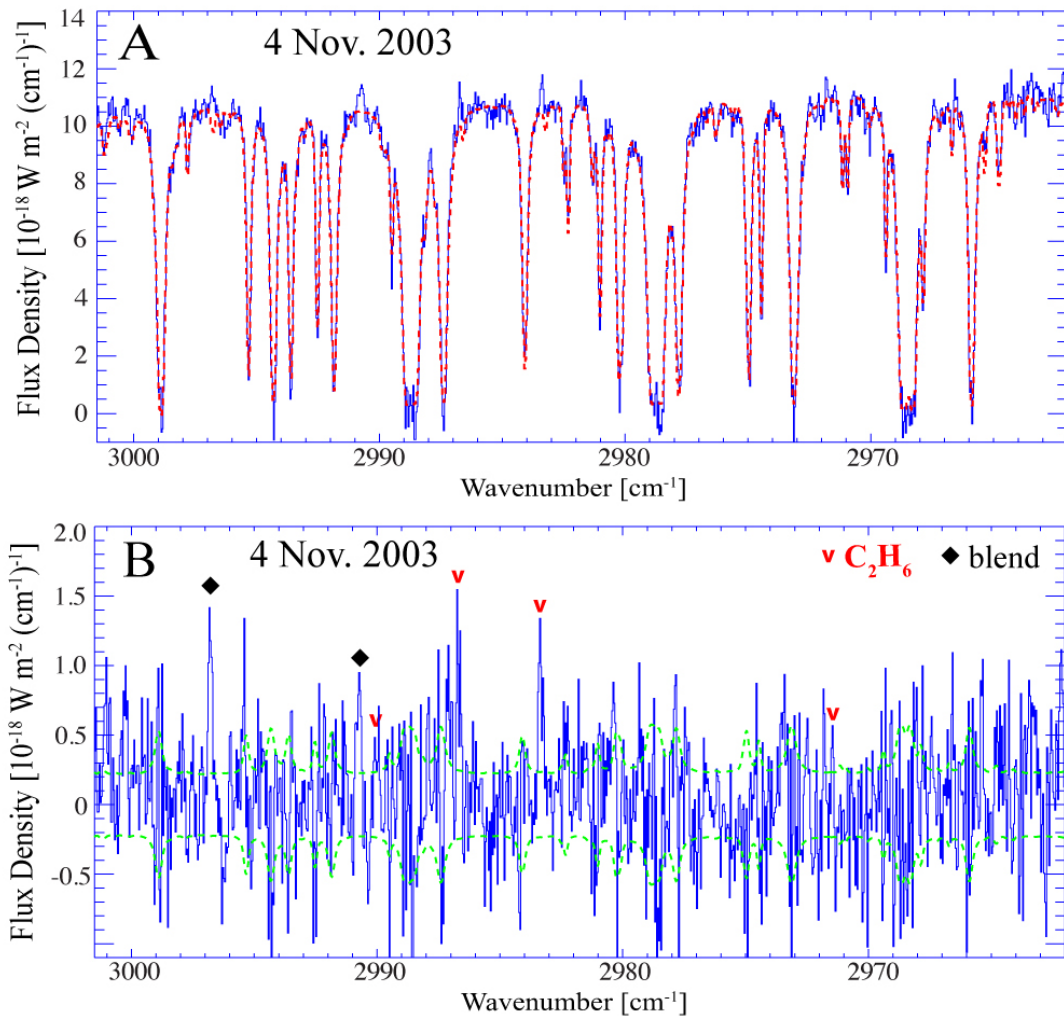


**Figure 5.2:** Encke cometary spectrum and superimposed terrestrial transmittance model (dashed red line) for 4 Nov. 2003 (panel A), and residual spectrum in panel B. Spectral lines of  $\text{C}_2\text{H}_6 \nu_7$ , and blends with  $\text{CH}_3\text{OH}$  and other species are seen. The flux density scale is shown at left, and the  $\pm 1\text{-}\sigma$  noise envelope is shown as dashed green lines centered on zero flux density, in panel B.

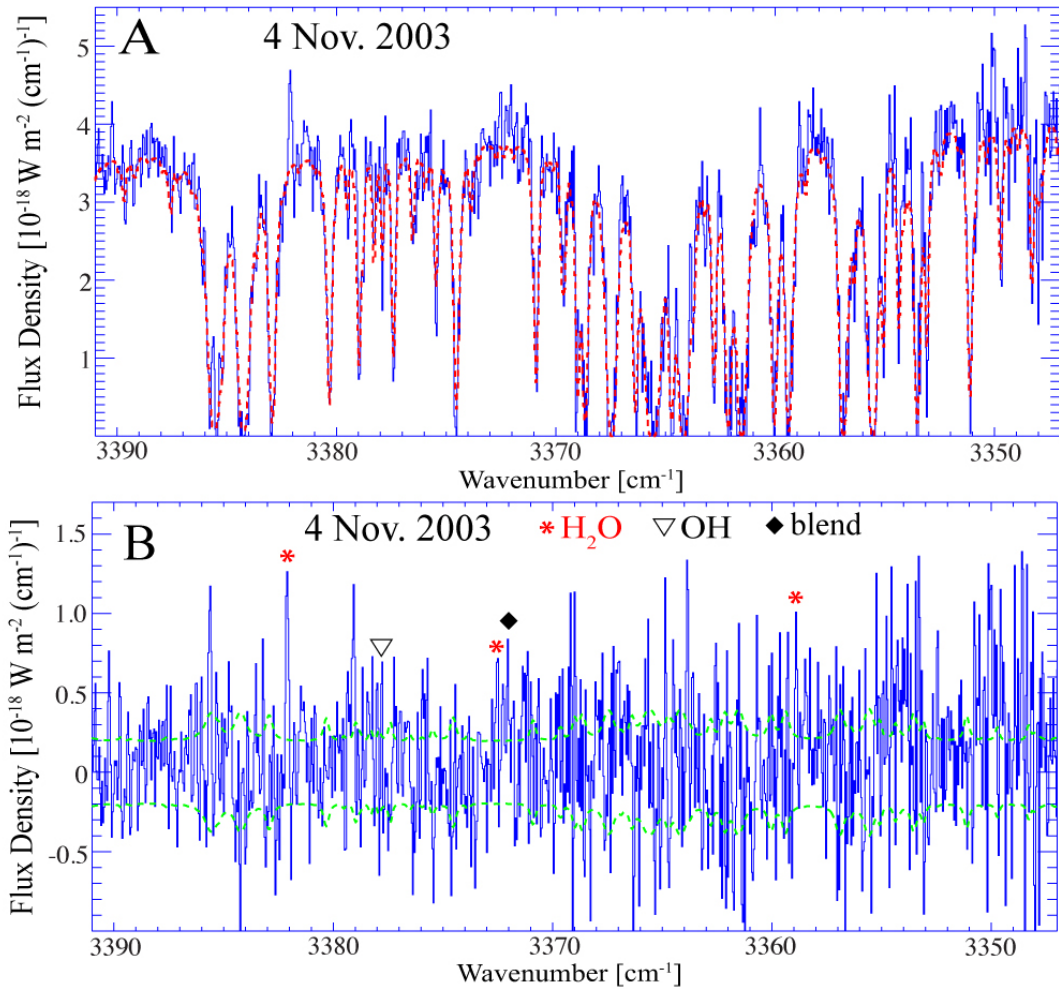


**Figure 5.3:** Encke cometary spectrum and superimposed terrestrial transmittance model (dashed red line) for 4 Nov. 2003 (panel A), and residual spectrum in panel B. Spectral lines of  $\text{H}_2\text{O}$ , OH and blends are seen. The flux density scale is shown at left, and the  $\pm 1\text{-}\sigma$  noise envelope is shown as dashed green lines centered on zero flux density, in panel B.

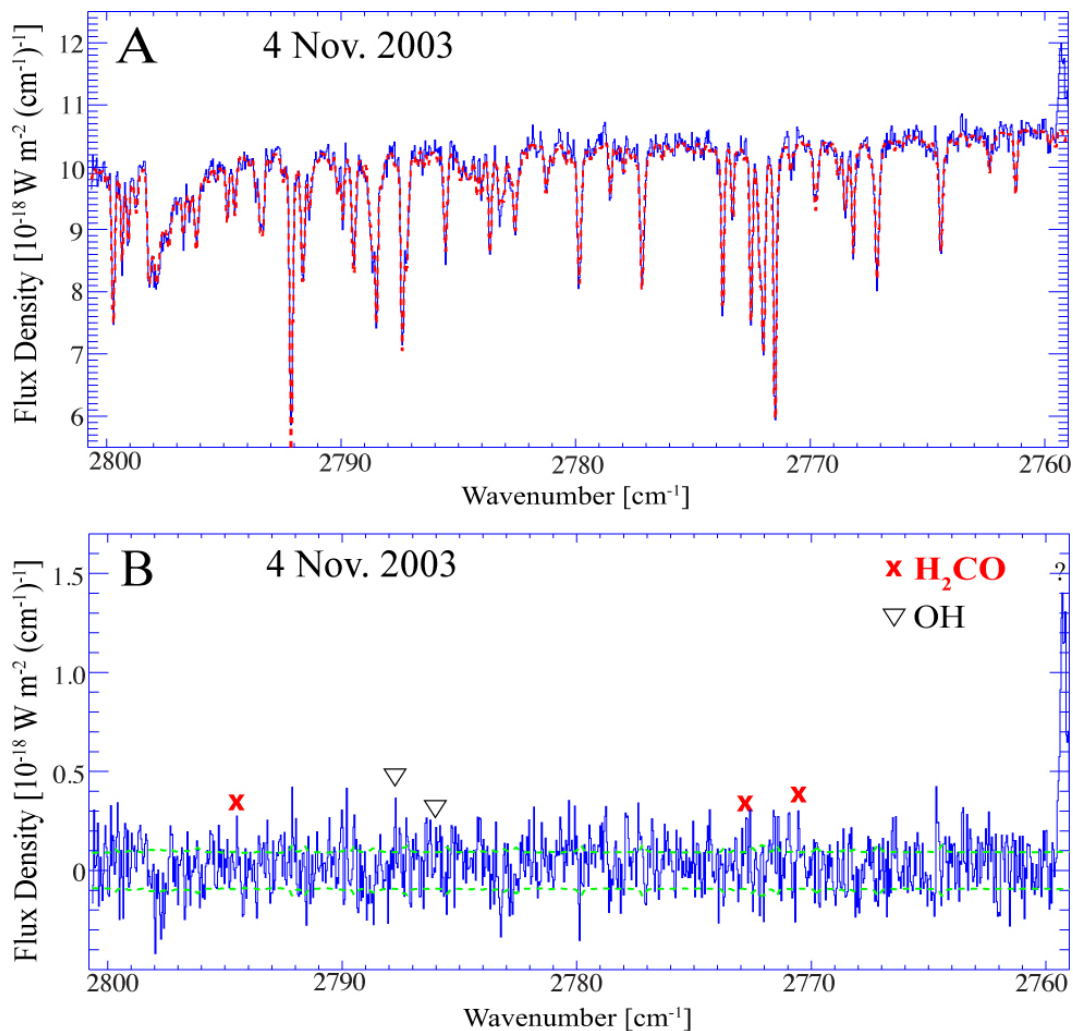


**Figure 5.4:** Encke cometary spectrum and superimposed terrestrial transmittance model (dashed red line) for 4 Nov. 2003 (panel A), and residual spectrum in panel B. Spectral lines of  $\text{H}_2\text{CO}$ ,  $\text{OH}$ , and an unknown species are seen. The flux density scale is shown at left, and the  $\pm 1\text{-}\sigma$  noise envelope is shown as dashed green lines centered on zero flux density, in panel B.



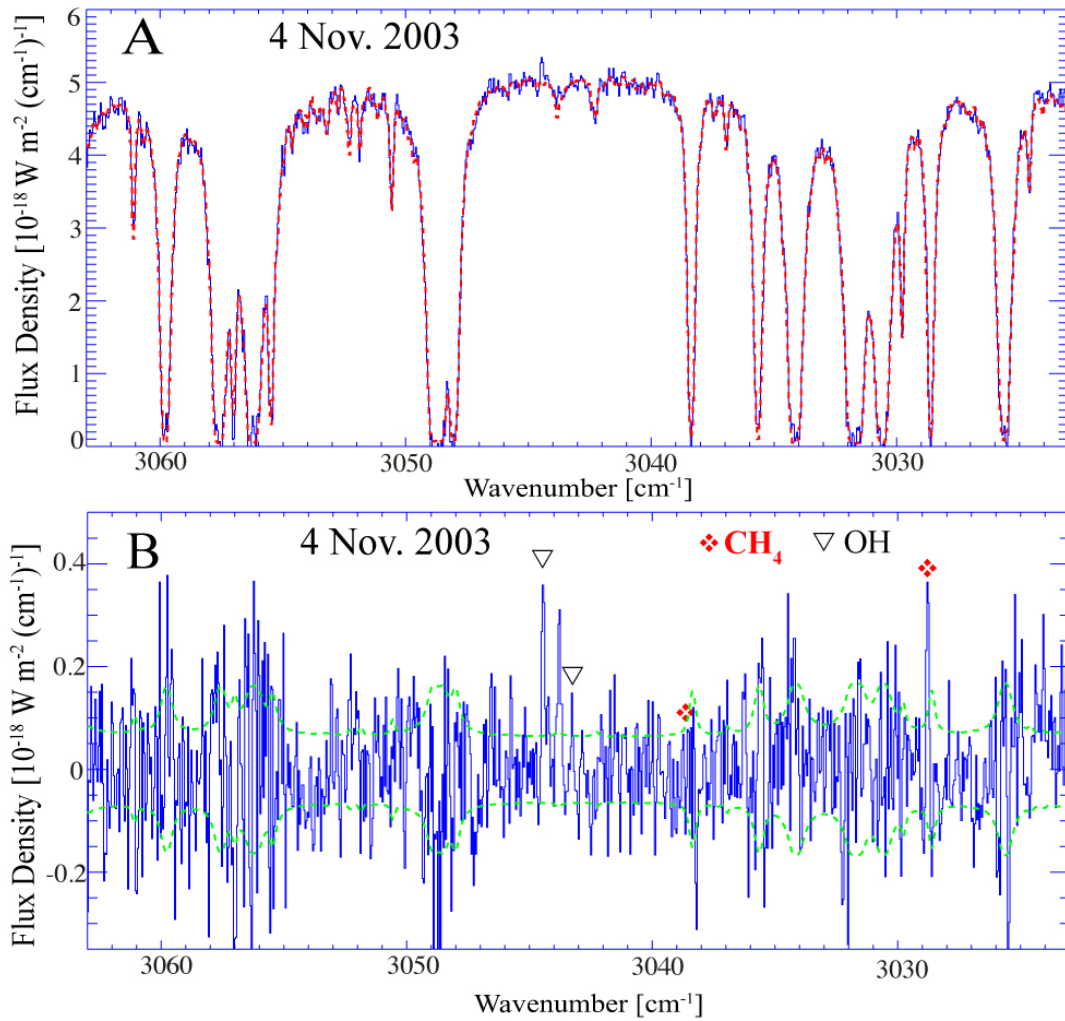


**Figure 5.5:** Encke cometary spectrum and superimposed terrestrial transmittance model (dashed red line) for 4 Nov. 2003 (panel A), and residual spectrum in panel B. Spectral lines of CH<sub>4</sub> and OH are seen. The flux density scale is shown at left, and the  $\pm 1\text{-}\sigma$  noise envelope is shown as dashed green lines centered on zero flux density, in panel B.

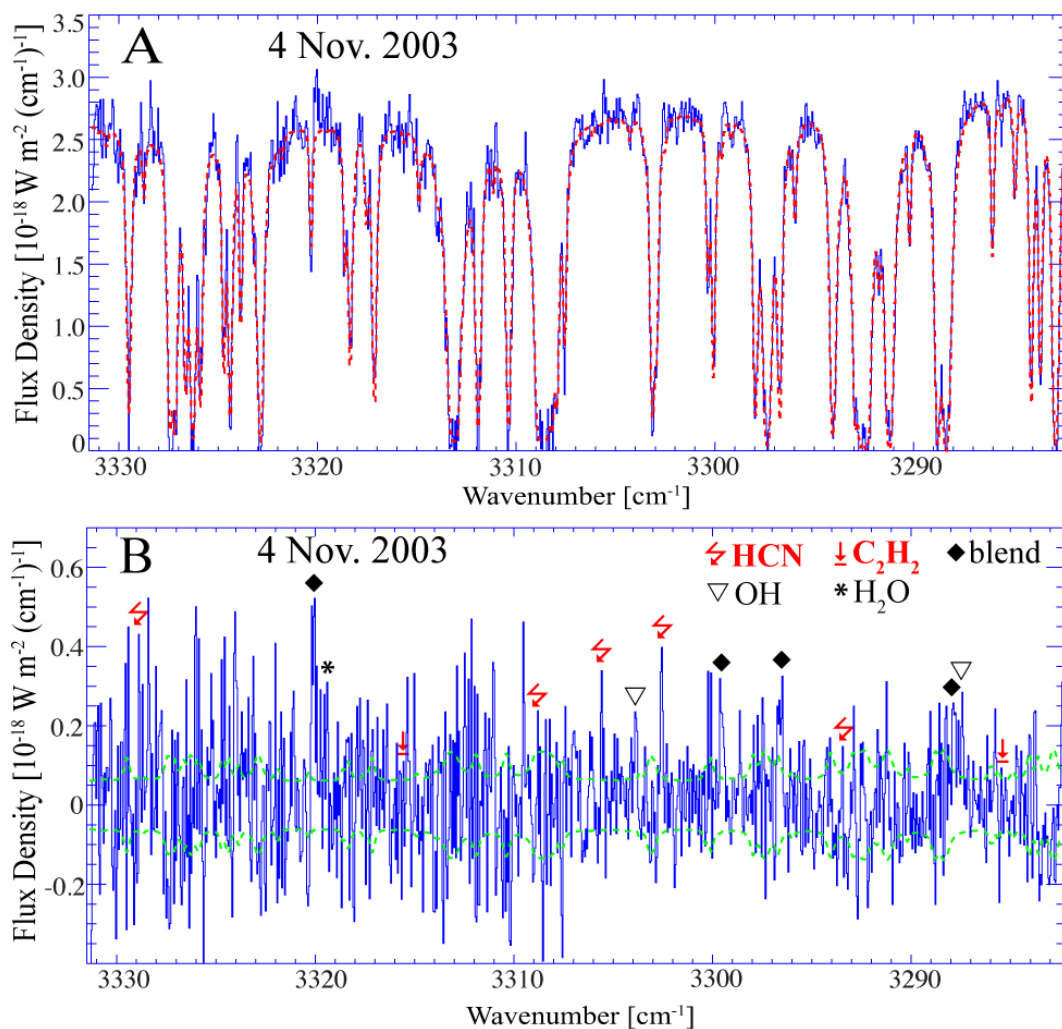


**Figure 5.6:** Encke cometary spectrum and superimposed terrestrial transmittance model (dashed red line) for 4 Nov. 2003 (panel A), and residual spectrum in panel B. Spectral lines of HCN,  $\text{C}_2\text{H}_2$ ,  $\text{H}_2\text{O}$ , OH and blends are seen. The flux density scale is shown at left, and the  $\pm 1\text{-}\sigma$  noise envelope is shown as dashed green lines centered on zero flux density, in panel B.

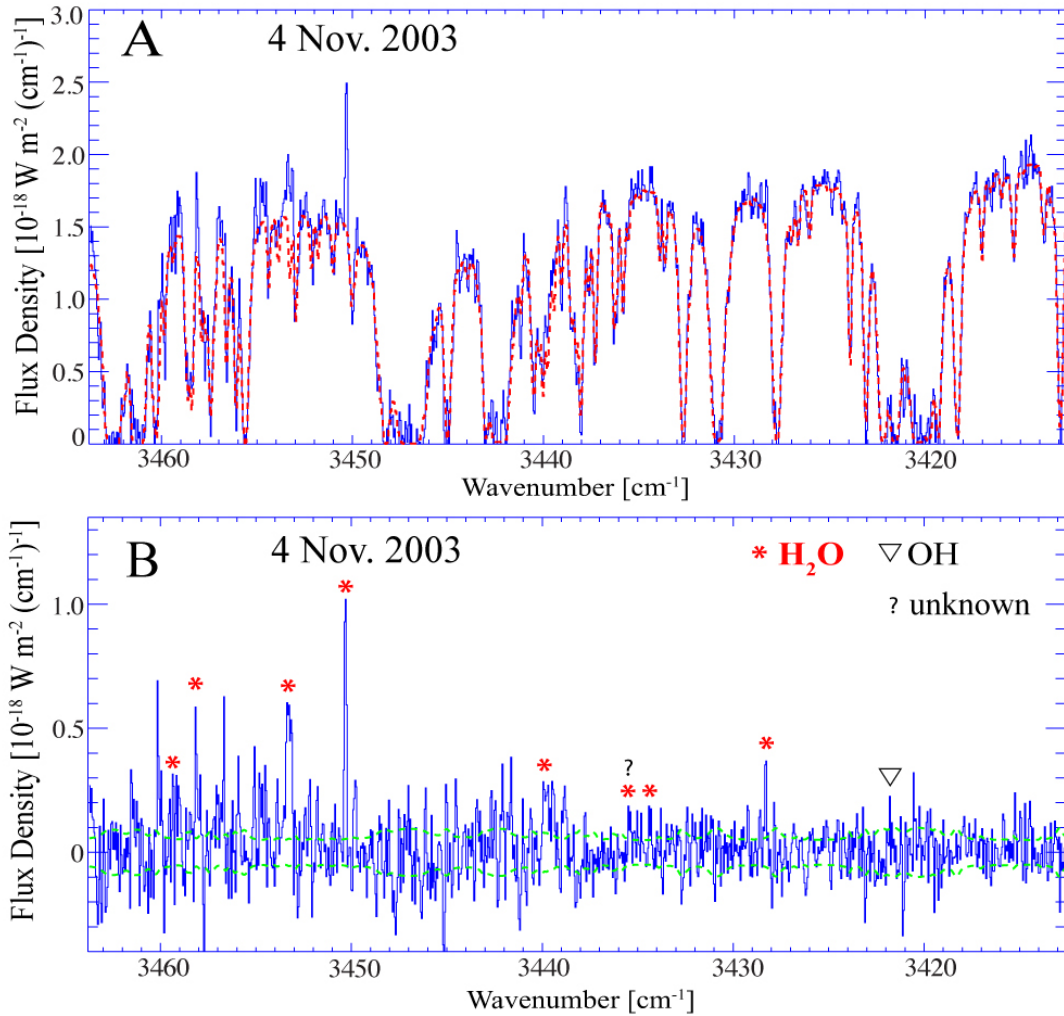


**Figure 5.7:** Encke cometary spectrum and superimposed terrestrial transmittance model (dashed red line) for 4 Nov. 2003 (panel A), and residual spectrum in panel B. Spectral lines of H<sub>2</sub>O and OH are seen. The flux density scale is shown at left, and the  $\pm 1\text{-}\sigma$  noise envelope is shown as dashed green lines centered on zero flux density, in panel B.

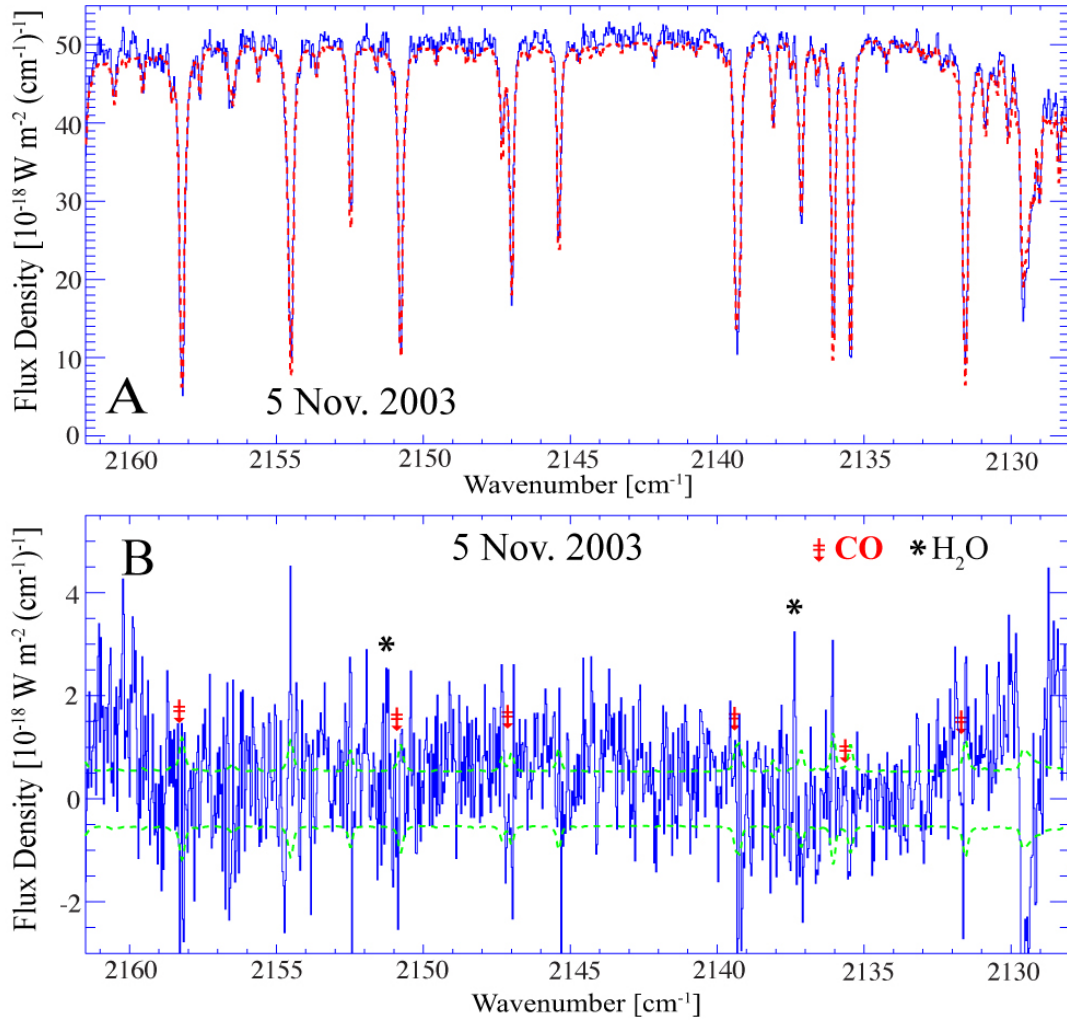


**Figure 5.8:** Encke cometary spectrum and superimposed terrestrial transmittance model (dashed red line) for 5 Nov. 2003 (panel A), and residual spectrum in panel B. Spectral lines of CO (at their expected position, given that no detection is claimed), and H<sub>2</sub>O are shown. The flux density scale is shown at left, and the  $\pm 1\text{-}\sigma$  noise envelope is shown as dashed green lines centered on zero flux density, in panel B.

### Rotational Temperatures and Production Rates

I derived rotational temperatures for H<sub>2</sub>O and HCN in 2P/Encke using procedures described in Section 3. The rotational temperatures are lower than for any other comet studied previously:  $T_{\text{rot}}(\text{H}_2\text{O}) = 24^{-6/+13}$  K and  $T_{\text{rot}}(\text{HCN}) = 28^{-7/+13}$  K, and agree within 1- $\sigma$  (I show standard errors, which dominate stochastic errors) (see Figure 5.9). The rotational temperature for H<sub>2</sub>O is not robust since it is based on only five lines with a small spread in excitation energy. Similarly, the rotational temperature for HCN is based on only five lines with a large spread around zero-slope. Thus, I also present correlation analysis for each species in Figure 5.9. Correlation analysis is useful in demonstrating the relative agreement between the data and synthetic model, however, it does not account for the spread in excitation energies of the sampled lines. Correlation analysis serves best to constrain the range of temperatures for which the model provides the best fit to the observed line intensities (for H<sub>2</sub>O the best fit is at 34 K, and for HCN at 39 K, in agreement within error with  $T_{\text{rot}}$  from excitation analysis).

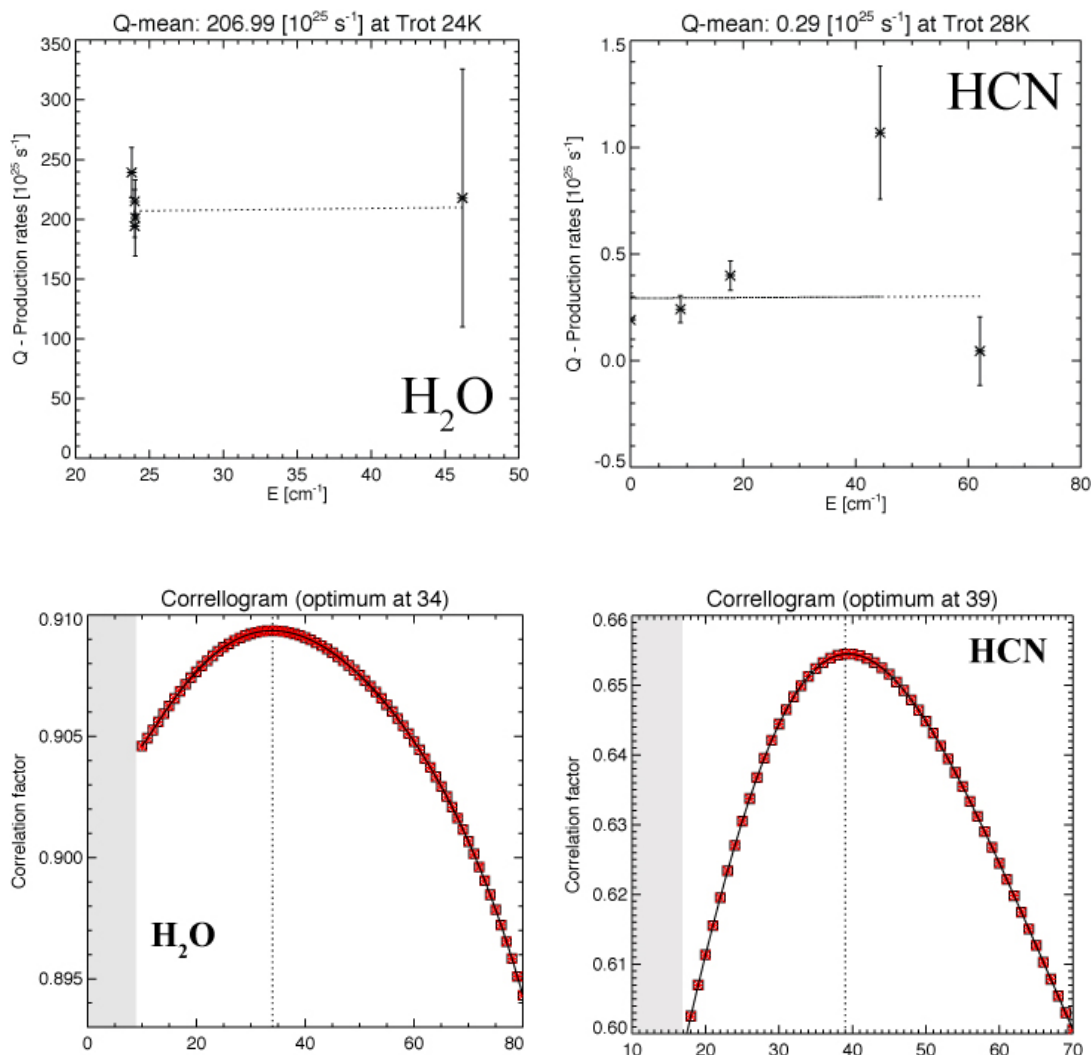


**Figure 5.9.** Excitation and correlation analysis for H<sub>2</sub>O and HCN on 4 Nov. 2003. These are fluxes measured above the terrestrial atmosphere, and from nucleus-centered extracts.  $T_{\text{rot}}(\text{H}_2\text{O}) = 24^{-6}/_{+13}$  K and  $T_{\text{rot}}(\text{HCN}) = 28^{-7}/_{+13}$  K from the excitation analysis (as described in Chapter 3).

I derived production rates for H<sub>2</sub>O in the KL1 and KL2 settings, and for the measured organic species: CH<sub>3</sub>OH, C<sub>2</sub>H<sub>6</sub>, H<sub>2</sub>CO, CH<sub>4</sub>, HCN, C<sub>2</sub>H<sub>2</sub>, and CO. Production rates and mixing ratios are presented in Table 5.2. I calculated the mixing

ratios from nucleus-centered production rates, which are most accurate since they are derived from the highest signal-to-noise data. C<sub>2</sub>H<sub>2</sub> and CO are not detected, thus 3- $\sigma$  upper limits are presented for the production rates and mixing ratios of these organic volatiles. The production rates of H<sub>2</sub>O agree within 1- $\sigma$  for the KL1 and KL2 settings on 4 Nov.

**Table 5.2.** Production rates and mixing ratios of volatiles in 2P/Encke.

Setting / Time on Source	Molecule (T <sub>rot</sub> )	Global Q [ $10^{25}$ s <sup>-1</sup> ]	Mixing Ratio %
4 Nov. 2003			
KL1 / 12 min	H <sub>2</sub> O (24 K) <sup>I</sup>	405.36 ± 162.28	100.00
	C <sub>2</sub> H <sub>6</sub> v <sub>7</sub> (24 K)	1.16 ± 0.31	0.29 ± 0.11
	CH <sub>3</sub> OH, Q branch (25 K)	8.00 ± 1.97	1.97 ± 0.76
KL2 / 40 min	H <sub>2</sub> O (24 <sup>-6</sup> / <sub>+13</sub> K) <sup>I</sup>	441.64 ± 78.35	100.00
	H <sub>2</sub> CO (24 K)	0.90 ± 0.27	0.20 ± 0.05
	CH <sub>4</sub> (24 K)	0.53 ± 0.21	0.12 ± 0.04
	HCN (28 <sup>-7</sup> / <sub>13</sub> K)	0.48 ± 0.14	0.11 ± 0.03
	C <sub>2</sub> H <sub>2</sub> (24 K)	< 0.79 at 3 $\sigma$	< 0.18 at 3 $\sigma$
5 Nov. 2003			
MWA / 12 min	H <sub>2</sub> O (60 K) <sup>I</sup>	501.45 ± 219.67	100.00

CO (24 K)

< 7.17 at 3 $\sigma$

< 1.43 at 3 $\sigma$

---

<sup>†</sup>The production rate of H<sub>2</sub>O has been calculated for OPR = 1.3 ± 0.2 (discussion of the OPR derivation and interpretation is beyond the scope of this dissertation, and would be presented in a separate publication). Assuming an equilibrium OPR of 3.0 would lead to a decrease in derived Q(H<sub>2</sub>O) in each setting by 20-30%, and corresponding increase in mixing ratios of 20-30%, which, however, does not significantly exceed the uncertainty provided for each mixing ratio.

### *The Organic Composition of Encke in Perspective*

The rotational temperatures derived for 2P/Encke are very low compared to those for any other comet. Typically rotational temperatures can be as low as 50 K (as in 8P/Tuttle) and as high as 126 K (as in C/2001 (A2 LINEAR)). For 2P/Encke  $T_{\text{rot}}(\text{H}_2\text{O}) = 24^{-6}/_{+13}$  K and  $T_{\text{rot}}(\text{HCN}) = 28^{-7}/_{+13}$  K, which could be explained by lower collision rates, insufficient to maintain the rotational level populations, due to overall low production rates for this comet.  $Q_{\text{H}_2\text{O}}$  in 2P/Encke is only  $4.4 \times 10^{27}$  molecules s<sup>-1</sup> (KL2 setting, 4 Nov. 2003), compared to  $Q_{\text{H}_2\text{O}}$  in C/2000 WM<sub>1</sub> of  $1.9 \times 10^{28}$  molecules s<sup>-1</sup> (KL2 setting, 25 Nov. 2001, Radeva et al. 2010), or  $Q_{\text{H}_2\text{O}}$  in C/2004 Q2 (Machholz) of  $1.4 \times 10^{29}$  molecules s<sup>-1</sup> (KL2 setting, 28 Nov. 2004, Bonev et al. 2009). The water production rate derived for Encke in this work is also confirmed by observations at millimeter wavelengths. Odin observations of the 557 GHz line of H<sub>2</sub>O at  $r_h = 1.01$  AU (Nov. 17. 2003) yield  $Q(\text{H}_2\text{O})$  of  $(4.9 \pm 0.7) \times 10^{27}$  molecules s<sup>-1</sup>, in agreement with our  $Q(\text{H}_2\text{O})$  of  $(4.4 \pm 0.8) \times 10^{27}$  molecules s<sup>-1</sup> (Biver et al. 2007).

To explore the effect of collision rates in terms of gas production rate, the collisional excitation rate can be calculated from  $C_{\text{lu}} = n_{\text{total}} \times \sigma_{\text{lu}} \times V_{\text{thermal}}$  ( $\sigma_{\text{lu}}$  is the



collisional excitation cross-section, and  $n_{\text{total}}$  is the number density). The number density (for neutral-neutral collisions) is

$$n_{\text{total}} \sim \frac{Q}{4\pi Vr^2} = \frac{4 \times 10^{27}}{4\pi 10^5 (3 \times 10^7)^2} = 3.5 \times 10^6 \text{ cm}^{-3}; \text{ for } Q_{\text{H}_2\text{O}} \text{ in Encke} \sim 4 \times 10^{27} \text{ s}^{-1}, V \sim$$

$10^5 \text{ cm s}^{-1}$ ,  $r \sim 300 \text{ km}$  (to cover the sampled inner region of the coma). Therefore, the neutral-neutral collision rate is

$$C_{\text{lu}} = n_{\text{total}} \times \sigma_{\text{lu}} \times V_{\text{thermal}} \sim 4 \times 10^6 \times 10^{-14} \times 10^4 = 4 \times 10^{-4} \text{ s}^{-1} \quad (\text{for comparison, the collision rate for } \text{WM}_1 \text{ would be 10 times higher at the same distance from the nucleus). However, electron-water collision rates at 300 km from the nucleus would be significantly higher: } C_{\text{lu}} = 0.4 \text{ s}^{-1} \text{ (using parameters presented in Chapter 2).}$$

To explore the issue of LTE (Local Thermal Equilibrium) in the inner coma, as related to overall production rate, rotational temperatures for H<sub>2</sub>O and HCN of a sample of comets are compared in Figures 5.10-5.11 as a function of heliocentric distance and of production rate. The cometary sample includes 153P/Ikeya-Zhang, 73P Schwassmann-Wachmann 3C (two measurements from different dates are presented), C/2001 A2 (LINEAR), 8P/Tuttle, 2P/Encke, C/2000 WM<sub>1</sub> (LINEAR), 6P/d'Arrest, C/2004 Q2 (Machholz), 9P Tempel 1 (post-impact) and 17P/Holmes, as shown in Table 5.3. Panel A in each figure presents measured rotational temperatures, and panel B presents temperatures corrected for the field-of-view for each comet (i.e. the sampled region of the coma). The scaling factor for this correction is  $(\frac{R_1}{200})^{-0.9}$ , where  $R_1$  is the beam radius for the observation (see Appendix

II). The correction is introduced because measured temperatures are expected to decrease due to adiabatic expansion of the gas close to the nucleus, and then increase

due to collisions with OH and fast H atoms for comets with very high gas production rate (Combi et al. 2004). The field of view is determined by the geocentric distance  $\Delta$ , and varies between  $\pm 52$  and  $\pm 1053$  km centered on the nucleus in this sample of comets. Figure 5.10B illustrates that after correcting for the field-of-view effect, there is no obvious correlation between rotational temperatures and  $r_h$  at the time of measurement. Figure 5.11B presents scaled  $T_{\text{rot}}$  as a function of  $Q_{\text{H}_2\text{O}}$ , and suggests a correlation between rotational temperatures and production rates. The values that deviate from the overall trend are HCN in comet A2 (LINEAR), which is discordant with rotational temperature measured from other species, and may be due to radiative cooling, as well as asymmetries in the HCN distribution (see Lin et al. 2007); and H<sub>2</sub>O and HCN in 8P/Tuttle, which has unusual organic composition, and may be a binary comet of dissimilar members (Bonev et al. 2008). Figure 5.11 clearly illustrates that 2P/Encke is an end-member in terms of H<sub>2</sub>O production rate in this sample. The low rotational temperatures in Encke (as well as in comet 6P/d'Arrest, which also has a very low gas production rate) may be related to the effects of insufficient collisions to maintain the rotational populations; or to low thermalization efficiency of fast H-atoms, perhaps coupled with more efficient radiative cooling (higher escape-to-space probability for molecules in the inner coma).

**Table 5.3.** Rotational temperatures of H<sub>2</sub>O and HCN in a sample of comets, mean  $r_h$  at time of measurement, geocentric distance  $\Delta$ , Field-of-view R, and overall production rate ( $Q_{\text{H}_2\text{O}}$ ), (weighted mean of  $Q_s$  are given when several settings or dates (as for WM<sub>1</sub> and Encke) are available).

	$r_h$ [AU]	$\Delta$ [AU]	R [km]	$\log(Q_{\text{H}_2\text{O}})$	$T_{\text{rot H}_2\text{O}}$ [K]	$T_{\text{rot HCN}}$ [K]
<b>I.</b> 153P/Ikeya-Zhang (April 14. 2002)	0.78	0.47	$\pm 300$	29.25	$94^{-3/+3}$	$114^{-17/+17}$
<b>II.</b> 73P SW-3 (May 14. 2006)	1.00	0.08	$\pm 52$	27.85	$92^{-3/+3}$	$77^{-2/+2}$
<b>III.</b> C/2001 A2 (LINEAR) (July 9. 2001)	1.16	0.28	$\pm 178$	28.58	$98^{-5/+6}$	$56^{-6/+6}$
<b>IV.</b> 8P/Tuttle (23 Dec. 2007)	1.16	0.31	$\pm 200$	28.36	$50^{-10/+10}$	$51^{-10/+10}$
<b>V.</b> 2P/Encke (Nov. 4-5. 2003)	1.20	0.31	$\pm 200$	27.64	$24^{-6/+13}$	$28^{-7/+13}$
<b>VI.</b> 73P SW-3 (April 7. 2006)	1.27	0.33	$\pm 213$	27.77	$55^{-10/+10}$	$52^{-10/+15}$
<b>VII.</b> C/2000 WM <sub>1</sub> (LINEAR) (Nov. 23-25. 2001)	1.34	0.37	$\pm 239$	28.32	$70^{-2/+2}$	$78^{-4/+5}$
<b>VIII.</b> 6P/d'Arrest (Aug. 11. 2008)	1.35	0.35	$\pm 229$	27.68	$39^{-2/+2}$	-
<b>IX.</b> C/2004 Q2 (Machholz) (Nov. 28. 2004)	1.49	0.65	$\pm 423$	29.18	$86^{-4/+4}$	$76^{-9/+9}$
<b>X.</b> 9P Tempel 1 (post-impact) (Jul. 4. 2005)	1.51	0.89	$\pm 575$	28.24	$38^{-6/+6}$	$37^{-3/+3}$

---

<b>XI.17P/Holmes</b> (Oct. 27. 2007)	2.45	1.63	$\pm 1053$	29.65	$73^{-7}/_{+9}$	$65^{-2}/_{+2}$
---	------	------	------------	-------	-----------------	-----------------

---

<sup>I</sup>HCN is taken from Magee-Sauer et al. 2002b, and H<sub>2</sub>O is taken from Dello Russo et al. 2004.

<sup>II</sup>Dello Russo et al. 2007.

<sup>III</sup>Magee-Sauer et al. 2008.

<sup>IV</sup>Bonev et al. 2008.

<sup>V</sup>This dissertation.

<sup>VI</sup>Villanueva et al. 2006.

<sup>VII</sup>This dissertation (published in Radeva et al. 2010).

<sup>VIII</sup>T<sub>rot</sub>(H<sub>2</sub>O) is the weighted mean from T<sub>rot</sub> in the KL1 and KL2 settings, which are presented by Dello Russo et al. 2009.

<sup>IX</sup>Bonev et al. 2009.

<sup>X</sup>Mumma et al. 2005.

<sup>XI</sup>Dello Russo et al. 2008.

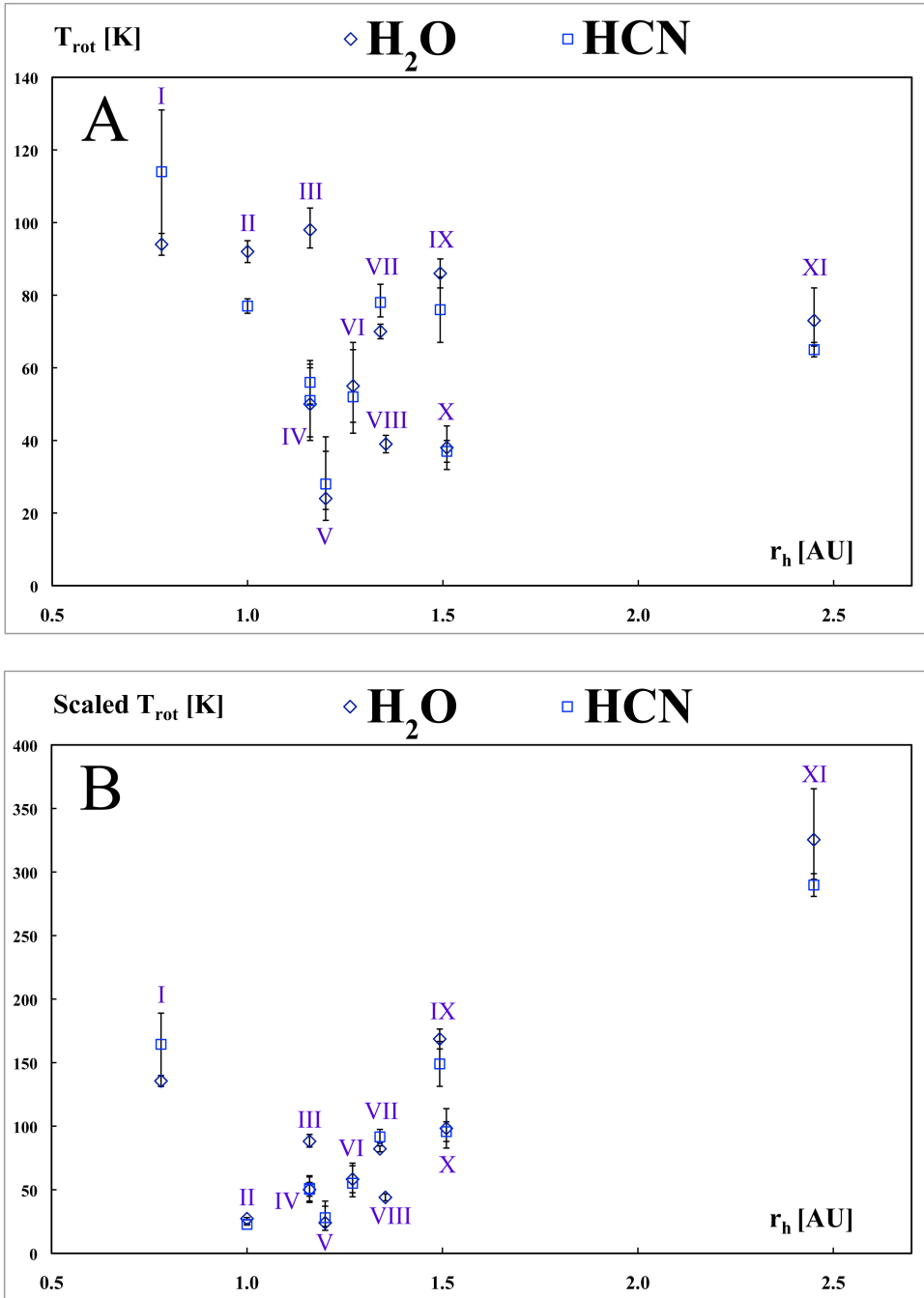


**Figure 5.10:** Panel A presents rotational temperatures of H<sub>2</sub>O and HCN measured for comets in this sample, as a function of mean r<sub>h</sub> at time of measurement. Panel B presents rotational temperatures scaled to a common beam size (200 km). No obvious correlation between T<sub>rot</sub> and r<sub>h</sub> is seen.

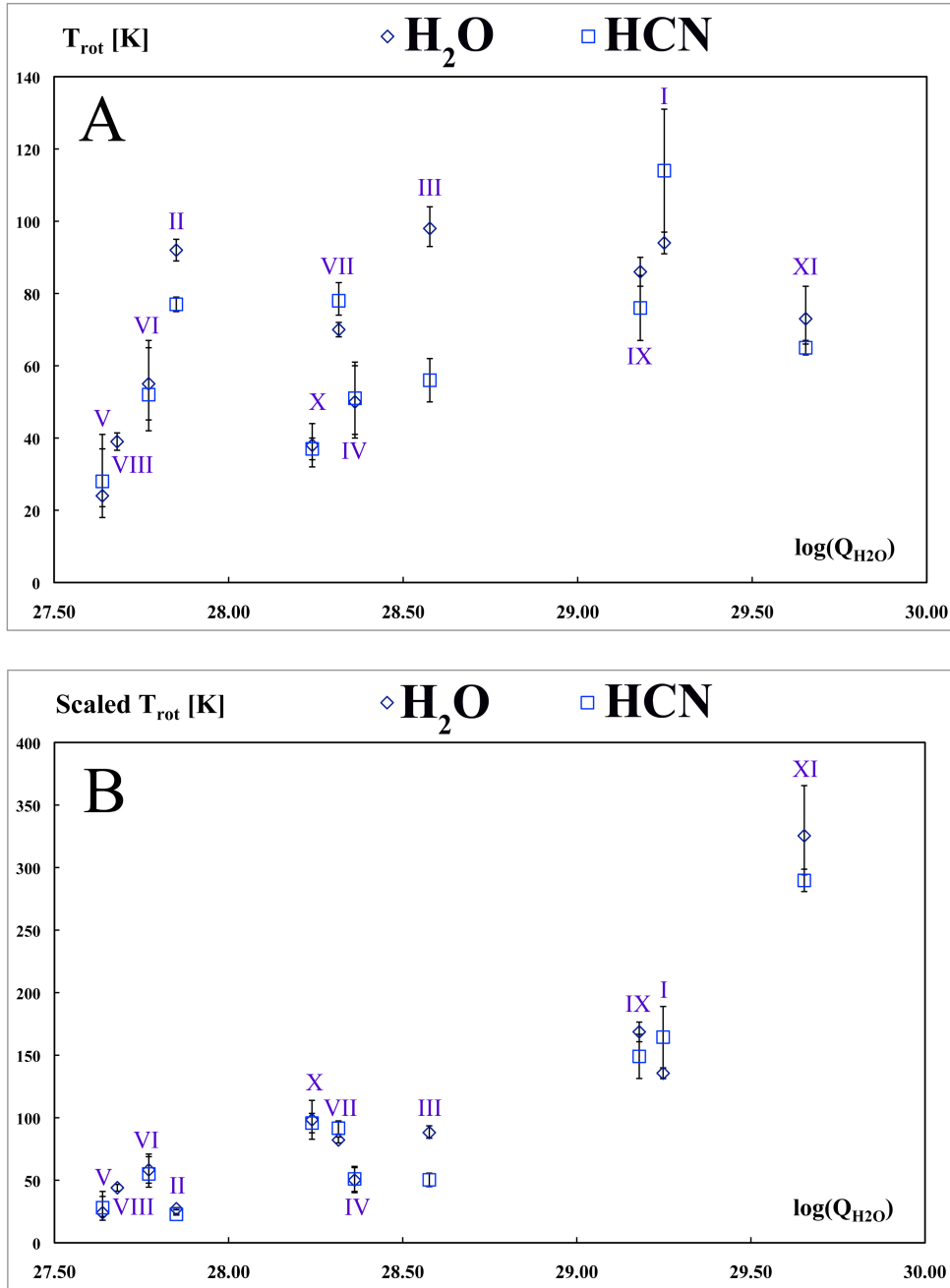


**Figure 5.11:** Panel A presents rotational temperatures of H<sub>2</sub>O and HCN measured for comets in this sample, as a function of production rate (weighted mean of  $Q_s$  when several settings or dates (as for WM<sub>1</sub> and Encke) are available). Panel B presents this variation after scaling rotational temperatures to remove the effect of the beam size (i.e. field-of-view) when

observed (see text and Appendix II). Rotational temperatures show a correlation with production rate.

2P/Encke is unusual not only in its rotational temperature. Compared with “organics-normal” comets 2P/Encke is depleted in  $C_2H_6$ ,  $C_2H_2$ , HCN,  $CH_4$  and CO, and normal in  $H_2CO$  and  $CH_3OH$  (see Table 2.1 for an overview of the organic composition of comets analyzed by the team at NASA GSFC; further mixing ratio discussion is presented in Chapter 6, including results for  $C_2H_6$   $v_5$ ). As previously proposed for the severely depleted comets C/1999 S4 and 73P/S-W 3-C, 2P/Encke may also have formed closer to the young Sun than organics-normal and organics-enriched comets.

Studies of Encke at radio wavelengths yield a mixing ratio for  $CH_3OH$  (4.1%), which is more than  $2\text{-}\sigma$  higher than the infrared measurement; an upper limit for  $H_2CO$  of  $<1.4\%$ ; and very low HCN (0.09%), in agreement with infrared measurements (Crovisier et al. 2007, Biver et al. 2005). Interestingly, optical observations show that 2P/Encke is normal in carbon-chain molecules (based on a sample of 85 comets) (A’Hearn et al. 1995), which disagrees with its infrared depletion in  $C_2H_6$  and  $C_2H_2$ . Since optical observations sample daughter species that can have multiple parents (including release from grains), it is possible that parent molecules, which have carbon chains, and which are not sampled in our infrared observations, are overabundant in Encke, as compared to “normal” comets. This would explain Encke’s infrared depletion in  $C_2H_6$  and  $C_2H_2$ , and typical abundances of  $C_2$  and  $C_3$ .

Furthermore, 2P/Encke is the shortest-period comet in the presented sample. Thus, it has orbited the Sun numerous times, which could contribute to its organic depletion. (CO and CH<sub>4</sub> are the most volatile ices: CO has a sublimation temperature of 25 K, and CH<sub>4</sub> has a sublimation temperature of 31 K (see Table 5.4, values from Yamamoto 1985)). Other short-period comets, however, do not show overall organic depletion despite their numerous orbits around the Sun (e.g. 9P/Tempel 1, 17P/Holmes). Possibly these comets formed later in time than Encke, when nebular clearing allowed more ionizing x-ray flux to reach farther from the Sun, producing higher H-atom densities, which at lower temperatures would contribute to more efficient H-atom addition reactions and produce some of the organic parents that we sample (e.g. C<sub>2</sub>H<sub>6</sub> from C<sub>2</sub>H<sub>2</sub> etc.). Also, 2P/Encke is not as depleted as the Oort cloud comet C/1999 S4, which has had few passes through the inner Solar System. Thus, the formative region of 2P/Encke, rather than its numerous orbits around the Sun, may provide a better explanation for its depletion.

**Table 5.4.** Sublimation temperatures for gas density of 10<sup>13</sup> molecules cm<sup>-3</sup> (Yamamoto 1987).

Molecule	Sublimation Temperature [K]
H <sub>2</sub> O	152
CH <sub>3</sub> OH	99
HCN	95
H <sub>2</sub> CO	64



C <sub>2</sub> H <sub>2</sub>	57
CH <sub>4</sub>	31
CO	25

To evaluate potential hydrogenation reactions on the surfaces of icy grains, converting C<sub>2</sub>H<sub>2</sub> into C<sub>2</sub>H<sub>6</sub> in 2P/Encke, the conversion efficiency for C<sub>2</sub>H<sub>2</sub> can be calculated as  $C_2H_6/(C_2H_2 + C_2H_6) > 0.5$ , which is not very high (and the mixing ratio for C<sub>2</sub>H<sub>6</sub> is comparable to the upper limit for C<sub>2</sub>H<sub>2</sub>). The hydrogenation efficiency for CO is  $(H_2CO + CH_3OH)/(CO + H_2CO + CH_3OH) = 0.6$ , which is comparable to the measurement in C/2000 WM<sub>1</sub>. H<sub>2</sub>CO and CH<sub>3</sub>OH are both normal in 2P/Encke, while CO is depleted, possibly suggesting a smaller initial abundance of CO among the formative ices, or that due to its high volatility CO was eventually depleted.

### Summary of Composition

I derived production rates and mixing ratios for parent volatiles (H<sub>2</sub>O, CH<sub>4</sub>, C<sub>2</sub>H<sub>2</sub>, C<sub>2</sub>H<sub>6</sub>, CH<sub>3</sub>OH, H<sub>2</sub>CO, CO, and HCN) in the ecliptic comet 2P/Encke, which is the shortest period comet, whose organic composition has been studied through high resolution infrared spectroscopy. I derived rotational temperatures for H<sub>2</sub>O and HCN, which agree within 1- $\sigma$  and are very low (20-30 K), as compared to measurements in other comets. 2P/Encke is depleted in C<sub>2</sub>H<sub>6</sub>, C<sub>2</sub>H<sub>2</sub>, HCN, CH<sub>4</sub> and CO, and normal in H<sub>2</sub>CO and CH<sub>3</sub>OH, in comparison to “organics-normal” Oort cloud comets, presented by Mumma et al. 2003, and the most enriched and most depleted comets in our

sample (A2 (LINEAR) and C/1999 S4, respectively). It is possible that 2P/Encke formed closer to the Sun than average comets, but further than the severely depleted C/1999 S4 or 73P/Schwassmann-Wachmann 3C. Differentiation among the influence of the cometary formation region, subsequent dispersion, and dynamical and chemical evolution, remains the complicating factor in interpreting the organic composition of a comet.

## Chapter 6: Development and Application of a Fluorescence Model of the C<sub>2</sub>H<sub>6</sub> $\nu_5$ Band

### Motivation

Production rates of parent volatiles are derived from the intensities of their rovibrational lines. The accuracy of production rates depends on the derived rotational temperature (which describes the rotational populations within the ground vibrational level), given that only a subset of lines is sampled, rather than the entire band. Until now, rotational temperatures could be extracted from H<sub>2</sub>O, HCN and CO, but not from C<sub>2</sub>H<sub>6</sub>. Production rates for C<sub>2</sub>H<sub>6</sub> have been derived from its  $\nu_7$  band at 3.3  $\mu\text{m}$ , however, its unresolved Q-branches cannot provide a reliable rotational temperature. Therefore, a theoretical fluorescence model of the C<sub>2</sub>H<sub>6</sub>  $\nu_5$  band at 3.45  $\mu\text{m}$  was developed, since its P, Q and R branches are resolved by NIRSPEC, and can be used to extract an accurate temperature. Also, while the  $\nu_7$  band is measured in a single setting with CH<sub>3</sub>OH and H<sub>2</sub>O, the  $\nu_5$  band is measured with H<sub>2</sub>CO, CH<sub>4</sub>, HCN, C<sub>2</sub>H<sub>2</sub>, CH<sub>3</sub>OH and H<sub>2</sub>O, which eliminates several systematic uncertainties. This also permits simultaneous measurement of the rotational temperatures of C<sub>2</sub>H<sub>6</sub>, H<sub>2</sub>O and HCN (and potentially C<sub>2</sub>H<sub>2</sub>), which provides further insights into the physics of the coma.

Development of the C<sub>2</sub>H<sub>6</sub> v<sub>5</sub> model

*Building the ground vibrational state*

C<sub>2</sub>H<sub>6</sub> is a symmetric top molecule (two of the three principal moments of inertia are equal), and it belongs to the D<sub>3d</sub> symmetry group. Therefore, C<sub>2</sub>H<sub>6</sub> has a 3-fold axis of symmetry (where rotation by 360°/p around a p-fold axis of symmetry results in the same configuration); three 2-fold axes perpendicular to the 3-fold axis; and 3 planes of symmetry (where reflection at a plane of symmetry results in the same configuration) going through the 3-fold axis and bisecting the angles between two successive 2-fold axes (Herzberg 1945). The molecule is illustrated on Figure 6.1, and its normal vibrations are described in Table 6.1 (frequencies obtained from the HITRAN spectroscopic database), and visualized on Figure 6.2.

**Table 6.1.** Normal vibrations of C<sub>2</sub>H<sub>6</sub> (from Herzberg 1945 & HITRAN).

<b>Vibrational Mode</b>	<b>Band Frequency [cm<sup>-1</sup>]</b>	<b>Type of Motion</b>	<b>IR or Raman active</b>
v <sub>1</sub>	2954	CH <sub>3</sub> stretching	Raman
v <sub>2</sub>	1388	CH <sub>3</sub> deformation	Raman
v <sub>3</sub>	995	C-C stretching	Raman

$\nu_4$	289	Torsion	IR
$\nu_5$	2896	CH <sub>3</sub> stretching	IR
$\nu_6$	1379	CH <sub>3</sub> deformation	IR
$\nu_7$	2969	CH <sub>3</sub> stretching	IR
$\nu_8$	1468	CH <sub>3</sub> deformation	IR
$\nu_9$	1190	Bending	IR
$\nu_{10}$	2985	CH <sub>3</sub> stretching	Raman
$\nu_{11}$	1469	CH <sub>3</sub> deformation	Raman
$\nu_{12}$	822	Bending	Raman

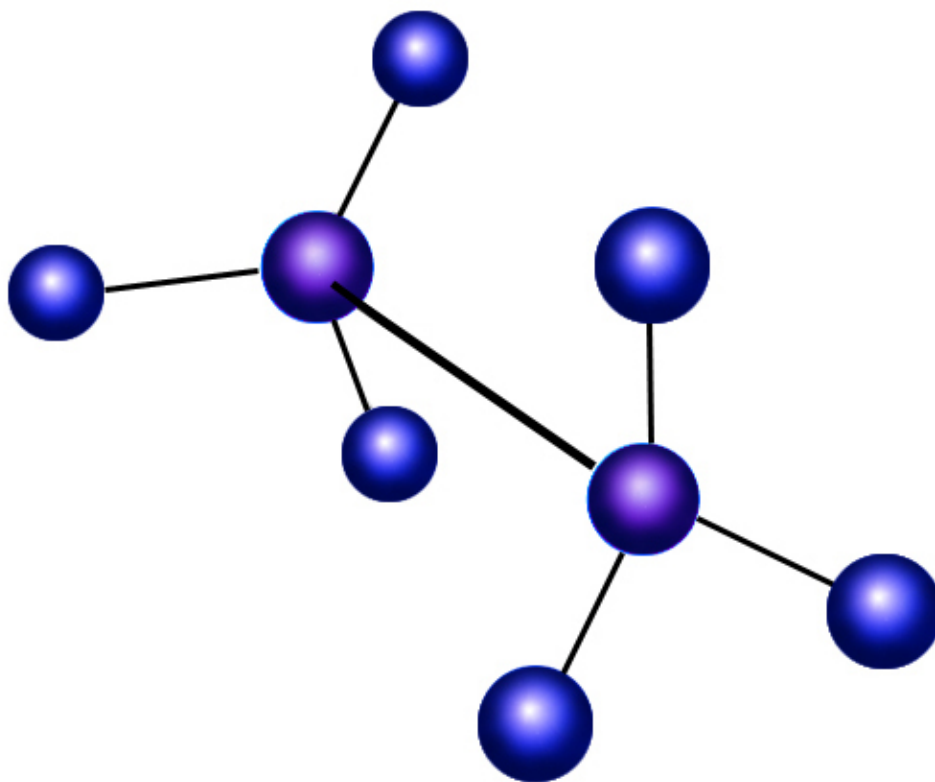


**Figure 6.1.** Illustration of the C<sub>2</sub>H<sub>6</sub> molecule.

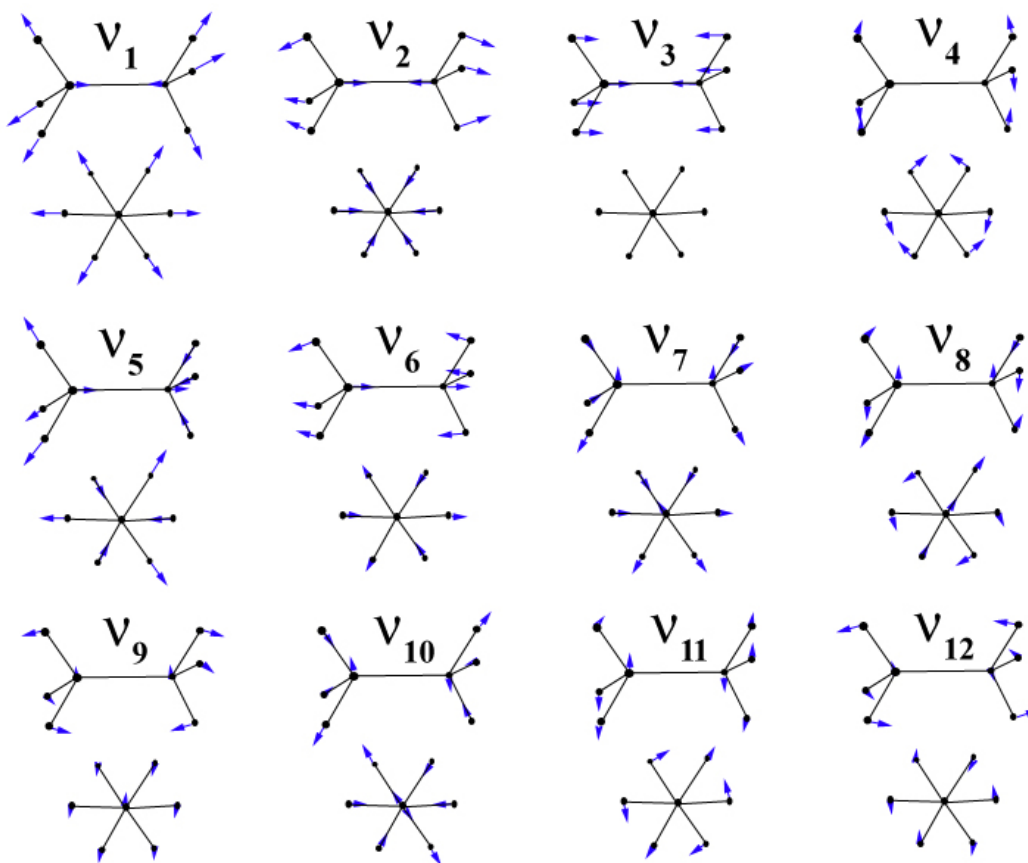


**Figure 6.2.** Vibrational modes of  $C_2H_6$ .

The energy of each rotational level in the ground vibrational state depends on the ground state rotational constants, which are provided in Pine & Lafferty (1982):  $A_0 = 2.671$ ;  $B_0 = 0.6630271$ ;  $D_{0K} = 1.09 \times 10^{-5}$ ;  $D_{0JK} = 2.660 \times 10^{-6}$ ;  $D_{0J} = 1.0312 \times 10^{-6}$  [ $cm^{-1}$ ]. Here  $A_0 = \frac{h}{8\pi c I_a}$  &  $B_0 = \frac{h}{8\pi c I_b}$ , and  $I_a$  and  $I_b$  are the moments of inertia about the principal axes 'a' and 'b', respectively.  $D_{0K}$ ,  $D_{0JK}$  and  $D_{0J}$  are the centrifugal distortion terms (correcting for the centrifugal force that stretches atoms away as the molecule rotates).

The energy [ $\text{cm}^{-1}$ ] of each rotational level is given by:

$$E_{\text{low}}(J'', K'') = (A_0 - B_0)K''^2 + B_0J''(J''+1) - D_{0J}J''^2(J''+1)^2 - D_{0JK}K''^2J''(J''+1) - D_0K''^4$$

(adapted from Herzberg 1945), where  $J''$  is the rotational quantum number, and  $K''$  is the quantum number that corresponds to the component of the total angular momentum vector along the figure axis ( $K \leq J$ , since  $K$  is the projection of  $J$ , see Figure 6.3). Ground state rotational energies are also available in Dang-Nhu et al. 1984. Statistical weights for the rotational levels were obtained from Dang-Nhu et al. 1984 (also Wilson 1938). Torsional splitting is ignored, since it cannot be resolved with current infrared instruments. The statistical weights are determined from the following rules:

- If  $K = 0$  and  $J$  is even, then  $g_s = 8$ .
- If  $K = 0$  and  $J$  is odd, then  $g_s = 16$ .
- If  $K \neq 0$  and  $K$  is divisible by 3, then  $g_s = 24$ .
- If  $K \neq 0$  and  $K$  is not divisible by 3, then  $g_s = 20$ .

The total statistical weight of a level is:  $g'' = g_s(2J''+1)$ .



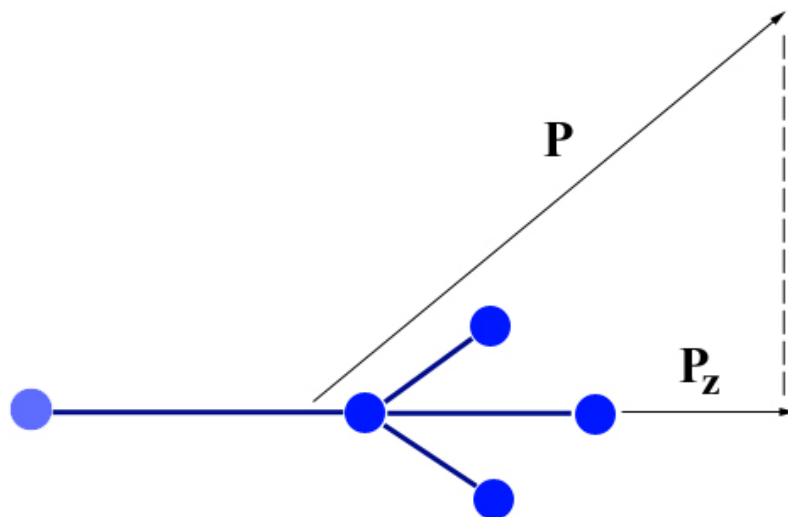


**Figure 6.3.** Symmetric top molecule: total angular momentum vector  $P$  (rotational quantum number  $J$ ), and its component (projection) along the figure axis -  $P_z$  (quantum number  $K$ ).

The rotational partition function is  $Z_{\text{rot}} = \sum_{J'', K''} g_s(2J''+1) e^{-hcE_{\text{low}} / kT_{\text{rot}}}$  (representing the sum of populations of all rotational levels), and the vibrational partition function is  $Z_{\text{vib}} = \left[ 1 - \exp\left(\frac{-hc\nu_4}{kT}\right) \right]^{-1}$ , where  $\nu_4$  is a low-frequency torsional mode at  $\sim 290 \text{ cm}^{-1}$  (Pine & Lafferty 1982) (see Table 6.2). The population  $N_{JK}$  in each rotational level ( $J''$ ,  $K''$ ) at a given rotational temperature is  $N_{JK} = g_s(2J_{\text{low}} + 1) e^{-hcE_{\text{low}} / kT}$  (thus, the fractional population is  $\frac{N_{JK}}{Z_{\text{tot}}}$ ). The total partition function is  $Z_{\text{tot}} = Z_{\text{vib}} Z_{\text{rot}}$  (which can be obtained from the HITRAN spectroscopic database (Simeckova et al. 2006)).

**Table 6.2.** Rotational and vibrational partition functions.  $Z_{tot} = Z_{vib}Z_{rot}$  (also provided in the HITRAN spectroscopic database).

	$T_{rot} = 70 \text{ K}$	$T_{rot} = 119 \text{ K}^I$
$Z_{rot}$	5948.44	13165.17
$Z_{vib}$	1.006	1.026
$Z_{tot}$	5983.812	13511.308

<sup>I</sup>Consistent with Dang-Nhu et al. 1984.

An important assumption in this calculation is that the rotational states of the ground vibrational state follow a Boltzmann distribution, since they are thermalized by collisional excitation (Xie & Mumma 1992) (also discussed in detail in Chapter 2).

To verify this assumption, the collisional excitation rate can be approximated as

$C_{lu} = n_{total} \times \sigma_{lu} \times V_{thermal}$ , where  $\sigma_{lu}$  is the collisional excitation cross-section, and  $n$  is the number density. The number density can be approximated as

$$n_{total} \sim \frac{Q}{4\pi V_{outflow} R^2} \sim \frac{10^{28}}{4\pi 10^5 (10^7)^2} \sim 10^8 [\text{cm}^{-3}] \quad (\text{for estimates, cf. Xie \& Mumma 1992});$$

assuming  $Q \sim 10^{28} \text{ s}^{-1}$ ,  $V_{outflow} \sim 10^5 \text{ cm s}^{-1}$ ,  $R \sim 100 \text{ km}$  (inner coma).

Therefore,  $C_{lu} = n_{total} \times \sigma_{lu} \times V_{thermal} \sim 10^8 [\text{cm}^{-3}] \times 10^{-14} [\text{cm}^2] \times 10^4 [\text{cm s}^{-1}] = 10^{-2} \text{ s}^{-1}$ ,

which dominates the radiative transition rate for rotational levels (negligible due to

the very weak solar flux at millimeter wavelengths). This demonstrates that collisional excitation thermalizes rotational levels.

Next, collisional excitation versus collisional de-excitation is explored. From the principle of detailed balance:  $\frac{dn_u}{dt} = \sigma_{lu} \times n_l - \sigma_{ul} \times n_u = 0$ , where  $n_u$  and  $n_l$  are the populations of the upper and lower state, and  $\sigma_{lu}$  and  $\sigma_{ul}$  are the cross-sections for transitions between the upper and lower states. From  $n_u = n_l \times e^{-\Delta E / kT_{\text{kinetic}}}$ , (where  $\Delta E$  is the energy gap between the lower and upper state),  $\sigma_{lu} = \sigma_{ul} \times e^{-\Delta E / kT_{\text{kinetic}}}$  is obtained, and collisional excitation dominates over de-excitation. Also, pure rotational lines are optically thick due to the high density and small escape probability for emitted photons. Thus, optical trapping results in an increased distance over which which collisions thermalize rotational levels, as discussed in Chapter 2. For a more detailed discussion refer to Weaver & Mumma (1984), Bockelee-Morvan (1996), and Xie & Mumma (1992).

### *Building the excited $\nu_5$ state*

The focus of this study is resonant fluorescence that takes place in the  $C_2H_6$  molecule, under the influence of the solar radiation. This refers to transitions that take place from the ground vibrational state to an excited vibrational state ( $\nu_5$ ), and subsequently from the excited to the ground state (see Crovisier 1983, Weaver and Mumma 1984, Reuter et al. 1989). This is a fundamental transition, compared to which, overtone and combination bands are very weak.

The center of the band is at  $2895.67 \text{ cm}^{-1}$ , and the band strength  $S(\nu_5) = 114.49 \text{ cm}^{-2} \text{ atm}^{-1}$  at  $T_{\text{ref}} = 296 \text{ K}$  (Dang-Nhu et al. 1984). For convenience in some calculations, this band strength can be converted to  $\text{cm}^{-1}(\text{molecule cm}^{-2})^{-1}$  as follows:

$$S(\nu_5) = \frac{114.49 \times T_{\text{ref}}}{273.15 \times L} \text{ cm}^{-1}(\text{molecule cm}^{-2})^{-1} \quad (\text{Simeckova et al. 2006}),$$

where  $L$  is the Loschmidt number ( $2.68676 \times 10^{19} \text{ molecules cm}^{-3}$ , the number density at standard temperature and pressure).  $S_{\nu_5}$  can be calculated for any temperature  $T$  using:

$$S_{\nu_5(T)} = \frac{S_{\nu_5(T_{\text{ref}})} \times Z_{\text{vib}}(T_{\text{ref}})}{Z_{\text{vib}}(T)} \times \frac{T_{\text{ref}}}{T} [\text{cm}^{-2} \text{ atm}^{-1}].$$

The energy [ $\text{cm}^{-1}$ ] of each rotational level in the upper vibrational state  $\nu_5$  is:

$$E_{\text{up}}(J', K') = \nu_{5 \text{ center}} + (A' - B')K'^2 + B'J'(J'+1) - D_J'J'^2(J'+1)^2 - D_{JK}'K'^2J'(J'+1) - D'K'^4$$

The lack of upper state rotational constants for  $\nu_5$  in the literature required fitting experimental data by Pine & Lafferty (1982) for each  $K$  ladder (thus, the  $K$  members of the equation are a constant for each ladder, since each ladder is subject to perturbations). Pine & Lafferty recorded the absorption spectrum of ethane with a tunable difference-frequency laser spectrometer, and they provide a frequency and intensity for each measured line and identifications of  $J''$ ,  $K''$ ,  $J'$  and  $K'$  for many lines. The results of the fit (for  $K \leq 7$  and  $J \leq 22$ , standard deviation of 0.03) were used to calculate  $E_{\text{up}}(J', K')$ , and subsequently, the frequency of each absorption line as:

$$\nu_{\text{line}} = E_{\text{up}}(J', K) - E_{\text{low}}(J'', K'').$$

Next, the intensity of a transition in absorption [ $\text{cm}^{-1} \text{ molecule}^{-1} \text{ cm}^2$ ] was calculated from (Dang-Nhu et al. 1984):

$$S_{\text{line}} = \frac{\nu_{\text{line}} S_{\nu_5}(T_{\text{rot}}) g'' (1 - e^{-hc\nu_{\text{line}}/(kT_{\text{rot}})}) e^{-hcE_{\text{low}}/(kT_{\text{rot}})}}{\nu_5 Z_{\text{rot}}} F_{\text{HW}} F_{\text{HL}}$$

, where  $\nu_{\text{line}}$  is the frequency of an absorption line,  $\nu_5$  is the band center frequency,  $S(\nu_5)$  is the band strength at  $T_{\text{rot}}$ ,  $g''$  is the statistical weight of the lower rotational state,  $F_{\text{HW}}$  is the Herman-Wallis factor, and  $F_{\text{HL}}$  is the Hönl-London factor.

The following selection rules apply to  $\text{C}_2\text{H}_6$   $\nu_5$  since it is a parallel band ( $\Delta K = 0$ ), (Herzberg 1945):

$$\Delta K = 0 \text{ and } \Delta J = 0, \pm 1 \quad \text{if } K_{\text{low}} \neq 0$$

$$\Delta K = 0 \text{ and } \Delta J = \pm 1 \quad \text{if } K_{\text{low}} = 0.$$

Herman-Wallis factors were calculated for each transition to correct for the rotational dependence of the transition moments due to rotation-vibration interactions

$$\text{(Watson 1992): } F_{\text{HW}} = \left( 1 + \alpha K_{\text{low}} \Delta K + \beta \Delta J \left( J_{\text{low}} + \frac{1}{2} + \frac{\Delta J}{2} \right) \right)^2. \text{ For } \nu_5 \text{ } \Delta K = 0 \text{ and}$$

Dang-Nhu et al. (1984) provide the necessary factor:  $\beta = 0.0048$ .

The Hönl-London factors (factors proportional to the square of the transition moment, summed over all orientations of  $J$ ) were determined from the formulas given in Herzberg (1945) (for  $J''$  and  $K''$ ):

$$F_{\text{HL}} = \frac{(J+1-K)(J+1+K)}{(J+1)(2J+1)}, \text{ if } \Delta J = +1$$

$$F_{\text{HL}} = \frac{K^2}{J(J+1)}, \text{ if } \Delta J = 0$$

$$F_{\text{HL}} = \frac{(J-K)(J+K)}{J(2J+1)}, \quad \text{if } \Delta J = -1.$$

The line intensities were used to calculate Einstein A coefficients [ $\text{s}^{-1}$ ] (Simeckova et al. 2006):

$$A_{\text{ul}} = \frac{8\pi c \nu_{\text{line}}^2 Z_{\text{tot}}(T_{\text{rot}}) S_{\text{line}}}{I_a g' (1 - e^{-hc\nu_{\text{line}}/(kT_{\text{rot}})}) e^{-hcE_{\text{low}}/(kT_{\text{rot}})}},$$

where  $I_a$  is the  $^{12}\text{C}_2\text{H}_6$  isotopic fraction (0.97699, HITRAN 2008), and  $g'$  is the upper level statistical weight. Excitation takes place from lower rotational levels “l” in the ground vibrational state to a rotational level “u” in the upper vibrational state (as allowed by selection rules), followed by radiative de-excitation from “u” to a rotational level “l” in the ground vibrational state.

#### *Determining pumping rates*

The pumping rate by the solar radiation from the ground vibrational state to the excited  $\nu_5$  state, was calculated as follows:  $g_{\text{pump}} = \rho_{\nu} \cdot B_{lu} \cdot n_{\text{low}}$ , where  $\rho_{\nu}$  is the solar radiation density at 1 AU,  $B_{12}$  is the Einstein B coefficient [ $\text{cm}^{-1} \text{molecule}^{-1} \text{cm}^2$ ], and  $n_{\text{low}}$  is the fractional population of the lower level [ $\frac{N_{JK}}{Z_{\text{tot}}}$ ] (Crovisier 1983).

The solar flux density is  $\rho_{\nu} = 2h\nu_{\text{line}}^3 \Omega_{\text{bb}} [e^{hc\nu_{\text{line}}/kT_{\text{bb}}} - 1]^{-1}$  in [ $\text{J s cm}^{-3}$ ]. The pumping rate from all lower levels into the upper level ( $J', K'$ ) are summed (the

selection rules are  $\Delta J = 0, \pm 1$ ):  $g_{\text{pump}(\text{total})} = \rho_{\nu} \sum_l B_{lu} \times n_{\text{low}} = \rho_{\nu} \sum S_{\text{line}}$  (at 1 AU, cf. Reuter, Mumma and Nadler 1989).

*Calculating fluorescence efficiency factors*

The final step is determining the fluorescence efficiency factors (g-factors) for the transitions from the excited vibrational state to the ground vibrational state. The transitions that take place are illustrated in Figure 6.4.

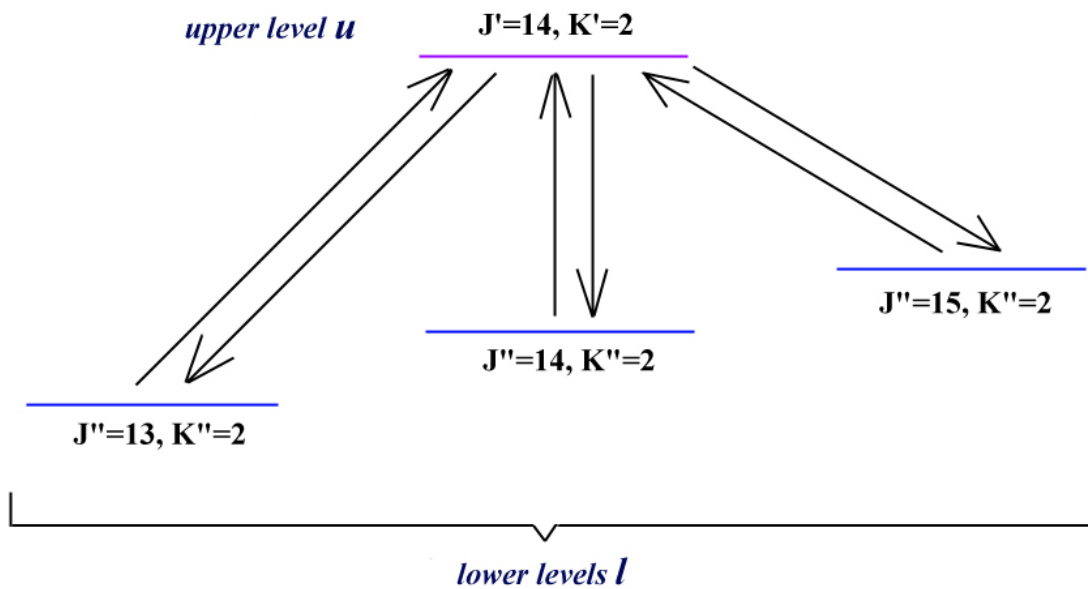


**Figure 6.4.** Illustration of transitions from lower levels “l” to upper level “u”, allowed by the selection rule  $\Delta J = 0, \pm 1$ .

$$\text{Thus, } g_{\text{factor}}(1 \text{ AU}) = g_{\text{pump}}(\text{total}) \cdot \frac{A_{ul}}{\sum_1 A_{ul}} \text{ [photons molecule}^{-1} \text{ s}^{-1}\text{]}, \text{ where } \frac{A_{ul}}{\sum_1 A_{ul}}$$

defines the branching ratio from the excited to the ground state.  $g$ -factors were calculated for a range of temperatures (20-150 K). We scale  $g$ -factors for the actual heliocentric distance of the comet as:  $g_{\text{factor}} = g_{\text{factor}}(1 \text{ AU}) \times R_h^{-2}$ .

Potential sources of uncertainty in the derived  $g$ -factors are the  $\nu_5$  band intensity, and the factors for Herman-Wallis calculations, all determined from lab measurements; as well as the fact that K-ladders in the  $\nu_5$  band have perturbations, as shown in the laboratory spectrum of  $\text{C}_2\text{H}_6$  (Pine & Lafferty 1982).

### *Application of the $\text{C}_2\text{H}_6$ $\nu_5$ model*

#### *Observing Log*

I applied the  $\text{C}_2\text{H}_6$   $\nu_5$  model to high-resolution spectra of comets 17P/Holmes, C/2000 WM<sub>1</sub> (LINEAR), C/2004 Q2 Machholz, C/2001 A2 (LINEAR), C/2007 N3 (Lulin), C/2007 W1 (Boattini), 8P/Tuttle, and 2P/Encke, acquired with NIRSPEC on Keck II. I analyzed the data following the usual procedures (described in Chapter 3; and Bonev 2005, DiSanti et al. 2006, and references therein). I present the observing log for the above comets in Table 6.3. Comets are arranged in the table from highest to lowest  $\text{C}_2\text{H}_6/\text{CH}_3\text{OH}$  ratio (approximately – unknown for Boattini and Lulin), since methanol features are often blended with  $\text{C}_2\text{H}_6$   $\nu_5$  (and are underlying the entire



spectrum), complicating interpretation of the observed spectra. I present all mixing ratios and rotational temperatures for the analyzed comets in the subsequent discussion.

**Table 6.3.** Observing log.

	Date	Mean UT	$r_h$ [AU] <sup>I</sup>	$\Delta$ [AU] <sup>I</sup>	$\dot{\Delta}$ [km s <sup>-1</sup> ] <sup>I</sup>
17P/Holmes	29 Oct. 2007	12:20	2.46	1.63	-2.55
C/2000 WM <sub>1</sub>	24 Nov. 2001	08:50	1.34	0.37	-21.36
Q2 Machholz	28 Nov. 2004	11:30	1.49	0.65	-21.79
A2 LINEAR	9 Jul. 2001	13:40	1.16	0.28	11.54
Lulin	30 Jan. 2009	14:30	1.25	0.99	-54.27
Boattini	9 Jul. 2008	14:40	0.89	0.35	12.92
8P/Tuttle	23 Dec. 2007	05:20	1.16	0.31	-18.18
2P/Encke	4 Nov. 2003	06:10	1.210	0.313	-13.59

<sup>I</sup> $R_h$  is the heliocentric distance,  $\Delta$  is the geocentric distance and  $\dot{\Delta}$  is the line-of-sight velocity.

## *Overview of Comets*

I. 17P/Holmes is a Jupiter-family comet, with a period of 6.9 years. It was observed by the NASA GSFC team on 29-30 Oct. 2007, and its organic composition is currently being analyzed. This work is based on data from 29 Oct. 17P/Holmes was also observed on 27, 31 Oct. and 2 Nov. 2007 with NIRSPEC, by Dello Russo et al. (2008). This comet is enriched in  $C_2H_6$ ,  $C_2H_2$  and HCN (27 Oct., Dello Russo et al. 2008), and normal in  $CH_3OH$ . However, 17P/Holmes was observed at a greater distance from the Sun ( $\sim 2.4$  AU), and if a certain portion of the water in the inner coma was in the form of ice (Yang et al. 2009) its enrichment in organic volatiles might be overestimated (if the ice has different mixing ratios from the ice). Its outburst at 2.4 AU was approximately 5 months after perihelion. Dello Russo et al. (2008) also present a  $g$ -factor for the  $qP(3)$  line of  $C_2H_6$   $v_5$  at 79 K, which agrees within 17% with the  $g$ -factor derived in this work. The mixing ratio and production rate presented by Dello Russo et al. (2008) for comet Holmes are based on both  $C_2H_6$   $v_7$  and  $v_5$ .

II. The Oort comet C/2000 WM<sub>1</sub> was observed on 23-25 Nov. 2001, and was determined to be severely depleted in CO and  $C_2H_2$ ; moderately depleted in  $CH_4$ ,  $CH_3OH$  and HCN; and normal in  $C_2H_6$  and  $H_2CO$ . Mixing ratios for organic species agree by 1 or 2- $\sigma$  for the three consecutive dates on which they were measured, thus, providing no evidence for heterogeneity of WM<sub>1</sub>'s nucleus. The organic composition of this comet is described in detail in Chapter 4, and has been presented in Radeva et al. (2010).

III. The Oort cloud comet Q2 Machholz was observed on 28-29 Nov. 2004 and 19 Jan. 2005, and its organic composition was presented by Bonev et al. (2009). The mixing ratios of parent species measured on 28 Nov. 2004 (1.5 AU) and on 19 Jan. 2005 (1.2 AU) agree within error (while production rates are approximately twice higher at 1.2 AU), which does not support heterogeneity of this cometary nucleus. The mixing ratios of  $C_2H_6$ ,  $CH_3OH$ , HCN and CO in Q2 Machholz are average, compared to organics normal comets; while the mixing ratios of  $H_2CO$  and  $C_2H_2$  are low, suggestive of depletion in these organic species (all measured on 28 Nov. 2004 except for CO, Bonev et al. 2009).  $CH_4$  in Q2 Machholz is in the high end of the range observed for organics-normal comets. Kawakita and Kobayashi (2009) observed Q2 Machholz in late January 2005, and report depletion in  $C_2H_2$  and  $C_2H_6$  and normal mixing ratios of HCN,  $CH_3OH$ ,  $CH_4$ , and  $H_2CO$ . The results derived here from  $C_2H_6$   $v_5$  are compared with results presented by Bonev et al. (2009), since the same dataset was used in the analysis, eliminating systematic effects.

IV. Comet A2 (LINEAR) was observed on 9 – 10 July, and 4 – 5 August 2001. In this work data from 9 July were analyzed. This is the most enriched Oort cloud comet in our database. It is enriched in  $C_2H_6$ ,  $C_2H_2$ , HCN, and  $CH_3OH$ , and normal in  $CH_4$ ,  $H_2CO$  and CO (Magee-Sauer et al. 2009). The organic enrichment of A2 (LINEAR) could be explained by this comet's formation further from the Sun, in a colder region of the proto-solar nebula, or by chemical processing, among other possible causes. Gibb et al. (2007) discuss the variation of mixing ratios in A2 (LINEAR):  $H_2CO$  varies significantly between 9 Jul. and 10 Jul., and  $CH_4$  varies

between July and August. This could be indicative of possible heterogeneity of this cometary nucleus.

V. Comet Lulin originates from the Oort cloud, and is undergoing analysis by the NASA GSFC team. It was observed on 30 Jan. - 1 Feb. 2009.

VI. Comet Boattini is also undergoing analysis by GSFC team members (Villanueva et al., in progress). It was observed on 9 July 2008.

VII. Comet 8P/Tuttle has a period of 13.6 years, and was observed on 22-23 Dec. 2007. Its organic composition was presented in Bonev et al. (2008). 8P/Tuttle has unusual composition, compared with other comets. It is enriched in CH<sub>3</sub>OH, normal in CH<sub>4</sub>, and depleted in HCN, H<sub>2</sub>CO, C<sub>2</sub>H<sub>2</sub>, and C<sub>2</sub>H<sub>6</sub>. CO is also depleted, although only a 3- $\sigma$  upper limit is available. Radar images of 8P/Tuttle suggest that this comet may be a binary, and Bonev et al. (2009) propose that if the nucleus is indeed a "contact binary", it could consist of fragments that formed in different regions of the Solar System, thus the difference in organic depletion/enrichment. In addition, Villanueva et al. (2009) present the first sensitive infrared measurement of D/H (from HDO/H<sub>2</sub>O) in a comet. D/H for 8P/Tuttle is reported to be  $4.09 \pm 1.45 \times 10^{-4}$ , which agrees with values measured for three other Oort cloud comets, and is  $2.62 \pm 0.93$  higher than D/H in Vienna Standard Mean Ocean Water (Villanueva et al. 2009).

VIII. The ecliptic comet 2P/Encke was observed on 4-5 Nov. 2003, and has the shortest period among comets sampled at infrared wavelengths. Encke is depleted in CO, C<sub>2</sub>H<sub>2</sub>, CH<sub>4</sub>, C<sub>2</sub>H<sub>6</sub> and HCN; and normal in H<sub>2</sub>CO and CH<sub>3</sub>OH. Its organic composition is described in detail in Chapter 5.

### *Spectral Gallery*

Calibrated frames and cometary spectra are presented in Figures 6.5-6.12. The calibrated frames (two beams and their sum (white) in the middle) are shown first; the cometary spectra and the superimposed terrestrial transmittance model are shown in the upper panel of each figure; and the residual emission features are shown in the lower panel. The  $\pm 1\text{-}\sigma$  noise envelope is shown as a green line centered around zero.

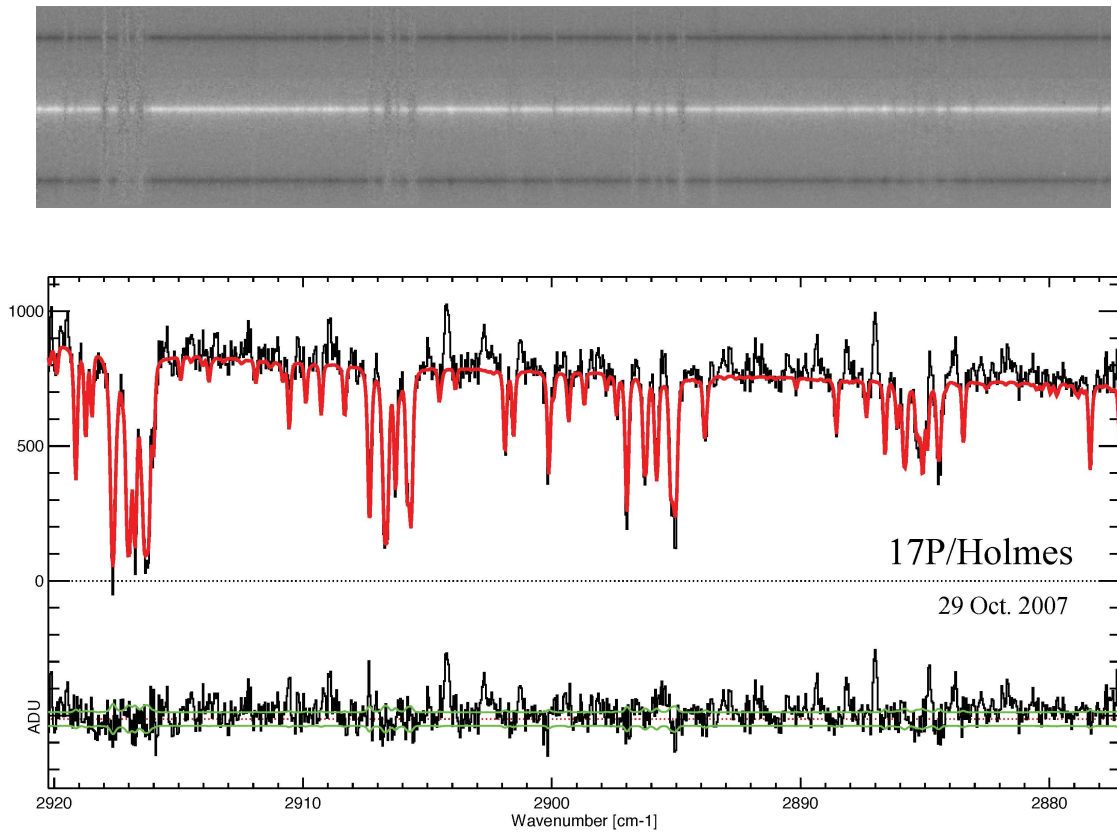


**Figure 6.5.** 17P/Holmes: calibrated frame; extracted spectrum with terrestrial transmittance model superimposed (in red); and residual spectrum (top to bottom panel). The green line represents the  $\pm 1\text{-}\sigma$  noise envelope.

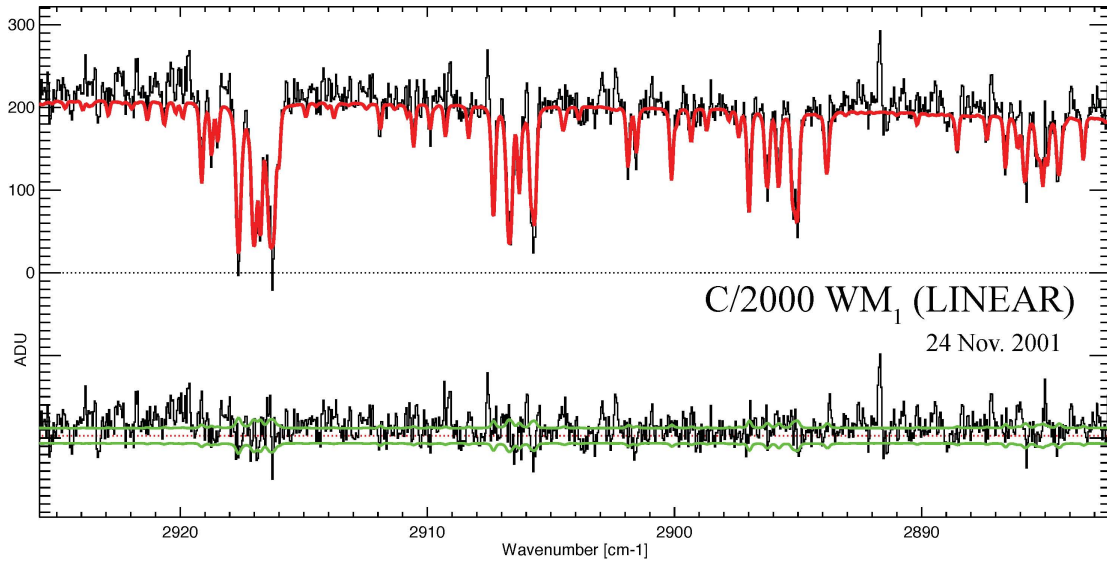
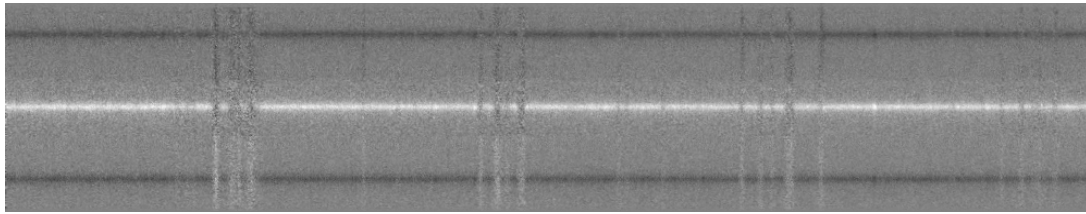


**Figure 6.6.** C/2000 WM<sub>1</sub> (LINEAR): calibrated frame; extracted spectrum with terrestrial transmittance model superimposed (in red); and residual spectrum (top to bottom panel). The green line represents the  $\pm 1\text{-}\sigma$  noise envelope.

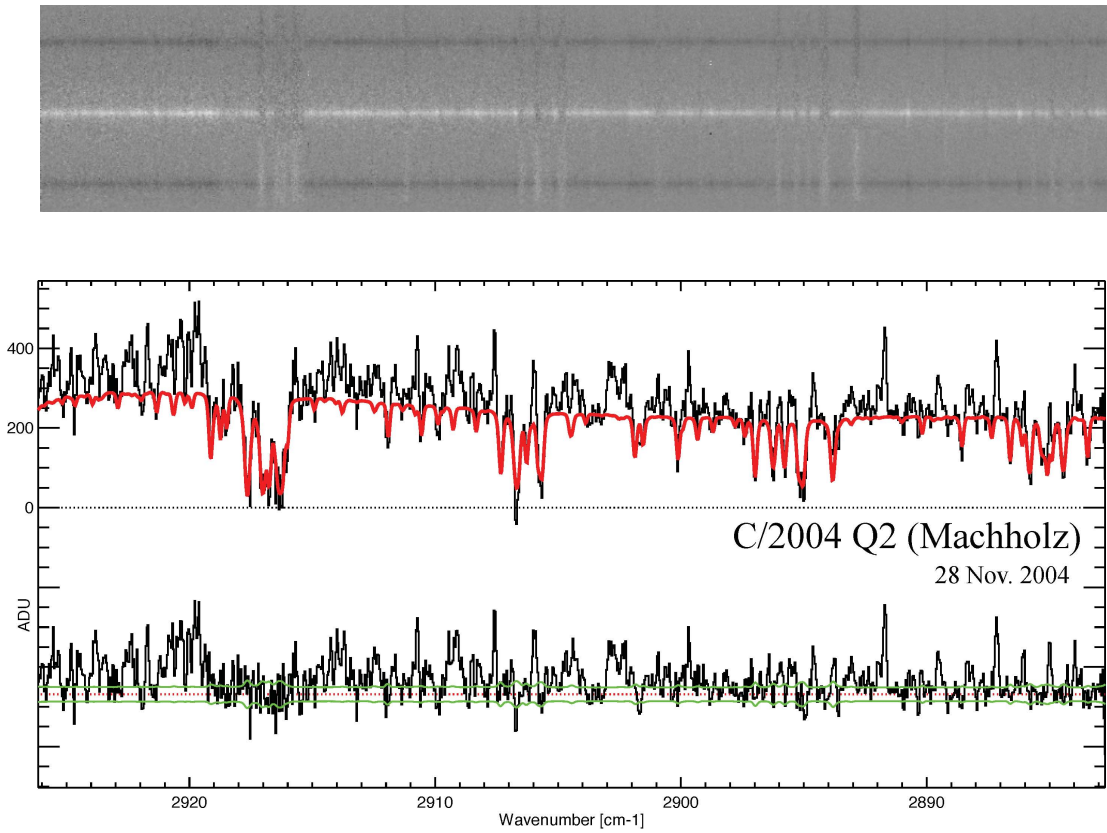


**Figure 6.7.** C/2004 Q2 (Machholz): calibrated frame; extracted spectrum with terrestrial transmittance model superimposed (in red); and residual spectrum (top to bottom panel). The green line represents the  $\pm 1-\sigma$  noise envelope.



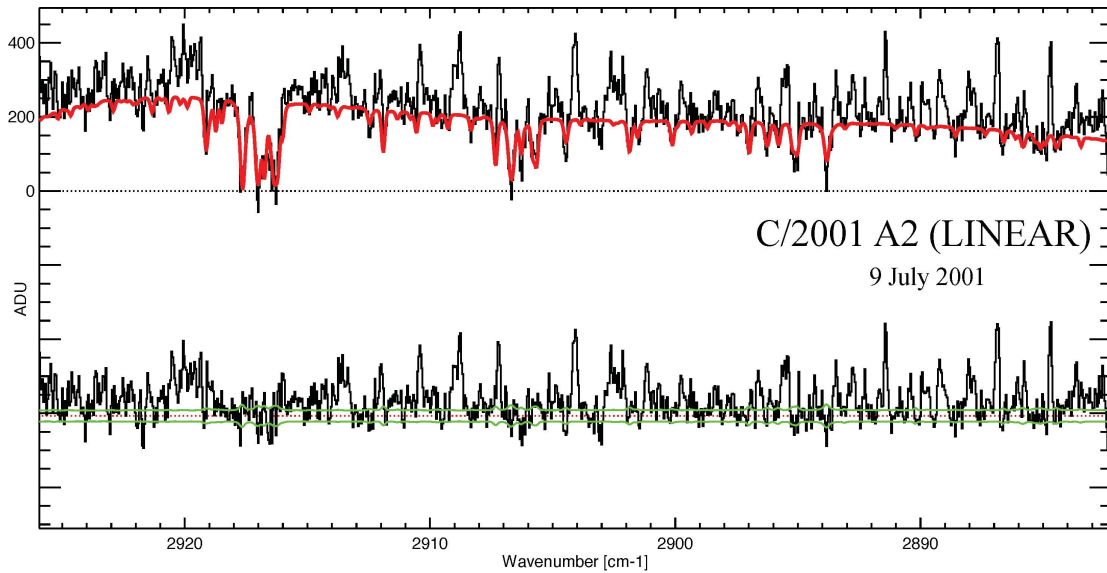
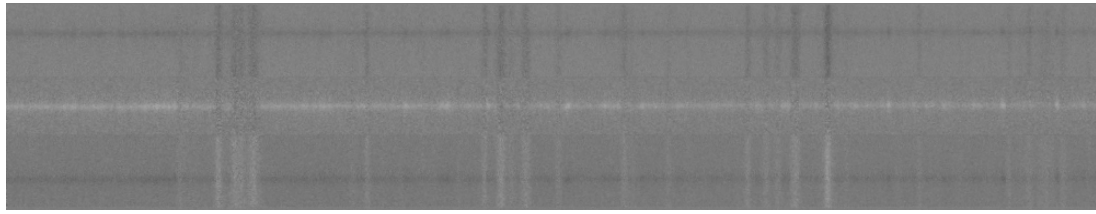


**Figure 6.8.** C/2001 A2 (LINEAR): calibrated frame; extracted spectrum with terrestrial transmittance model superimposed (in red); and residual spectrum (top to bottom panel). The green line represents the  $\pm 1\text{-}\sigma$  noise envelope.

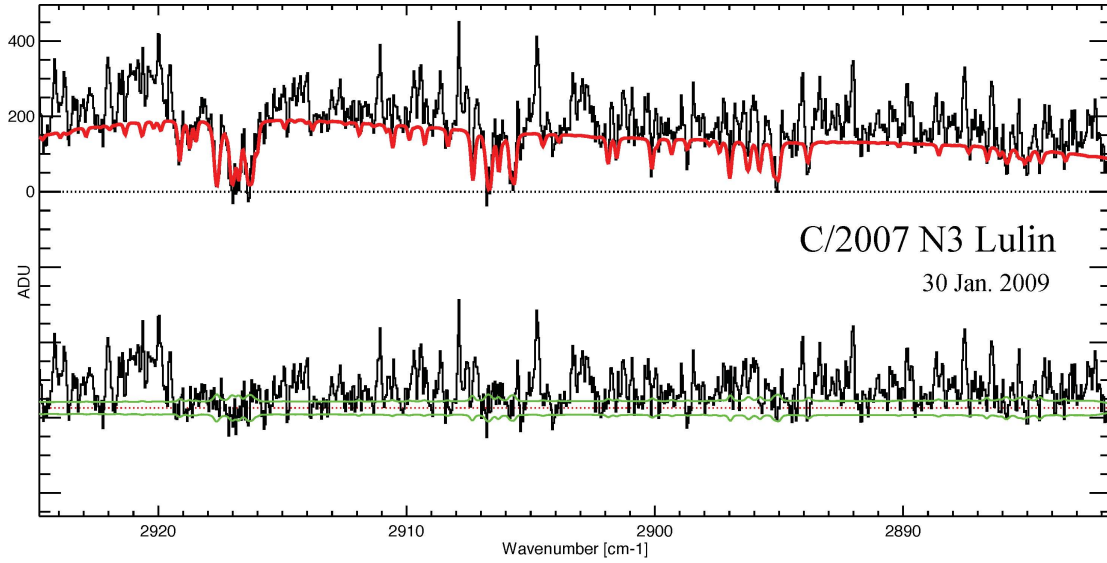
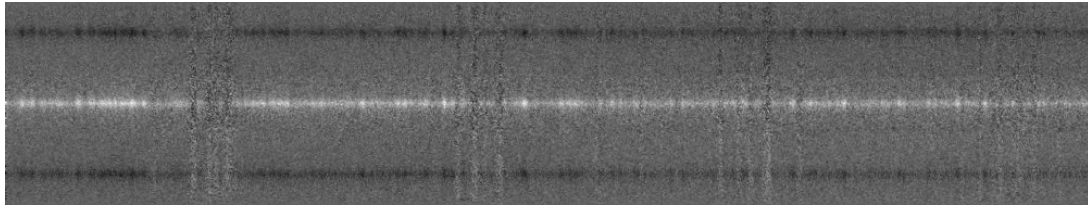


**Figure 6.9.** C/2007 N3 (Lulin): calibrated frame; extracted spectrum with terrestrial transmittance model superimposed (in red); and residual spectrum (top to bottom panel). The green line represents the  $\pm 1\text{-}\sigma$  noise envelope.

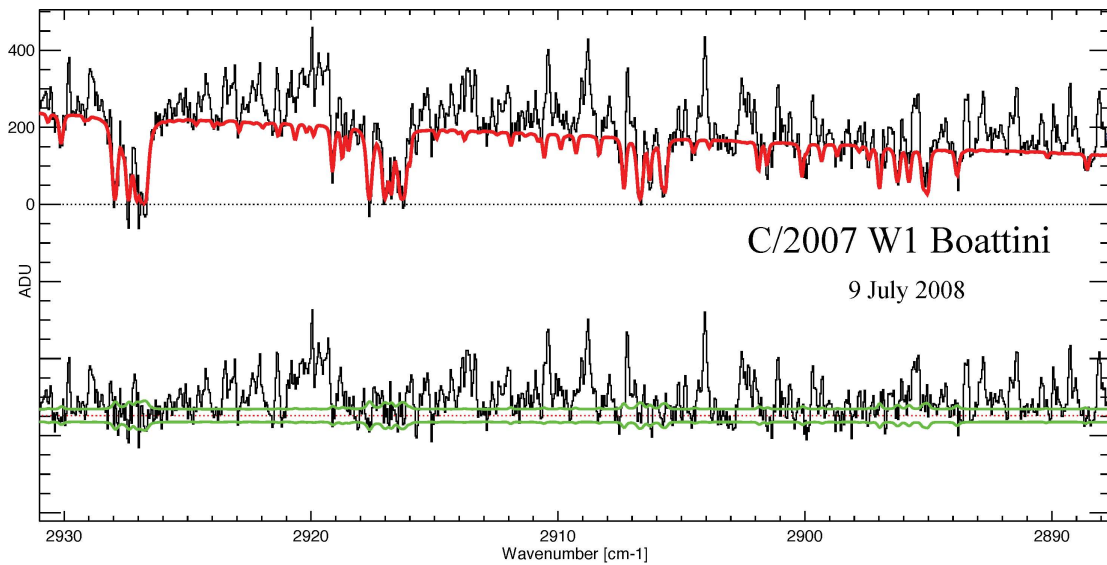
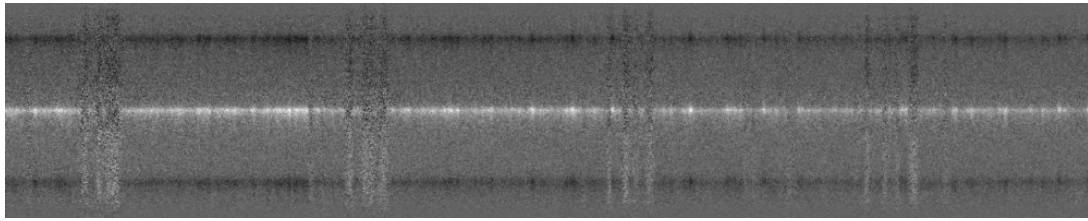


**Figure 6.10.** C/2007 W1 (Boattini): calibrated frame; extracted spectrum with terrestrial transmittance model superimposed (in red); and residual spectrum (top to bottom panel). The green line represents the  $\pm 1\text{-}\sigma$  noise envelope.

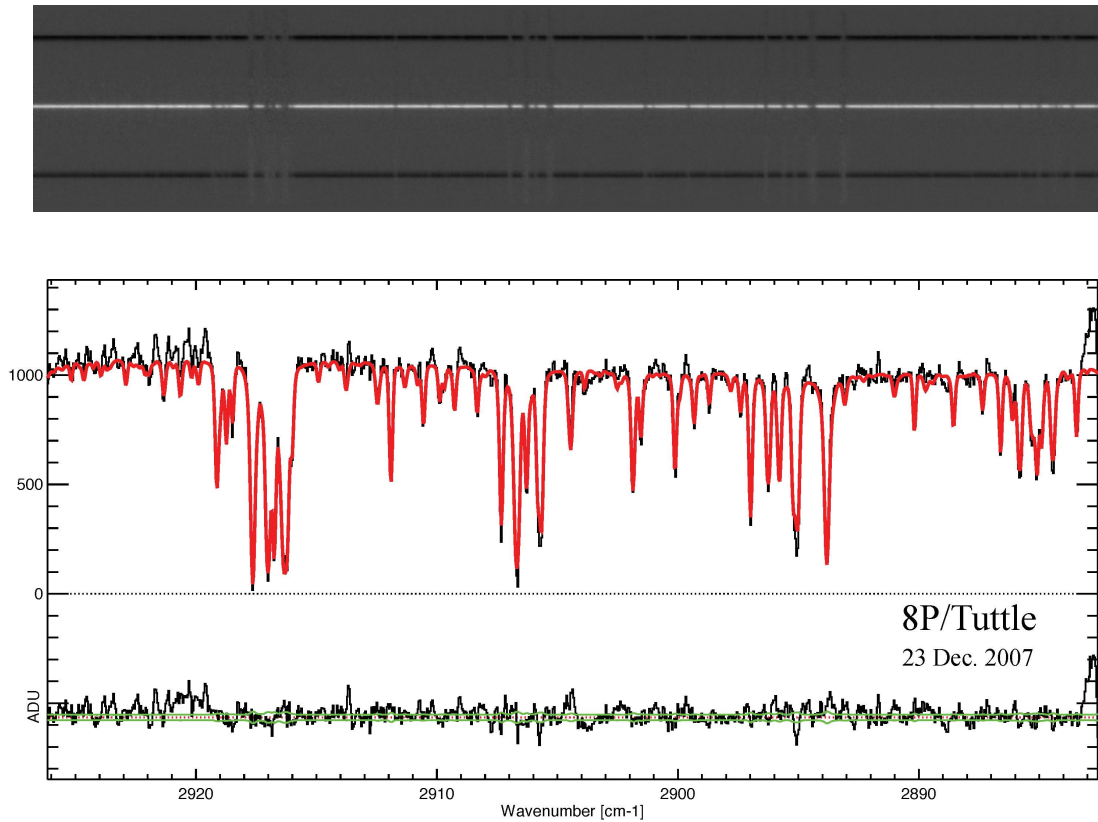


**Figure 6.11.** 8P/Tuttle: calibrated frame; extracted spectrum with terrestrial transmittance model superimposed (in red); and residual spectrum (top to bottom panel). The green line represents the  $\pm 1\text{-}\sigma$  noise envelope.

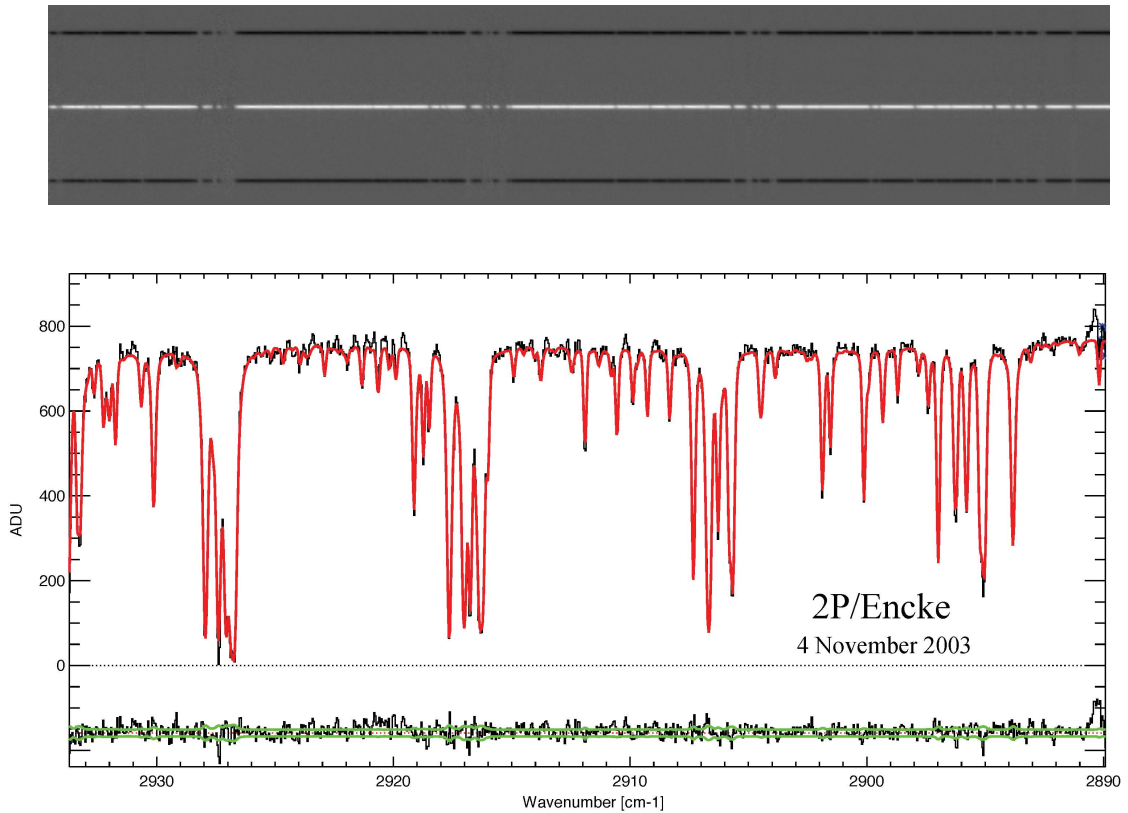


**Figure 6.12.** 2P/Encke: calibrated frame; extracted spectrum with terrestrial transmittance model superimposed (in red); and residual spectrum (top to bottom panel). The green line represents the  $\pm 1\text{-}\sigma$  noise envelope.

*Rotational Temperatures, Mixing Ratios and Production Rates*

The fluorescence model of the  $C_2H_6$   $v_5$  band was applied to the residual cometary spectra – the model is superimposed on the spectra in Figures 6.13-6.20. Rotational temperatures were derived for comets 17P/Holmes, C/2000 WM<sub>1</sub> (LINEAR), C/2004 Q2 Machholz, C/2001 A2 (LINEAR) and C/2007 N3 (Lulin), and were assumed for C/2007 W1 (Boattini), 8P/Tuttle and 2P/Encke (as discussed later). The excitation analysis for  $C_2H_6$  is shown on Figures 6.21-6.28, which present the spread in production rates extracted from each sampled line at the optimal value of  $T_{rot}$ .

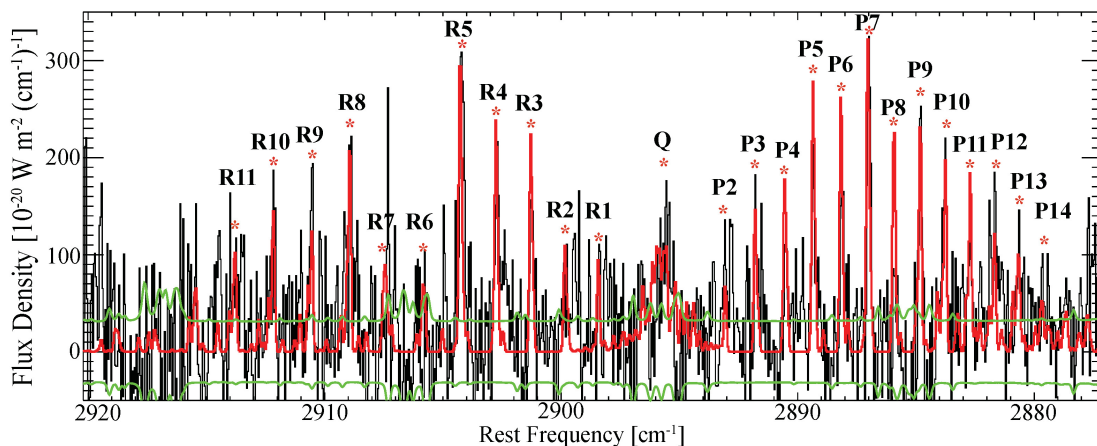


**Figure 6.13.** 17P/Holmes residual spectrum with  $C_2H_6$   $v_5$  synthetic model superimposed in red. The green line represents the  $\pm 1-\sigma$  noise envelope.

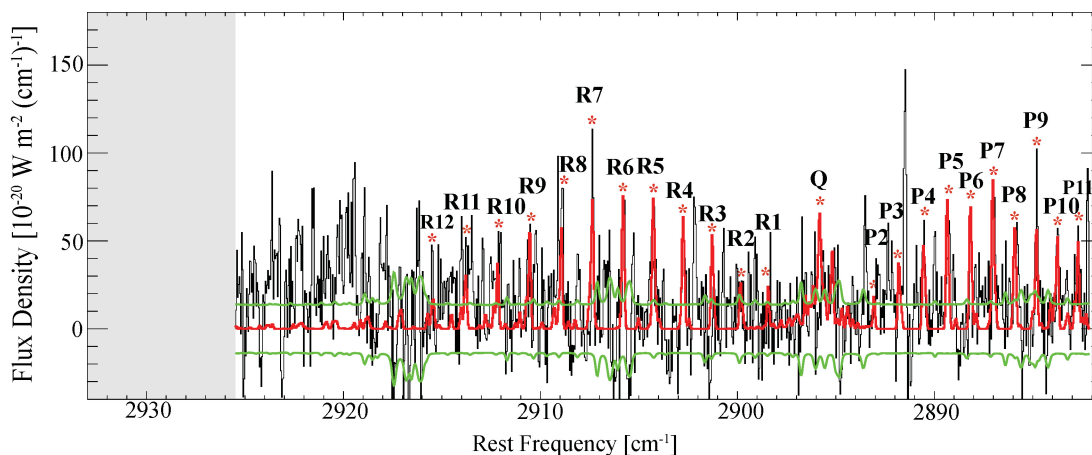


**Figure 6.14.** C/2000 WM<sub>1</sub> (LINEAR) residual spectrum with  $C_2H_6$   $v_5$  synthetic model superimposed in red. The green line represents the  $\pm 1-\sigma$  noise envelope.

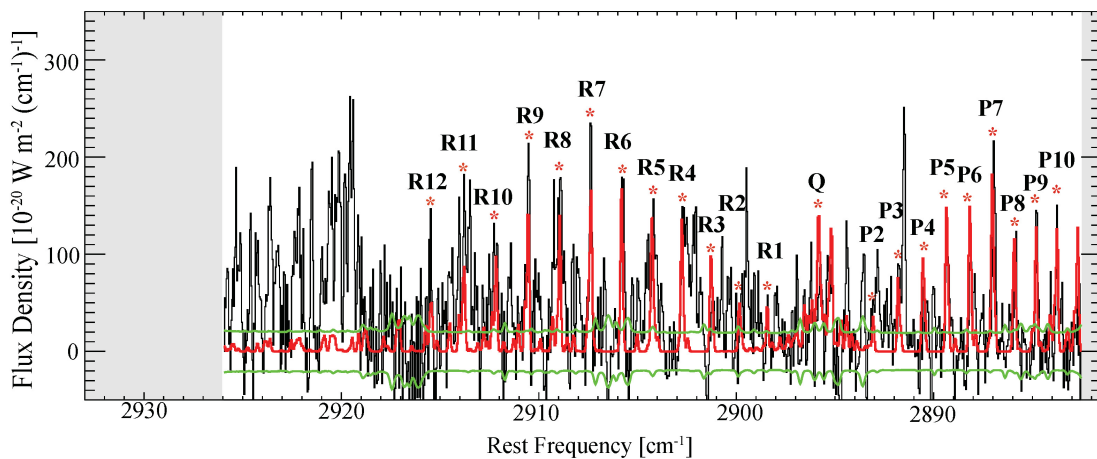


**Figure 6.15.** C/2004 Q2 (Machholz) residual spectrum with C<sub>2</sub>H<sub>6</sub> v<sub>5</sub> synthetic model superimposed in red. The green line represents the  $\pm 1\text{-}\sigma$  noise envelope.

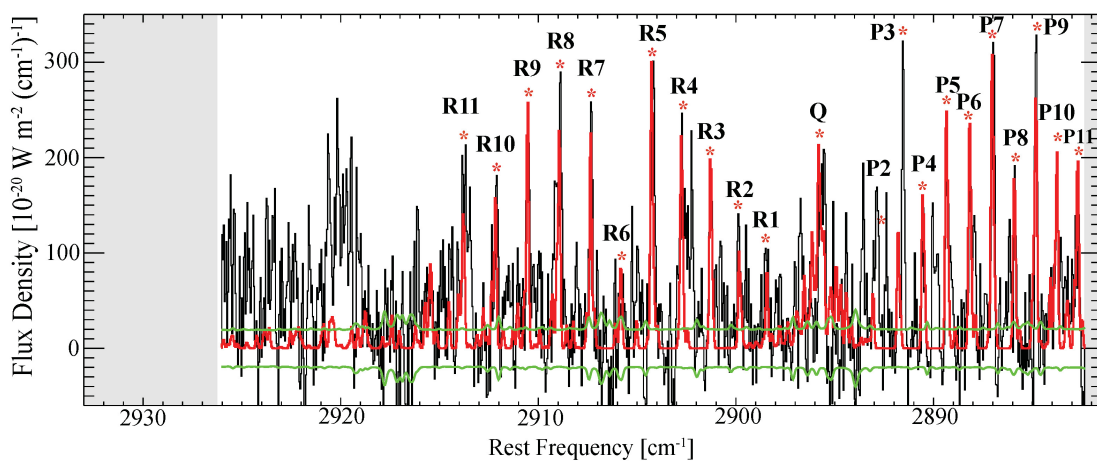


**Figure 6.16.** C/2001 A2 (LINEAR) residual spectrum with C<sub>2</sub>H<sub>6</sub> v<sub>5</sub> synthetic model superimposed in red. The green line represents the  $\pm 1\text{-}\sigma$  noise envelope.



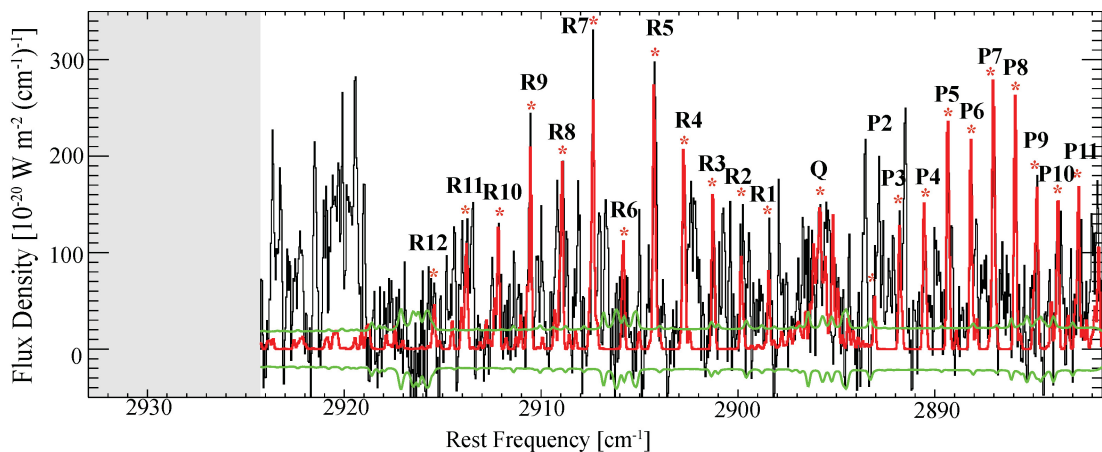


**Figure 6.17.** C/2007 N3 (Lulin) residual spectrum with  $C_2H_6$   $v_5$  synthetic model superimposed in red. The green line represents the  $\pm 1\text{-}\sigma$  noise envelope.

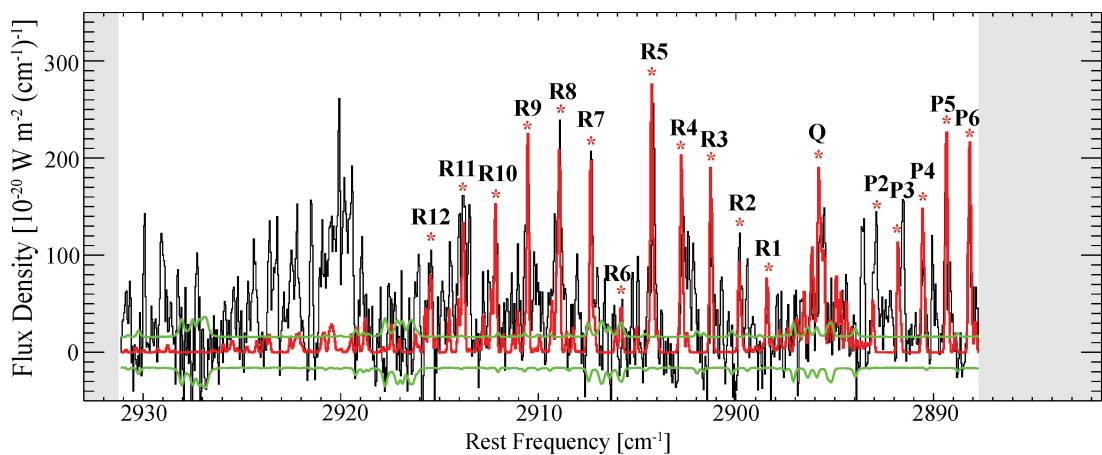


**Figure 6.18.** C/2007 W1 (Boattini) residual spectrum with  $C_2H_6$   $v_5$  synthetic model superimposed in red. The green line represents the  $\pm 1\text{-}\sigma$  noise envelope.

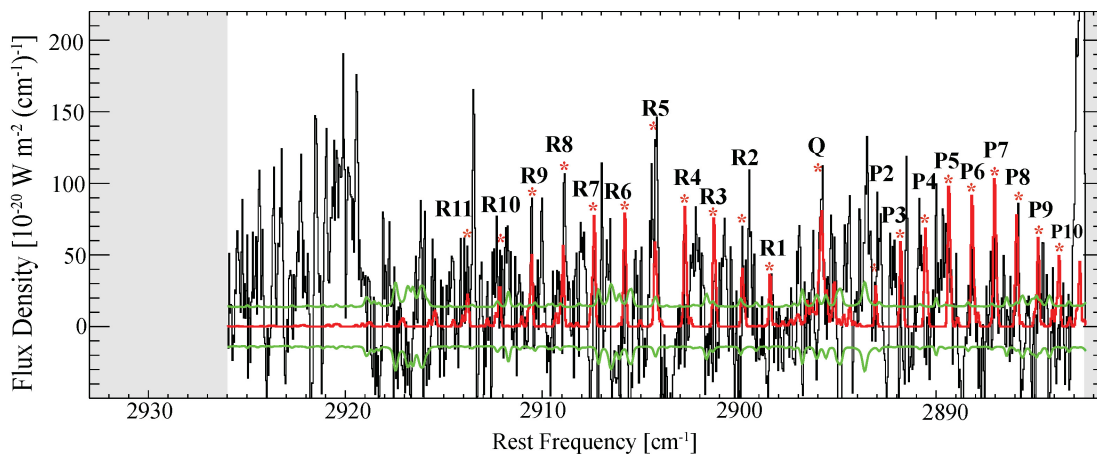


**Figure 6.19.** 8P/Tuttle residual spectrum with  $\text{C}_2\text{H}_6$   $\nu_5$  synthetic model superimposed in red. The green line represents the  $\pm 1\text{-}\sigma$  noise envelope.

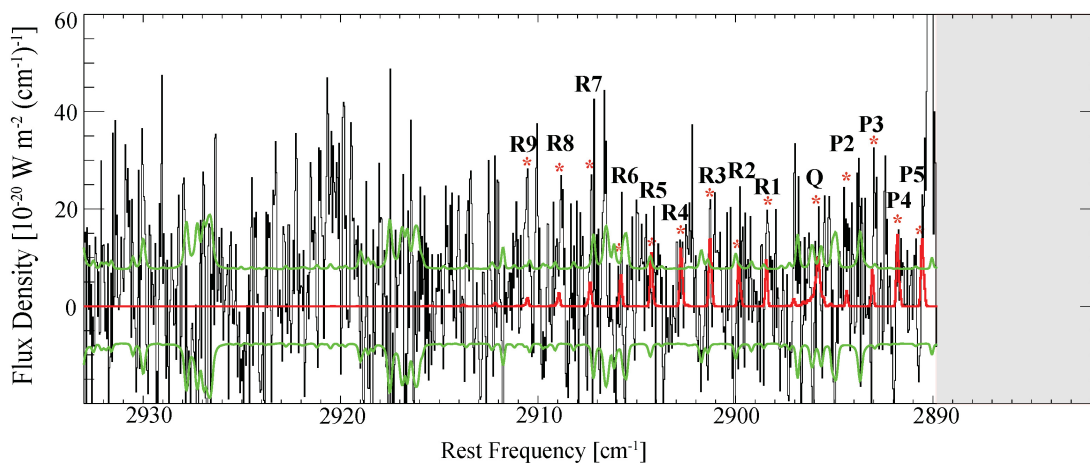


**Figure 6.20.** 2P/Encke residual spectrum with  $\text{C}_2\text{H}_6$   $\nu_5$  synthetic model superimposed in red. The green line represents the  $\pm 1\text{-}\sigma$  noise envelope.

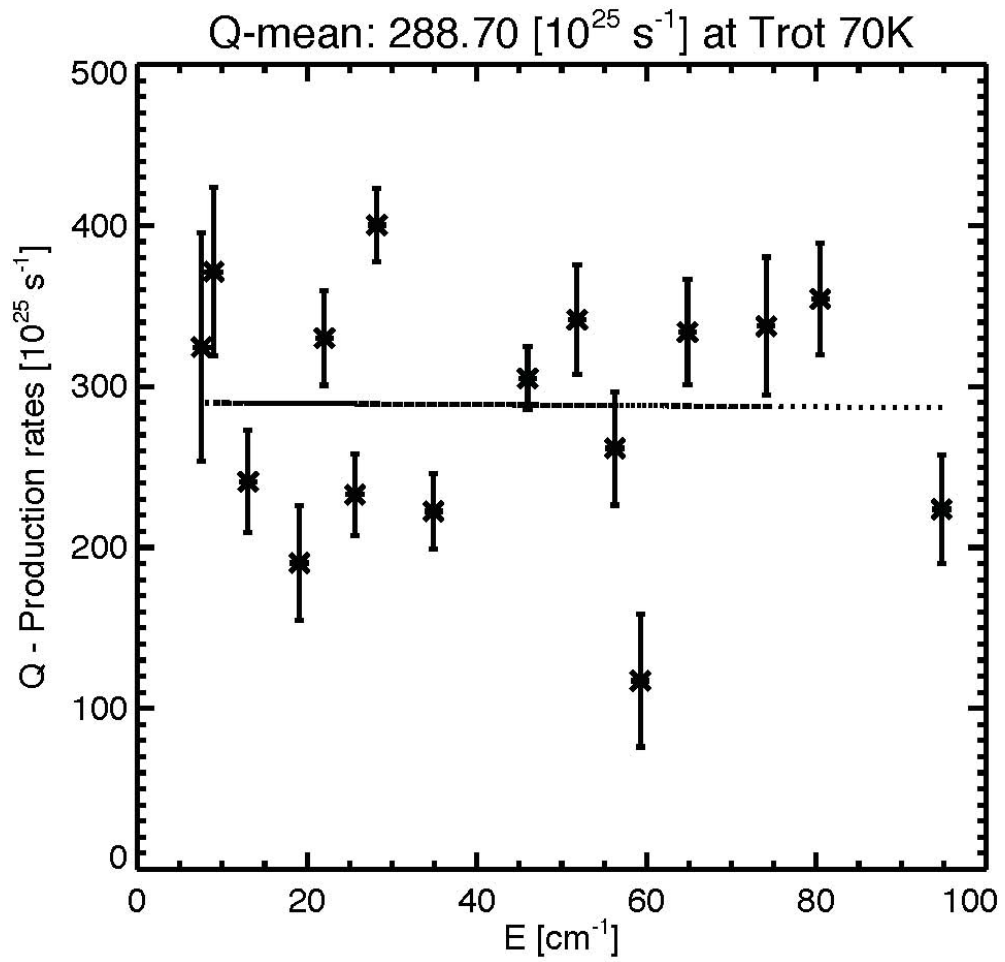


**Figure 6.21.** Spread in production rates from individual lines vs. rotational energy at the optimal  $T_{\text{rot}} = 70^{-10}_{+11}$  K for 17P/Holmes.

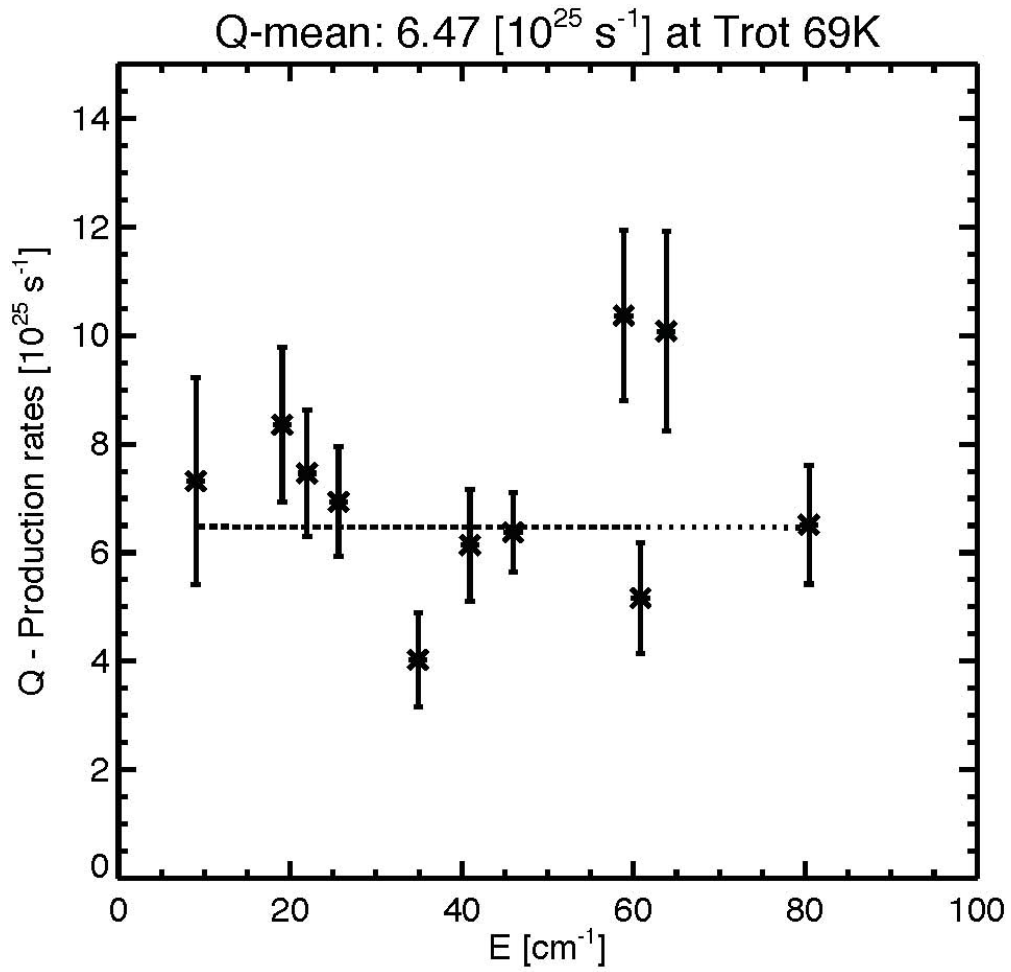


**Figure 6.22.** Spread in production rates from individual lines vs. rotational energy at the optimal  $T_{\text{rot}} = 69^{-13}/_{+14}$  K for C/2000 WM<sub>1</sub> (LINEAR).

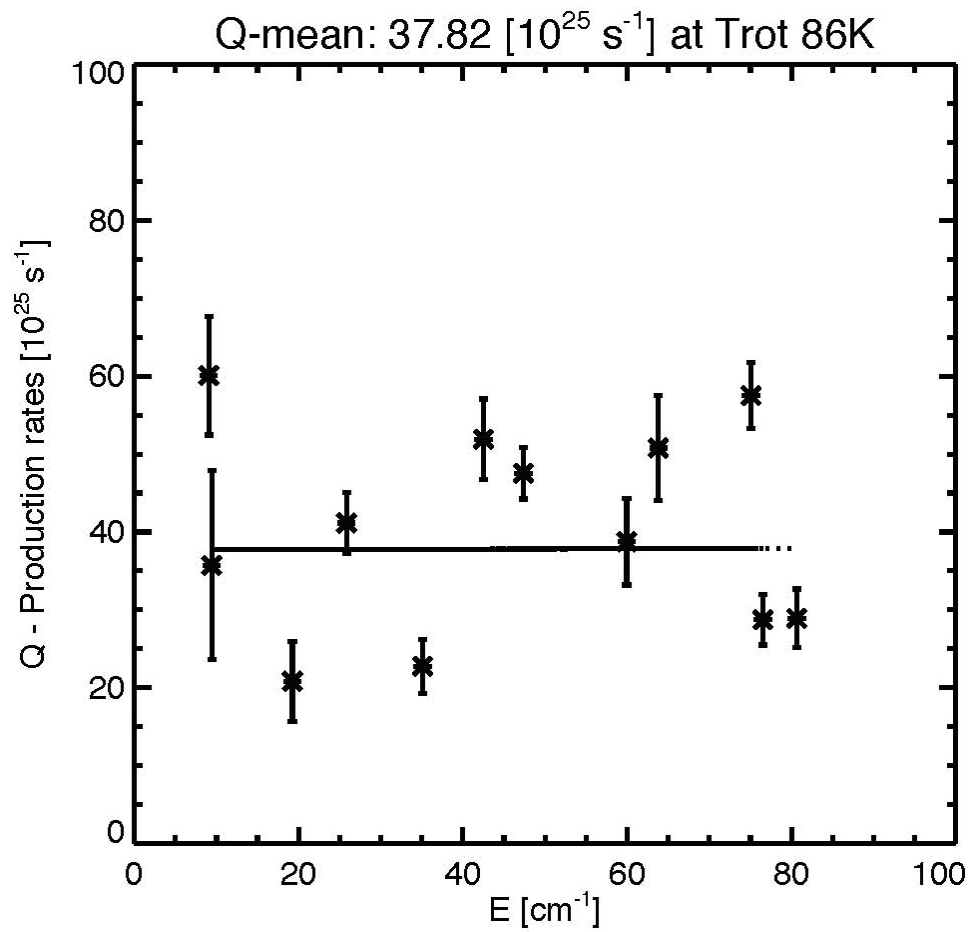


**Figure 6.23.** Spread in production rates from individual lines vs. rotational energy at the optimal  $T_{\text{rot}} = 86^{-17}/_{+18} \text{ K}$  for C/2004 Q2 (Machholz).

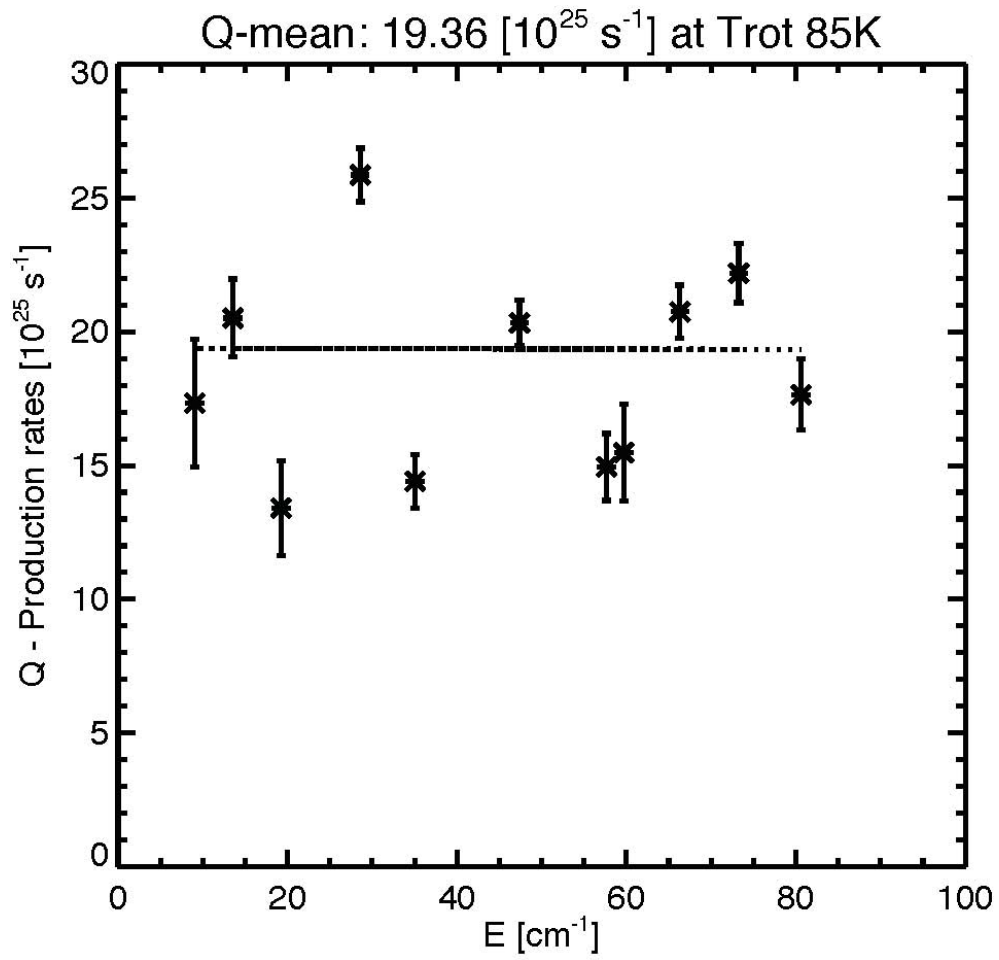


**Figure 6.24.** Spread in production rates from individual lines vs. rotational energy at the optimal  $T_{\text{rot}} = 85^{-14}/_{+13}$  K for C/2001 A2 (LINEAR).

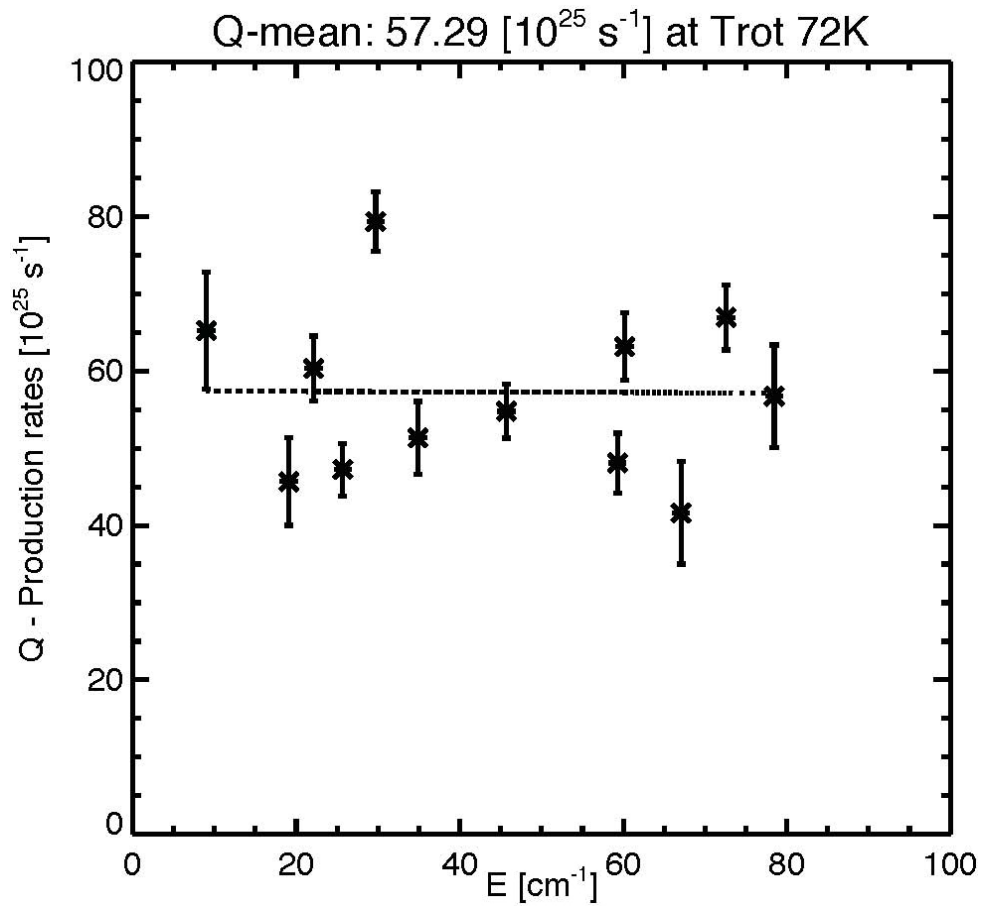


**Figure 6.25.** Spread in production rates from individual lines vs. rotational energy at the optimal  $T_{\text{rot}} = 72^{-11}/_{+12} \text{ K}$  for C/2007 N3 (Lulin).

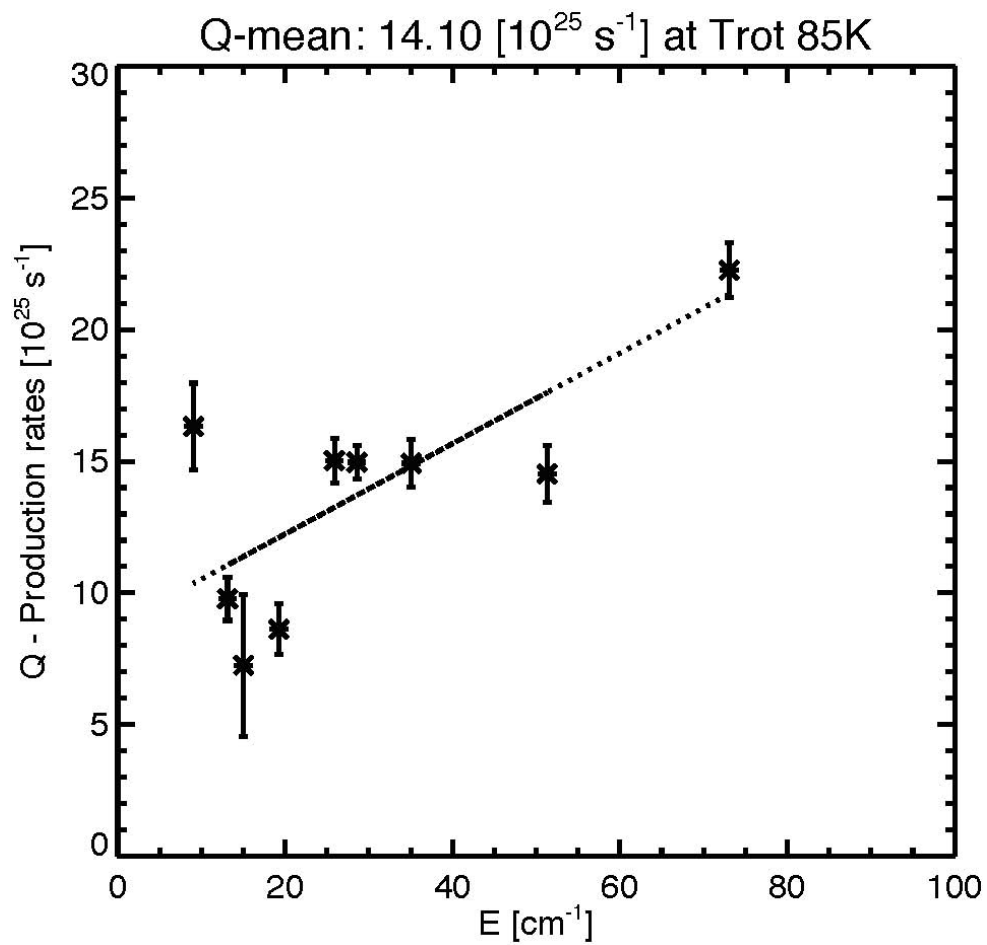


**Figure 6.26.** Spread in production rates from individual lines vs. rotational energy at the assumed  $T_{\text{rot}} = 85 \text{ K}$  for C/2007 W1 (Boattini).



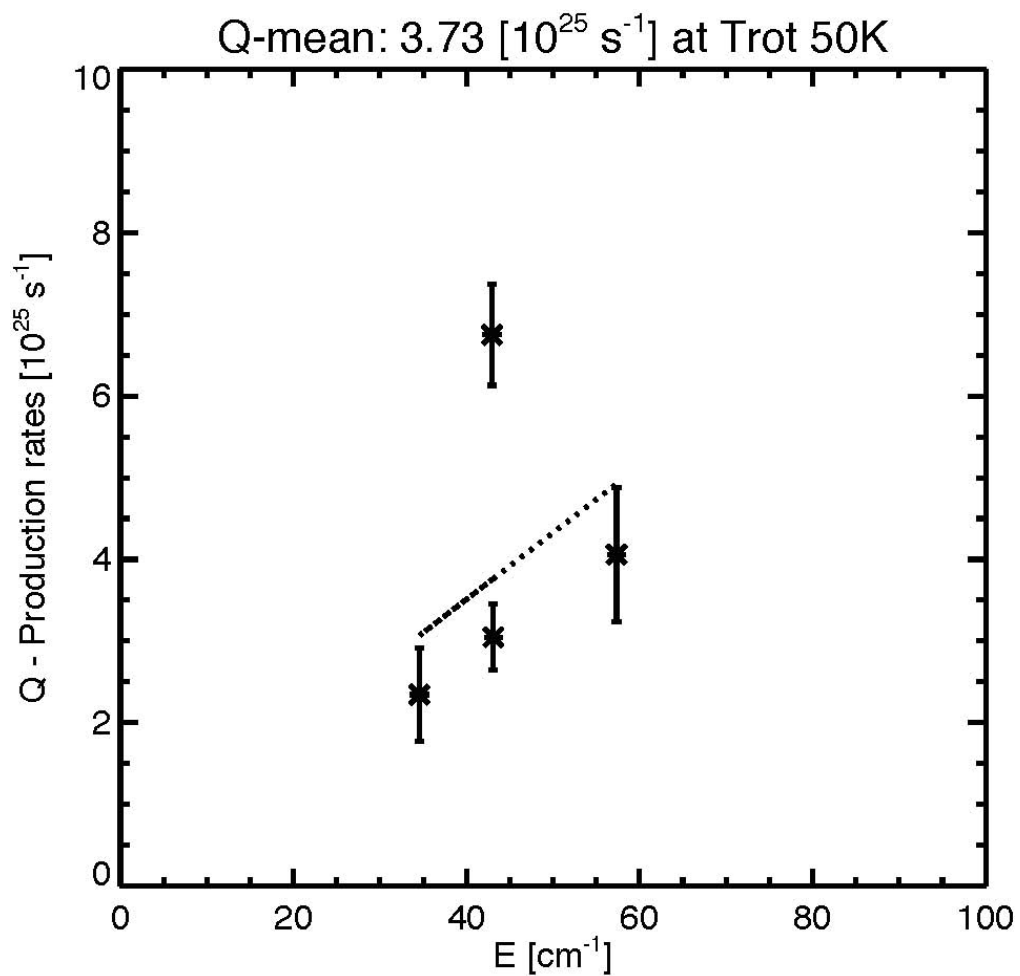


**Figure 6.27.** Spread in production rates from individual lines vs. rotational energy at the assumed  $T_{\text{rot}} = 50 \text{ K}$  for 8P/Tuttle.

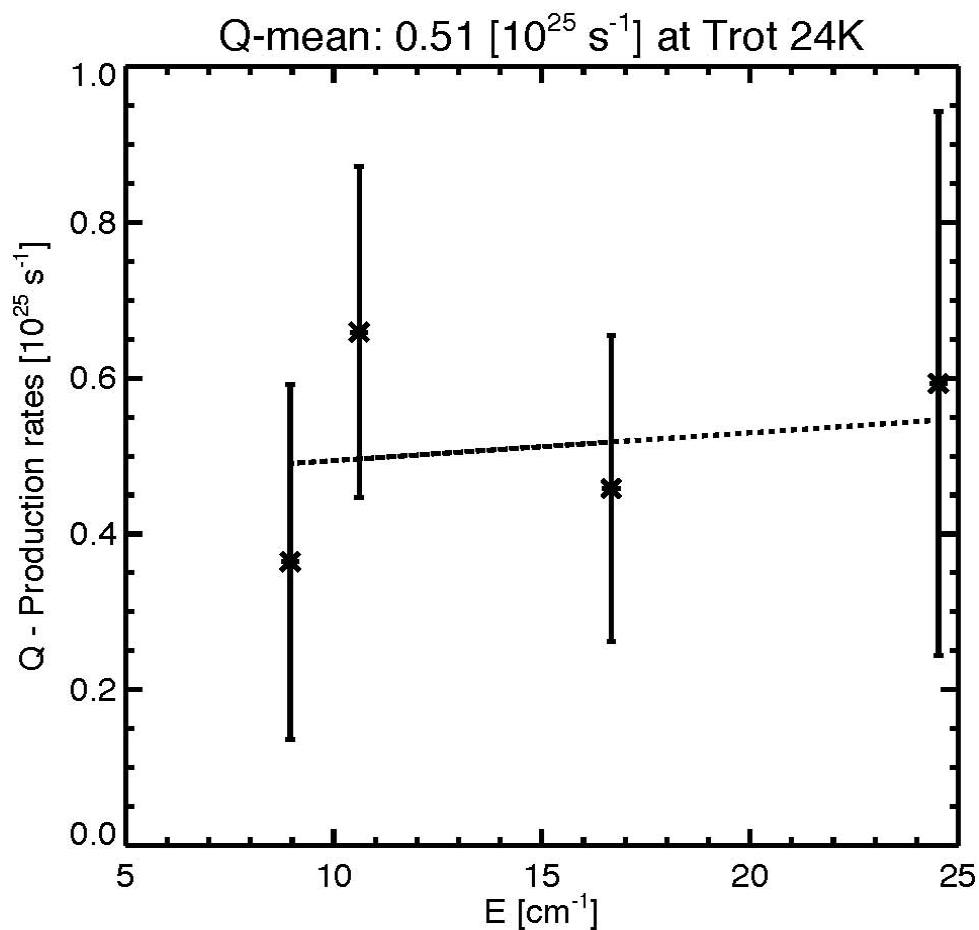


**Figure 6.28.** Spread in production rates from individual lines vs. rotational energy at the assumed  $T_{\text{rot}} = 24 \text{ K}$  for 2P/Encke.

A list of spectral lines with designations and g-factors at  $T_{\text{rot}} = 70 \text{ K}$  (chosen as a representative average temperature), as measured in comet 17P/Holmes, is presented in Table 6.4. This excludes obvious blends. The mean rest frequencies of the used lines are listed, since there are hundreds of lines in the  $\text{C}_2\text{H}_6 \nu_5$  model, and each listed line combines many individual lines of different intensities. Production

rates (including uncertainty) from sampled lines in all analyzed comets are presented in Appendix I.

**Table 6.4.** Designations, mean rest frequencies and combined g-factors of  $C_2H_6$   $\nu_5$  lines at  $T_{rot} = 70$  K (there are several hundred lines in this model, and each listed line combines several individual lines). This excludes several blends, and is based on the analysis of comet Holmes.

Designation	Transitions	Frequency [ $cm^{-1}$ ]	g-factor [photons molecule $^{-1}$ s $^{-1}$ ]
R9	$J'' = 9 \rightarrow J' = 10$	2910.6	6.64E-06
R8	$J'' = 8 \rightarrow J' = 9$	2908.9	4.67E-06
R5	$J'' = 5 \rightarrow J' = 6$	2904.2	8.84E-06
R4	$J'' = 4 \rightarrow J' = 5$	2902.7	6.72E-06
R3	$J'' = 3 \rightarrow J' = 4$	2901.3	6.11E-06
R1	$J'' = 1 \rightarrow J' = 2$	2898.4	2.10E-06
Q	$\Delta J = 0$	2895.5	2.07E-05
P3	$J'' = 3 \rightarrow J' = 2$	2891.8	3.12E-06

P4	$J'' = 4 \rightarrow J' = 3$	2890.5	5.28E-06
P5	$J'' = 5 \rightarrow J' = 4$	2889.3	7.59E-06
P6	$J'' = 6 \rightarrow J' = 5$	2888.2	7.23E-06
P7	$J'' = 7 \rightarrow J' = 6$	2887.0	9.33E-06
P8	$J'' = 8 \rightarrow J' = 7$	2885.9	8.22E-06
P9	$J'' = 9 \rightarrow J' = 8$	2884.8	7.38E-06
P10	$J'' = 10 \rightarrow J' = 9$	2883.8	5.69E-06
P11	$J'' = 11 \rightarrow J' = 10$	2882.7	5.49E-06

The rotational temperatures derived for  $C_2H_6$   $v_5$ , and the temperatures previously derived for HCN and  $H_2O$  (or CO and  $H_2CO$ , if available) are presented in Table 6.5 and Figure 6.29. A rotational temperature could not be derived for 2P/Encke, 8P/Tuttle and Boattini. In the case of Encke, the mixing ratio for  $C_2H_6$   $v_5$  was very low and the unblended spectral lines were insufficient for the derivation of a rotational temperature for this molecule. Thus,  $T_{rot} = 24$  K (from  $H_2O$ ) was assumed for  $C_2H_6$ . 8P/Tuttle also has a very low  $C_2H_6$  mixing ratio, and Boattini is very enriched in  $CH_3OH$  (Villanueva et al., personal communication), which blends with the  $C_2H_6$   $v_5$  features. For 8P/Tuttle  $T_{rot} = 50$  K was assumed, which is consistent with  $T_{rot}$  derived from  $H_2O$  in the same instrument setting (Bonev et al. 2008). For other

comets there is excellent agreement among rotational temperatures derived from C<sub>2</sub>H<sub>6</sub> v<sub>5</sub> and other species (when available: results for the comets Lulin and Boattini have not been published yet – T<sub>rot</sub> for Boattini was assumed), except for HCN in comet A2, which disagrees with T<sub>rot</sub> from H<sub>2</sub>O, C<sub>2</sub>H<sub>6</sub>, H<sub>2</sub>CO and CO.

**Table 6.5.** Comparison of rotational temperatures derived from C<sub>2</sub>H<sub>6</sub> v<sub>5</sub> (this work), H<sub>2</sub>O, HCN and CO (temperatures for 2P/Encke, 8P/Tuttle and Boattini are assumed).

	<b>T<sub>rot</sub> C<sub>2</sub>H<sub>6</sub> v<sub>5</sub><sup>I</sup></b>	<b>T<sub>rot</sub> H<sub>2</sub>O</b>	<b>T<sub>rot</sub> HCN</b>	<b>T<sub>rot</sub> C<sub>2</sub>H<sub>2</sub></b>	<b>T<sub>rot</sub> H<sub>2</sub>CO</b>
	<b>[K]</b>	<b>[K]</b>	<b>[K]</b>	<b>[K]</b>	<b>[K]</b>
17P/Holmes (Oct. 29. 2008)	<b>70<sup>-10/+11</sup></b>	73 <sup>-7/+9</sup> <sup>II</sup>	65 <sup>-2/+2</sup> <sup>II</sup>	63 <sup>-5/+8</sup> <sup>II</sup>	-
	Derived from R9-R8, R5-R3, R1, Q-branch, P3-P11				
C/2000 WM <sub>1</sub> (Nov. 24. 2001)	<b>69<sup>-13/+14</sup></b>	69 <sup>-3/+3</sup> <sup>III</sup>	70 <sup>-7/+9</sup> <sup>III</sup>	-	-
	Derived from: R6, R4, Q-branch, P3-P10				
Q2 Machholz (Nov. 28. 2004)	<b>86<sup>-17/+18</sup></b>	86 <sup>-4/+4</sup> <sup>IV</sup>	76 <sup>-9/+9</sup> <sup>IV</sup>	-	-
	Derived from R9, R6, R1, Q-branch, P3-P10				
A2 (LINEAR) (Jul. 9. 2001)	<b>85<sup>-14/+13</sup></b>	98 <sup>-5/+6</sup> <sup>V</sup>	56 <sup>-6/+6</sup> <sup>V</sup>	-	104 <sup>-18/+20</sup> <sup>V</sup>
	Derived from R9, R5, R3, Q-branch, P3-P4, P6-P10				

Lulin	<b>72</b>	<sup>-11</sup> / <sub>+12</sub>	-	-	-	-
(Jan. 30. 2009)	Derived from R9, R5-R4, Q-branch, P3-P10					
Boattini	<b>85</b>		-	-	-	-
(Jul. 9. 2008)	<b>(assumed)</b>					
Derived from R9, R5, R3, R1, Q-branch, P3-P6						
8P/Tuttle	<b>50</b>	50 <sup>-10</sup> / <sub>+10</sub> <sup>VI</sup>	51 <sup>-10</sup> / <sub>+10</sub> <sup>VI</sup>	-	-	-
(Dec. 23. 2007)	<b>(assumed)</b>					
Derived from P6-P8						
2P/Encke <sup>I</sup>	<b>24</b>	24 <sup>-6</sup> / <sub>+13</sub> <sup>VI</sup>	28 <sup>-7</sup> / <sub>+13</sub>	-	-	-
(Nov. 4. 2003)	<b>(assumed)</b>					
Derived from R3, Q-branch, P3-P4						

<sup>I</sup>This work.

<sup>II</sup>Dello Russo et al. 2008 (data from 27 Oct. 2008): this work also presents  $T_{\text{rot}} = 79 \text{ } ^4_{+4} \text{ K}$  from the author's model of  $\text{C}_2\text{H}_6 \nu_5$ , and a g-factor for the qP(3) line at 79 K.  $T_{\text{rot}}(\text{C}_2\text{H}_6 \nu_5)$  presented in this dissertation is based on data from 29 Oct. 2008.

<sup>III</sup>Radeva et al. 2010.

<sup>IV</sup>Bonev et al. 2009.

<sup>V</sup>Magee-Sauer et al. 2008: this work also presents  $T_{\text{rot}} = 102 \text{ } ^{-12}_{+13} \text{ K}$  from the very bright lines of  $\text{C}_2\text{H}_6 \nu_7$ . Usually it is very difficult to extract a reliable rotational temperature from this band of ethane. This work also discusses the low rotational temperature derived for HCN, and proposes radiative cooling of its rotational levels, or a different distribution of HCN in the aperture, as possible explanations for this discrepancy.

<sup>VI</sup>Bonev et al. 2008.

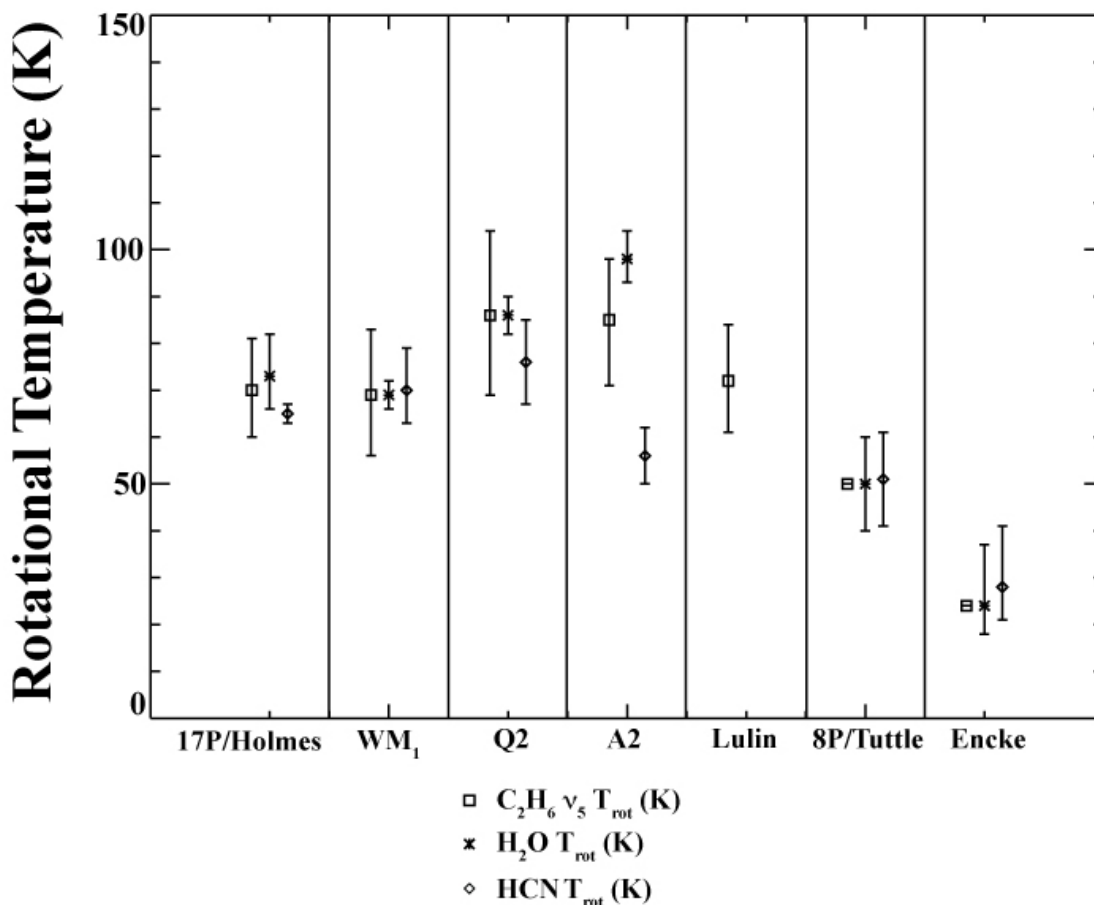


**Figure 6.29.** Comparison of rotational temperatures of  $C_2H_6 \nu_5$ ,  $H_2O$  and  $HCN$  among comets.

This comparison serves as a test of the physical processes taking place in the coma, such as the distance from the nucleus at which the given species is measured. Measured temperatures are expected to decrease adiabatically away from the nucleus, (due to the adiabatic expansion of the gas). However, in comets with high gas production rates ( $10^{29}$ - $10^{31}$  molecules  $s^{-1}$ ), at distances farther than 100 km from the nucleus, temperatures would then increase due to collisions with the energetic OH

and fast-H atoms, which are products of the photodissociation of H<sub>2</sub>O molecules (Combi et al. 2004). The heating efficiency depends on the gas production rate (and thus, gas density), and the heliocentric distance of the comet, due to the dependence of photodissociation rates on solar radiation density (Combi et al. 2004). Also, if the rotational temperature for a given species is radically different from that for other species measured simultaneously, the explanation could be in radiative cooling controlling its rotational populations, or a different distribution in the aperture, as suggested for the discrepant in rotational temperature HCN in A2 LINEAR by Magee-Sauer et al. (2009). Furthermore, HCN and H<sub>2</sub>O are polar molecules, while C<sub>2</sub>H<sub>6</sub> is non-polar (with no allowed pure rotational transitions), but their rotational temperatures agree. This suggests that collisional excitation and de-excitation, rather than radiative processes, are controlling rotational level populations (as discussed in Chapters 2 and 5). This validates the assumption of collisional thermalization of the rotational levels.

Mixing ratios derived from C<sub>2</sub>H<sub>6</sub>  $\nu_5$  (this work) and the C<sub>2</sub>H<sub>6</sub>  $\nu_7$  band are compared in Table 6.6 and Figure 6.30 (production rates from sampled lines in all analyzed comets are presented in Appendix I). The confidence limits for each mixing ratio account for the largest among the stochastic, standard uncertainties, and uncertainties in  $T_{\text{rot}}$ . In most cases, standard uncertainties dominate. Agreement within 1- $\sigma$  is found between the mixing ratios for C<sub>2</sub>H<sub>6</sub>  $\nu_5$  and  $\nu_7$  for all comets except for A2 LINEAR (2- $\sigma$ ) (A2 LINEAR is also the comet with the biggest discrepancies in  $T_{\text{rot}}$ ). The mixing ratio of CH<sub>3</sub>OH is also presented Table 6.6, since methanol enrichment can complicate the analysis of the C<sub>2</sub>H<sub>6</sub>  $\nu_5$  band due to blends.



**Table 6.6.** Comparison of mixing ratios (%) derived from C<sub>2</sub>H<sub>6</sub> v<sub>5</sub> (this work) and C<sub>2</sub>H<sub>6</sub> v<sub>7</sub> (mixing ratios for CH<sub>3</sub>OH are also provided).

	MR C <sub>2</sub> H <sub>6</sub> v <sub>5</sub> <sup>I</sup>	MR C <sub>2</sub> H <sub>6</sub> v <sub>7</sub>	MR CH <sub>3</sub> OH
17P/Holmes	1.61 ± 0.20	1.78 ± 0.26 <sup>II</sup>	2.25 ± 0.43 <sup>II</sup>
C/2000 WM <sub>1</sub>	0.42 ± 0.04	0.40 ± 0.04 <sup>III</sup>	1.08 ± 0.13 <sup>III</sup>
Q2 Machholz	0.47 ± 0.06	0.56 ± 0.03 <sup>IV</sup>	2.03 ± 0.11 <sup>IV</sup>
A2 (LINEAR) <sup>V</sup>	1.04 ± 0.13	1.7 ± 0.2 <sup>V</sup>	3.9 ± 0.4 <sup>V</sup>
Boattini	1.68 ± 0.24	-	-
8P/Tuttle	0.25 ± 0.07	0.24 ± 0.03 <sup>VI</sup>	2.18 ± 0.07 <sup>VI</sup>
Encke	0.19 ± 0.04	0.29 ± 0.11 <sup>I</sup>	1.97 ± 0.76 <sup>I</sup>

<sup>I</sup>This work. Lulin is excluded from this table, since Q(H<sub>2</sub>O) is unavailable.

<sup>II</sup>Dello Russo et al. 2008 (data from 27 Oct. 2009, combining v<sub>5</sub> from the author's model and v<sub>7</sub>), compared with our data from 29 Oct. 2009 (our mixing ratio for C<sub>2</sub>H<sub>6</sub> v<sub>5</sub> is measured relative to Q(H<sub>2</sub>O) derived by the NASA GSFC team (personal communication) from the same data for T<sub>rot</sub> = 60 K).

<sup>III</sup>Radeva et al. 2010.

<sup>IV</sup>Bonev et al. 2009.

<sup>V</sup>Magee-Sauer et al. 2008.

<sup>VI</sup>Bonev et al. 2008.

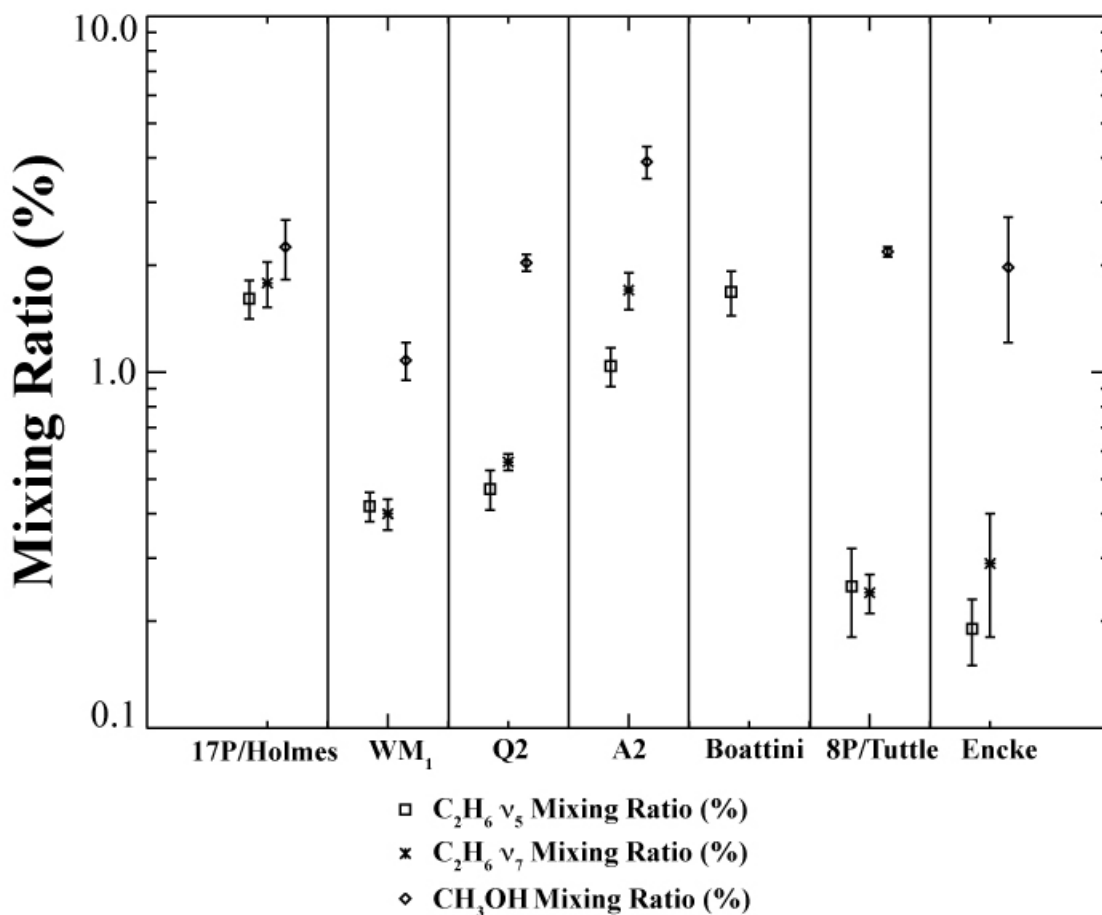


**Figure 6.30.** Comparison of mixing ratios of  $C_2H_6 v_5$  and  $C_2H_6 v_7$  among comets ( $CH_3OH$  mixing ratios are also included).

The production rates for  $C_2H_6 v_5$  and  $C_2H_6 v_7$  are presented in Table 6.7. These production rates are measured in two different instrument settings, and at different times. If the cometary nucleus is heterogeneous, the activation of different vents on its surface during rotation would produce variability in the  $v_5$  and  $v_7$  production rates. Mixing ratios, however, are determined relative to the production

rate of H<sub>2</sub>O measured simultaneously in the same respective setting, which eliminates some systematic offsets (due to seeing, flux calibration etc.). Therefore, mixing ratios provide a more reliable comparison than do production rates of species measured at different times.

**Table 6.7.** Comparison of production rates ( $10^{26}$  molecules s<sup>-1</sup>) derived from C<sub>2</sub>H<sub>6</sub> v<sub>5</sub> (this work) and C<sub>2</sub>H<sub>6</sub> v<sub>7</sub>. (References are identical to those for Tables 6.5 and 6.6).

	<b>T<sub>rot</sub> [K] for Q (C<sub>2</sub>H<sub>6</sub> v<sub>5</sub>)</b>	<b>Q (C<sub>2</sub>H<sub>6</sub> v<sub>5</sub>) x 10<sup>26</sup></b>	<b>T<sub>rot</sub> [K] for Q (C<sub>2</sub>H<sub>6</sub> v<sub>7</sub>)</b>	<b>Q (C<sub>2</sub>H<sub>6</sub> v<sub>7</sub>) x 10<sup>26</sup></b>
17P/Holmes	70	44.46 ± 3.62	-	-
C/2000 WM <sub>1</sub>	69	0.98 ± 0.08	70	0.95 ± 0.12
Q2 (Machholz)	86	6.73 ± 0.70	86	8.62 ± 0.35
A2 (LINEAR)	85	3.44 ± 0.29	102	6.3 ± 0.6
Lulin	72	9.17 ± 1.52	-	-
Boattini	85	2.21 ± 0.25	-	-
8P/Tuttle	50	0.59 ± 0.15	60	0.55 ± 0.07
2P/Encke	24	0.08 ± 0.02	24	0.12 ± 0.03

*Blends in the C<sub>2</sub>H<sub>6</sub> v<sub>5</sub> region*

The C<sub>2</sub>H<sub>6</sub> v<sub>5</sub> region includes, in addition to C<sub>2</sub>H<sub>6</sub> v<sub>5</sub> spectral features, spectral features of CH<sub>3</sub>OH, H<sub>2</sub>CO, and OH, and blends of these species. This complicates the derivation of a reliable rotational temperature of C<sub>2</sub>H<sub>6</sub> v<sub>5</sub>, and could lead to overestimates of the C<sub>2</sub>H<sub>6</sub> v<sub>5</sub> production rate. The R7 line at 2907.3 cm<sup>-1</sup> (blend with H<sub>2</sub>CO) has been excluded from the analysis for all comets (see Figure 6.31). Lines, which provided a markedly overestimated production rate (compared to the weighted mean production rate), and were suspected blends, were also excluded. Deviations of individual lines on the rotational temperature diagrams can be explained by blends with species, for which models are not available.

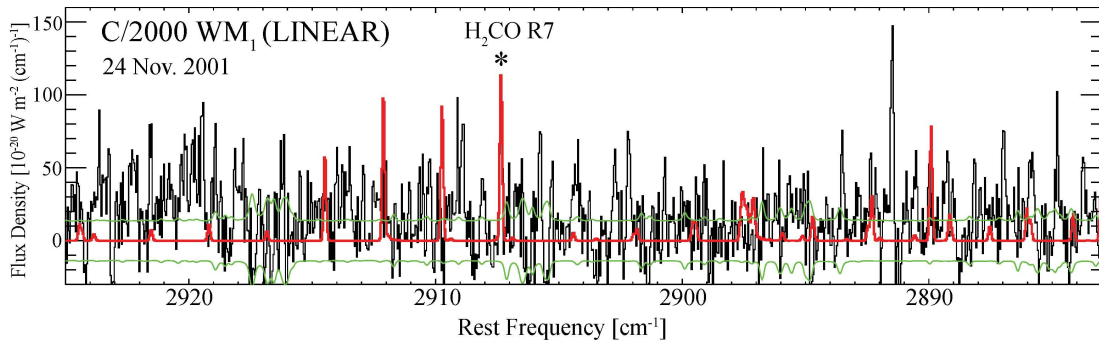


**Figure 6.31.** Model of H<sub>2</sub>CO (in red) in the C<sub>2</sub>H<sub>6</sub> v<sub>5</sub> region. The R7 line of C<sub>2</sub>H<sub>6</sub> v<sub>5</sub> at 2907.3 cm<sup>-1</sup> (blend with H<sub>2</sub>CO) was excluded from the analysis for all comets.

### Overall Organic Composition

The application of the newly developed  $C_2H_6$   $\nu_5$  model to comets 17P/Holmes, C/2000 WM<sub>1</sub>, Q2 Machholz, 8P/Tuttle and 2P/Encke, confirmed the mixing ratios of  $C_2H_6$   $\nu_7$  measured previously, and 2- $\sigma$  agreement was found between the mixing ratios of  $C_2H_6$   $\nu_5$  and  $C_2H_6$   $\nu_7$  measured for comet A2 (LINEAR). Weighted mean values from  $C_2H_6$   $\nu_5$  and  $C_2H_6$   $\nu_7$  mixing ratios are presented in Table 6.8, and are used in a comparison of the overall organic composition of a sample of comets (Table 6.9). The organic compositions of C/2000 WM<sub>1</sub> and 2P/Encke in particular, are visualized in Figure 6.32, and are compared to the compositions of the organics-enriched end-member A2 (LINEAR), and the organics-depleted end-member S4 (LINEAR).

**Table 6.8.** Weighted-mean mixing ratios [%] of  $C_2H_6$ .

Comet	MR	$\sigma$ (MR)	MR	$\sigma$ (MR)	MR	$\sigma$ (MR)
	$C_2H_6$ $\nu_5$	$C_2H_6$ $\nu_5$	$C_2H_6$ $\nu_7$	$C_2H_6$ $\nu_7$	$C_2H_6$	$C_2H_6$
<b>17P/Holmes</b>	1.61	0.2	1.78	0.26	1.67	0.16
<b>C/2000 WM<sub>1</sub></b>	0.42	0.04	0.47	0.03	0.45	0.02
<b>Q2 Machholz</b>	0.47	0.06	0.56	0.03	0.54	0.03
<b>A2 (LINEAR)</b>	1.04	0.13	1.7	0.2	1.24	0.11
<b>Boattini</b>	1.68	0.24	-	-	1.68	0.24
<b>8P/Tuttle</b>	0.25	0.07	0.24	0.03	0.24	0.03
<b>2P/Encke</b>	0.19	0.04	0.29	0.11	0.20	0.04

**Table 6.9.** The organic composition of comets analyzed by the team at NASA GSFC (mixing ratios as percentages relative to H<sub>2</sub>O; upper limits are 3- $\sigma$ ).

Mixing Ratio %	C <sub>2</sub> H <sub>6</sub>	C <sub>2</sub> H <sub>2</sub>	HCN	CH <sub>4</sub>	H <sub>2</sub> CO	CH <sub>3</sub> OH	CO
73P/S-W 3-C <sup>I</sup>	0.107 ± 0.011	0.049 ± 0.020	0.242 ± 0.014	<0.25	0.147 ± 0.033	0.149 ± 0.029	0.53 ± 0.13
C/1999 S4 (LINEAR) <sup>II</sup>	0.11 ± 0.02	< 0.12	0.10 ± 0.03	0.18 ± 0.06	-	< 0.15	0.9 ± 0.3
<b>2P/Encke<sup>III</sup></b>	<b>0.20</b> ± <b>0.04</b>	<b>&lt; 0.18</b>	<b>0.11</b> ± <b>0.03</b>	<b>0.12</b> ± <b>0.04</b>	<b>0.20</b> ± <b>0.05</b>	<b>1.97</b> ± <b>0.76</b>	<b>&lt; 1.4</b>
<b>C/2000 WM<sub>1</sub></b> <b>(LINEAR)<sup>IV</sup></b>	<b>0.47</b> ± <b>0.03</b>	<b>&lt; 0.05</b>	<b>0.15</b> ± <b>0.01</b>	<b>0.34</b> ± <b>0.03</b>	<b>0.20</b> ± <b>0.03</b>	<b>1.30</b> ± <b>0.08</b>	<b>0.52</b> ± <b>0.12</b>
Five "organics- normal" Oort cloud comets <sup>II</sup>	0.6	0.2-0.3	0.2-0.3	0.5-1.5	-	2	1.8-17
153P/Ikeya- Zhang <sup>II</sup>	0.62 ± 0.13	0.18 ± 0.05	0.18 ± 0.05	0.51 ± 0.06	0.62 ± 0.18	2.5 ± 0.5	4.7 ± 0.8
8P/Tuttle <sup>V</sup>	0.24	< 0.04	0.07	0.37	< 0.04	2.18	< 0.37

	± 0.03		± 0.01	± 0.07		± 0.07	
C/2004 Q2 (Machholz) <sup>VI</sup>	0.54 ± 0.03	< 0.06	0.14 ± 0.02	1.26 ± 0.10	0.10 ± 0.03	2.03 ± 0.11	5.07 ± 0.51
17P/Holmes <sup>VII</sup>	1.67 ± 0.16	0.344 ± 0.053	0.538 ± 0.075	-	-	2.25 ± 0.43	-
C/2001 A2 (LINEAR) <sup>VIII</sup>	1.24 ± 0.11	0.5 ± 0.1	0.6 ± 0.1	1.2 ± 0.2	0.24 ± 0.05	3.9 ± 0.4	3.9 ± 1.1

<sup>I</sup>Results from 14.5 May 2006 (Dello Russo et al. 2007), with the exception of CH<sub>4</sub> (7 Apr. 2006, Villanueva et al. 2006), and CO (27, 30 May 2006, DiSanti et al. 2007).

<sup>II</sup>Mumma et al. 2003.

<sup>III</sup>2P/Encke on 4 Nov. 2003, except for CO (5 Nov. 2003).

<sup>IV</sup>Radeva et al. (2010): weighted means of mixing ratios from 23, 24 and 25 Nov. 2001. C<sub>2</sub>H<sub>2</sub> is the 3-σ upper limit of the most sensitive measurement (23 & 25 Nov.); and CO is measured on 25 Nov.

<sup>V</sup>Results from 22-23 Dec. 2007 (Bonev et al. 2008). The mixing ratio for C<sub>2</sub>H<sub>6</sub> is the weighted mean from C<sub>2</sub>H<sub>6</sub> v<sub>7</sub> (Bonev et al. 2008) and C<sub>2</sub>H<sub>6</sub> v<sub>5</sub> (this work).

<sup>VI</sup>Results from 28 Nov. 2004 (Bonev et al. 2009), except for CO (29 Nov. 2004). The mixing ratio for C<sub>2</sub>H<sub>6</sub> is the weighted mean from C<sub>2</sub>H<sub>6</sub> v<sub>7</sub> (Bonev et al. 2009) and C<sub>2</sub>H<sub>6</sub> v<sub>5</sub> (this work).

<sup>VII</sup>Results from 27.6 Oct. 2007 (Dello Russo et al. 2008). The mixing ratio for C<sub>2</sub>H<sub>6</sub> is the weighted mean from C<sub>2</sub>H<sub>6</sub> v<sub>7+5</sub> (Dello Russo et al. 2008) and C<sub>2</sub>H<sub>6</sub> v<sub>5</sub> (this work).

<sup>VIII</sup>Results from 9.5 July 2001, except for CO (10.5 July 2001) (Magee Sauer et al. 2008). The mixing ratio for C<sub>2</sub>H<sub>6</sub> is the weighted mean from C<sub>2</sub>H<sub>6</sub> v<sub>7</sub> and C<sub>2</sub>H<sub>6</sub> v<sub>5</sub> (this work).

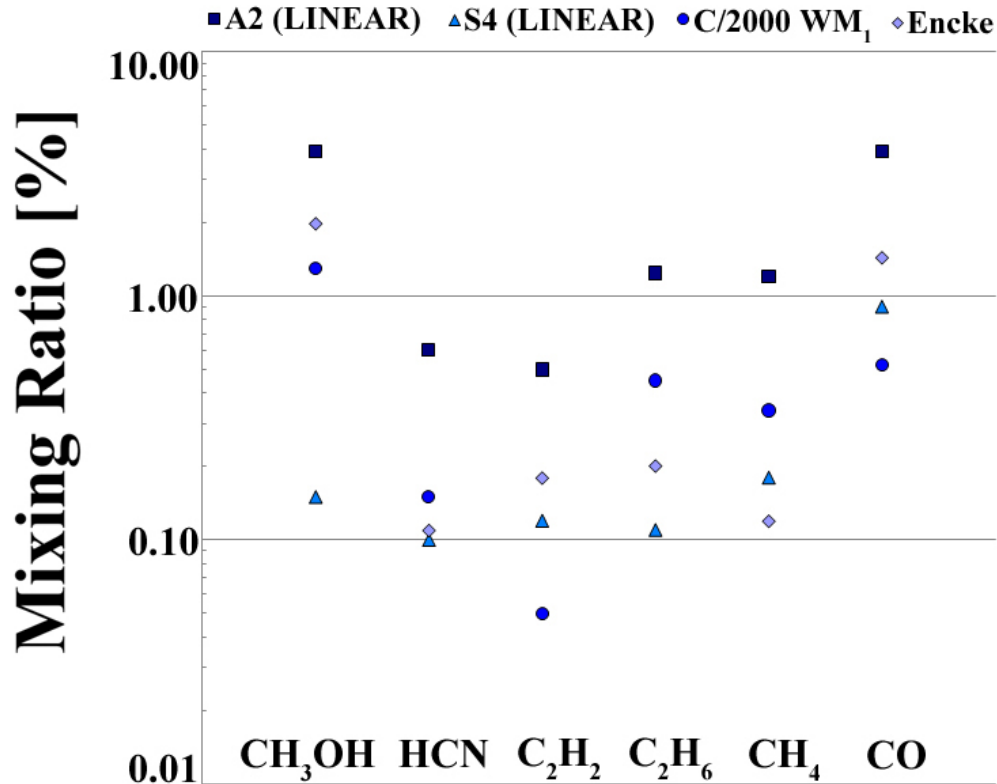


**Figure 6.32.** Mixing ratios in WM<sub>1</sub> and Encke, compared to the organics-enriched comet A2 (LINEAR), and the organics-depleted comet S4 (LINEAR). Molecules are in order of highest to lowest sublimation temperature (Table 5.4).

Table 6.9 illustrates the variety of organic composition among comets: it includes the severely depleted end-members (Oort cloud comet C/1999 S4, and ecliptic comet 73P/Schwassmann-Wachmann 3C); the organics normal comets; comets with unusual composition (such as 8P/Tuttle); and the enriched end-member (Oort cloud comet C/2000 A2 (LINEAR)). No correlation is seen between the dynamical and chemical classification of a comet. Figures 6.33-6.35 present mixing ratios in several comets as a function of their Tisserand parameter. The comets



comprising this sample and their parameters (dynamical and other) are listed in Table 6.10 (this is a larger sample than the one shown in Table 6.9, however, Table 6.9 is intended to give a “snapshot” of the organic composition in terms of relative depletion and enrichment). The organic composition of comets as function of heliocentric distance (at time of measurement), inverse semi-major axis, or overall production rate (which would show the effects of inner coma chemistry) was also investigated, and no correlations were observed.

**Table 6.10.** Comets analyzed by the team at NASA GSFC and their parameters (arranged by increasing  $T_J$ ).

Comet	Date	$T_J$	$r_h$ [AU]	$\log(Q_{H_2O})$
C/2007 N3 <sup>I</sup> (Lulin)	Jan. 30. 2009	-1.365	1.25	-
C/1999 S4 (LINEAR) <sup>II</sup>	Jul. 13. 2000	-0.934	0.81	28.65
C/1999 H1 (Lee) <sup>III</sup>	Aug 21. 1999	-0.896	1.06	29.10
C/1996 B2 (Hyakutake) <sup>III</sup>	March 24. 1996	-0.338	1.06	29.40
C/1995 O1 (Hale-Bopp) <sup>III</sup>	April 6. 1997	0.040	0.918	31.03
C/1999 T1 (McNaught-Hartley) <sup>III</sup>	Jan. 14. 2001	0.234	1.28	29.20
C/2000 WM <sub>1</sub> (LINEAR) <sup>I</sup>	Nov. 23-25. 2001	0.275	1.34	28.32
153P/Ikeya-Zhang <sup>III</sup>	March 22. 2002	0.878	0.51	29.82
C/2001 A2 (LINEAR) <sup>IV</sup>	July 9.2001	0.882	1.16	28.58
C/2004 Q2 (Machholz) <sup>V</sup>	28 & 29 Nov. 2004	1.066	1.493	29.18

C/2007 W1 (Boattini) <sup>I</sup>	Jul. 9. 2008	1.125	0.89	-
8P/Tuttle <sup>VI</sup>	22 & 23 Dec. 2007	1.601	1.16	28.36
73P SW-3C <sup>VII</sup>	April - May 2006	2.784	1.08	27.85
17P/Holmes <sup>VIII</sup>	Oct. 27. 2007	2.858	2.45	29.65
9P Tempel 1 (post-impact) <sup>IX</sup>	Jul. 4. 2005	2.970	1.51	28.24
2P/Encke <sup>I</sup>	Nov. 4-5. 2003	3.025	1.20	27.64

<sup>I</sup>This dissertation (WM<sub>1</sub> published in Radeva et al. 2010)

<sup>II</sup>Mumma et al. 2001 & Mumma et al. 2003.

<sup>III</sup>Mumma et al. 2003 (DiSanti et al. 2002 for H<sub>2</sub>CO in Ikeya-Zhang).

<sup>IV</sup>Magee-Sauer et al. 2003.

<sup>V</sup>Bonev et al. 2009.

<sup>VI</sup>Bonev et al. 2008.

<sup>VII</sup>Dello Russo et al. 2007, with the exception of CH<sub>4</sub> (7 Apr. 2006, Villanueva et al. 2006), and CO (27, 30 May 2006, DiSanti et al. 2007).

<sup>VIII</sup>Dello Russo et al. 2008. The mixing ratio for C<sub>2</sub>H<sub>6</sub> is the weighted mean from C<sub>2</sub>H<sub>6</sub> v<sub>7</sub> (Dello Russo et al. 2008) and C<sub>2</sub>H<sub>6</sub> v<sub>5</sub> (this work).

<sup>IX</sup>Mumma et al. 2005.

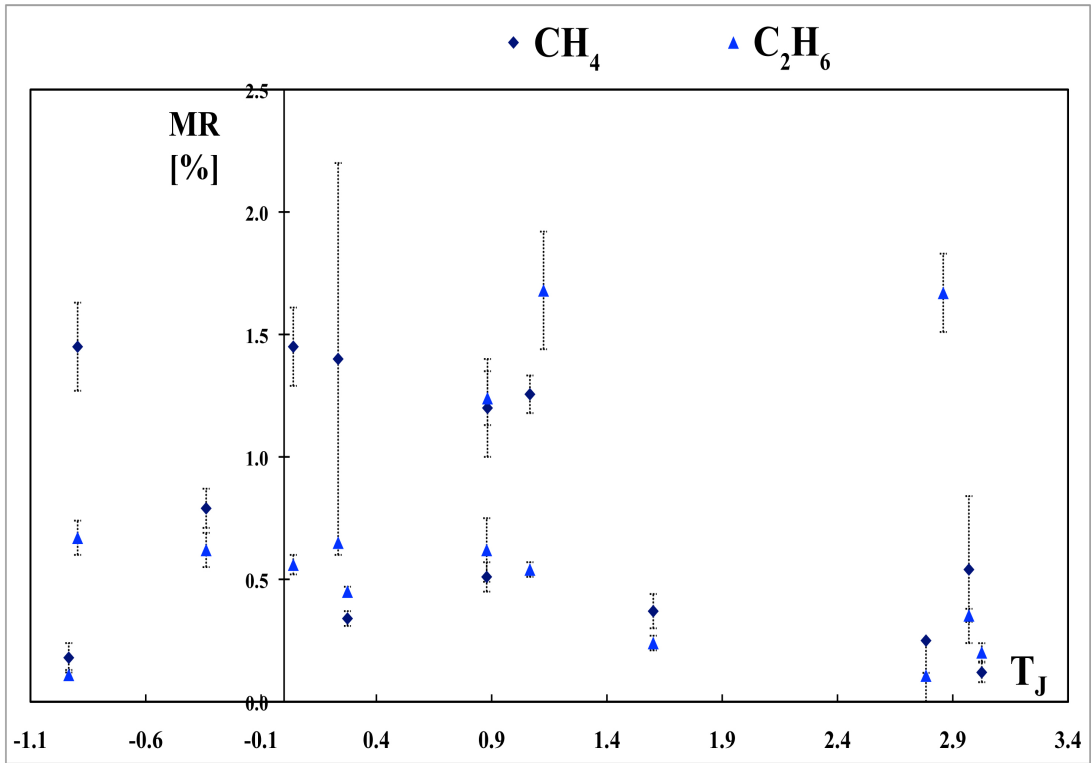


**Figure 6.33.** Mixing ratios of CH<sub>4</sub> and C<sub>2</sub>H<sub>6</sub> in comets as a function of T<sub>J</sub>.

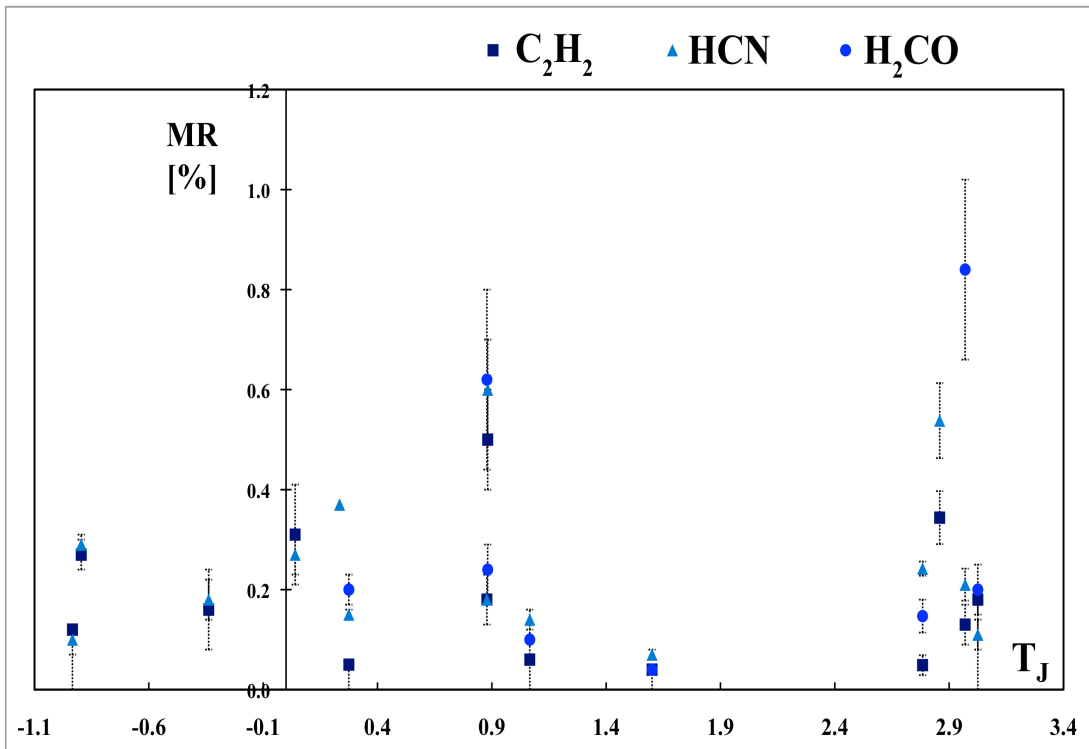


**Figure 6.34.** Mixing ratios of  $C_2H_2$ , HCN and  $H_2CO$  in comets as a function of  $T_J$ .

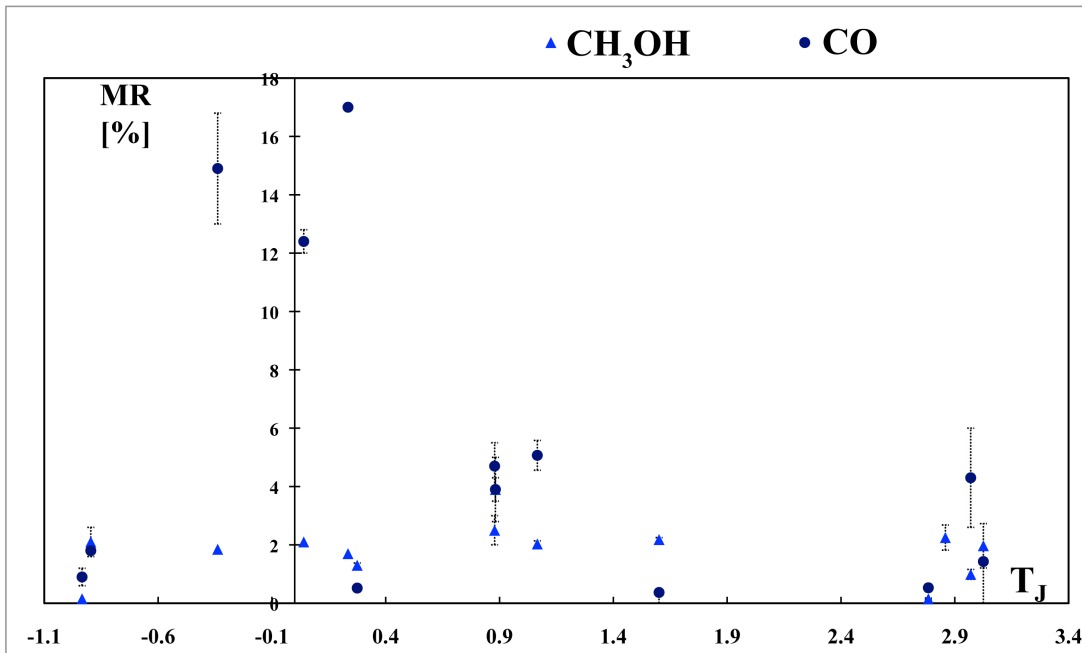


**Figure 6.35.** Mixing ratios of CH<sub>3</sub>OH and CO in comets as a function of  $T_J$ .

The lack of correlation between dynamical class and organic enrichment or depletion of comets (illustrated in Figures 6.33-6.35), supports significant radial mixing in the proto-solar nebula. It is also possible that cometary nuclei contain fractions that formed in different regions, and these fractions would have diverse chemical composition. Heliocentric distance of formation alone is not sufficient to explain the relative depletion or enrichment of comets. Processes that need to be considered include localized heating in the protosolar nebula and the specific chemical reactions that took place in different regions. Another explanation for the possible enrichment of a comet may be its formation farther from the Sun, but at a later point in time when the ionizing solar flux reached greater distances (after

nebular clearing) and produced higher H-atom densities. This, combined with low temperatures to ensure retention on grain surfaces, would contribute to more efficient H-atom addition reactions.

While we do not see a correlation between the chemical composition of a comet and its Tisserand parameter, Jupiter-family comets have a higher probability of being depleted than Oort cloud comets. Among Jupiter-family comets studied at infrared wavelengths, Schwassmann-Wachmann 3, 21P/Giacobini–Zinner (Weaver et al. 1999), 2P/Encke and 6P/d'Arrest (except for CH<sub>3</sub>OH and H<sub>2</sub>CO) are depleted, while 9P/Tempel 1 is normal, and 17P/Holmes is enriched (although organic abundances may be overestimated in this comet due to water-ice). This is consistent with optical observations of daughter species, which show that half of Jupiter family comets are depleted in carbon-chain species (C<sub>2</sub> and C<sub>3</sub>) (A'Hearn et al. 1995). The taxonomy of comets studied at optical wavelengths is based on 85 comets, and further comparison with this database will be feasible when the number of comets analyzed in the infrared also becomes statistically significant.

### *Summary*

Our group is building a taxonomy of comets based on their parent volatile composition, and has identified diversity in the chemistry of observed ecliptic and nearly isotropic comets. A reliable rotational temperature is essential to obtaining accurate production rates of organic volatiles. The newly developed model of the infrared C<sub>2</sub>H<sub>6</sub>  $\nu_5$  band makes C<sub>2</sub>H<sub>6</sub> the fourth molecule, along with H<sub>2</sub>O, HCN and CO, from which a reliable rotational temperature can be determined. Furthermore,

$C_2H_6$   $\nu_5$  is observed simultaneously with  $H_2CO$ ,  $OH$ ,  $CH_4$ ,  $HCN$ ,  $C_2H_2$  and  $H_2O$ , which minimizes some systematic uncertainties in the derived mixing ratios. I applied the new  $C_2H_6$   $\nu_5$  model to high-resolution spectra of comets 17P/Holmes, C/2000 WM<sub>1</sub> (LINEAR), C/2004 Q2 Machholz, C/2001 A2 (LINEAR), C/2007 N3 (Lulin), C/2007 W1 (Boattini), 8P/Tuttle and 2P/Encke. The following findings are reported:

- Mixing ratios extracted for  $C_2H_6$   $\nu_5$  and  $C_2H_6$   $\nu_7$  agree within  $1-\sigma$ , except for the comet A2 (LINEAR). In the case of comet A2, the disagreement may result from temporal variability due to nuclear heterogeneity given the short rotation period of this comet (3 or 6 hours, Nolan et al. 2006, Woodney et al. 2001).
- Rotational temperatures derived from  $C_2H_6$   $\nu_5$ ,  $H_2O$  and  $HCN$  agree within  $1-\sigma$  (except for  $HCN$  in A2 (LINEAR), which disagrees with all other temperatures). This comparison shows that polar species ( $H_2O$ ,  $HCN$ ) and the non-polar  $C_2H_6$  provide similar rotational temperatures. The agreement in temperatures supports the assumption that collisions thermalize rotational populations in the inner coma. Deviations of individual lines in rotational temperature diagrams are explained by blends with other species found in the  $C_2H_6$   $\nu_5$  region:  $H_2CO$ ,  $OH$  and  $CH_3OH$ , although obvious blends were excluded from the analysis. In the case of  $HCN$  in A2 (LINEAR), radiative cooling might be controlling the rotational populations, or  $HCN$  may have a different distribution in the aperture.

- The fluorescence model of  $\text{C}_2\text{H}_6$   $v_5$  can be used to derive reliable production rates and rotational temperatures, and this work establishes a robust method for quantifying additional physical parameters for ethane in comets.



## Chapter 7: Summary of Results

This dissertation contributes to the establishment of a cometary taxonomy based on parent volatile composition, through analysis of the organic composition of the Oort cloud comet C/2000 WM<sub>1</sub> (LINEAR) and the ecliptic comet 2P/Encke, and through the development of a new fluorescence model for the infrared C<sub>2</sub>H<sub>6</sub> v<sub>5</sub> band.

I. The Oort cloud comet C/2000 WM<sub>1</sub> (LINEAR) was observed on 23, 24 and 25 Nov. 2001 with the Near Infrared Echelle Spectrograph on the Keck II telescope. The analysis of the organic composition of this comet showed that WM<sub>1</sub> is severely depleted in CO and C<sub>2</sub>H<sub>2</sub> and moderately depleted in HCN, CH<sub>4</sub> and CH<sub>3</sub>OH. The previously reported depletions of CH<sub>3</sub>OH (Biver et al. 2006) and CO (Biver et al. 2006; Lupu et al. 2007), as well as the mixing ratio for H<sub>2</sub>CO (Biver et al. 2006), were confirmed. The H<sub>2</sub>O production rate measured by SWAS (Bensch and Melnick 2006) on 23 Nov. 2001, and presented by Combi et al. (2008), was also confirmed. The weighted mean rotational temperatures for H<sub>2</sub>O ( $T_{\text{rot}} = 70^{-2}/_{+2}$  K) and HCN ( $T_{\text{rot}} = 78^{-4}/_{+5}$  K) agree within 2- $\sigma$ , and are typical, compared to other comets. The mixing ratios extracted for H<sub>2</sub>CO, CH<sub>3</sub>OH, C<sub>2</sub>H<sub>6</sub>, CH<sub>4</sub>, HCN and C<sub>2</sub>H<sub>2</sub> agree day-by-day for 23-25 Nov. 2001, which suggests homogeneity of this cometary nucleus at the level of accuracy sampled. Considering WM<sub>1</sub>'s levels of depletion, this comet may incorporate material that formed in an organics

depleted region of the Solar System. If such depletion is related to heliocentric distance, WM<sub>1</sub> may have originated closer to the young Sun than "organics-normal" comets (presented in Mumma et al. 2003), but possibly farther than the severely-depleted S4 and 73P/S-W.

- II. The ecliptic comet 2P/Encke was observed on 4, 5 and 6 Nov. 2003 with NIRSPEC on Keck II. I analyzed data from 4 Nov. (KL2 and KL1 settings) and 5 Nov. (MW\_A setting). Production rates and mixing ratios were derived for H<sub>2</sub>O, CH<sub>4</sub>, C<sub>2</sub>H<sub>2</sub>, C<sub>2</sub>H<sub>6</sub>, CH<sub>3</sub>OH, H<sub>2</sub>CO, CO, and HCN. Rotational temperatures for H<sub>2</sub>O ( $T_{\text{rot}} = 24^{-6}_{+13}$  K) and HCN ( $T_{\text{rot}} = 28^{-7}_{+13}$  K), agree within 1- $\sigma$  and are very low compared to those in other comets. The explanation for this may lie in the very low gas production rates in 2P/Encke (a factor of 10 lower than in WM<sub>1</sub> and a factor of 100 lower than in Q2 Machholz), or in the low thermalization efficiency of fast H-atoms, coupled with more efficient radiative cooling. 2P/Encke is depleted in C<sub>2</sub>H<sub>6</sub>, C<sub>2</sub>H<sub>2</sub>, HCN, CH<sub>4</sub> and CO, and normal in H<sub>2</sub>CO and CH<sub>3</sub>OH, in comparison to "organics-normal" comets (Mumma et al. 2003). 2P/Encke has a very short period of 3.3 years and repeated sublimation during its numerous orbits around the Sun could be contributing to its depletion. It is also possible that 2P/Encke formed closer to the Sun than average comets, as previously suggested for WM<sub>1</sub>, but farther than the severely depleted C/1999 S4 or 73P/Schwassmann-Wachmann.
- III. A new fluorescence model for the C<sub>2</sub>H<sub>6</sub>  $\nu_5$  band was developed and used to derive reliable rotational temperatures for this organic molecule. This now

makes C<sub>2</sub>H<sub>6</sub> the fourth molecule, along with H<sub>2</sub>O, HCN and CO, that can be used to derive accurate rotational temperatures, which are essential to obtaining production rates of organic volatiles. Furthermore, C<sub>2</sub>H<sub>6</sub> v<sub>5</sub> is observed simultaneously with H<sub>2</sub>CO, OH, CH<sub>4</sub>, HCN, C<sub>2</sub>H<sub>2</sub> and H<sub>2</sub>O, thus, minimizing systematic uncertainties in the derived mixing ratios. The C<sub>2</sub>H<sub>6</sub> v<sub>5</sub> model was applied to high-resolution spectra of the comets C/2000 WM<sub>1</sub> (LINEAR), 2P/Encke, C/2007 N3 (Lulin), C/2004 Q2 Machholz, 8P/Tuttle, 17P/Holmes, C/2001 A2 (LINEAR) and C/2007 W1 (Boattini). Mixing ratios extracted for C<sub>2</sub>H<sub>6</sub> v<sub>5</sub> and C<sub>2</sub>H<sub>6</sub> v<sub>7</sub> agree within 1- $\sigma$ , except for the comet A2 (LINEAR) (2- $\sigma$ ). Rotational temperatures for C<sub>2</sub>H<sub>6</sub> v<sub>5</sub>, H<sub>2</sub>O and HCN agree within 1- $\sigma$  (except for HCN in A2 (LINEAR)). This supports the assumption that collisions thermalize rotational populations in the inner coma. In the case of HCN in A2 (LINEAR), radiative cooling might be controlling the rotational populations. In conclusion, the fluorescence model of C<sub>2</sub>H<sub>6</sub> v<sub>5</sub> can be used to derive reliable production rates and rotational temperatures for this organic molecule, which is uniquely sampled at infrared wavelengths.

Reliable rotational temperatures and production rates are essential to the accurate analysis of the organic composition of comets. The high resolution infrared study of C/2000 WM<sub>1</sub> presented this comet as the first intermediately depleted member of the sample, analyzed by the team at NASA's GSFC. The value of the analysis of comet 2P/Encke lies in it being the shortest period comet (with smallest perihelion distance) observed in the infrared, which makes it an end-member in the

dynamical sense. Its low rotational temperatures and intermediate organic depletion also pose interesting questions, such as: did this comet form in a warmer region of the proto-solar nebula; did the most volatile species sublime away during its numerous orbits around the Sun; and do low gas production rates explain its very low rotational temperatures?

The sample of comets whose composition has been studied through infrared spectroscopy is increasing, and the current chemical taxonomy includes "organics-depleted", "organics-normal", and "organics-enriched" comets, coming from both main reservoirs: the Oort cloud and the Kuiper belt. However, many more comets need to be observed in order to have a statistically significant sample, which is dynamically and chemically diverse. Currently, no correlation is seen between the dynamical reservoir (Tisserand parameter) and organic composition of a given comet. A statistically significant sample is also necessary in order to explore cosmogonic parameters in comets. Such parameters include the ortho-to-para ratio of H<sub>2</sub>O (providing the formation temperature of the molecule), D/H ratio (from HDO), and isotopic abundances.

Comets are exciting objects that hold the key to understanding how the Solar System formed and evolved. They likely delivered organics and water to the young Earth, and are also potentially dangerous to our home planet. High-resolution infrared spectroscopy provides us with the opportunity to explore cometary origins and the history of our Solar System, and thus, to discover the answers to essential astrobiological questions.

## Appendices

### Appendix I.

Designations, mean frequencies, and nucleus-centered production rates (including sigma), are presented for C<sub>2</sub>H<sub>6</sub> ν<sub>5</sub> lines measured in 2P/Encke, C/2000 WM<sub>1</sub> (LINEAR), C/2007 N3 (Lulin), C/2004 Q2 Machholz, 8P/Tuttle, 17P/Holmes, C/2001 A2 (LINEAR) and C/2007 W1 (Boattini).

**Table A.1.** Quantitative parameters for spectral lines measured in the comets 2P/Encke ( $T_{\text{rot}} = 24$  K, assumed), 8P/Tuttle ( $T_{\text{rot}} = 50$  K, assumed), C/2000 WM<sub>1</sub> (LINEAR) ( $T_{\text{rot}} = 69^{-13}/_{+14}$  K), 17P/Holmes ( $T_{\text{rot}} = 70^{-10}/_{+11}$  K), C/2007 N3 (Lulin) ( $T_{\text{rot}} = 72^{-11}/_{+12}$  K), C/2001 A2 (LINEAR) ( $T_{\text{rot}} = 85^{-14}/_{+13}$  K), C/2007 W1 (Boattini) ( $T_{\text{rot}} = 85$  K, assumed), and C/2004 Q2 Machholz ( $T_{\text{rot}} = 86^{-17}/_{+18}$  K) (listed in order of increasing  $T_{\text{rot}}$ ).

C <sub>2</sub> H <sub>6</sub> ν <sub>5</sub>				
Comet	Line ID	Rest Frequency [cm <sup>-1</sup> ]	Nucleus-centered Production Rate [s <sup>-1</sup> ]	Stochastic Uncertainty of Production Rate [s <sup>-1</sup> ]
17P/Holmes	R9 J'' = 9 → J' = 10	2910.57	3.37E+27	4.30E+26
Lulin			6.70E+26	4.21E+25
A2 (LINEAR)			2.22E+26	1.10E+25
Boattini			2.23E+26	1.04E+25

Q2 Machholz			5.75E+26	4.26E+25
17P/Holmes	R8 $J'' = 8 \rightarrow J' = 9$	2908.91	3.41E+27	3.40E+26
C/2000 WM <sub>1</sub>	R6		6.14E+25	1.03E+25
Q2 Machholz	$J'' = 6 \rightarrow J' = 7$	2905.80	5.19E+26	5.16E+25
17P/Holmes			4.00E+27	2.27E+26
Lulin	R5	2904.20	7.94E+26	3.82E+25
A2 (LINEAR)	$J'' = 5 \rightarrow J' = 6$		2.59E+26	1.00E+25
Boattini			1.50E+26	6.23E+24
C/2000 WM <sub>1</sub>	R4		7.46E+25	1.17E+25
17P/Holmes	$J'' = 4 \rightarrow J' = 5$	2902.74	3.30E+27	2.94E+26
Lulin			6.03E+26	4.20E+25
Encke			6.59E+24	2.13E+24
17P/Holmes	R3	2901.26	2.41E+27	3.17E+26
A2 (LINEAR)	$J'' = 3 \rightarrow J' = 4$		2.05E+26	1.46E+25
Boattini			9.77E+25	8.20E+24
17P/Holmes			3.24E+27	7.10E+26
Boattini	R1	2898.40	7.25E+25	2.70E+25
Q2 Machholz	$J'' = 1 \rightarrow J' = 2$		3.57E+26	1.22E+26
Encke	Q	2895.51	5.93E+24	3.49E+24
8P/Tuttle	branch		6.75E+25	6.18E+24

C/2000 WM <sub>1</sub>			5.16E+25	1.02E+25
17P/Holmes			2.62E+27	3.52E+26
Lulin			6.32E+26	4.35E+25
A2 (LINEAR)			1.49E+26	1.25E+25
Boattini			1.45E+26	1.08E+25
Q2 Machholz			2.87E+26	3.24E+25
Encke	P3 $J'' = 3 \rightarrow J' = 2$	2891.79	3.64E+24	2.28E+24
C/2000 WM <sub>1</sub>			7.32E+25	1.91E+25
17P/Holmes			3.71E+27	5.24E+26
Lulin			6.52E+26	7.59E+25
A2 (LINEAR)			1.73E+26	2.39E+25
Boattini			1.63E+26	1.65E+25
Q2 Machholz			6.01E+26	7.62E+25
Encke	P4 $J'' = 4 \rightarrow J' = 3$	2890.54	4.58E+24	1.96E+24
C/2000 WM <sub>1</sub>			8.36E+25	1.42E+25
17P/Holmes			1.90E+27	3.56E+26
Lulin			4.57E+26	5.68E+25
A2 (LINEAR)			1.34E+26	1.77E+25
Boattini			8.62E+25	9.67E+24
Q2 Machholz			2.08E+26	5.13E+25
C/2000 WM <sub>1</sub>	P5	2889.33	6.94E+25	1.01E+25

17P/Holmes	$J'' = 5 \rightarrow J' = 4$		2.33E+27	2.53E+26
Lulin			4.73E+26	3.41E+25
Boattini			1.50E+26	8.46E+24
Q2 Machholz			4.11E+26	3.91E+25
8P/Tuttle	P6 $J'' = 6 \rightarrow J' = 5$	2888.16	2.34E+25	5.67E+24
C/2000 WM <sub>1</sub>			4.03E+25	8.66E+24
17P/Holmes			2.22E+27	2.34E+26
Lulin			5.14E+26	4.70E+25
A2 (LINEAR)			1.44E+26	1.00E+25
Boattini			1.49E+26	8.99E+24
Q2 Machholz			2.28E+26	3.47E+25
8P/Tuttle			P7 $J'' = 7 \rightarrow J' = 6$	2886.99
C/2000 WM <sub>1</sub>	6.37E+25	7.38E+24		
17P/Holmes	3.05E+27	1.96E+26		
Lulin	5.48E+26	3.47E+25		
A2 (LINEAR)	2.03E+26	8.50E+24		
Q2 Machholz	4.75E+26	3.31E+25		
8P/Tuttle	P8 $J'' = 8 \rightarrow J' = 7$	2885.88	4.06E+25	8.24E+24
C/2000 WM <sub>1</sub>			1.04E+26	1.57E+25
17P/Holmes			1.17E+27	4.12E+26
Lulin			4.81E+26	3.87E+25



A2 (LINEAR)			1.55E+26	1.82E+25
Q2 Machholz			3.87E+26	5.55E+25
C/2000 WM <sub>1</sub>	P9 $J'' = 9 \rightarrow J' = 8$	2884.81	1.01E+26	1.84E+25
17P/Holmes			3.34E+27	3.29E+26
Lulin			4.16E+26	6.62E+25
A2 (LINEAR)			2.08E+26	9.98E+24
Q2 Machholz			5.08E+26	6.79E+25
C/2000 WM <sub>1</sub>			P10 $J'' = 10 \rightarrow J' = 9$	2883.80
17P/Holmes	3.54E+27	3.46E+26		
Lulin	5.67E+26	6.64E+25		
A2 (LINEAR)	1.76E+26	1.33E+25		
Q2 Machholz	2.89E+26	3.76E+25		
17P/Holmes	P11 $J'' = 11 \rightarrow J' = 10$	2882.71		

## Appendix II.

Measured rotational temperatures are expected to decrease due to adiabatic expansion of the gas within several hundred kilometers of the nucleus, and then to increase due to collisions with OH and fast H atoms for comets with very high gas production rate (Combi et al. 2004). The field-of-view of the cometary coma varies between  $\pm 52$  and  $\pm 1053$  km for the sample of comets discussed in Chapter 5. Measurements of rotational temperatures from a smaller field-of-view should yield higher values since they would represent a region closer to the cometary surface. The field-of-view is directly proportional to the cometary geocentric distance  $\Delta$ .

The nuclear surface temperature depends on the solar radiation flux at a given heliocentric distance  $r_h$ , the cometary albedo, latent heat of sublimation, and other factors. A simplified relationship between rotational temperatures and  $r_h$  is:

$T_{rh} = T_1 r_h^{-0.5}$ , where  $T_1$  is the surface temperature at  $r_h = 1$  AU. For adiabatic expansion of water vapor:  $TV^{\gamma-1} = \text{const}$  or  $\frac{T_2}{T_1} = \left(\frac{V_1}{V_2}\right)^{\gamma-1}$ , where the volume of a

sphere is  $V = \frac{4}{3}\pi R^3$ , and the adiabatic index  $\gamma$  is approximately 1.3. For a nucleus of

radius  $R_N$  the temperature at nucleocentric distance  $r$  is then:  $T_R = T_N \left(\frac{R_N}{r}\right)^{0.9}$ .

[Note: The size of the nucleus does not affect the gas temperature at its surface, therefore a larger nucleus would cause a displacement of the coma temperature profile to larger distances.]

The gas number density is expressed as:  $n_{\text{total}} = \frac{Q_{\text{H}_2\text{O}}}{4\pi r^2 V_{\text{outflow}}}$  (assuming

spherically symmetric coma), as discussed in chapter 1. The weighted mean coma temperature for parent volatiles within a nucleocentric beam radius  $R_0$  is then:

$$\langle T_{R_0} \rangle = \frac{\int_{R_N}^{R_0} T_r 4\pi r^2 n_{\text{tot}} dr}{\int_{R_N}^{R_0} 4\pi r^2 n_{\text{tot}} dr} = T_N R_N^{0.9} \frac{\int_{R_N}^{R_0} r^{-0.9} dr}{\int_{R_N}^{R_0} dr} = 10 T_N R_N^{0.9} \frac{(R_0^{0.1} - R_N^{0.1})}{R_0 - R_N}.$$

At a different beam radius ( $R_1$ ),  $\langle T_{R_1} \rangle = 10 T_N R_N^{0.9} \frac{(R_1^{0.1} - R_N^{0.1})}{R_1 - R_N}$ .

The scaling factor would be:  $\frac{\langle T_{R_1} \rangle}{\langle T_{R_0} \rangle} = \frac{(R_1^{0.1} - R_N^{0.1}) R_0 - R_N}{(R_0^{0.1} - R_N^{0.1}) R_1 - R_N}$ . The

average nucleus size  $R_N$  is approximately 2 km, which is negligible compared to the beam size and can be ignored. This provides an effective scaling factor of:

$\frac{\langle T_{R_1} \rangle}{\langle T_{R_0} \rangle} = \left(\frac{R_1}{R_0}\right)^{-0.9}$ , which is used to correct the temperatures presented in Fig.

5.10B and Fig. 5.11B.  $R_0$  is set to 200 km, based on the median of the beam sizes for the sampled comets.

## Bibliography

- A'Hearn, M. F., Belton, M. J. S., Delamere, W. A., Kissel, J., Klaasen, K. P., McFadden, L. A., Meech, K. J., Melosh, H. J., Schultz, P. H., Sunshine, J. M., Thomas, P. C., Veverka, J., Yeomans, D. K., Baca, M. W., Busko, I., Crockett, C. J., Collins, S. M., Desnoyer, M., Eberhardy, C. A., Ernst, C. M., Farnham, T. L., Feaga, L., Groussin, O., Hampton, D., Ipatov, S. I., Li, J.-Y., Lindler, D., Lisse, C. M., Mastrodemos, N., Owen, W. M. (Jr.), Richardson, J. E., Wellnitz, D. D., White, R. L., Deep Impact Impact: Excavating Comet Tempel 1. *Science* 310, 258-264
- A'Hearn, M. F., Millis, R. C., Schleicher, D. O., Osip, D. J., and Birch, P. V., 1995. The Ensemble Properties of Comets: Results from Narrowband Photometry of 85 Comets, 1976-1992. *Icarus*, 118, 2, 223-270
- Arkin, H., & Colton, R. R. 1970, *Statistical Methods* (New York: Barnes & Noble)
- Bensch, F., and Melnick, G. J., 2006. AAS, DPS Meeting #38, #33.04
- Bevington, P. R., & Robinson, D. K. 1992, *Data Reduction and Error Analysis for the Physical Sciences* (New York: McGraw-Hill)
- Biver, N., Bockelée-Morvan, D., Crovisier, J., Lecacheux, A., Frisk, U., Hjalmarson, A., Olberg, M., Florén, H-G., Sandqvist, A., and Kwok, S., 2007. Submillimetre observations of comets with Odin: 2001–2005. *Planetary and Space Science*, 55, 9, 1058-1068
- Biver, N., Bockelée-Morvan, D., Crovisier, J., Lis, D. C., Moreno, R., Colom, P.,

- Henry, F., Herpin, F., Paubert, G., and Womack, M., 2006. Radio wavelength molecular observations of comets C/1999 T1 (McNaught-Hartley), C/2001 A2 (LINEAR), C/2000 WM<sub>1</sub> (LINEAR) and 153P/Ikeya-Zhang. *A&A*, 449 (3), 1255-1270
- Biver, N., Bockelée-Morvan, D., Boissier, J., Colom, P., Crovisier, J., Lecacheux, A., Moreno, R., Paubert, G., Lis, D. C., Sumner, M., Frisk, U., Hjalmarsson, A., Sandqvist, Aa., Kwok, S., Rickman, H., A'Hearn, M. F., and Meech, K., 2005. Radio observations of comet 9P/Tempel 1 before and after Deep Impact. *Bull. Amer. Astron. Soc.* 37, 710.
- Biver, N., Bockelee-Morvan, D., Crovisier, J., Davies, J. K., Matthews, H. E., Wink, J. E., Rauer, H., Colom, P., Dent, W. R. F., Despois, D., Moreno, R., Paubert, G., Jewitt, D., and Senay, M., 1999a. Spectroscopic monitoring of comet C/1996 B2 (Hyakutake) with the JCMT and IRAM radio telescopes. *Astron. J.*, 118, 1850-1872
- Bockelee-Morvan, D., Crovisier, J., Mumma, M. J., and Weaver, H. A., 2004. The Composition of Cometary Volatiles. *Comets II*. Edited by Festou, M. C., Keller, H. U., and Weaver, H. A., The University of Arizona Press, Tucson, Arizona
- Bonev, B. P., Mumma, M. J., Gibb, E. L., DiSanti, M. A., Villanueva, G. L., Magee-Sauer, K., and Ellis, R. S., 2009. Comet C/2004 Q2 (Machholz): Parent Volatiles, a Search for Deuterated Methane, and Constraint on the CH<sub>4</sub> Spin Temperature. *ApJ*, 699, 1563-1572

- Bonev, B. P., Mumma, M. J., Radeva, Y. L., DiSanti, M. A., Gibb, E. L., and Villanueva, G. L., 2008. The Peculiar Volatile Composition of Comet 8P/Tuttle: A Contact Binary of Chemically Distinct Cometesimals. *ApJ*, 680, L61-L64
- Bonev, B. P., Mumma, M. J., Villanueva, G. L., DiSanti, M. A., Ellis, R. S., Magee-Sauer, K., and Dello Russo N., 2007. A Search for Variation in the H<sub>2</sub>O Ortho-Para Ratio and Rotational Temperature in the Inner Coma of Comet C/2004 Q2 (Machholz). *ApJ*, 661, L97-L100
- Bonev, B. P. 2005, Towards a chemical taxonomy of comets: infrared spectroscopic methods for quantitative measurements of cometary water, University of Toledo, dissertation
- Bonev, B. P., Mumma, M. J., Dello Russo N., Gibb, E. L., DiSanti, M. A., and Magee-Sauer, K., 2004. Infrared OH Prompt Emission as a Proxy of Water production in Comets: Quantitative Analysis of the Multiplet Near 3046 cm<sup>-1</sup> in Comets C/1999 H1 (Lee) and C/2001 A2 (LINEAR). *ApJ*, 615, 1048-1053
- Brownlee, D., et al., 2006. Comet 81P/Wild 2 Under a Microscope. *Science*, 314 (5806), 1711-1716
- Carusi, A., Kresák, L., and Valsecchi, G. B., 1995. Conservation of the Tisserand Parameter at Close Encounters of Interplanetary Objects with Jupiter. *Earth, Moon, and Planets*, 68 (1-3), 71-94
- Chin, G., and Weaver, H. A., 1984. Vibrational and rotational excitation of CO in comets: Nonequilibrium calculations. *ApJ*, 285, 858-869
- Clough, S. A., Shephard, M. W., Mlawer, E. J., Delamere, J. S., Iacono, M. J., Cady-Pereira, K., Boukabara, S. and Brown, P. D., 2005. Atmospheric radiative transfer

- modeling: a summary of the AER codes, Short Communication, *J. Quant. Spectrosc. Radiat. Transfer*, 91, 233-244
- Combi, M. R., Makinen, J. T. T., Henry, N. J., Bertaux, J.-L., and Quemerais, E., 2008. Solar and Heliospheric Observatory/Solar Wind Anisotropies observations of five moderately bright comets: 1999-2002, *Astron. J.*, 135, 1533-1550
- Combi, M. R., Harris, W. M., and Smyth, W. H., 2004. Gas Dynamics and Kinetics in the Cometary Coma: Theory and Observations. *Comets II*. Edited by Festou, M. C., Keller, H. U., and Weaver, H. A., The University of Arizona Press, Tucson, Arizona
- Crovisier, J., Cometary diversity and cometary families. In *XVIIIemes Rencontres de Blois: Planetary Science: Challenges and Discoveries* (in press), edited by L. Celnikier (arXiv:astro-ph/0703785, 2007)
- Crovisier, J., Biver, N., Bockelee-Morvan, D., Boissier, J., Colom, P., Moreno, R., Lis, D.C., Paubert, G., Despois, D., Gunnarsson, M., Weaver, H.A., 2005. Chemical diversity of comets observed at radio wavelengths in 2003–2005. *Bull. Am. Astron. Soc.*, 37, 646
- Crovisier, J., 1994. Photodestruction rates for cometary parent molecules. *J. Geophysical Research*, 99, E2, 3777-3781
- Crovisier, J., and Encrenaz, Th., 1983. Infrared fluorescence of molecules in comets - The general synthetic spectrum. *A&A*. 126 (1), 170-182
- Dang-Nhu, M., Pine, A. S., and Lafferty, W. J., 1984, Les intensites dans les bandes  $\nu_5$ ,  $\nu_7$ , et  $\nu_8 + \nu_{11}$  de l'ethane  $^{12}\text{C}_2\text{H}_6$ . *Can. J. Phys.* 62, 512–519

- De Pater, I. and Lissauer, J. J., 2005. Planetary Sciences. Cambridge University Press, United Kingdom
- Dello Russo, N., Vervack, R. J., Weaver, H. A., Kawakita, H., Kobayashi, H., Biver, N., Bockelée-Morvan, D., and Crovisier, J., 2009. The Parent Volatile Composition of 6P/d'Arrest and a Chemical Comparison of Jupiter-family Comets Measured at Infrared Wavelengths. *ApJ*, 703, 187-197
- Dello Russo, N., Vervack, R. J., Weaver, H. A., Montgomery, M. M., Deshpande, R., Fernandez, Y.R., and Martin, E. L., 2008. The volatile composition of comet 17P/Holmes after its extraordinary outburst. *ApJ*, 680, 793-802
- Dello Russo, N., Vervack, R. J., Weaver, H.A., Biver, N., Bockelée-Morvan, D., Crovisier, J., and Lisse, C. M., 2007. Compositional homogeneity in the fragmented comet 73P/Schwassmann-Wachmann 3. *Nature* 448, 172 – 175
- Dello Russo, N., DiSanti, M. A., Magee-Sauer, K., Gibb, E. L., Mumma, M. J., Barber, R. J., and Tennyson, J., 2004. Water production and release in comet 153P/Ikeya-Zhang (C/2002 C1): accurate rotational temperature retrievals from hot-band lines near 2.9- $\mu\text{m}$ . *Icarus*, 168, 186-200
- Dello Russo, N., Mumma, M. J., DiSanti, M. A., Magee-Sauer, K., and Novak, R., 2001. Ethane production and release in comet C/1999 O1 Hale-Bopp. *Icarus* 153, 162-179
- DiSanti, M. A., and Mumma, M. J., 2008. Reservoirs for comets: compositional differences based on infrared observations. *Space Sci. Rev.*, 138, 127-145



- DiSanti, M.A., Anderson, W. M., Villanueva, G. L., Bonev, B. P., Magee-Sauer, K., Gibb, E. L., and Mumma, M. J., 2007. Depleted carbon monoxide in fragment C of the Jupiter-family comet 73P/Schwassmann-Wachmann 3. *ApJ* 661, L101-104
- DiSanti, M. A., Bonev, B. P., Magee-Sauer, K., Dello-Russo, N., Mumma, M. J., Reuter, D. C., and Villanueva, G. L., 2006. Detection of Formaldehyde Emission in Comet C/2002 T7 (LINEAR) at Infrared Wavelengths: Line-by-line Validation of Modeled Fluorescent Intensities. *ApJ*, 650, 470-483
- DiSanti, M. A., Dello Russo, N., Magee-Sauer, K., Gibb, E. L., Reuter, D. C., and Mumma, M. J., 2002. CO, H<sub>2</sub>CO, and CH<sub>3</sub>OH in comet 2002 C1 (Ikeya-Zhang), in *Proceedings Asteroids, Comets, Meteors 2002*. ESA-SP, vol. 500 (Berlin, 2002), 571–574
- DiSanti, M. A., Mumma, M. J., Dello-Russo, N., Magee-Sauer, K., 2001. Carbon Monoxide production and excitation in comet C/1995 O1 (Hale-Bopp): Isolation of native and distributed CO sources. *Icarus*, 153, 361-390
- Dones, L., Weissman, P. R., Levison, H. F., and Duncan, M. J., 2004, In *Comets II*, ed. M. C. Festou, H. U. Keller, H. A. Weaver, (Tucson, AR: Univ. Arizona Press), 153
- Duncan, M. J., 2008. Dynamical origin of comets and their reservoirs. *Space Sci. Rev.*, 138, 109-126
- Edwards, D. P., 1992, GENLN2: A general line-by-line atmospheric transmittance and radiance model, Version 3.0 description and users guide, NCAR/TN-367-STR, National Center for Atmospheric Research, Boulder, CO

- Fink, U., 2009, A taxonomic survey of comet composition 1985–2004 using CCD spectroscopy. *Icarus*, 201, 1, 311-334
- Francis, P. J., 2008. The Demographics of Long-Period Comets. *ApJ*, 635 (2), pp. 1348-1361
- HORIZONS Web-Interface, JPL, Caltech: <http://ssd.jpl.nasa.gov/horizons.cgi>
- Gibb, E. L., DiSanti, M. A., Magee-Sauer, K., Dello Russo, N., Bonev, B. P., Mumma, M. J., 2007. The organic composition of C/2001 A2 (LINEAR) II. Search for heterogeneity within a comet nucleus. *Icarus*, 188, 224-232
- Gibb, E. L., Mumma, M. J., Dello Russo, N., DiSanti, M. A. and Magee-Sauer, K., 2003. Methane in Oort cloud comets. *Icarus*, 165, 391-406
- Gladman, B. 2005, The Kuiper Belt and the Solar System's Comet Disk. *Science*, 307, 71-75
- Haghighipour, N., 2009, Dynamics, Origin, and Activation of Main Belt Comets. eprint arXiv:0911.4154; To appear in the proceedings of IAU Symposium 263: Icy Bodies of the Solar System (Eds. D. Lazzaro, D. Prialnik, o. Schulz and J.A. Fernandez), Cambridge Univ. Press
- Herzberg, G., 1949, *Molecular Spectra and Molecular Structure. II. Infrared and Raman Spectra of Polyatomic Molecules*, D. Van Nostrand Company, Inc., New York
- Hoel, P. G. 1984, *Introduction to Mathematical Statistics* (New York: Wiley)
- Hollas, J. M., 1996, *Modern Spectroscopy*, John Wiley & Sons Ltd, England
- Hsieh, H. H., and Jewitt, D., 2006. A Population of Comets in the Main Asteroid Belt. *Science*, 312, 561-563

- Kelley, M. S., and Wooden, D. H., 2009. The composition of dust in Jupiter-family comets inferred from infrared spectroscopy. *Planetary & Space Sci.*, 57 (10), 1133-1145
- Kim, S-J., 1996. The Swings effects of the A-X system and  $v'' = 1-0$  band of CO. *Journal of the Korean Astron. Soc.*, 29, 223-243
- Kobayashi, H., and Kawakita, H., 2009. Formation Conditions of Icy Materials in Comet C/2004 Q2 (Machholz). I. Mixing Ratios of Organic Volatiles. *ApJ*, 703 (1), 121-130
- Lamy, P. L., Toth, I., Fernandez, Y. R., and Weaver, H. A., 2004. The Sizes, Shapes, Albedos and Colors of Cometary Nuclei. *Comets II*. Edited by Festou, M. C., Keller, H. U., and Weaver, H. A., The University of Arizona Press, Tucson, Arizona
- Lecacheux, A., Biver, N., Crovisier, J., Bockelée-Morvan, D., Baron, P., Booth, R. S., Encrenaz, P., Floren, H.-G., Frisk, U., Hjalmarson, A., Kwok, S., Mattila, K., Nordh, L., Olberg, M., Olofsson, A. O. H., Rickman, H., Sandqvist, Aa., Scheele, F. von, Serra, G., Torchinsky, S., Volk, K., and Winnberg A., 2003. Observations of water in comets with Odin, *A&A*, 402, L55-L58
- Lecuyer, C., Gillet, P., and Robert, F., 1998. The hydrogen isotope composition of seawater and the global water cycle. *Chem. Geology*, 145, 3-4, 249-261
- Levison, H.F. 1996, Comet taxonomy, ASP Conference Series, 107, 173-191
- Li, J-Y, A'Hearn, M. F., Belton, M. J. S., Crockett, C. J., Farnham, T. L., Lisse, C. M., McFadden, L. A., Meech, K. J., Sunshine, J. M., Thomas, P. C., and Veverka, J. 2007. Deep Impact photometry of Comet 9P/Tempel 1, *Icarus* 187, 1,

- Lin, Z.-Y., Chang, C.-P., and Ip, W.-H., 2007. A Spectrophotometric Study of the Coma of Comet C/2001 A2 (LINEAR). *Astron. J.* 133, 1861-1867
- Lupu, R. E., Feldman, P. D., Weaver, H. A. and Tozzi G., 2007. The fourth positive system of carbon monoxide in the Hubble Space Telescope spectra of comets, *ApJ* 670, 1473-1484
- Magee-Sauer, K., Mumma, M. J., DiSanti, M. A., Dello Russo, N., Gibb, E. L., Bonev, B. P., and Villanueva, G. L., 2008. The organic composition of comet C/2001 A2 (LINEAR) I. Evidence for an unusual organic chemistry. *Icarus*, 194, 347-356
- Magee-Sauer, K., Dello Russo, N., DiSanti, M.A., Gibb, E., Mumma, M.J., 2002b. Production of HCN and C<sub>2</sub>H<sub>2</sub> in Comet C/2002 C1 Ikeya-Zhang on UT April 13.8 2002. In: Warmbein, B. (Ed.), *The Proceedings for the Asteroids, Comets, Meteors Conference, Berlin, Germany 2002*. In: ESA SP, vol. 500. ESA, Noordwijk, 549-552.
- McLean, I. S., Becklin, E. E., Bendiksen, O., Brims, G., Canfield, J., Figer, D. F., Graham, J. R., Hare, J., Lacayanga, F., Larkin, J. E., Larson, S. B., Levenson, N., Magnone, N., Teplitz, H., and Wong, W., 1998. Design and development of NIRSPEC: a near-infrared echelle spectrograph for the Keck II telescope. *Proc. SPIE Vol. 3354*, p. 566-578, *Infrared Astr. Instr.*, Albert M. Fowler; Ed.
- Mumma, M. J., DiSanti, M. A., Magee-Sauer, K., Bonev, B. P., Villanueva, G. L., Kawakita, H., Dello Russo, N., Gibb, E. L., Blake, G. A., Lyke, J. E., Campbell,

- R. D., Aycock, J., Conrad, A., and Hill, G. M., 2005. Parent Volatiles in Comet 9P/Tempel 1: Before and After Impact. *Science*, 14, 270-274
- Mumma, M. J., DiSanti, M. A., Dello Russo, N., Magee-Sauer, K., Gibb, E., and Novak, R., 2003. Remote infrared observations of parent volatiles in comets: a window on the early solar system. *Adv. Space Res.*, 31(12), 2563-2575
- Mumma, M. J., Dello Russo, N., DiSanti, M. A., Magee-Sauer, Novak, R., Brittain, S., Rettig, T., McLean, I. S., Reuter, D. C., Xu, and Li-H., 2001. Organic composition of C/1999 S4 (LINEAR): A comet formed near Jupiter? *Science*, 292(5520), 1334-1339
- Nakano, S., OAA Computing Section Circular NKK 955, 13 Aug 2003, <http://www.oaa.gr.jp/~oaacs/nk/nk955.htm>
- Nolan, M. C., Harmon, J. K., Howell, E. S., Campbell, D. B., and Margot, J-L., 2006. Detection of large grains in the coma of Comet C/2001 A2 (LINEAR) from Arecibo radar observations. *Icarus* 181, 2, 432-441
- Pine, A. S., and Lafferty, W. J., 1982, Torsional splittings and assignments of the Doppler-limited spectrum of ethane in the C-H stretching region. *J. Res. Natl. Bur. Standard.* 87, 237–256
- Porter, M. J., 2000. Spectroscopy on Small Telescopes: the Echelle Spectrograph. *Astrophysics and Space Science* 273, 217–224
- Radeva, Y. L., Mumma, M. J., Bonev, B. P., DiSanti, M. A., Villanueva, G. L., Magee-Sauer, K., Gibb, E., and Weaver, H. A., 2010. The organic composition of

- comet C/2000 WM<sub>1</sub> (LINEAR) revealed through infrared spectroscopy. *Icarus*, 206, 764- 777
- Reuter, D. C., Mumma, M. J., and Nadler, S., 1989. Infrared fluorescence efficiencies for the nu<sub>1</sub> and nu<sub>5</sub> bands of formaldehyde in the solar radiation field. *ApJ*, 341, 1045-1058
- Salyk, C., Blake, G. A., Mumma, M. J., Bonev, B. P., DiSanti, M. A., Villanueva, G. L., Radeva, Y. L., Magee-Sauer, K., and Gibb, E. L., 2007. Comet 17P/Holmes. *IAU Circ.*, 8890, 1 (2007). Edited by Green, D. W. E.
- Sekanina, Z., 1991. Encke, the comet. *Royal Astronomical Society of Canada, Journal* (ISSN 0035-872X), 85, 324-376
- Simeckova, M., Jacquemart, D., Rothman, L. S., Gamache, R. R., and Goldman, A., 2006. Einstein A-coefficients and statistical weights for molecular absorption transitions in the HITRAN database, *J. Quant. Spectrosc. Radiat. Transfer*, 98 (2), 130-155
- Swings P., 1941. Complex structure of cometary bands tentatively ascribed to the contour of the solar spectrum. *Lick Obs. Bull.*, 508, 131–136
- Tozzi G. P., Feldman P. D., and Festou M. C., 1998. Origin and production of C(<sup>1</sup>D) atoms in cometary comae. *Astron. Astrophys.*, 330, 753–763.
- Tsiganis, K., Gomes, R., Morbidelli, A., and Levison, H. F. 2005. Origin of the orbital architecture of the giant planets of the Solar System. *Nature*, 435, 459-461
- Villanueva, G. L., Mumma, M.J., Bonev, B. P., DiSanti, M. A., Gibb, E. L., Boehnhardt, H., and Lippi, M., 2009. A sensitive search for deuterated water in comet 8P/Tuttle. *ApJ* 690, L5–9.

- Villanueva, G. L., Bonev, B. P., Mumma, M.J., Magee-Sauer, K., DiSanti, M. A., Salyk, C., and Blake, G. A., 2006. The volatile composition of the split ecliptic comet 73P/Schwassmann-Wachmann 3: a comparison of fragments C and B. *ApJ* 650, 87-90
- Watson, J., 1992. Quadratic Herman-Wallis factors for symmetric- and asymmetric-top molecules. *Journal of Molecular Spectroscopy*. 153, 211-224
- Weaver, H. A., Chin, G., Bockelée-Morvan, D., Crovisier, J., Brooke, T. Y., Cruikshank, D. P., Geballe, T. R., Kim, S. J., and Meier, R., 1999. An Infrared Investigation of Volatiles in Comet 21P/Giacobini-Zinner. *Icarus*, 142, 2, 482-497
- Weaver, H. A., Mumma, M. J., 1984. Infrared molecular emissions from comets. *ApJ*, 276, 782-797
- Wilson, E. B., 1938. Nuclear Spin and Symmetry Effects in the Heat Capacity of Ethane Gas. *J. Chem. Physics*, 6, 740-745
- Woodney, L.M., Schleicher, D.G., Greer, R., 2001. Activity and morphology of Comet LINEAR (2001 A2). *Bull. Am. Astron. Soc.* 33, 1121
- Xie, X., and Mumma, M.J. 1996. Monte Carlo simulation of cometary atmospheres: application to comet P/Halley at the time of the Giotto Spacecraft encounter. I. Isotropic Model. *ApJ* 464, 442-456
- Xie, X., and Mumma, M.J. 1996. Monte Carlo simulation of cometary atmospheres: application to comet P/Halley at the time of the Giotto Spacecraft encounter. II. Axisymmetric Model. *ApJ* 464, 457-475

- Xie, X., and Mumma, M.J. 1992. The effect of electron collisions on rotational populations of cometary water. *ApJ* 386, 720-728
- Yamamoto, T., 1985. Formation environment of cometary nuclei in the primordial solar nebula. *Astron. Astrophys.* 142, 31-36
- Yamamoto, T., 1982. Evaluation of infrared line emission from constituent molecules of cometary nuclei. *Astron. Astrophys.* 109, 326-330
- Yang, B., Jewitt, D., Schelte, B. J., 2009. Comet 17/P/Holmes in outburst: The near infrared spectrum. *AJ*, 137, 5, 4538-4546